Identification
of an atypical peptide binding mode
of the BTB domain
of the transcription factor MIZ1
with a HUWE1-derived peptide

Identifikation eines neuen Bindungsmodus zwischen der BTB-Domäne des Transkriptionsfaktors MIZ1 und eines Peptids aus der HECT-E3-Ligase HUWE1

Doctoral thesis

for a doctoral degree

at the Graduate School of Life Sciences,

Julius-Maximilians-Universität Würzburg,

Section Biomedicine

submitted by

Barbara Orth

from

Limburg a. d. Lahn, Germany

Würzburg 2021

Submitted on: ……………………………………

Members of the Thesis Committee

Chairperson: Prof. Dr. Thomas Dandekar

Primary Supervisor: Dr. Sonja Lorenz

Supervisor (Second):   Prof. Dr. Martin Eilers

Supervisor (Third):   Prof. Dr. Volker Dötsch

Date of Public Defence: ……………………………………

Date of Receipt of Certificates: ……………………………………

Table of contents

Summary

Ubiquitination is a posttranslational modification with immense impact on a wide range of cellular processes, including proteasomal degradation, membrane dynamics, transcription, translation, cell cycle, apoptosis, DNA repair and immunity. These diverse functions stem from the various ubiquitin chain types, topologies, and attachment sites on substrate proteins. Substrate recruitment and modification on lysine, serine or threonine residues is catalyzed by ubiquitin ligases (E3s). An important E3 that decides about the fate of numerous substrates is the HECT-type ubiquitin ligase HUWE1. Depending on the substrate, HUWE1 is involved in different processes, such as cell proliferation and differentiation, DNA repair, and transcription. One of the transcription factors that is ubiquitinated by HUWE1 is the MYC-interacting zinc finger protein 1 (MIZ1). MIZ1 is a BTB/POZ (Bric-à-brac, Tramtrack and Broad-Complex/Pox virus and zinc finger) zinc finger (ZF) protein that binds to DNA through its 13 C2H2-type zinc fingers and either activates or represses the transcription of target genes, including genes involved in cell cycle arrest, such as *P21CIP1* (*CDKN1A*). The precise functions of MIZ1 depend on its interactions with the MYC-MAX heterodimer, but also its heterodimerization with other BTB-ZF proteins, such as BCL6 or NAC1. How MIZ1 interacts with HUWE1 has not been studied and, as a consequence, it has not been possible to rationally develop tools to manipulate this interaction with specificity in order to better understand the effects of the interaction on the transcriptional function of MIZ1 on target genes or processes downstream. One aspect of my research, therefore, aimed at characterizing the MIZ1-HUWE1 interaction at a structural level. I determined a crystal structure of the MIZ1-BTB-domain in complex with a peptide, referred to as AS^C, derived from a C-terminal region of HUWE1, previously named 'activation segment'. The binding mode observed in this crystal structure could be validated by binding and activity assays *in vitro* and by cell-based co-IP experiments in the context of N-terminally truncated HUWE1 constructs. I was not able to provide unambiguous evidence for the identified binding mode in the context of full-length HUWE1, indicating that MIZ1 recognition by HUWE1 requires yet unknown regions in the cell. While the structural details of the MIZ1-HUWE1 interaction remains to be elucidated in the context of the full-length proteins, the binding mode between $MIZ1^{BTB}$ and AS^C

revealed an interesting, atypical structural feature of the BTB domain of MIZ1 that, to my knowledge, has not been described for other BTB-ZF proteins: The B3 region in MIZ1[BTB] is conformationally malleable, which allows for a HUWE1-AS[C]-peptide-mediated β-sheet extension of the upper B1/B2-strands, resulting in a mixed, 3-stranded β-sheet. Such β-sheet extension does not appear to occur in other homo- or heterodimeric BTB-ZF proteins, including MIZ1-heterodimers, since these proteins typically possess a pre-formed B3-strand in at least one subunit. Instead, BCL6-co-repressor-derived peptides (SMRT and BCOR) were found to extend the lower β-sheet in BCL6[BTB] by binding to an adjacent 'lateral groove'. This interaction follows a 1:1 stoichiometry, whereas the MIZ1[BTB]-AS[C]-complex shows a 2:1 stoichiometry. The crystal structure of the MIZ1[BTB]-AS[C]-complex I determined, along with comparative binding studies of AS[C] with monomeric, homodimeric, and heterodimeric MIZ1[BTB] variants, respectively, suggests that AS[C] selects for MIZ1[BTB] homodimers. The structural data I generated may serve as an entry point for the prediction of additional interaction partners of MIZ1 that also have the ability to extend the upper β-sheet of MIZ1[BTB]. If successful, such interaction partners and structures thereof might aid the design of peptidomimetics or small-molecule inhibitors of MIZ1 signaling. Proof-of-principle for such a structure-guided approach targeting BTB domains has been provided by small-molecule inhibitors of BCL6[BTB]-co-repressors interactions. If a similar approach led to molecules that interfere with specific interactions of MIZ1, they would provide intriguing probes to study MIZ1 biology and may eventually allow for the development of MIZ1-directed cancer therapeutics.

Zusammenfassung

Ubiquitinierung ist eine posttranslationale Modifikation mit weitreichendem Einfluss auf eine Vielzahl von zellulären Prozessen, wie proteasomale Degradation, Membrandynamik, Transkription, Translation, Zellzyklus, Apoptose, DNA-Reparatur und Immunität. Grundlage für diese Diversität ist die Möglichkeit, dass Substrate an unterschiedlichen Stellen mit verschiedenen Ubiquitin-Kettentypen modifiziert werden können. Die Substratrekrutierung und -modifikation an Lysin-, Serin oder Threonin-Resten wird durch Ubiquitin-Ligasen (E3s) katalysiert. Eine wichtige Ubiquitin-Ligase, die zahlreiche Substrate reguliert, ist die HECT-Ligase HUWE1. Abhängig vom Substrat ist HUWE1 an verschiedenen Prozessen, wie der Zellproliferation und -differenzierung, DNA-Reparatur, aber auch Transkription beteiligt. Ein Transkriptionsfaktor, der von HUWE1 ubiquitiniert wird, ist MIZ1 (MYC-interacting zinc finger protein 1). MIZ1 ist ein BTB/POZ (Bric-à-brac, Tramtrack and Broad-Complex/Pox Virus and Zinc finger) Zinkfinger(ZF)-Protein, das über seine 13 C2H2-Zinkfinger an DNA bindet und so die Transkription von verschiedenen Zielgenen aktivieren oder reprimieren kann. MIZ1-Zielgene sind unter anderem am Zellzyklusarrest beteiligt, wie z.B. das Gen *P21CIP1 (CDKN1A)*. Die biologischen Funktionen von MIZ1 werden unter anderem durch seine Interaktion mit dem MYC-MAX-Heterodimer, aber auch durch Heterodimerisierung mit anderen BTB-ZF-Proteinen, wie BCL6 oder NAC1, reguliert.

Wie MIZ1 mit der HUWE1-Ligase interagiert, wurde bislang strukturell noch nicht untersucht, weshalb noch nicht gezielt kleine Moleküle zur Manipulation der Interaktion entwickelt werden konnten, um Einfluss auf die transkriptionellen Funktionen von MIZ1 oder seiner Zielgene zu nehmen. Meine Untersuchungen zielten daher unter anderem darauf ab, die MIZ1-HUWE1-Interaktion auf struktureller Ebene zu charakterisieren. Ich konnte eine Kristallstruktur der MIZ1-BTB-Domäne in Komplex mit dem HUWE1-Peptid AS^C lösen, dessen Sequenz in der C-terminalen Region von HUWE1 zu finden ist und zuvor als „activation segment" definiert wurde.

Der in dieser Kristallstruktur beobachtete Bindungsmodus konnte durch Bindungs- und Aktivitätsassays *in vitro* und durch co-IP-Experimente in zellbasierten Assays validiert werden, jedoch nur im Zusammenhang mit N-terminal verkürzten

HUWE1-Konstrukten. Es war mir nicht möglich, diesen Bindungsmodus im Kontext des HUWE1-Proteins voller Länge nachzuweisen, was darauf hindeutet, dass bei der MIZ1-Erkennung durch HUWE1 in der Zelle andere Regionen beteiligt sein könnten. Während die strukturellen Details der MIZ1-HUWE1-Interaktion im Kontext der Proteine voller Länge noch aufgeklärt werden müssen, zeigte der Bindungsmodus zwischen MIZ1^{BTB} und AS^C ein atpyisches Strukturmerkmal der BTB-Domäne von MIZ1, das meines Wissens bislang in keinem anderen BTB-ZF-Protein beschrieben wurde: Die B3-Region in MIZ1^{BTB} zeigt eine untypische konformationelle Flexibilität, die es erlaubt, dass das HUWE1-AS^C-Peptid die B1/B2-Stränge im oberen Segment von MIZ1^{BTB} zu einem 3-strängigen β-Faltblatt erweitert. Eine solche β-Faltblatt-Erweiterung scheint in anderen homo- oder heterodimeren BTB-ZF-Proteinen, einschließlich MIZ1-Heterodimeren, nicht aufzutreten, da diese Proteine typischerweise bereits einen B3-Strang in mindestens einer Untereinheit aufweisen. Stattdessen konnte beobachtet werden, dass Peptidliganden, wie sie von den BCL6-Co-Repressoren SMRT und BCOR abgeleitet wurden, ein β-Faltblatt im unteren Segment von BCL6^{BTB} erweitern, indem sie in der sogenannten „lateral groove" binden, die in unmittelbarer Nähe des betreffenden β-Faltblattes lokalisiert ist. Während die Interaktion von BCL6^{BTB} mit Co-Repressor-Peptiden eine 1:1 Stöchiometrie zeigt, beobachtete ich für den MIZ1^{BTB}-AS^C-Komplex eine 2:1 Stöchiometrie. Die Kristallstruktur des MIZ1^{BTB}-AS^C-Komplexes, zusammen mit Bindungsassays, die die Interaktion zwischen AS^C und monomerem, homodimerem bzw. heterodimerem MIZ1^{BTB} untersuchten, deuten darauf hin, dass AS^C spezifisch mit MIZ1^{BTB}-Homodimeren interagiert. Daher könnten die von mir gewonnenen Strukturinformationen dazu dienen, weitere MIZ1-Bindungspartner vorherzusagen. Falls erfolgreich, könnten die neu identifizierten Interaktionspartner und zugehörige Strukturen dazu genutzt werden, Peptidomimetika und niedermolekulare Inhibitoren zu entwickeln, die spezifische Interaktionen von MIZ1 und die zugehörigen zellulären Prozesse stören und somit als Werkzeuge zum besseren Verständnis der MIZ1-Biologie dienen könnten. Vorbild dabei können zahlreiche niedermolekulare Verbindungen sein, die zur Störung der Co-Repressor-Peptid-Bindung an BCL6^{BTB} entwickelt wurden. Wenn es auf ähnliche Weise gelänge, spezifischen Einfluss auf die transkriptionelle

Funktion von MIZ1 zu nehmen, so könnte dies von hohem therapeutischen Nutzen in der Bekämpfung verschiedener Krebsarten sein.

1 Introduction

1.1 Ubiquitination – a posttranslational modification by a ubiquitous cellular regulator

Ubiquitination is a posttranslational modification (PTM) in eukaryotic cells and describes the covalent attachment of ubiquitin to a target protein through the formation of an isopeptide bond between the carboxy-terminus of ubiquitin and typically the ε-amino group of a lysine residue of the target protein [1], [2]. However, non-lysine residues, like serine/threonine (Ser/Thr) or cysteine (Cys), can also be ubiquitinated, leading to hydroxyester (Ser/Thr) or more labile thioester (Cys) linkages [3]. In addition, N-terminal ubiquitination is known, which describes the attachment of ubiquitin to the N-terminal α-amino group of a target protein [4]-[6].

Ubiquitin was first discovered by Gideon Goldstein et al. in 1975 in the context of thymopoietin and isolated from bovine thymus [7]. Two years later, Goldknopf et al. showed that histone 2a (H2a) is modified with ubiquitin [8]. We now know that ubiquitination is one of the most common PTMs after phosphorylation [9], [10]. By using an improved ubiquitin-directed antibody for enrichment combined with mass spectrometry, more than 63000 unique ubiquitination sites on 9200 proteins could be detected in two human cell lines (of note, the antibody did not recognize linear ubiquitination, making the total number of sites even higher) [4], [6]. More than 1000 proteins are involved in ubiquitination, a fraction of which makes up the ubiquitin-proteasome system (UPS) [11], [12], a major intracellular pathway for protein degradation, besides lysosomal degradation [13], [14]. However, ubiquitination is also involved in a range of other, non-proteolytic cellular processes, including intracellular trafficking, DNA repair, immunity, assembly of multi-protein complexes, regulation of enzymatic activities, receptor internalization and regulation, as well as autophagy [2], [15], [16].

Ubiquitin is a 8.5 kDa evolutionarily conserved protein that comprises 76 amino acids [11], [15]. Its fold is characterized by a five-stranded β-core that wraps around a single α-helix and is therefore known as 'β-grasp' fold (β-GF) (**Figure 1A**) [17], [18]. This fold is not restricted to ubiquitin and ubiquitin-like proteins only, but occurs in a wide range of diverse proteins showing various

insertions [19], [20]. The β-GF serves as a multi-functional scaffold for protein interactions in diverse biological processes, e. g., interactions of various enzymes, iron-sulfur clusters, and RNA co-factors [20], [21]. Ubiquitin is a rather rigid protein, except for its flexible C-terminal tail and the Leu 8-containing β1/β2-loop, the flexibility of which is needed for the interaction of ubiquitin with ubiquitin-binding domains (UBD) (**Figure 1**) [2], [22], [23]. **Figure 1B** shows four important patches on the ubiquitin surface that are relevant for distinct functions, as listed in **Table 1**.
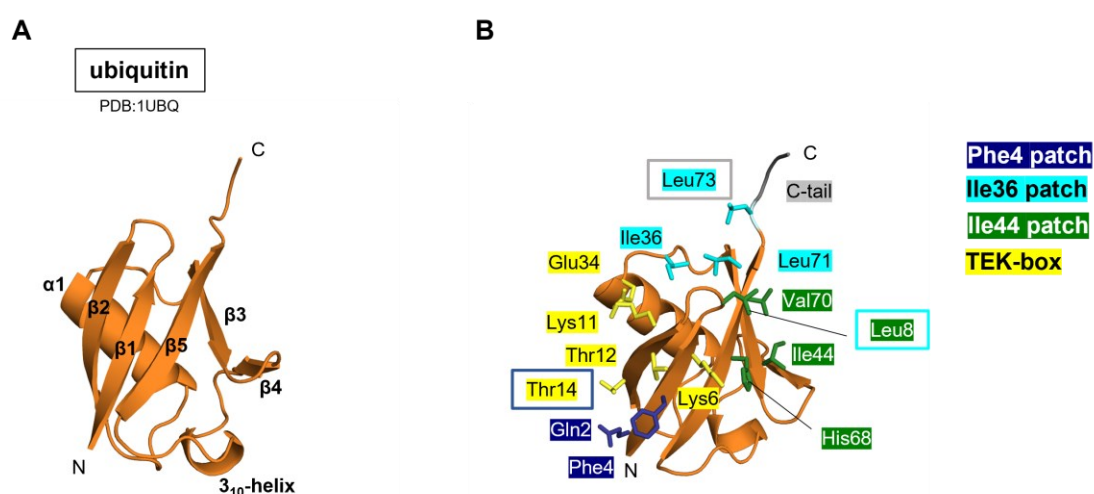
Figure 1 (modified from [2], [24]): Secondary structure elements and hydrophobic patches of ubiquitin
(A) Nomenclature of secondary structure elements of ubiquitin (PDB: 1UBQ). (B) Important surface residues of ubiquitin with particular functions (see Table 1) and color coded according to the associated surface patches or elements. Side chains are represented as sticks. Residues that belong to two patches are boxed accordingly.

Table 1: Functions of surface patches of ubiquitin according to [2]

Patch of the ubiquitin molecule	Mediates interaction…
Phe4 patch	- with the USP domain of DUBs [25] - with UBAN domains [26] - involved in trafficking [27]
Ile36 patch	- between Ub moieties in a ubiquitin chain - with UBDs [28], HECT ligases [29], DUBs [25]
Ile 44 patch	- with UBDs and the proteasome [27], [30], [31]
TEK-box	- drives mitotic protein degradation [32]

A central question is how ubiquitin encodes specificity in regulating many aspects of cell and tissue homeostasis. The answer lies in the immense diversity of ubiquitin chain types that are assembled in the cell. Because ubiquitin has seven lysine residues, as shown in **Figure 2A**, target proteins can not only be (poly) monoubiquitinated, but ubiquitin chains can be built, in which one of the seven lysine residues or the N-terminus of a target-linked ubiquitin is linked to the C-terminus of a second ubiquitin molecule (**Figure 2**). The linkage type is determined by which amino group forms the (iso)peptide bond between the ubiquitin molecules. In human cells, the most abundant chain type is linked through Lys 48, thus encoding the proteasomal degradation of the target protein [2]. Besides, Lys 48-linked chains, other chain types, such as Lys 11- [32]-[34], Lys 29- [35] and in rare cases Lys 63 [36]-[38]-chains, have also been shown to induce protasomal degradation [2]. However, Lys 63-linked chains are mainly involved in NF-κB-signaling and DNA-repair [39]. The diversity of ubiquitin chains is not limited to linkage types, but is further expanded by the possibility of branching or mixing linkages within a single chain. Such chains are referred to as heterotypic. In sum, the variability of ubiquitin chains in length, linkage type and topology offers numerous possibilites to induce different cellular outcomes (**Figure 2B**) [2], [11].

Finally, the versatility of ubiquitn signaling is further increased by posttranslational modifications of ubiquitin itself, such as acetylation, SUMOylation, and phosphorylation (**Figure 2B**) [11]. The intimate crosstalk of ubiquitination and phosphorylation has been illustrated the phosphorylation of Ser 65 of ubiquitin by the kinase PINK1 and plays a critical role regarding the PARKIN-mediated ubiquitination of mitochondrial membrane proteins [9], [40]-[44].
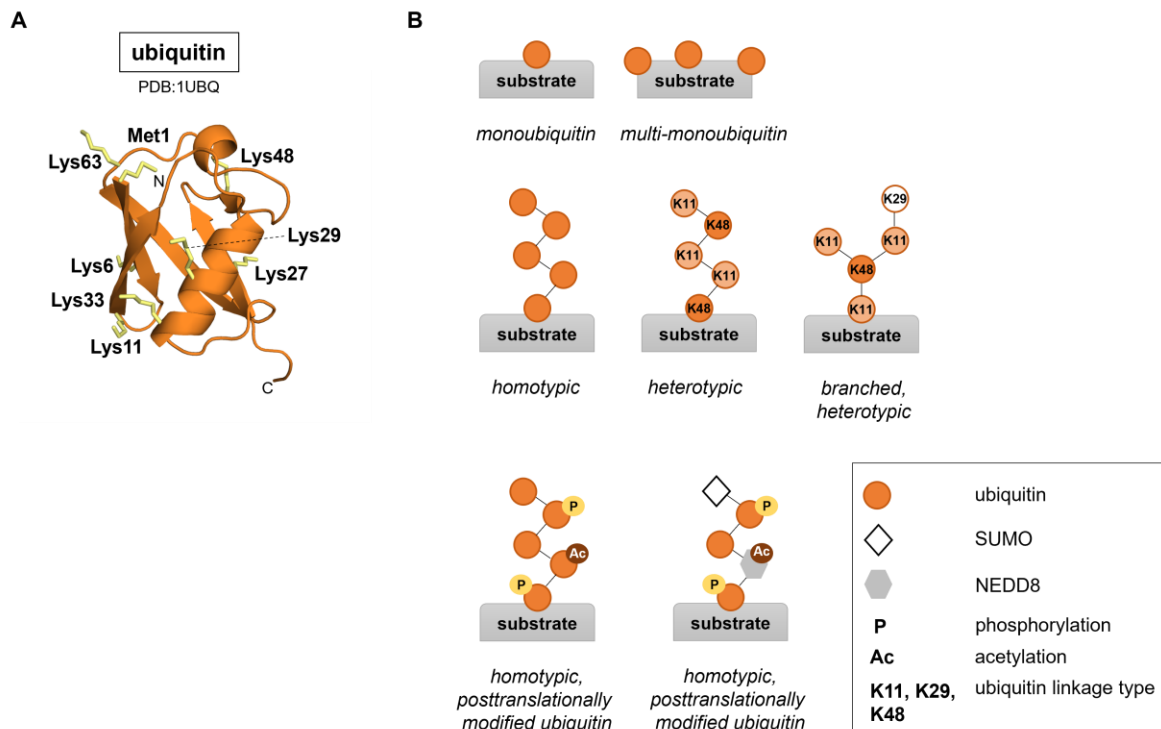
Figure 2: Overview of ubiquitin linkage and chain types (modified from [2], [11])
(A) Crystal structure of ubiquitin (PDB: 1UBQ) with the side chains of the seven lysine residues (Lys 6, Lys 11, Lys 27, Lys 29, Lys 33, Lys 48, Lys 63) and methione 1 (Met 1) displayed as sticks. (B) Overview of ubiquitin chain types and exemplary combinations of the most prominent posttranslational modifications.

1.2 The ubiquitination machinery

The diversity of ubiquitin chains is typically generated by three enzymes that act in sequence: a ubiquitin-activating enzyme (E1), a ubiquitin-conjugating enzyme (E2) and a ubiquitin ligase (E3) [45]-[47].

The human proteome contains two ubiquitin-directed E1s, UBA1 [48] and UBA6 [49]-[51]. These enzymes consume ATP to adenylate the C-terminal carboxyl group of ubiquitin (yielding Ub-AMP), while pyrophosphate is released [52]-[54]. Subsequently, a tetrahedral intermediate (Ub-AMP-E1) is formed through the nucleophilic attack of the catalytic cysteine of the E1 on the carboxyl group of Ub-AMP, resulting in the release of AMP and thioester bond formation between Ub and the catalytic cysteine. This thioesterification reaction involves the noncovalent binding of a second Ub at the adenylation site of the E1 [52], [55]. In the following transthioesterification reaction, the Ub is transferred from the catalytic cysteine of the E1 enzyme (Ub~E1) to the catalytic cysteine of one of the approximately 40 human E2 enzymes [52], [56]. The final step in the ubiquitination cascade is

dependent on the class of E3 involved. RING (Really Interesting New Gene)-type E3s [57] serve as scaffolds that bring the substrate and the Ub~E2 into close proximity and facilitate the nucleophilic attack of a primary amino group of the substrate onto the carbonyl group of the thioester-linked Ub, giving rise to an isopeptide bond between the substrate and ubiquitin [58]. In contrast, HECT (homologous to E6AP carboxy terminus)-type E3s contain a catalytic cysteine within their catalytic HECT domain and form a thioester bond with ubiquitin before substrate modification (**Figure 3**) [58]-[60]. A third class of E3s are RBR (RING-between-RING) ligases, which combine the properties of RING- and HECT-E3-ligases [61]-[63]. RBR ligases consist of two RING-like domains which are separated by an IBR (in-between-RING)-domain. While the RING1 domain binds to the Ub~E2, similar to RING ligases, the RING2 domain contains a catalytic cysteine to which ubiquitin is linked in an intermediate step of catalysis. The IBR domain as well as two regions that flank the RING1 and RING2-domains are flexible, as required for the distinct conformations driving this multistep process [61].

The human genome encodes more than 600 E3s [64], threreof 28 HECT-type ligases [65], [66] and 14 RBR-ligases [67]; the RING-E3-ligases represent the largest class [58]. Taking into account that one E3 typically targets multiple substrates, and one substrate is often targeted by several E3s, these numbers showcase once more the diversity of the ubiquitin system and suggest that most proteins are ubiquitinated during their lifetime [11]. Furthermore, they reinforce the notion that E3 enzymes have a dominant role in determining the specificity of the system (see section 1.3). Yet, E2s also contribute to specificity, especially in the context of RING-type ligases: By orienting the acceptor ubiquitin such that one lysine is positioned toward the active site E2s can determine the linkage specificity of ubiquitin chain formation [45], [68], [69]. E2s can also influence the rate of chain formation and its processivity, thus detemining chain length [45]. In this context, processivity describes the number of ubiquitin moieties that are attached to a substrate while it is bound to the E3. Processivity is dependent on the affinity between E3 and substrate as well as the efficiency of ubiquitin transfer from the E2 to to the substrate (in the case of RING ligases) [45], [70]. Typically, ubiquitin transfer from a RING-bound E2 to a substrate occurs one by one (sequential addition). However, certain E2s pre-assemble ubiquitin chains and transfer a

ubiquitin chain *en bloc* to the substrate (e. g., UBE2G2) [45], [71]. Some E2s have dedicated roles in ubiquitin chain initation or elongation. For example UBE2C initiates K11-linked ubiquitin chain formation on APC/C substrates [72], whereas UBE2S elongates them [34]. Other E2s fullfill both functions [45], such as CDC34 [73]-[75].
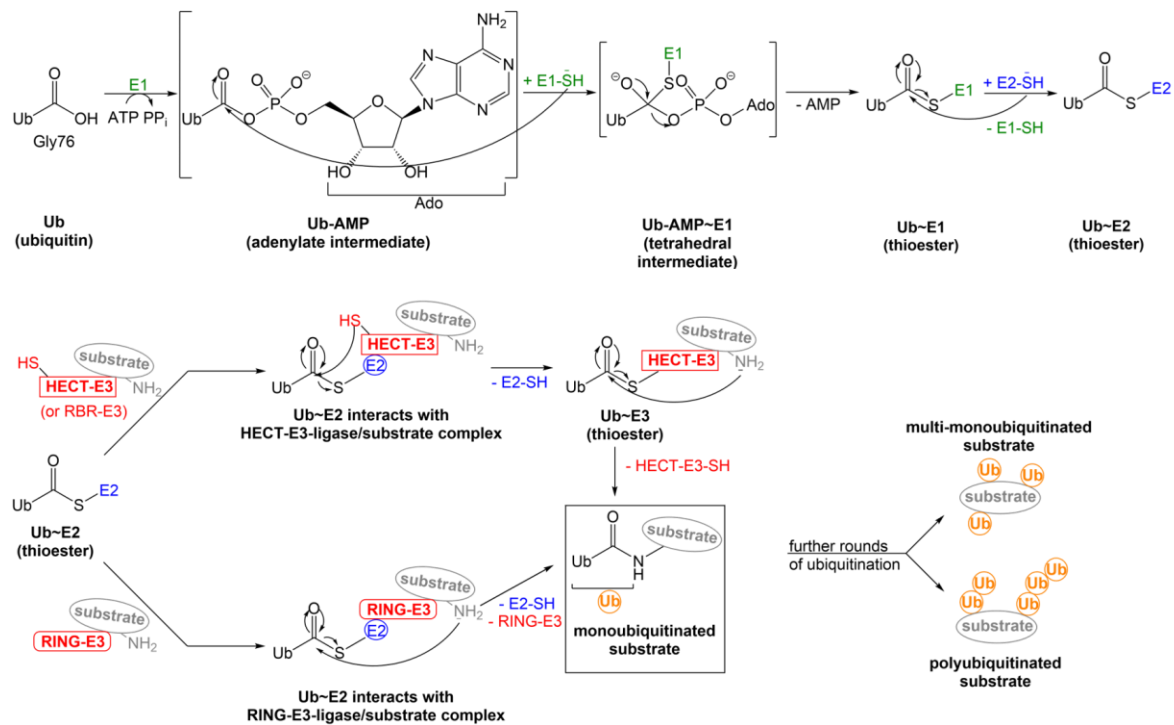
Figure 3: (modified from [52], [58]): The ubiquitination cascade
Overview of the ubiquitination cascade, focusing on the bonds that are formed and broken as well as important intermediates. For details, see text.

Ubiquitination is a reversible modification. The disassembly of ubiquitin modifications is carried out by ~ 100 deubiquitinating enzymes (DUBs) in the human proteome. DUBs are divided into seven families: ubiquitin-specific proteases (USPs), ubiquitin C-terminal hydrolases (UCHs), ovarian tumor proteases (OUTs), Machado-Joseph-domain or Josephine domain proteases (MJDCs/Josephins), motif-interacting with Ub-containing novel DUB family (MINDY), zinc-finger-containing ubiquitin peptidase 1 (ZUP1), and JAB$_1$/MPN/MOV$_{34}$ (JAMM/MPN). Except for the JAMM/MPN family, which is made up of metalloproteases, DUBs are cysteine proteases. DUBs hydrolize peptide and isopeptide bonds either in a linkage or substrate-specific manner or non-specifically. Some DUB activities are also dependent on the length of the ubiquitin chain to be cleaved. DUBs further differ in the way by which they edit ubiquitin

chains: Some cleave ubiquitin chains off the substrate *en bloc* (e. g., proteasomal DUBs), others shorten the ubiquitin chain step by step starting from the distal ubiquitin (*exo* DUB activity) or within the chain (*endo* DUB activity). Some can remove mono-ubiquitin from a substrate (e.g. histone-directed DUBs), while others can not. Besides having important functions in encoding the specificity of ubiquitin signaling, DUB activities enable the recycling of ubiquitin, thereby helping to maintain the ubiquitin concentration in the cell [76]-[79]. Moreover, DUB activities regulate the ubiquitin level also at the stage of its synthesis: ubiquitin is encoded by four genes (*UBB, UBC, RPS27A, UBA52*) [4], [80], [81], which give rise to a linear fusion protein that is subsequently cleaved by DUBs [76], [82].

Apart from its cell signaling functions, one of the main tasks of the ubiquitin system is the control of the protein homeostasis by proteasomal degradation. Proteasomal degradation includes three major steps: deubiquitination, unfolding and degradation at the 26S proteasome. The 26S proteasome has a molecular weight of 2.5 MDa and comprises a 20S proteolytic core that is enclosed by two 19S regulatory complexes. The lid of the 19S regulatory particle incorporates three DUBs (USP14, UCHL5, PSMD14) and ubiquitin receptors. To be degraded in the central cavity of the 26S proteasome, a ubiquitinated protein ought to be deubiquitinated and unfolded. As a consequence, ubiquitin that is released at the lid of the 19S regulatory particle (for example, through *en bloc* cleavage of a chain off a substrate by PSMD14/PSMD7 [83], [84]) can be recycled, which renders the UPS economical. The deubiquitinated protein is then unfolded by AAA ATPases that are located at the entrance of the proteolytic core of the proteasome, where the protein is hydrolized [3], [76], [85], [86].

1.3 E3 classes

1.3.1 RING E3s

RING E3s are the largest class within the over 600 E3s in the human proteome. As described in section 1.2, RING E3s differ from other types of ligases in the mechanism of how they mediate ubiquitin transfer from the E2 to the substrate. The RING, a specialized Zn^{2+}-ion coordinating domain, provides a platform for the binding of the E2~Ub conjugate. Similar to RING ligases, the members of the U-box family also position the E2~Ub conjugate, but do not coordinate zinc [58]. Some RING domains dimerize, as exemplified by the homodimeric RING domains of cIAP, RNF4, BIRC7, and CHIP [87]-[90] or the heterodimeric RING arrangements of BRCA1-BARD1 or MDM2/MDMX (homolog in humans: HDMX/HDM4) [58], [91], [92]. Of note, both MDM2 and MDMX also exist as homodimers, with MDM2 being active and MDMX being inactive. In the context of the heterodimer, however, MDMX contributes partially to the recruitment of the E2 [58], [91], [93]. Dimerization of RING-type ligases can be mediated by the RING domain itself, including its C-terminal tail (e. g., MDM2-MDMX), or by regions outside of the RING-domain (e. g., BRCA1-BARD1) (**Figure 4**) [58], [91], [92].
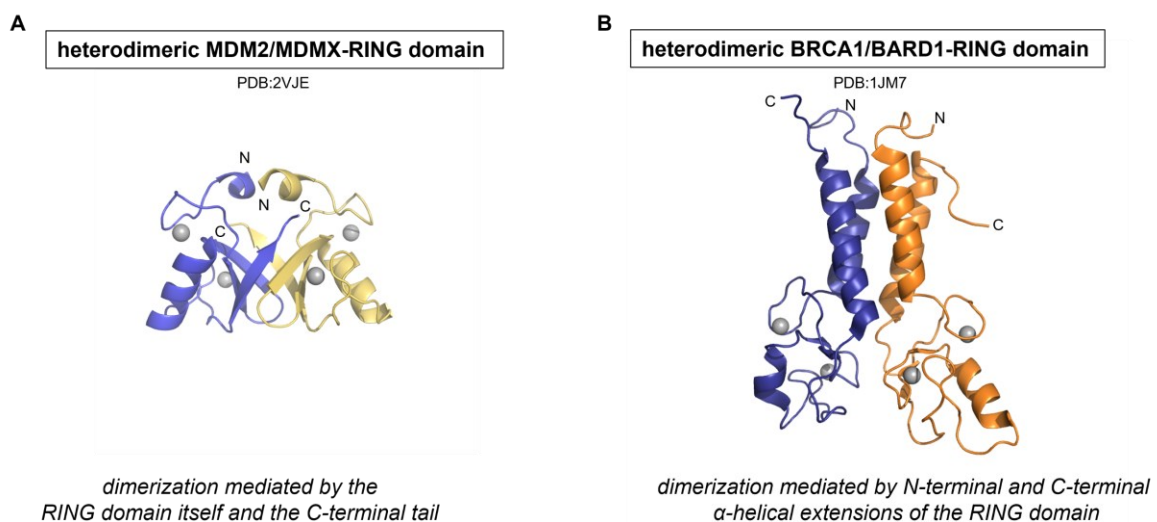
Figure 4: Dimerization interfaces of heterodimeric RING E3s
(A) Crystal structure of the RING domains of the MDM2/MDMX-heterodimer (PDB: 2VJE), with the MDM2 RING domain shown in blue and the MDMX RING domain in pale yellow. The coordinated Zn^{2+}-ions are represented as grey spheres. The dimerization is mainly mediated by the RING domain itself and the C-terminal tail. (B) Crystal structure of the RING domain of the BRCA1/BARD1-heterodimer (PDB: 1JM7), with the BRCA1 RING domain shown in dark blue and the BARD1 RING domain in orange. The coordinated Zn^{2+}-ions are represented as grey spheres. The BRCA1/BARD1 dimerization is mainly mediated by N- and C-terminal α-helical extensions of the RING domain.

A well-studied RING E3-subfamily comprises the cullin-RING-ligases (CRLs) [58], [94]. Prominent members of this subfamily are the SKP1-Cullin-F-box (SCF)-ligases (**Figure 5**) and the anaphase-promoting complex/cyclosome (APC/C). SCF-ligases consist of two scaffold proteins - SKP1 and CUL1 -, a RING-finger domain (RBX1) and an adaptable F-box protein that can be exchanged (with the help of NEDD8 and conformational changes) and allows the recruitment of different substrates. Approximately 69 human F-box proteins are found in the human proteome, allowing for great diversity in the composition of SCF-type complexes. The APC/C consists of 16 subunits and associates also with several adaptor proteins (CDC20, CDH1, CORTEX, AMA1, MFR1). Accordingly, signaling through the APC/C occurs in different celllular processes, most notably cell proliferation and development. Of note, CRLs also regulate each other [58], [95]-[97]. For example, the APC/C CDH1 targets SKP2 for degradation in early G1, thus stabilizing P27 and preventing premature G1-S transition [98].
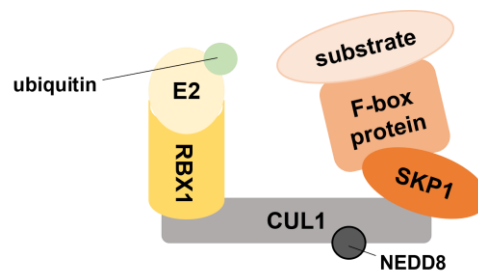
Figure 5: Schematic of a multi-subunit SCF ubiquitin ligase complex
Cullin 1 (CUL1) serves as scaffold, the BTB-domain-containing SKP1 bridges CUL1 and one of the 69 substrate-binding F-box proteins. CUL1 also binds the RING-box protein 1 (RBX1), which recruits a ubiquitin-loaded E2. Substrate ubiquitination by the SCF is activated by NEDD8ylation of CUL1.

In the context of RING E3s, it is typically the E2 that determines the specificity in ubiquitin linkage formation (section 1.2). The main function of the RING domain is to activate ubiquitin transfer from the E2 to the substrate by stabilizing the E2-bound ubiquitin molecule in a 'closed' conformation with respect to the E2 and straining the thioester linkage between them [99], [100]-[103].

1.3.2 HECT E3s

The name of this class of ligases originates from its founding member, the human papillomavirus (HPV) E6-associated protein (E6AP), identified in 1993. The human HECT family has 28 members. The first crystal structure of the characteristic HECT domain of these enzymes was determined for E6AP in 1999, both in its *apo* form and in complex with the E2 enzyme UBCH7 [66], [104], [105]. E6AP promotes tumorigenesis in HPV-infected cervical cells by forming a trimeric complex with the HPV oncoprotein E6 and the human tumor suppressor P53 and promoting proteasomal degradation of P53 [106]. E6AP was also described as an oncoprotein in B-cell lymphoma by degrading PML, a regulator of senescence [65], [107]. However, E6AP can also act as a tumor suppressor in breast, prostate, and non-small cell lung cancer [65], [108]-[110]. Such bivalent functions are also found in other HECT E3s, depending on the particular signaling pathways, tissues, and mutational backgrounds they act in. Interestingly, several HECT ligases were shown to be associated with the proteasome, including E6AP and HUWE1 [111], [112] suggesting that they may enhance the recruitment and maintenance of substrates at the proteasome.

HECT E3s share a C-terminal catalytic HECT domain [59], which consists of two lobes [66]. The N-terminal (N-) lobe contains the E2-binding site [105] and can include a non-covalent ubiquitin binding site, as observed for example in RSP5 and NEDD4, which was suggested to form interactions with a growing Ub-chain, thereby improving processivity during ubiquitination [113]-[115]. In contrast, the C-terminal (C-) lobe contains a catalytic cysteine and an interaction site for the thioester-linked donor ubiquitin [66]. The two lobes are connected by a flexible linker ('hinge loop') that allows for conformational changes between an L-shape, as seen during substrate ubiquitination, or an inverted-T shape, as required for thioester formation with the donor ubiquitin (**Figure 6**) [29], [105], [116]. Notably, the lobes can also rotate around the inter-lobe linker thus increasing the conformational freedom and allowing for various conformations besides the L- and inverted-T states, at least in crystal structures [117].
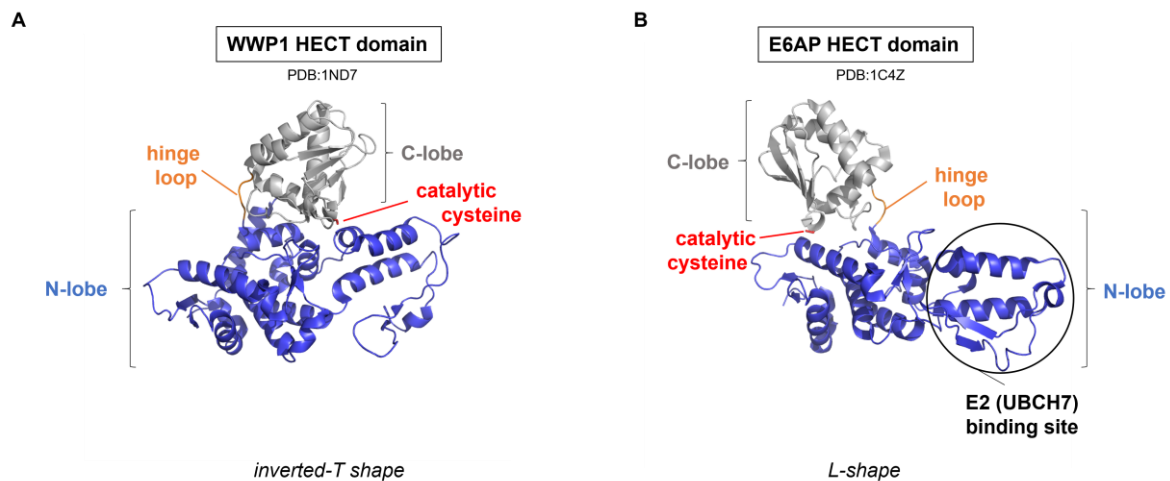
Figure 6: Structure of the HECT domain
(A) Crystal structure of the HECT domain of WWP1 (PDB: 1ND7) in an inverted-T shape. The C-lobe (grey) contains the catalytic cysteine (side chain represented as red sticks) and is connected by the hinge loop (orange) with the N-lobe (blue). (B) Crystal structure of a truncated HECT domain of E6AP (PDB: 1C4Z), in a L-shape. The colour code is the same as in (A). The E2-binding site in the N-lobe is encircled in black.

An important feature of the C-lobe is its C-terminal tail. Although its role is not yet entirely clear, it has emerged that the C-terminal 4 residues, and in particular a phenylalanine at the minus-4 position, are important in positioning the donor ubiquitin and thus enhance catalytic activity, but not specificity in ubiquitin linkage formation [115], [118].

HECT E3s have been grouped into three subfamilies: the NEDD4-subfamily, the HERC-subfamily and 'other HECTs' (**Figure 7**). The NEDD4-family comprises 9 human family members: NEDD4-1, NEDD4-2, WWP1, WWP2, SMURF1, SMURF2, ITCH, HECW1, and HECW2. Besides the HECT domain, NEDD4-type ligases contain 2 to 4 WW domains and a N-terminal C2-domain [66], [119]. The C2-domain targets NEDD4-type ligases to phospholipid-containing membranes in a Ca^{2+}-dependent manner [120], [121]. The WW domains function in substrate recruitment. They contain two conserved tryptophan residues, separated by 21 amino acids, that interact with proline-rich motifs (PPxY or PY) as well as phosphor-serine/threonine residues [120]-[123].

The HERC family comprises 6 ligases. The two large HERC proteins (HERC1 and HERC2) have a molecular weight (MW) of over 500 kDa [124], whereas the small HERC proteins (HERC 3-6) are of 100 to 120 kDa [125]. HERC ligases are involved in diverse processes, including neurodevelopment, DNA damage

response, cell proliferation, cell migration and immune response. Depending on the context, they can act as tumor suppressor proteins or oncoproteins [125]-[127]. All HERC proteins contain one or more regulator of chromosome condensation 1 (RCC1)-like domain (RLD) N-terminally of the HECT domain. These domains serve as guanine nucleotide exchange factor (GEF) for the small GTPase RAN in membrane trafficking [65], [126], [128].

The group of 'other HECTs' comprises E6AP, HUWE1, HACE1, TRIP12, UBR5, UBE3B, UBE3C, HECTD1 to 4, G2E3 and AREL1. Besides HUWE1, the human full-length structure of which could recently be solved by cryo-EM [129] as well as crystallographically for the fungal ortholog HUWE1$_N$ [130] (section 1.5.4), few domains of these proteins are structurally characterized and large parts were proposed to be intrinsically disordered or have only few secondary structure elements. As a result, little is known about the substrate recruitment mechanisms or common features of this seemingly diverse group of enzymes [66].

Across all three HECT E3-subfamilies, mechanisms regulating the catalytic activity have been identified, for example by intramolecular interactions, as seen for members of the NEDD4-family [131]-[135] and HUWE1 [136], or by intermolecular interactions (e. g., E6AP) [65], [104], [105], [137], [138]. Interestingly, HECT E3s can also regulate each other's activities, as seen for HERC2, the binding of which to E6AP increases the activity of the latter [65], [139]. In addition, PTMs regulate HECT E3 activities, e. g., phosphorylation of ITCH leads to its activation [140], whereas phosphorylation of E6AP was found to be inhibitory [65], [141].
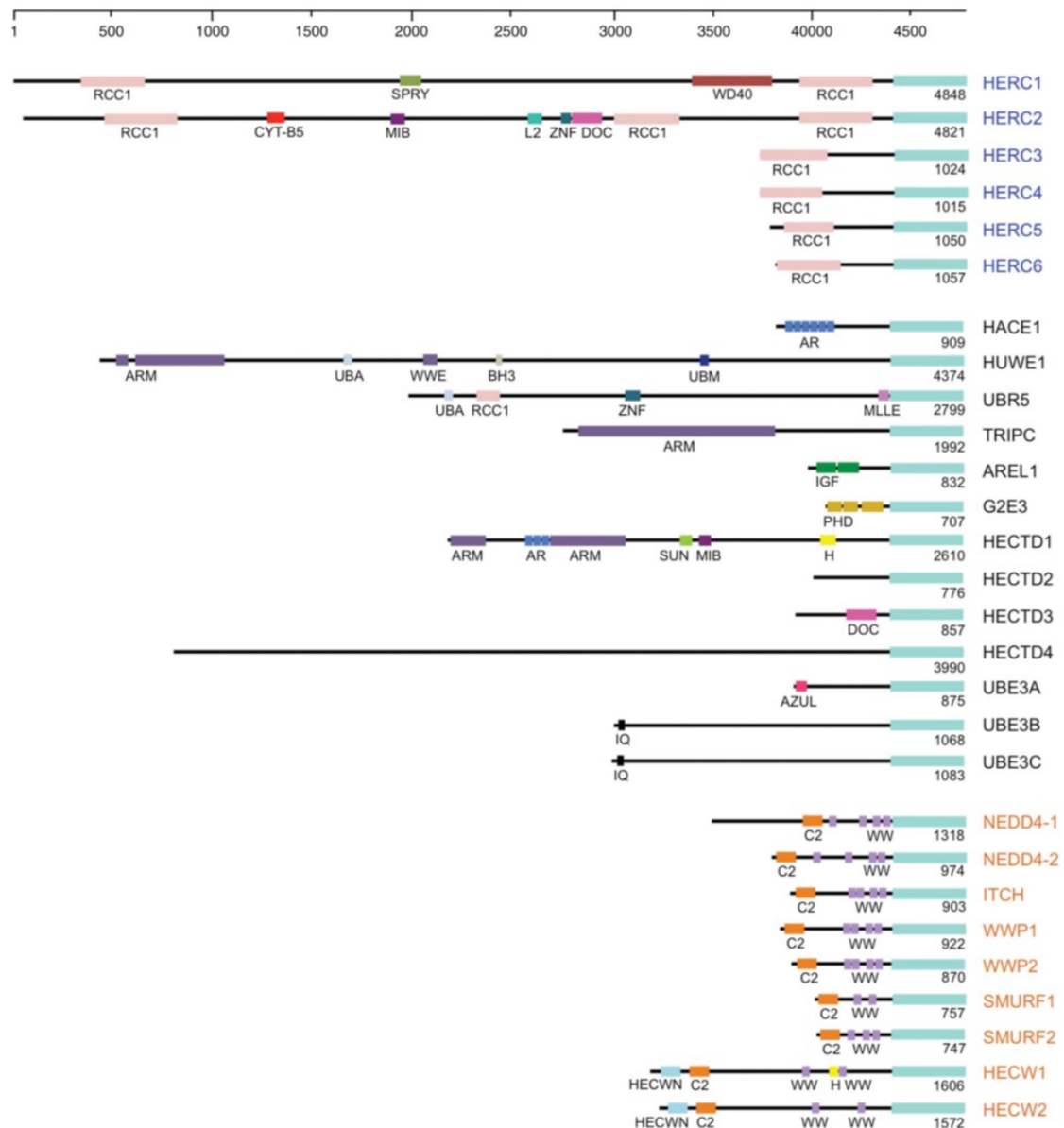
Figure 7 (taken from [66]): Domain organization of the human HECT E3s
The domain organization is based on predicitions of the InterPro server [142] and/or available crystal structures. An amino acid scale bar is shown at the top. Domain abbreviations: RCC1, Regulator of Chromosome Condensation 1 repeat domain; SPRY, B30.2/SPRY (SPIA and RYanodine Receptor) domain (overlaps in HERC1 with predicted concanavalin A-like lectin/glucanase domain); WD40, WD40/YVTN repeat-like-containing domain; CYT-B5, Cytochrome B5-like heme/steroid binding domain; MIB, MIB-HERC2 domain (overlaps in HECTD1 with CPH domain); L2, ribosomal protein L2 domain (overlaps in HERC2 with predicted CPH domain); ZFF, zinc finger; DOC, APC10/DOC domain (overlaps in HERC2 and in HECTD3 with galactose-binding domain-like region; AR, ankyrin repeat-containing domain; ARM, armadillo-type fold domain (overlaps in TRIPC with a predicted WWE domain); UBA, ubiquitin-associated domain; WWE, WWE domain; BH3, BCL-2 homology region 3 domain; UBM, ubiquitin-binding motif; MLLE, Mademoiselle/PABC domain; IGF, immunoglobulin-like fold (overlaps in AREL1 with predicted filamin repeat-like fold); PHD, PHD-type zinc finger; SUN, SAD1/UNC domain (overlaps in HECTD1 with predicted galactose-binding-like domain); AZUL, AZUL domain/ N-terminal zinc-binding domain; IQ, IQ domain/ EF-hand binding site; C2, C2 domain; WW, WW domain; HECWN, HECW1/2 N-terminal domain; H, helical bundle (HECTD1) and helical box domain (HECW1), respectively. Predicted coiled-coil regions are not included [66].

13

1.3.3 RBR E3s

The 14 human RBR ligases are RING/HECT-hybrids that catalyze a 2-step reaction, similar to HECT-E3-ligases [61] (see section 1.2). Probably the best studied RBRs are PARKIN, HHARI (Human Homolog of Ariadne), and HOIP [61]-[63], [143]. While PARKIN is involved in mitophagy [144], [145] and mutations in the *PARKIN* gene are associated with autosomal juvenile parkinsonism [146], [147], HHAR1 regulates developmental processes, protein translation and cellular proliferation [148]-[151]; the signaling functions of HHARI1 further increase by its interactions with CRLs [67], [152]-[154]. HOIP is the only known E3 that assembles linear ubiquitin chains [67], [155]. It is part of the linear ubiquitin chain assembly complex (LUBAC), which also contains the RBR E3 HOIL-1L and the SHANK-associated RH domain-interacting protein in postsynaptic density (SHARPIN). Each of these components is essential for the physiological functions of LUBAC [67], [156]-[159]. These functions include inflammation and autoimmune diseases through the LUBAC-induced activation of the NF-kB-pathway [160], [161], apoptosis, cancer and B-cell function [67], [162]. Overall, the substrate spectrum and recognition of RBRs is incompletely understood and requires further investigation [67].

Several RBR ligases were found to be auto-inhibited, due to intramolecular interactions enabled by the flexible linkers between the RING1 and IBR or IBR and RING2 domains [67], [163]. Crystal structures of auto-inhibited states of HHARI (PDB: 4KBL) and PARKIN (PDB: 4K95) revealed the catalytic cysteine or the E2-binding site buried, thereby explaining the auto-inhibition [67], [164], [165]. To release this auto-inhibition, conformational changes are required and can be triggered by various events, including phosphorylation (triggered by the kinase PINK in the case of PARKIN [43], [166]), interactions with other ligases (e.g., HHARI and CUL1-4 [152], [153]) or complex assembly (HOIP with HOIL-1L and SHARPIN [167]) [67].

1.3.4 RCR E3 and RING domain-independent ligase activity of RNF213

In addition to RING/U-box, HECT, and RBR E3s, new ligase types have recently been identified: MYCBP2, an E3 associated with nervous system development and axon degeneration, has an N-terminal RING domain and a C-terminal tandem

cysteine (TC) domain, which comprises two catalytic residues, C4520 and C4572. Instead of lysine ubiquitination, MYCBP2 preferentially promotes the ubiquitination of hydroxyl groups, with enhanced selectivity for threonine over serine residues. This esterification activity is based on an intramolecular cysteine-relay mechanism. Therefore, Pao et al. classified MYCBP2 as a RING-Cys-relay (RCR) E3. In this relay mechanism ubiquitin is transferred from the E2~Ub to the first catalytic residue, C4520, in the TC domain, followed by an intramolecular transthioesterification to C4572. In the final esterification reaction Ub is transferred from C4572 to a threonine or serine residue of a substrate. Due to its esterification activity, MYCBP2 might also play a role in the ubiquitination of non-protein substrates [168]. In this context Otten et al. recently reported that the largest human E3, RNF213 (584 kDa), mediates the ubiquitination of lipopolysaccharides (LPS) on the surface of *Salmonella*. The ubiquitin coat surrounding the bacterium leads to the recruitment of the LUBAC E3, the assembly of M1-linked ubiquitin chains, and the recruitment of receptor proteins involved in autophagy, which prevents proliferation of the bacteria in the cytosol of the host. The ubiquitination of LPS on *Salomonella* by RNF213 is independent of its RING domain and instead depends on a RZ finger (RNF213-ZNFX1 finger), a 27-amino-acid peptide with sequence similarity to ZNFX1 (NFX1-type zinc finger containing protein) [169]. In line with this, Ahel et al. previously reported that RING domain-depleted RNF213 shows WT-like auto-ubiquitination and that UBCH7, a cysteine-reactive E2 that cooperates with HECT and RBR E3s, worked best with RNF213. The mechanism of RNF213 points to a new subclass of E3s with a RING-independent and Cys-dependent ligase activity, but with an overall distinct fold from HECT, RBR or the RCR E3 MYCBP2 [170], [171]. In addition, ATP-binding to the ATPase core is required to promote RNF213 activity [171]. In sum, these recent findings highlight once more the diversity of the ubiquitination machinery, not only in Ub-linkage formation, but also with regard to the mechanistic variability of the E3 family.

1.4 Therapeutic targeting of the ubiquitin system

Intact ubiquitination is essential for cellular and tissue homeostatis. As a consequence perturbations of the ubiquitination machinery cause various human diseases, including onset and progression of cancer, metabolic syndromes, neurodegenerative, autoimmune, infectious, and inflammatory disorders as well as muscle dystrophies. The molecular basis of these pathologies can lie in non-native complex assembly due to mutations in the involved genes, the overexpression or lack of particular components, the accumulation of misfolded proteins or protein mislocalization [15], [172], [173].

Proteasome inhibitors, such as Bortezomib, proved successful in cancer therapy [9], [174], [175]. Analogs of Bortezomib (e. g., Carfilzomib, Oprozomib, Delanzomib) were also developed and show improved efficacy or oral bioavailability. However, the application of all these compounds is limited by off-target effects, toxicity, and resistances [9], [176]. In addition, targeting the proteasome, i.e. the last step of the UPS is less specific than manipulating the preceding steps of the ubiquitination cascade.

More than 40 small-molecule inhibitors of the E1 have been developed, targeting the tip of the ubiquitination, sumoylation and neddylation cascades. This strategy clearly has 'global' effects and is thus expected to have side effects in patients. UBA1 inhibitors targeting the initiation of ubiquitination comprise adenosine sulfamates, nitro-based compounds, natural compounds, ubiquitin adenylate analogs and disulfides [177]. So far only the UBA1 inhibitor TAK-243 (MLN7243) [178], an adenosine sulfamate, reached phase-I clinical trials for advanced malignant solid tumors. The adenosine sulfamate MLN7243 inhibits cellular ubiquitin conjugation by forming a MLN7243-ubiquitin adduct and potently inhibits UBA1 *in vitro*. This UBA1 inihibitor was developed based on the NAE-inhibitor MLN4924 [179], which has progressed to phase-III of clinical trials. MLN4924 prevents NEDD8ylation of CRLs by preventing the interaction between NEDD8 and NAE through its irreversible complex formation with NEDD8 [9], [177] (**Figure 8**).

The number of small-molecule inhibitors targeting E2s or their interactions with E1s or E3s is limited: Leucettamol A [180] and the more potent manadosterol A and B [181] are natural compounds, whereas CC0651 [182] is the first synthetic inhibitor of an E2. Leucettamol A and manadosterol A and B prevent the

interaction of Ubc13 and Uev1A, a heterodimeric complex that promotes K63-linked ubiquitin chain formation [183], with Ubc13 being involved in p53 localization and activity [184]. Instead, CC0651 [182] is an allosteric inhibitor of the human CDC34 and limits tumor cell proliferation by stabilizing the SCF^{SKP2} substrate p27^{KIP1,} a cyclin-dependent kinase inhibitor (**Figure 8**) [9]. To my knowledge no E2 inhibitor has reached clinical trials.

A major current focus of drug discovery efforts in the ubiquitin system is on DUBs and E3s, due to their specificities. A challenge lies in the fact that members of both families often have more than one function in the cell and can act as tumor suppressors and oncoproteins, depending on the tissue context, tumor stage and additional factors [9], [185]. Therefore, it would be promising not to target the overall activity of an E3 or DUB globally, but a specific protein interaction these enzymes form, e.g., with a crucial substrate in a particular pathway. However, it is often difficult to assign such substrates, since their affinities for ubiquitination enzymes are typically weak (in the micromolar range), with rapid dissociation rates - properties that are probably required to maintain the dynamic nature of the ubiquitin system [136], [186]. Among the first synthetic MDM2 (E3) inhibiting compounds were the nutlins, which block the degradation of the tumor suppressor P53 by binding to the ligase MDM2 (**Figure 8**) [9], [187], [188]. Unfortunately, it turned out that only tumor cells with WT P53 are sensitive to nutlins, but not P53-deleted or -mutated cells, as found in many types of cancer. Furthermore, nutlins also block the recognition of MDM2 substrates other than P53, thus causing off-target effects, similar to those seen with the small-molecule inhibitor RITA (reactivation of P53 and induction of tumor cell apoptosis) [9], [189].

Thalidomide and its structural analogs lenalidomide and pomalidomide are immunomodulatory drugs (IMiDs) that directly bind the substrate receptor CRBN in the RING-E3 complex CUL4-RBX1-DDB1-CRBN [190], [191]. In the 1950s thalidomide was a commonly prescribed sedative, e.g., to treat morning sickness in pregnant women, which was later realized to have teratogenic effects, leading to limb malformations in ~10.000 newborn children worldwide [192]-[195]. Today the drug is repurposed to successfully fight hematological cancers, such as multiple myeloma. The clinical effects of the IMiDs can be explained based on the crystal structures of CRL4^{CRBN} with thalidomide and pomalidomide. Binding of IMiDs to CRBN prevents the K48-linked polyubiquitination of CRBN, thus stabilizing it and

also reprograming it to promote the degradation of neo-substrates, including the IKAROS transcription factors IKZF1 and IKZF3 [190], [191], [196].

Another promising tool to manipulate E3s are proteolysis-targeted chimeras (PROTACs) [197], [198]. These are hybrid compounds that consist of two functional units connected by a linker. One unit binds to a degradative E3 (e. g., thalidomide targeting CRBN), the second unit recruits a (pathogenic) target protein. The PROTAC-induced proximity mediates E3-driven ubiquitination of the target protein and ensuing proteasomal degradation. Compared to ligase inhibitors that bind their targets stoichiometrically, PROTACs thus act as 'catalysts' and can stimulate the sequential degradation of many target molecules. Furthermore, PROTACs provide an excellent strategy to eliminate pathogenic proteins with no enzymatic activity, i.e. targets that can not be accessed by classical inhibitors, such as many transcription factors. Notably, however, small-molecule binders to such targets ought to be identified and linked to the ligase-binding unit in a suitable way, which also presents a considerable challenge. Also, due to their bifunctional nature, PROTACs are rather large compounds, which may limit their cell permeability. Dosage is another important factor, since an excess of PROTAC may cause monovalent binding to the E3 and target rather than bringing the two together (a phenomenon known as the 'hook effect'). Furthermore, it is important that the ligase and target are colocalized in the relevant tissue for the PROTAC strategy to be effective [199], [200]. Among the first PROTACs was ARV-825, developed by Arvinas, that connects a small molecule BRD4 (Bromodomain-containing protein 4)-binding moiety (OTX015) with pomalidomide to target CRBN. BRD4 is often located at enhancers upstream of several oncogenes and regulates their expression. ARV-825 showed more pronounced effects than small-molecule inhibitors of BRD4 on the expression levels of the oncogene C-MYC, cell proliferation inhibition and apoptosis induction in Burkitt lymphoma cell lines [201], [202]. In 2019, ARV-110 and ARV-471 (Arvinas) were the first two PROTACs to reach clinical trials. Both are orally bioavailable and recruit cereblon as part of a E3 complex, while the second moieties in ARV-110 and in ARV-471 target the androgen receptor (AR) and the oestrogen receptor (ER), respectively. Today both compounds are in phase-II clinical trials, ARV-110 for prostate cancer and ARV-471 for breast cancer [203]-[206].

Targeting DUBs, both broad-spectrum (e. g., NSC632839 against USP2 and USP7) [207] and specific inhibitors (e. g., IU1 against USP14 or P5091, FT671, FT827 against USP7) [208]-[210] were developed (**Figure 8**) [9]. Although any DUB inhibitor can cause off-target effects or side effects the risk is higher for broad-spectrum/unspecific inhibitors, which may cause an accumulation of polyubiquitinated proteins, unanchored polyubiquitin chains or misfolded proteins, or affect the activities of DUBs or oncoproteins in additional unwanted ways. Therefore, the trend is moving toward the development of specific DUB inhibitors [9]. For example, numerous inhibitors of USP7 are in preclinical research [211], [212]. But due to toxicity, low bioavailability and stability, first-generation DUB inhibitors did not reach phase-I/II clinical trials or were taken back because of toxicity and side effects [211]. The conformational flexibility of DUBs poses a challenge to predict new scaffolds in a structure-based manner. Additionally, DUBs (just like E3s) are often part of multi-protein complexes, which are mostly structurally uncharacterized and often not even identified. Furthermore, structural similarities of the DUB catalytic domains make it hard to develop specific inhibitors. Nevertheless, DUBs are attractive targets due to their high relevance in diverse diseases, particularly in cancer [211], [213]. In addition, the well-defined active site of DUBs, the accessibility of Cys-reactive DUBs by electrophilic inhibitors, the growing body of structural knowledge, improvements in screening technologies, and promising preclinical results on USP7 inhibitors [209], [210], [214]-[216] are indicators that DUB inhibitors may progress to therapeutics in the not-too-distant future [211], [213].

Regardless of which component in the UPS is targeted, a central challenge in preclinical and clinical studies (as for all drugs) is to prevent adverse effects and resistances. To address these, multi-targeted combination treatments may prove sucessfully. In line with this notion, clinical studies have demonstrated improved sensitivity of the proteasome inhibitor Bortezomib in combination with conventional chemotherapy [9], [217]-[219]. To exploit the ubiquitin system for therapeutic use it will be important to gain more structural insight into the mechanisms that regulate ubiquitination and deubiquitinating enzymes as a basis for rational drug design approaches. Also, enhanced genomics and proteomics approaches are expected to help identify suitable target proteins and vulnerabilities within this at least partially redundant signaling system [9].
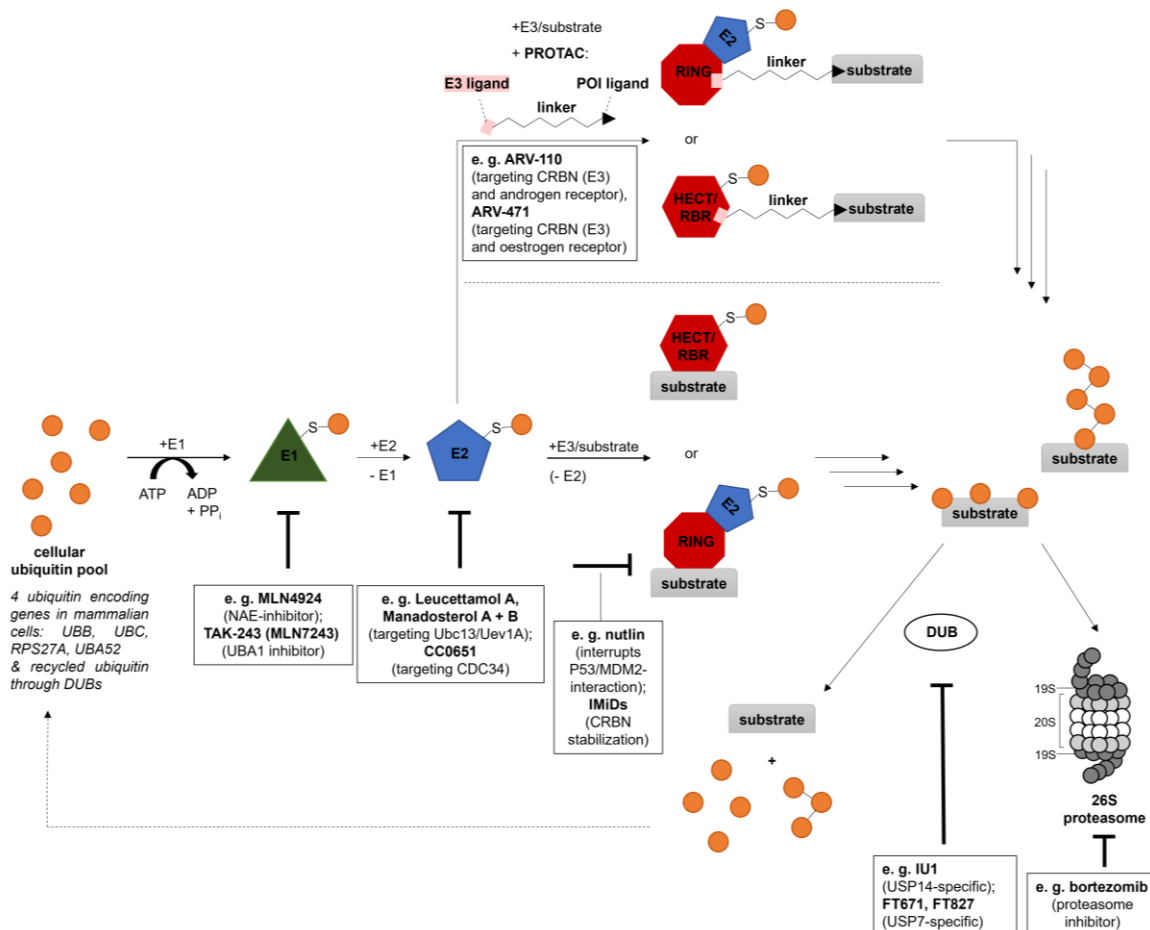
Figure 8: Selected drugs to target individual components of the ubiquitin system
MLN4924 inhibits the NEDD8-activating E1 enzyme (NAE) and thereby prevents the neddylation-induced activation of cullin-RING-ligases; TAK-243 inhibits cellular ubiquitin conjugation by forming a TAK243-ubiquitin adduct inhibiting UBA1. Leucettamol A and Mandastoreol A and B prevent complex formation between Ubc13 and Uev1A; CC0651 inhibits CDC34. Nutlins prevent binding of P53 to the RING ligase MDM2, thus stabilizing P53; immunomodulatory drugs (IMiDs; e. g., thalidomide and analogs thereof) bind to cereblon (CRBN) in the CRL4^{CRBN}-RING-E3 complex and alter the substrate specificity of CRL4^{CRBN} by preventing CRBN ubiquitination. The PROTACs ARV-110 and ARV-471 target the androgen and oestrogen receptor for ubiquitination by linking them to the E3 CRBN; 'POI' denotes protein of interest. IU1 specifically targets USP14; FT671 and FT827 specifically target USP7. The proteasome can be reversibly inhibited by bortezomib and analogs thereof.

1.5 The HECT E3 HUWE1

## 1.5.1 Overview of functions

HUWE1, also known as ARF-BP1, MULE, LASU1, and HECTH9, was first discovered by Nagase et al. in a size-fractionated human brain cDNA library. In 2005 Liu et al. identified the HUWE1 protein as a 482 kDa HECT-type E3 mediating histone ubiquitination during spermatogenesis [186], [220], [221]. HUWE1 is highly conserved in mammals with an amino acid sequence identity between human and mouse of > 90 % [186], [222]. The HUWE1 protein is mainly

expressed in the cytoplasm [223], [224], except for the nucleus of spermatogenia, primary spermatocytes, and neuronal cells [225]. HUWE1 expression levels were detected in different mouse, rat and human tissues (e.g. brain, heart, lung, breast, colon, kidney, liver, testis), indicating that HUWE1 is involved in different cellular pathways [225], [226].

Its diverse functions are also underlined by the fact that HUWE1 can assemble different ubiquitin linkage types. HUWE1, which has several ubiquitination and phosphorylation sites itself, can modify target proteins with mono-ubiquitin, but also forms K6-, K11-, K48- or K63-linked ubiquitin chains [186], [227]-[230]. Michel et al. and Heidelberger et al. identified HUWE1 as a major ligase forming K6-linked chains, and suggested that its role for K6-linked chain biology may be comparable to that of the RBR-ligase HOIP in the assembly of M1-linked chains [227], [229], [231]. Whether K6-chains induce proteasomal degradation or encode other roles in cell signaling needs further investigation. Michel et al. provided evidence that the HUWE1 substrate mitofusin-2 (MFN2), which is a major player in mitochondrial biology, is modified with K6-linked ubiquitin chains by HUWE1 [227], [232]. Taken together, the variety of ubiquitin linkages assembled by HUWE1 and possibly also heterotypic or branched chains increases the possibilities of this ligase to induce different cellular outcomes compared to a ligase that exclusively attaches one chain type to substrates.

In addition, the size of HUWE1 with 4374 amino acids provides a platform to recruit many different substrates (**Figure 9**). HUWE1 has been assigned roles in proliferation/differentiation, apoptosis, DNA repair, and stress response signaling (for details, see section 1.5.2) [186]. Furthermore, HUWE1 is involved in cell migration (e. g., via its substrate TIAM1) [233], myogenesis (e. g., MYOD) [234], histone-ubiquitination (H2AX) [235], spermatogenesis (H1, H2A, H2B, H3, H4) [221], tumor metabolism, cancer stem cell expansion (HK2) [236], hepatitis lipid catabolism (PPARα) [237], and differentiation of muscles (e. g., TBP) [238] and neurons (**Figure 9**) [186], [239], [240].
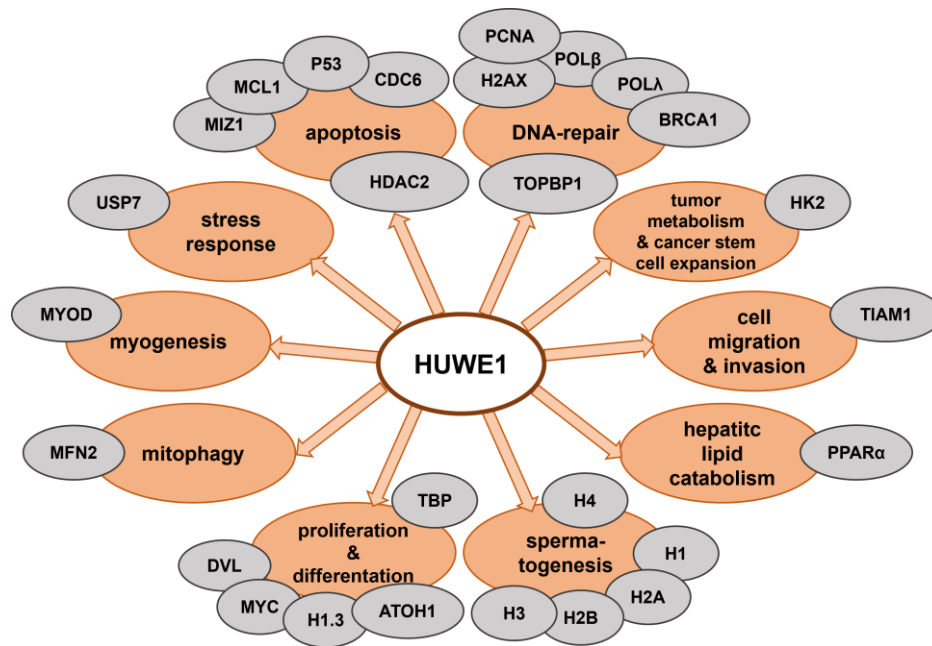
Figure 9: Overview of a selection of the best known HUWE1 substrates and the associated cellular pathways
HUWE1-substrates are shown in grey circles. The corresponding cellular processes they are mainly associated with are in orange circles.

Similar to the ER-associated protein degradation (ERAD) machinery [243], which degrades unassembled protein subunits, HUWE1 is part of a protein quality control mechanism that ubiquitinates substrates with exposed hydrophobic residues for degradation [223]. HUWE1 thus complements the existing N-end rule quality control pathway [244] in the degradation of unassembled soluble proteins and preventing protein aggregation, non-specific interactions, and transcriptional inhibition due to incompletely assembled and only partially functional proteins [223], [242].

Dysregulation of HUWE1, either in the form of overexpression or through mutations in the *HUWE1* gene, is associated with cancer (see also 1.5.3) and neurodevelopmental diseases [186], [242]. Loss of HUWE1 is embryonically lethal in mice [239], [245]-[247], indicating that HUWE1 has essential roles in cellular processes. HUWE1 overexpression was reported in several tumors, including oesophageal, gastric [248], colorectal [249], uterine, cervical, prostate [250], and lung cancer [251] as well as multiple myeloma [252] and melanoma [253] and was linked to poor prognosis in patients [242]. Mutations or submicroscopic duplication of *HUWE1* were associated with X-linked intellectual disability (XLID), which is characterized by delayed or absent speech, short stature with small hands and

feet and facial dysmorphism [254]-[256]. Historically, HUWE1 variants had been associated with severe XLID in males only; however, this picture changed when *HUWE1* mutations (e. g., Arg110Gln) in female patients with a severe syndromic XLID were identified [255]. Interestingly, many XLID-associated *HUWE1* mutations are located in the catalytic HECT domain [226]. One of these mutations, R4187C, was found to encode a hyperactive ligase, resulting in the downregulation of Polλ and thus in an impaired response of cells to oxidative stress and a decreased DNA repair capacity [256]. These effects were rescued by inhibiting USP7S, a DUB known to target HUWE1 [257]. This study illustrates one scenario of how *HUWE1* mutations may contribute to XLID [256]. Notably, other mutations on *HUWE1* found in XLID patients are predicted to be disruptive of the fold and/or activity of this ligase – an idea that is supported by recent studies of Hunkeler et al. [129]. A full understanding of the functions and alterations of HUWE1 in disease thus await futher study.

1.5.2 Role in proliferation/differentiation, apoptosis, DNA repair, and stress response

To illustrate the versatility of HUWE1 as an E3, I will highlight a selection of HUWE1 substrates and the associated cellular processes in the following paragraph. The oncoprotein MYC serves as an example of how HUWE1 mediates proliferation and differentiation. MYC is overexpressed in many tumors and binds as a transcription factor to active promoters and enhancer elements [258], [259]. By attaching K63-linked ubiquitin chains to C-MYC it was suggested that HUWE1 facilitates the recruitment of the cofactor P300 to the MYC-MAX complex, thereby promoting the transactivation activity of C-MYC [186], [228]. Another study showed that HUWE1 modifies C-MYC with K48-linked ubiquitin chains, thus leading to C-MYC degradation. In line with this idea, HUWE1 knockout in embryonic stem cells was shown to stabilize C-MYC [186], [260]. In addition, HUWE1 can modify N-MYC, the neuronal MYC paralogue, with K48-linked ubiquitin chains, thus inducing its proteasomal degradation, an arrest of cellular proliferation, and induction of differentiation in neural stem/progenitor cells. By regulating N-MYC levels, HUWE1 also plays a role in the maintenance and lymphoid commitment of hematopoietic stem cells [186], [260]. However, HUWE1 is not the only E3 that

regulates MYC protein levels and functions. SKP2, FBXO28, FBW7 and FBXL14 are also known to ubiquitinate MYC [186], [261]-[264]. This exemplifies the complexity of the UPS, in which a given substrate may be modified by different E3s and, *vice versa*, one E3 may modify numerous substrates.

In apoptosis, HUWE1 was shown to modify MCL1, P53, and MIZ1, among other substrates. The anti-apoptotic factor MCL1, a member of the BCL2 family, binds to the BH3 domain of HUWE1 (see section 1.5.4) and is modified with K48-linked ubiquitin chains upon DNA damage. This was shown to be important for the regulatory functions of HUWE1 in the mitochondria-mediated apoptotic pathway [186], [222], [265]. However, HUWE1-mediated ubiquitination of the tumor suppressor P53 does not induce apoptosis, but suppresses it [266]. This process can be prevented by the tumor suppressor P14-ARF, which inhibits the ligase activity of HUWE1 and stabilizes P53 [266]. In the context of MYC-driven B-cell lymphomas, the stabilization of P53 upon HUWE1 suppression leads to growth arrest and apoptosis [267]. This indicates that HUWE1 acts as an oncoprotein in this context [186], [266], [267].

HUWE1 is also a regulator of the MYC-interacting zinc finger protein 1 (MIZ1). Upon TNFα-stimulation, MIZ1 was reported to be modified by HUWE1 with K48-linked ubiquitin chains, leading to its proteasomal degradation, releaving the inhibitory function of MIZ1 toward TRAF2 K63-polyubiquitination, and thus activating JNK and apoptosis [186], [230].

HUWE1 also regulates DNA repair via the tumor suppressor BRCA1, which is frequently mutated in breast and ovarian cancer. The lack or deregulation of BRCA1 often causes genomic instability due to defects in homologous recombination or non-homologous end joining, the two major DNA repair pathways [186], [268]-[270]. By polyubiquitinating and degrading BRCA1 upon DNA damage, HUWE1 represses DNA repair in breast cancer cells, while HUWE1 depletion results in increased resistance to ionizing radiation and mitomycin [186], [271].

HUWE1 also plays a role in the response to hypoxic stress. Under hypoxic conditions, HUWE1 decorates USP7 with K63-linked ubiquitin chains, thereby enhancing the activity of USP7 toward HIF-1α. Since HIF-1α promotes tumor progression, the stabiliziation of HIF-1α by HUWE1 upon hypoxia has a tumor-promoting effect [186], [272], [273].

Notably, the levels of HUWE1 itself are also regulated by the UPS, e. g., by the DUBs USP4 and USP7S [257], [274] and the E3 CUL4B [275]. Upon DNA-damage, for instance, HUWE1-levels are downregulated, which promotes apoptosis, cell-cycle arrest, and DNA-damage repair due to a stabilization of HUWE1 substrates which are involved in the corresponding pathways (e. g., MCL1, BRCA1, P53, MFN2) [222], [271], [275], [276]. At the same time, USP7S is downregulated during DNA damage, leading to enhanced HUWE1 auto-ubiquitination and proteasomal degradation, which in turn results in the stabilization of P53 and base-excision repair enzymes [257]. The downregulation of HUWE1 upon DNA-damage is also mediated by CUL4B, which is activated by neddylation and ubiquitinates HUWE1. Therefore, inhibition of CUL4B upregulates HUWE1 levels and sensitizes cells to DNA damage-induced apoptosis, probably due to enhanced proteasomal degradation of the anti-apoptotic MCL1 [275]. These examples indicate that the regulation of HUWE1 levels, here in the context of genotoxic stress, is critical for the control of proliferation, apoptosis, and DNA-repair and that inhibiting HUWE1 – or one of its regulators – have the potential of shifting cellular responses in the one or the other direction.

1.5.3 Tumor suppressor or oncogene?

As described in the previous section, it depends on the substrate whether HUWE1 acts as tumor suppressor or oncoprotein. For example, the findings that P53 stabilization, and thus cellular growth arrest and apoptosis, occurs upon HUWE1 depletion in MYC-driven B-cell lymphomas [267] and that HUWE1 stabilizes HIF-1α in hypoxia [272], [273], highlight tumor-promoting functions of HUWE1 [186]. Regarding MYC, one study describes that K63-ubiquitination by HUWE1 enhances the transcriptional activation of MYC target genes and thus promotes tumorigenesis, whereas MYC-ubiquitination by HUWE1 is prevented by the binding of MIZ1 to the MAX-MYC heterodimer [228], [242]. In the context of colorectal cancer it was shown that HUWE1 inhibiton by small-molecule inhibitors prevents MYC-dependent transcriptional activation in colorectal cancer cells due to the formation of a repressive trimeric complex of MYC/MAX/MIZ1 at the promoter [277]. Furthermore, it could be shown that HUWE1 regulates the ubiquitination and degradation of the RAC activator TIAM1, thereby stimulating

human lung cancer cell invasiveness [233], [242]. These examples in which HUWE1 acts as a tumor-driver are contrasted with the following studies in which HUWE1 is described as tumor suppressor: HUWE1 ubiquitinates and degrades the histone deacetylase 2 (HDAC2), a major epigenetic modulator. Histone deacetylase inhibitors (HDACi) can induce growth inhibition, differentiation and apoptosis of cancer cells, but these effects are diminished in HUWE1-deficient mouse embryonic fibroblasts due to the accumulation of HDAC2. The accumulation of HDAC2 then compromises the DNA damage-induced acetylation of P53, transcriptional activation, and apoptosis [242], [278]. In contrast to the above-mentioned study by Peter at al. [277], Myant et al. report an acceleration of tumorigenesis upon genetic deletion of HUWE1 in colon cancer and a stabilization of MYC upon loss of HUWE1, concluding that increasing levels of MYC are a critical driving force in tumorigenesis [279]. In line with the idea that HUWE1 modifies MYC with degradative ubiquitin chains, Heidelberger et al. show that HUWE1 attaches K48-ubiquitin chains to C-MYC to prepare for degradation in a VCP (P97)-dependent manner [229]. Another study showed that HUWE1 knockout mice developed DMBA/PMA-induced skin carcinogenesis, dependent on oncogenic Ras signaling. Loss of HUWE1 induced the accumulation of C-MYC/MIZ1 complexes which, in turn, mediate CDKN1A (P21), and CDKN2B (P15INK4B) downregulation. As a consequence, increased penetrance, number and severity of skin tumors was observed, but could be reversed by knockout of C-MYC [280].

In sum, these examples (summarized in **Table 2**) indicate that the tumor-promoting and suppressing functions of HUWE1 depend on the cellular context and/or stage of tumorigenesis. In addition, the precise functions of HUWE1 are substrate-dependent, as both tumor suppressor proteins (e. g., P53) and oncoproteins (e. g., C-MYC) are among the spectrum of substrates [242].

Table 2: (taken from [242]): Examples of the bivalent role of HUWE1 in tumorigenesis

Types of cancer	Tumor cell lines/mice models	Substrates or targets	Modification types	Ubiquitination site/type	Effect on tumor
Lung cancer	H1299、H358、H522(Lost p53)	TIAM1	Ubiquitination degradation	K48-mediated ubiquitination	Cancer promotion (metastasis)
	A549	p53	Ubiquitination degradation	Unknown	Cancer promotion
Colon cancer	Ls174T cells (HCT116-SW480-HT29)	MIZ1(MYC / MIZ1)		Unknown	Cancer promotion
	Apc mouse model (*Huwe1* conditional knockout)	MYC		Unknown	Tumor suppression
Skin tumors	K14Cre: Mule(flox / flox(y)) (Mule Kko)mice, DMBA/PMA Induced skin cancer	c-Myc(MYC/MIZ1)	Ubiquitination degradation	K48-mediated ubiquitination	Tumor suppression
Prostate cancer	CaP, PC3 and DU145 cell lines	c-Myc			Tumor suppression
Ovarian cancer	Conditional *Huwe1*L/L knockout mice	Histone H1.3	Ubiquitination degradation		Cancer promotion
Glioblastoma	Database survey	N-Myc (In neurodevelopme-nt)			
Medulloblastoma	Ptch1+/- mice	Atoh1	Ubiquitination degradation	Unknown	Tumor suppression
Thyroid cancer	Human thyroid cancer cell lines (WRO, FTC133, BCPAP)	p53			Tumor suppression

1.5.4 HUWE1 domain organization and structure

The cryo-EM structure of human full-length HUWE1, solved in 2020 [129], provides the first structure of a full-length HECT E3 [66]. Previously characterized structures of individual domains of HUWE1 comprised the catalytic HECT domain (PDB: 5LP8 [136], 6FYH [281], 3H1D, 3G1N) [282], the MCL1-binding BH3 domain (PDB: 5C6H) [222], [283], a WWE domain (PDB: 6PFL, 6MIW) [284], a UBM1 domain (PDB: 2MUL), also known as ubiquitin-interacting motif (UIM) [223], a ubiquitin-associated domain UBA (PDB: 2EKK), and the Armadillo repeat-like domains ARLD1 and ARLD2 (also known as 'domains of unknown function', DUF908 and DUF913) (**Figure 10**) [186], [223]. Sander et al. showed that an extended version of the catalytic HECT domain (PDB: 5LP8) can form an auto-inhibited dimer when crystallized in the absence of the N-terminal region of HUWE1. A region N-terminal to the dimerization region (DR; aa 3982-3991), known as the activation segment (AS; aa 3843-3895), was shown to be capable of interacting with the DR intramolecularly, thus releasing the autoinhibition and rendering the C-terminal fragment of HUWE1 monomeric (**Figure 10**).
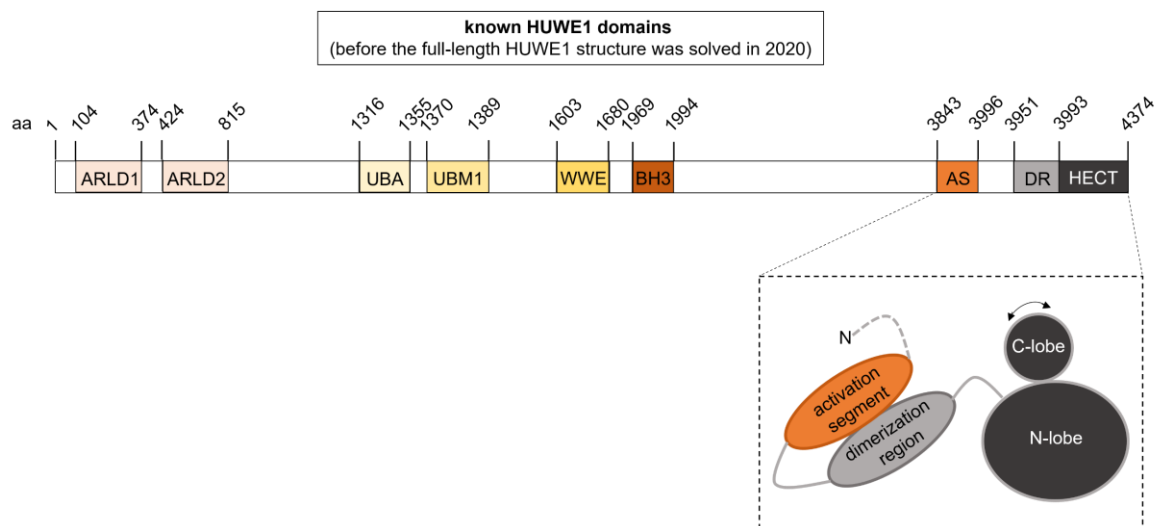
Figure 10: Identified and structurally characterized HUWE1 domains before 2020
The N-terminus of HUWE1 comprises two Armadillo repeat-like domains ARLD1 (aa 104-374) and ARLD2 (aa 424-815), also known as domains of unknown function (DUF908 and DUF913). Residues 1000 to 2000 contain a ubiquitin-associated domain UBA (aa 1316-1355, PDB: 2EKK), a UBM1 domain (aa 1370-1389, PDB: 2MUL) also described as ubiquitin interacting motif (UIM), a WWE domain (aa 1603-1680, PDB: 6PFL, 6MIW), and a BH3 domain (aa 1969-1994, PDB: 5C6H) that is known to bind MCL1. The C-terminus of HUWE1 includes the catalytic HECT domain (aa 3993-4374, PDB: 5LP8, 6FYH, 3H1D, 3G1N), with a dimerization region (DR, aa 3951-3993) and an activation segment (AS, aa 3843-3896) in close proximity that are able to interact intramolecularly in the context of the C-terminal part (aa 3843-4374) preventing dimerization (dotted box).

This intramolecular interaction can be prevented by a peptide derived from P14-ARF (aa 45-64), a HUWE1 inhibitor [266], which binds to the AS and induces the auto-inhibited dimeric state of the C-terminal region of HUWE1. Whether the activation segment may serve as a platform for other HUWE1 interactors needs further investigation. Interestingly, the AS also contains a PIP-box (aa 3880-3887), that was reported to recruit the HUWE1-substrate PCNA [136], [241]. These results provided a starting point for the first experiments performed during this PhD project (see section 4: Results and Discussion). The new structure shows full-length HUWE1 to contain four Armadillo repeat-like domains (ARLDs) with ring closure occurring between ARLD1 and ARLD4 (**Figure 11**). Except for the previously identified BH3 domain, which lies below the ring, all other domains and modules, such as the UBA, UIM, WWE, and HECT domain, are positioned above the ring. The authors defined a WWE-module, which includes the WWE domain itself, a 'HUWE1 WWE module associated' (HWA) domain and a helix-turn-helix motif located in a largely disordered region between ARLD3 and ARLD4, which is described as 'tower'. In close proximity to the tower there is the UB module 2,

which consists of three UBM-domains (**Figure 11**). AS and DR, connected by a flexible linker, form a 3-3 helix bundle that makes up a transient interface between the HECT domain and ARLD4 that allows for high flexilibity of the HECT domain with respect to the ring-shaped architecture. This flexibility appears to provide a key to HUWE1 activity, since it may enable the HECT domain to reach differently-bound substrates on the ring. To-date, only two substrate-binding motifs are known in HUWE1, the WWE domain (for PARylated substrates) and the BH3 domain (for MCL1), and how they are presented to the catalytic domain has remained unclear. Hunkeler et al. suggest that other substrates bind at the concave side of the ring via the helical repeats (**Figure 11**), as supported by a cryo-EM structure of full-length HUWE1 in complex with phosphorylated DDIT4. Partial density observed in this structure points to two peptide-like stretches of DDIT4 binding to a hydrophobic groove in ARLD2 and a positively charged pocket of ARLD1 [129].
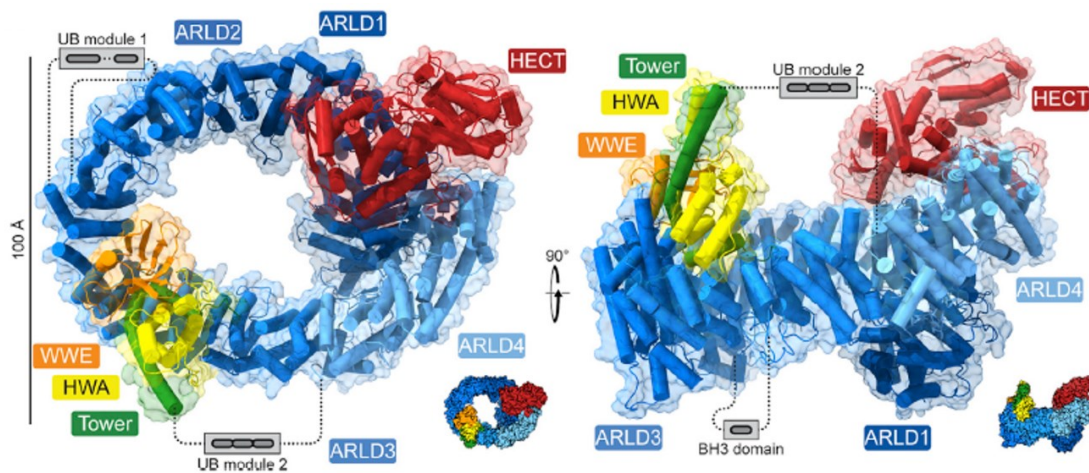
Figure 11: (taken from [129]): Cryo-EM structure of full-length HUWE1
Ring-shaped structure of human HUWE1 including four Armadillo-repeat like domains (ARLD1-ARLD4; blue), the BH3-domain/MCL1 binding (grey), the catalytic HECT domain (red), the UB module 1 (grey), the UB module 2 (grey), consisting of three repetitive UBM domains and the WWE module, consisting of the WWE domain (orange), the HUWE1 WWE associated (HWA) domain (yellow), and a helix-turn-helix motif, named as the 'tower' (green), shown in combined cartoon and surface representation [129].

In line with the cryo-EM structure of human full-length HUWE1 [129] the crystal structure of a fungal ortholog HUWE1$_N$ (287 kDa, 2490 residues) from the parasite *Nematocida* sp. ERTm5, solved by Grabarczyk et al., shows an overall similar fold and domain organization. This suggests that the core structure of HUWE1 with its ring-shaped architecture is conserved in less complex eukaryotes. Cryo-EM analysis of HUWE1$_N$ as well as cross-linking mass spectrometry indicate high flexibility of the intramolecular contacts and of the catalytic domain. This allows the catalytic domain to reach different substrate binding sites within the ring. [130].

1.6 The MYC interacting zinc finger protein 1 (MIZ1)

1.6.1 Cellular functions and interplay with MYC

MIZ1 (ZBTB17) is a BTB/POZ (Bric-à-brac/pox-virus and zinc finger)-domain containing protein [285]-[289] that is localized in the nucleus and cytoplasm [288], [290]-[292]. Its activating and repressing functions as a transcription factor are well-studied [293] and discussed below. However, data on its cytosolic functions are rather sparse. Ziegelbauer et al. showed that MIZ1 associates with microtubules and upon treatment with microtubule-depolymerizing drugs, MIZ1 is imported into the nucleus. It was speculated that MIZ1 requires a yet unknown protein for nuclear import [291].

MIZ1 was identified as an interaction partner of C-MYC, with only weak interactions to N-MYC and L-MYC, in a two-hybrid screen [288]. MIZ1 consists of an N-terminal BTB/POZ-domain, which mediates homo- and heterooligomerization, and 13 C2H2-type zinc-fingers (ZF), which allow for DNA binding. C-MYC interacts via its C-terminal helix-loop-helix-domain with a C-terminal region of MIZ1 that is located between the 12th and 13th ZF (aa 683-715) (**Figure 12A**) [288], [293].

In 2013 Wolf et al. identified a direct, non-palindromic MIZ1 binding site, based on CHIP-seq data and MEME-CHIP from neural progenitor cells, that is present in 181 of 261 sites and which was confirmed by mutagenesis of conserved and non-conserved residues [294]. However, another study showed two putative MIZ1-binding DNA motifs (ATCGGTAATC and ATCGAT), which account for MIZ1-activated transcription independently of MYC [295], but differ from the DNA-binding motif identified by Wolf et al. [294]. Due to the numerous ZFs in MIZ1

it is conceivable that MIZ1 binds to diverse independent motifs in a context-dependent manner. DNA-binding might be dependent on interactions of MIZ1 with other binding partners, such as MYC. Whether MIZ1 binds to core promoters or distantly from the transcription start site is also controversial and might depend on the context [295].

Well-studied target genes of MIZ1 encode the cell-cycle inhibitors *P15INK4B* (*CDKN2B*) [296], [297] *P21CIP1* (*CDKN1A*) [298] and *P57KIP2* (*CDKN1C*) [299], [300], whose expression is induced by the recruitment of the MIZ1 co-activators p300 and nucleophosmin 1 (NPM1) [293], [296], [301]. In addition, activation of MIZ1 target genes is regulated in dependency of antimitogenic signals (e. g., TGF-β-dependent) that relief MYC and regulate upstream transcription factors (e. g., SMAD) [293], [297]. Instead, upon DNA-damage, *P21CIP1* expression is repressed due to complex formation of MIZ1 with the MYC-MAX-heterodimer [293]. Notably, MIZ1 interacts with MYC, but not MAX, preventing the expression of MIZ1 target genes [296]-[300]. This repression occurs through the displacement of the MIZ1 coactivators p300 and NPM1 by MYC (**Figure 12B**) [288], [293], [296], [301]. Also, MYC is stabilized in complex with MIZ1, preventing its proteasomal degradation [293], [302] and it was proposed that the MYC/MIZ1 complex recruits DNA-methylases which may contribute to the transcriptional repression [293], [303], [304].
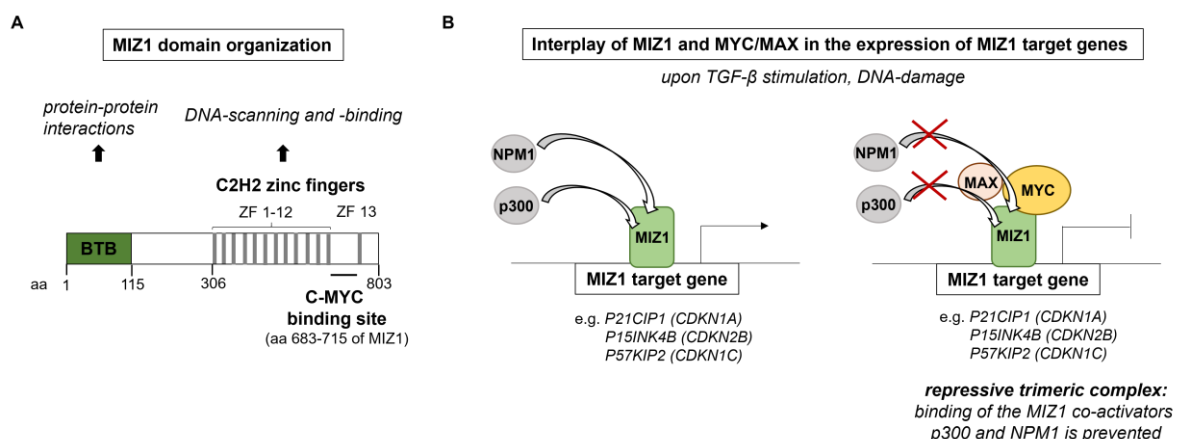
Figure 12: (modified from [293]): MIZ1 domain organization and regulation of MIZ1 target gene expression by the MYC/MAX-heterodimer
(A) Characteristic structural features of the MYC-interacting zinc finger protein 1 (MIZ1) including the N-terminal BTB-domain (aa 1-115) and the 13 C2H2 ZFs. (B) MIZ1 target gene expression is activated upon binding of the MIZ1 co-activators p300 and nucleophosmin 1 (NPM1) and in dependency of antimitogenic signals that regulate upstream transcription factors. Complex formation of MIZ1 with the MYC/MAX-heterodimer prevents binding of the co-activators p300 and NPM1 and represses MIZ1 target gene expression.

Besides MYC, other interaction partners of MIZ1, such as BCL6 and GFI-1, are also known to repress MIZ1-mediated transcriptional activation. While the MIZ1/BCL6-heterodimer (further details see 1.6.4) represses *P21CIP1* expression [305], GFI-1 forms a heterotrimeric complex with MYC and MIZ1 and represses *P15INK4B* and *P21CIP1* expression during lymphomagenesis [293], [306], [307].

Historically, MIZ1 function had mainly been associated with growth arrest due to its regulatory effects on different cell cycle inhibitors [288], [293]. However, in the past years, it was shown that the MIZ1/MYC complex also represses integrin expression, which is strongly enhanced by the ARF tumor suppressor protein. ARF interacts with the coactivator NPM1 and MIZ1 and promotes assembly of the MYC/MIZ1 complex [293], [308], [309].

Furthermore, MIZ1 is involved in the expression of BCL-2 upon interleukin-7 (IL-7) stimulation during B cell development [293], [310]-[312] and required for hair follicle structure and hair morphorgenesis by controlling exit from the cell cycle during the hair cycle [313]. Another, function of MIZ1 lies in vesicle transport, endocytosis and autophagy. Mice that express MIZ1 without the BTB/POZ domain, display a neurodegenerative phenotype, which was attributed to reduced autophagic flux through reduced expression of proteins involved in early and late stages of the autophagic pathway. The phenotypes observed upon deletion of the BTB/POZ domain are generally less severe than a homozygous MIZ1 knockout in mice (leading to apoptosis of ectodermal cells during gastrulation). Yet, both deletions are lethal either in early or later embryonic development, indicating that MIZ1 is essential during embryogenesis, a function that appears to be MYC-independent [293], [294].

Human *MIZ1* is localized at 1p36.13 [288]. While MIZ1 point mutations are rarely reported in the context of human tumors, deletions within 1p36 are associated with different tumors, indicating that 1p36 encodes genes with tumor suppressive functions [293], [314]. In line with this, Ikegaki et al. reported tumor suppressive functions of MIZ1 in neuroblastoma [293], [315].

A crucial question is whether the trimeric complex of MYC/MAX/MIZ1 is specific to promote tumorigenesis or which physiological functions are associated with it during normal homeostasis. If the MYC/MIZ1 assembly only occurs at supra-physiological levels of MYC and has exclusively pathophysiological

consequences, it would be an attractive cancer-therapeutic target [293]. In line with this idea, the MYC/MIZ1 complex antagonizes TGF-β-induced senescence in lymphomagenesis [300] and repression of P21CIP1 is critical during skin carcinogenesis [316]. Interesingly, perturbance of the MYC/MIZ1 complex by the V394D mutation in MYC decelerates colorectal cancer growth, which suggests the interface to be an interesting site for therapeutic interference [293].

MIZ1 was also found to inhibit TNFα-dependent JNK activation and cell death. In the presence of MIZ1, K63-linked polyubiquitination of TRAF2, with one of its downstream targets being JNK, is inhibited. Thereby MIZ1 abrogates JNK activation and cell death. However, upon TNFα-stimulation, HUWE1-mediated ubiquitination of MIZ1 with K48-linked chains results in JNK activation and cell death [230], [290]. Surprisingly, in this context, the HUWE1-MIZ1-interaction appears to be independent of the BTB domain [230]. In contrast, a previous study using an N-terminally truncated HUWE1 (aa 2473-4374) construct reported the BTB domain to be crucial for the interaction [228]. This discrepancy may be explained by the ring-shaped architecture of full-length HUWE1 [129], which may have led to artifactual results upon applying truncations.

Notably, MIZ1 is phosphorylated by the kinase AKT at Ser 428 and possibly at additional, yet unknown sites. Phosphorylation of MIZ1 promotes binding of 14-3-3η to the ZF region, prevents binding of MIZ1 to DNA, and transcriptional repression of target genes, such as *P21CIP1*. This, in turn, results in the release of cells from arrest in G1-phase following DNA-damage. MIZ1 phosphorylation does not occur in unstressed, proliferating cells, in which MIZ1 forms a transcriptionally inert complex with the topoisomerase II binding protein (TOPBP1) [292], [317].

1.6.2 Classification within the BTB domain-containing protein family

A characteristic feature of MIZ1 is its N-terminal BTB domain. This domain was first identified in the transcription factors Bric-a-brack, Tramtrack and Broad complex (BTB) in *Drosophila melanogaster*. At the same time, another study identified this conserved sequence in some Poxvirus proteins as well as in certain zinc finger proteins (ZID, GAGA, ZF5). Therefore the domain is also known as Pox virus and Zinc finger (POZ) domain [285]-[287], [318].

BTB-containing proteins exist in viruses and eukaryotes, including fungi, plants and metazoans, but not archaebacteria or bacteria, except for *Candidatus Protochlamydia amoebophila*. Based on available databases, such as Interpro, over 350 BTB-containing proteins exist in the human proteome. However, this number may underestimate the real number due to the low sequence similarity across BTB domains, which makes it challenging to predict BTB domains [318]. The low sequence similarity provides the key to the diverse functions and interactions of BTB domains, which have an overall conserved core fold, but differ in their surface-exposed residues and flanking structural elements [318], [319]. In 2005, Stogios et al. defined the core BTB fold as five α-helices (A1-A5) and three β-strands (**Figure 13A**) [319]. Dependent on N-terminal or C-terminal extensions to this core, BTB domain proteins are divided into 4 classes, described in the following [318], [319].
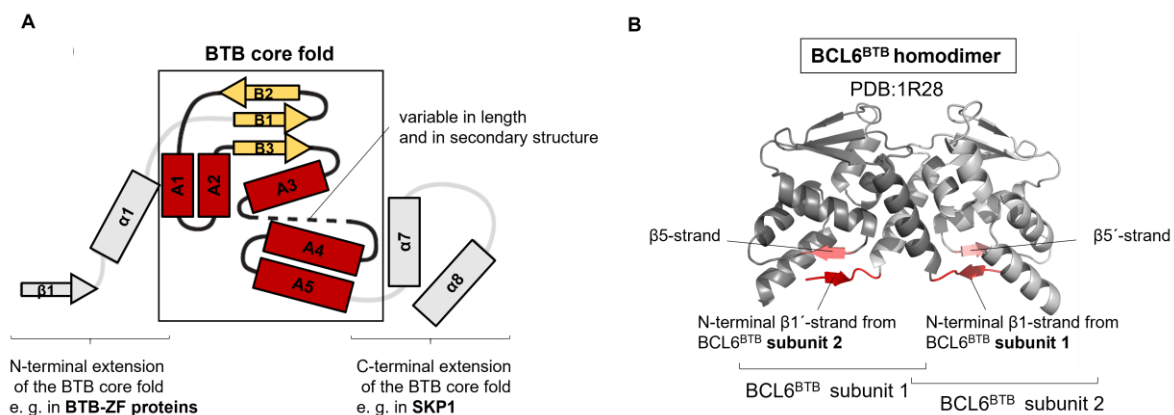
Figure 13: Nomenclature of secondary structure elements in the BTB domain (A) and structural features of a domain-swapped β-sheet in BTB-ZF proteins (B)
(A, modified from [319]) The BTB core fold (encircled with a rectangle) consists of five α-helices, A1-A5 (dark red) and three β-strands, B1-B3 (yellow). The doted line indicates a segment that varies in length and secondary structure depending on the BTB domain. BTB-ZF proteins often extend the BTB core fold N-terminally with an α1-helix and a β1-strand (grey). A C-terminal extension is observed in SKP1 with two additional α-helices α7 and α8 (grey). (B) Crystal structure of the homodimeric BTB domain of BCL6 (PDB: 1R28), exemplary for BTB-ZF proteins, featuring a domain swapped β-sheet. The N-terminal β1-strand (red) of subunit 1 (dark grey) interacts with the β5´-strand (pink) in subunit 2 and *vice versa*.

A BTB domain that only consists of the BTB core fold is the T1-domain in voltage-gated potassium channels (Kv channels). In this case, the BTB domain mediates tetramerization, as required for the protein to modulate channel gating and assembly [319]-[323].

In contrast, elongin C, an adapter in CRLs, only contains a BTB core fold and misses the terminal A5 helix [319]-[327]. Elongin C connects elongin B and the substrate-binding VHL tumor suppressor that targets HIF-1α for degradation [319], [328]-[331]. Similarly, SKP1 is part of a CRL, the SCF complex, in which it bridges the CUL1 scaffold protein and substrate-binding F-box proteins [318], [332]. Despite these related functions, the BTB domains of elongin C and SKP1 fall into separate classes. In contrast to elongin C, the BTB domain of SKP1 has two C terminal helices in addition to the BTB core fold (**Figure 13A**) [319].

Another class of BTB domains includes, among others, those found in BTB-ZF proteins, MATH-BTB proteins, and BTB-kelch proteins. This class of BTB domains is also able to bind CUL3 and recruit substrates to CRLs for proteasomal degradation [318], [333]-[336]. BTB-kelch proteins, however, are mostly involved in the stability and dynamics of actin filaments [319], [337]-[340] and typically contain a BTB and carboxy-terminal kelch (BACK) domain, in addition to the BTB domain and several Kelch motifs. The BACK domain is associated with a role in substrate orientation in the context of CRLs [319], [341]. The over 40 BTB-ZF proteins in the human proteome largely act as transcription factors [318], [319], [342], MIZ1 being one of them [288]. MIZ1 consists of the BTB core fold, with a flexible B3-region instead of a pre-formed B3-strand, and N-terminally extended with an α1-helix (**Figure 13A**) [319], [343]. Other BTB-ZF proteins are BCL6 [344]-[346] and PLZF [347], [348] which have two N-terminal elements, β1 and α1, in addition to their BTB core fold (**Figure 13A**) [319]. BTB-ZF proteins generally contain a BTB domain at their N-terminus and C-terminal C2H2-type ZFs (**Figuer 12A**), interspaced by a linker of ~ 100-375 residues with low sequence complexity. The linker is predicted to be unstructured, but interacts with accessory proteins involved in chromatin remodeling and transcriptional repression. While the C2H2 ZFs mediate DNA binding, the BTB domain mediates protein-protein interactions (**Figure 12A**). This includes self-association (homodimerization) and heterodimerization with BTB domains of other proteins (e. g., PLZF/FAZF [349], BCL6/BAZF [350], MIZ1/BCL6 [305], MIZ1/NAC1 [351], MIZ1/ZBTB4 [352], MIZ1/ZBTB49 [353]) (see section 1.6.4), higher-order oligomerization (e. g., GAF-BTB, Drosophila [354], [355]), and the recruitment of non-BTB proteins (e. g., MIZ1/GFI-1 [306], BCL6/co-repressors SMRT (see section 1.6.3), NCOR, BCOR [346], [356], [357]) [319]. Crystal structures of

dimeric BTB domains of BTB ZF proteins have been determined, for example of MIZ1 (PDB: 3M52), BCL6 (PDB: 1R28) or PLZF (PDB: 1BUO), and their dimerization was also studied in solution [319], [343], [346], [348]. Dimerization may involve a domain-swapped antiparallel β-sheet at the lower end of the BTB domain (**Figure 13B**), but is not seen in a group of BTB-ZF proteins that lack β1 while still being dimeric [319], [358]. One BTB-ZF that dimerizes independently of a domain-swapped β-strand, is FAZF (PDB: 3M5B). In this case, each N-terminal β-strand associates with its own chain [343]. In contrast, the dimeric BTB-domain of MIZ is lacking the region that makes up the β1-strand and thus also lacks a domain-swapped β-sheet [343].

The C-terminal part of MIZ1 comprises 12 adjacent C2H2 ZFs and a 13th ZF separated by 79 amino acids from the 12th ZF [288], [359]. The region between the 12th and 13th ZF is involved in protein-protein interactions and mediates the interaction with MYC [288] (see section 1.6.1). Based on the available structural data on the MIZ1 ZFs, it was suggested that the ZFs 1 to 6 are relevant for scanning the DNA for a specific binding motif, whereas the ZFs 7 to 12 mediate the actual DNA binding [360]. This notion was based on the observation that ZF1 and 6 undergo conformational dynamics in isolation and that ZF3 and 4 form a stable super-tertiary structure, which limits their flexibility [359], [361]. In contrast, ZFs 8 to 10 adopt canonical folds, which likely bind to DNA in a stable manner [359], [362]. The 13th ZF also has a classical C2H2 ZF structure, but its function is not yet clear [359]. It is unlikely that an isolated zinc finger is sufficient for DNA binding, although not impossible [359], [363]. It is also conceivable that ZF13 supports ZFs 1 to 6 in their DNA scanning function, as previously shown for other ZFs with low affinity for DNA [359], [364], [365]. Other hypothetical scenarios include an involvement of ZF13 in protein-protein interactions, RNA interactions or contributions to the MIZ1-MYC interaction [288], [359], [366], [367].

1.6.3 BCL6 contains a druggable BTB domain.

The anti-apoptotic transcription factor B-cell lymphoma 6 (BCL6), that belongs to the BTB-ZF protein family, is known for its oncogenic role, especially in diffuse large B-cell lymphomas (DLBCL). DLBCL is the most common type of non-Hodgkin lymphomas, with more than 18000 cases per year worldwide. Under

physiological conditions, BCL6 is upregulated upon activation of B-cells for the formation of germinal centers (GC) and downregulated thereafter [368], [369]. Failure of BCL6-downregulation, e. g., due to mutations of its genomic locus, is often pathological, because upregulated BCL6 represses DNA damage sensing, cell cycle, cell death and checkpoint genes and prevents the differentiation of DLBCL cells, thereby promoting lymphomagenesis [305], [368], [370]-[375]. Therefore, many studies have focused on targeting BCL6 therapeutically in order to reactivate BCL6 target genes and induce the death of DLBCL cells [375].

BCL6 downregulates about 500 target genes, involved in cell cycle control, gene transcription, DNA damage sensing, protein ubiquitination, and chromatin structure [375], [376]. BCL6 homodimerization through the BTB domain is required for its function as a transcriptional repressor by recruiting co-repressors, such as SMRT, NCOR, and BCOR [346], [356], [357], [377]. Crystal structures of the BTB domain in complex with co-repressor-derived peptides (PDB: 1R2B, 3BIM, 5H7G, 5H7H) [346], [378], [379] show that these co-repressors use a conserved, 17-amino acid sequence, known as BCL6 binding domain (BBD), to bind to a 'lateral groove' near the inter-subunit interface of each BTB subunit, and along the lower domain-swapped β-sheet of each subunit (**Figure 14**) [368], [375].
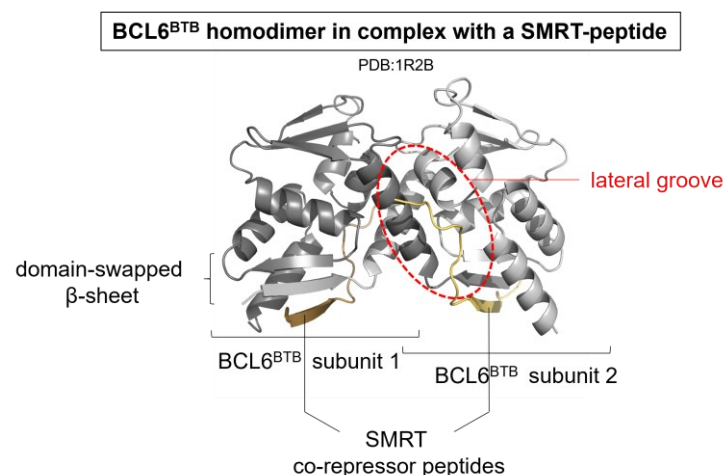
Figure 14: Crystal structure of the homodimeric BTB domain of BCL6 in complex with a co-repressor-derived peptide, PDB: 1R2B
The peptide derived from the co-repressor SMRT (silencing mediator for retinoid and thyroid hormone receptors) (ocher and pale yellow) binds to the BCL6 binding domain (BBD) with a 1:1 stoichiometry. The lateral groove of BCL6^{BTB} subunit 2 is encircled in red.

The residues in the lateral groove that are involved in the co-repressor binding are not conserved across the BTB domain family [368], [380]. This provides the opportunity to selectively target the lateral groove in BCL6. Polo et al. thus used the known co-repressor peptide sequences as templates to generate peptides that compete with the natural co-repressors for binding to the BTB domain of BCL6, thereby reactivating the expression of BCL6 target genes. Indeed, such peptides were found to induce the death of DBLCL cells, indicating that targeting the lateral groove may have therapeutic potential in the context of B-cell lymphomas [344]. Based on this BBD-peptide, reported by Polo et al., the retroinverso BCL6 peptide inhibitor RI-BPI was designed, which is shorter than the original peptide and contains D-amino acids in addition to a fusogenic motif. These changes made the compound more potent and stable, killed primary human DLBCL cells, but had no effect on normal lymphoid tissue or other tumors [381]. However, the synthesis of these peptide variants is challenging and they showed poor bioavailability. Therefore, numerous small-molecule inhibitors with reversible or irreversible binding to the lateral groove of the BCL6-BTB-domain were generated. Encouragingly, these compounds were found to reactivate BCL6 target gene expression and thereby induce cell death and growth arrest of xenograft DLBCL tumors *in vivo* and primary DLBCL cells from patients without being toxic. While BCL6-KO-mice die within weeks of acute inflammatory disease due to a loss of function in T cells and macrophages, these effects were not observed when blocking the lateral groove. This supports the idea that the lateral groove may provide a therapeutic window [368], [382]. PROTACs have also been designed to target BCL6 for proteasomal degradation. Notably, although BCL6 knockout is lethal, mice tolerated the PROTAC-treatment [368]. A major bottle neck in clinical applications of any of these small molecules is their limited bioavailability [368], [382] and the fact that the promising effects observed *in vitro* and *in vivo* were based on rather high concentrations [383].

Another interesting BCL6-directed degrader was published recently: This compound, BI-3802, functions as a degrader of BCL6 by binding to a groove between two BTB domain dimer, thereby inducing higher-order assembly into helical filaments. This in turn enhances the interaction of a VxP-motif (residues 249-251) of BCL6 with the E3 SIAH1, triggering rapid ubiquitination and degradation of BCL6 in a manner that is comparable to a BCL6 knockout.

Microscopically, the treatment with BI-3802 results in the reversible formation of intracellular foci that contain BCL6 and SIAH1 [383]. This strategy may offer new opportunities in treating BCL6 malignancies in combination with available B-cell lymphoma therapeutics, such as anti-CD20 antibodies [375], [384], [385]. Furthermore, it offers the intriguing possibility of being applied to the therapeutic manipulation of other transcription factors or yet undrugged pathogenic proteins.

1.6.4 MIZ1 homodimer and heterodimer formation regulates its transcriptional activity.

Depending on whether MIZ1 forms a homodimer, heterodimer, or other multimeric complexes, the cellular outcome can be different. MIZ1 can form repressive heterodimeric complexes with BCL6, NAC1 and ZBTB4 [305], [351], [352], [386], but also induces repression with non-BTB-domain-containing partner proteins, such as C-MYC and GFI-1 [288], [293], [296]; in contrast, homodimer formation of MIZ1 with ZBTB49 has an activating role [353]. Co-IP experiments in GC B-cells revealed that BCL6 interacts with MIZ1 through its BTB domain, and this interaction is independent of MYC. The MIZ1-BCL6 heterodimer recruits BCL6 to a target gene of MIZ1, *CDKN1A*, repressing its expression. As a consequence, cell cycle arrest is prevented, which is a desirable outcome during the proliferative expansion of germinal centers under normal conditions, but becomes pathological in B-cell lymphomas (**Figure 15A**) [305]. MIZ1 is also associated with ovarian serous carcinomas through the formation of a repressive MIZ1-NAC1 heterodimer [351]. NAC1 was originally identified as the protein product of a cocaine-inducible transcript in the nucleus accumbens of the rat brain [351], [387] and, more recently, as a transcriptional repressor during embryonic stem cell renewal [351], [388]. NAC1 is located in nuclear 'NAC1 bodies' and relocated to distinct bodies within the nucleus upon binding to MIZ1 [351], [389]. Binding between NAC1 and MIZ1 was demonstrated based on yeast two-hybrid assays and co-IPs in mammalian cells [351]. That knockdown of NAC1 in ovarian cancer cells activates the expression of the MIZ1 target gene *CDKN1A* suggested that the MIZ1-NAC1 heterodimer represses *CDKN1A* expression and promotes tumorigenesis by overwriting cell cycle arrest mechanisms (**Figure 15A**) [351]. Whether MIZ1 target genes are globally repressed by the MIZ1-BCL6 and MIZ1-

NAC1 heterodimers, respectively, requires further investigation [305], [351]. Notably, heterodimerization of MIZ1 with ZBTB49 was shown to activate *CDKN1A* expression; in this case, however, both MIZ1 and ZBTB49 induce *CDKN1A* expression independently [353]. Heterodimer formation of MIZ1 with BCL6 and NAC1, respectively, is mediated by the BTB domains, as corroborated by crystal structures (PDB: 4U2M, 4U2N). Of note, the BTB domains of MIZ1 and BCL6 or NAC1 were fused by a linker to facilitate crystallization (**Figure 15B-D**) [386].
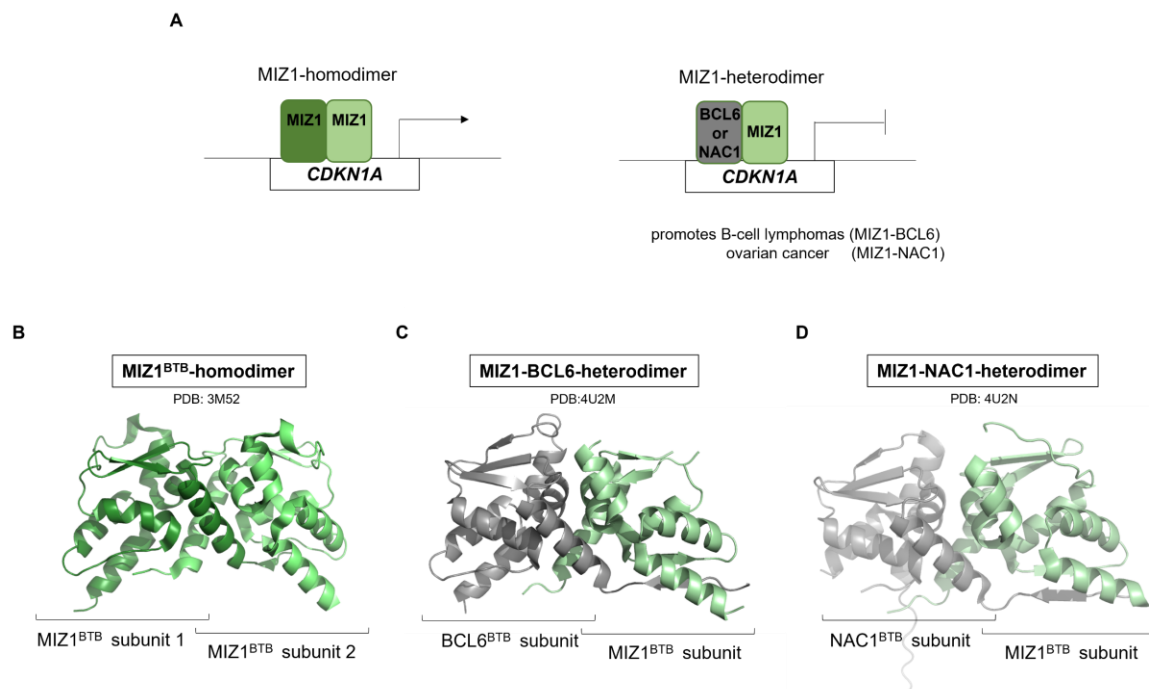
Figure 15: MIZ1 homodimer and MIZ1 heterodimers and their impact on MIZ1 target gene expression
(A) Upon binding of the MIZ1 homodimer to the promoter of the MIZ1 target gene, here exemplary shown for *CDKN1A*, gene expression is activated. Heterodimerization of BCL6 or NAC1 with MIZ1 inhibits MIZ1 target gene expression. In the context of MIZ1-BCL6, this repression is associated with B-cell lymphomas; the MIZ1-NAC1 heterodimer promotes ovarian cancer due to abrogation of cell cycle arrest. (B) Crystal structure of the homodimeric MIZ1-BTB-domain (PDB: 3M52) with MIZ1^{BTB} subunit 1 coloured in dark green, and MIZ1^{BTB} subunit 2 in light green. (C) Crystal structure of the MIZ1-BCL6-heterodimer (PDB: 4U2M), consisting of a BCL6-BTB-domain (dark grey) and a MIZ1-BTB-domain (green). The dimerization was enhanced by a covalent linker between the C-terminus of MIZ1^{BTB} and the N-terminus of BCL6^{BTB} (linker not modeled). (D) Crystal structure of the MIZ1-NAC1 heterodimer (PDB: 4U2N), consisting of a NAC1-BTB-domain (light grey) and a MIZ1-BTB-domain (pale green). The subunits were fused as described in (C).

1.7 The transcriptional repressive BTB-ZF protein KAISO/ZBTB33

Interactomics [390] and CHIP-seq analyses [391], [392] identified KAISO (ZBTB33) as an interaction partner of HUWE1. However, nothing is known about the respective binding sites or physiological roles of this interaction. Like MIZ1, KAISO is a BTB-ZF protein. It functions as a transcriptional repressor and has the ability to bind to both methylated and non-methylated DNA, provided the DNA sequence contains a KAISO binding site (KBS) [393]-[395]. KAISO dimerizes via its N-terminal BTB domain and has three ZFs at the C-terminus. It is located in the nucleus and interacts with its C-terminal region with the cell adhesion cofactor p120ctn that is structurally similar to β-catenin [395]-[397]. KAISO also interacts with the co-repressor NCOR and mediates DNA-methylation-dependent transcriptional repression [394], [395], [398]. Furthermore, KAISO is a critical regulator of p53-mediated cell cycle arrest and apoptosis upon genotoxic stress in mammalian cells [399]. Upon DNA-damage, KAISO expression increases and KAISO interacts with the p53-p300 complex, thereby inducing p53-acetylation at K320 and K382 by p300 and inhibiting acetylation at K381. The modifications enhance the affinity of p53 to p53 response elements of *CDKN1A* and apoptosis genes, enhancing their expression. This in turn results in cell cycle arrest and apoptosis (**Figure 16**). Consequently, knockout of KAISO in mouse embryonic fibroblast (MEF) cells diminished p53 binding to the p53 response elements, resulting in reduced expression of *CDKN1A* and apoptotic genes [399]. Since both, p53 and KAISO, are interaction partners of HUWE1, it is conceivable that HUWE1 affects the levels of these proteins during their interplay in a yet unknown way.
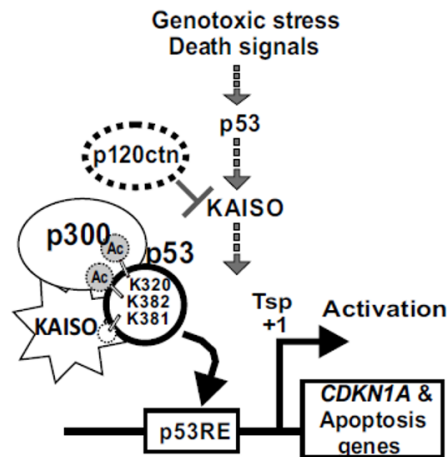
Figure 16 (taken from [399]): KAISO promotes cell cycle arrest and apoptosis upon genotoxic stress by stabilizing the p53/p300-interaction.
Upon genotoxic stress, expression of KAISO is enhanced which stabilizes the interaction of p53 with the acetyltransferase p300, thereby promoting p53-acetylation at K320 and K382 and preventing acetylation at K381. Acetylated p53 shows enhanced binding to the p53 response elements (p53RE) of *CDKN1A* and other apoptotic genes, thereby induces cell cycle arrest and apoptosis [399], while DNA binding of KAISO is prevented through binding of p120ctn to the C-terminal DNA-binding region of KAISO [395].

1.8 A SCF^FBXL17-dependent quality control pathway prevents the accumulation of BTB domain heterodimers.

Protein quality control pathways are essential to prevent diseases caused by the accumulation of atypical complex assemblies or misfolded proteins that pathologically affect signal transduction [400], [401]. Aberrant complex formation in form of heterodimeric complexes of BTB-proteins can promote tumorigenesis, as described in the previous section 1.6. To prevent the accumulation of inactive BTB heterodimers a quality control pathway has evolved that was shown to be mediated by the CRL SCF^FBXL17. Certain (but not all) BTB domain homodimers contain a domain-swapped β-sheet at the lower part of the domain, as described in section 1.6.2, while certain BTB heterodimers or mutated variants fail to form this intramolecular interaction. Residues in this β-sheet are rather divers across BTB domains. Therefore, Mena et al. have described the N-terminal β-strand as a 'molecular barcode' for BTB domain dimerization that makes abberant BTB dimers recognizable for SCF^FBXL17. This E3 is thought to scan complementarity and shape of BTB domains via a large binding surface that allows for the involvement of different surface residues depending on characteristics of the BTB-domain. Aberrant BTB heterodimers may dissociate more rapidly due to the failure to form

42

a stable domain-swapped β-sheet and are selectively recognized by SCF^{FBXL17}, while homodimers are unaffected. Binding of SCF^{FBXL17} induces dimer dissociation and ubiquitination of monomers, which are subsequently degraded by the proteasome (**Figure 17**) [401], [402]. Interestingly, HUWE1 was also described to ubiquitinate and degrade unassembled proteins with exposed hydrophobic residues (see section 1.5.1) [223], corroboration the notion that there are distinct quality control systems to ensure the correct assembly of protein complexes in the cell and prevent the accumulation of aggregation-prone components, which frequently cause disease [401], [402].
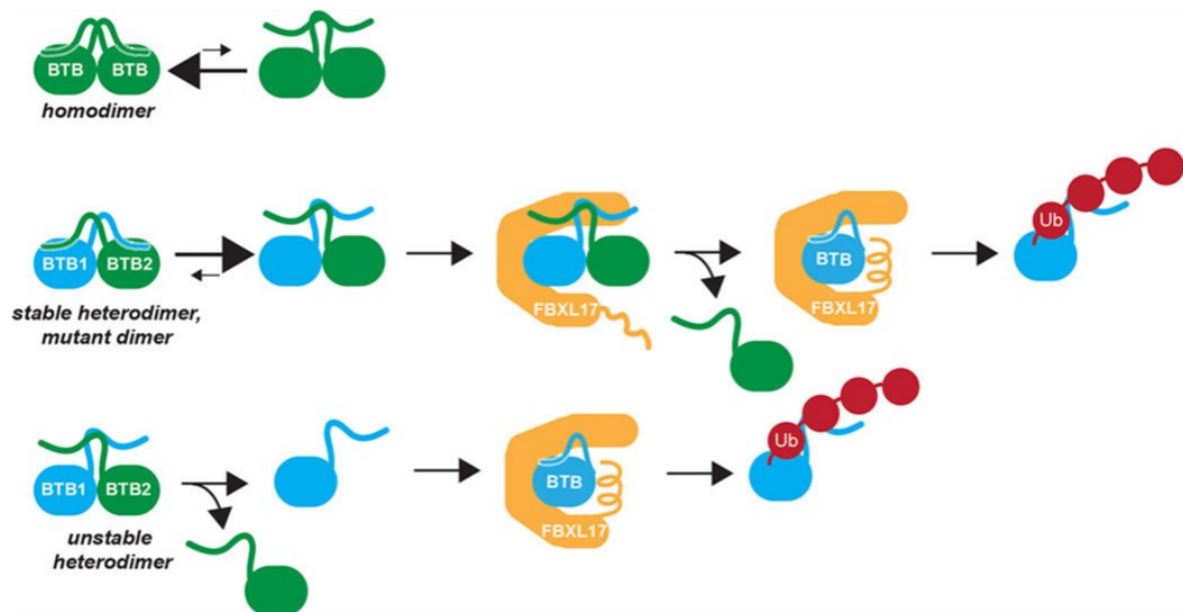
Figure 17: (taken from [402]): Schematic representation of the dimerization quality control for homodimeric and heterodimeric BTB-domain-containing proteins by the SCF^{FBXL17}
Intact BTB-homodimers often form a domain-swapped β-sheet and are therefore not bound by SCF^{FBXL17} (top row); in contrast, mutant or unstable BTB-heterodimers have a less stable domain-swapped β-sheet, which serves as a recognition feature for the CRL SCF^{FBXL17} (2nd and 3rd row). Unstable heterodimers often dissociate before binding by the SCF^{FBXL17}, followed by the ubiquitination and degradation of the BTB-monomer (3rd row); stable, but mutated BTB-heterodimers tend to dissociate only upon binding to SCF^{FBXL17}.

2 Materials

2.1 Bacterial strains and cell lines

2.1.1 Bacterial strains

Table 3: Bacterial strains used for cloning and recombinant protein expression

Organism	Strain	Genotype	Supplier	Application
E. coli	One Shot TOP10	F- *mcrA* Δ(*mrr-hsd*RMS-*mcr*BC) Φ80*lacZ*ΔM15 Δ *lac*X74 *rec*A1 *ara*D139 Δ(*araleu*)7697 *gal*U *gal*K *rps*L (StrR) *end*A1 *nup*G	Thermo Fisher Scientific; Cat# C404006	cloning
E. coli	LOBSTR-BL21(DE3)- RIL	E. coli B F- ompT hsdS(rB - mB -) dcm+ Tetr E. coli gal λ (DE3) endA Hte [argU ileY leuW Camr] (ArnA, SlyD knockout)	Kerafast; Cat# EC1002	protein expression
E. coli	NEB Stable Competent *E. coli*	F´proA+B+lacIq Δ(lacZ)M15 zzf::Tn10(TetR)/ Δ(ara-leu) 7697 araD139 fhuA ΔlacX74 galK16 galE15 e14- Φ80dlacZΔM15 recA1 relA1 endA1 nupG rpsL (StrR) rph spoT1 Δ(mrr-hsdRMS-mcrBC)	New England Biolabs; Cat# C3040H	cloning lentiviral vectors

2.1.1.1 Media for bacterial cell culture

Lysogeny broth (LB) medium

40 g LB medium/l

  ⇨ autoclaved
  ⇨ supplemented with the appropriate antibiotic(s) (see 2.1.1.2)

<u>LB agar</u>

20 g/l LB medium

10 g/l Agar-Agar

⇨ autoclaved
⇨ supplemented with the appropriate antibiotic(s) (see 2.1.1.2), prior to pouring into 10 cm-dishes

2.1.1.2 Antibiotics for bacterial cell culture

Table 4: Stock concentrations and dilution of antibiotics used for bacterial cell culture

Antibiotic	Stock concentration	Dilution
Ampicillin	100 mg/mL	1:1000
Kanamycin	50 mg/mL	1:1000
Chloramphenicol	34 mg/mL	1:1000

2.1.1.3 Induction of bacterial protein expression

Table 5: Used induction agents for bacterial cell culture

Promoter	Inducing agent	Final concentration
T7	Isopropyl-β-D-thiogalactopyranosid (IPTG)	0.5 mM
pBAD	L(+)-arabinose	0.5 g/l

2.1.2 Cell lines

Table 6: Mammalian cell lines used in this study

Cell line	Description	Source
HeLa	human cervical cancer cell line	Martin Eilers, Biocenter, University Würzburg
HEK293T	human embryonic kidney cell line	Martin Eilers, Biocenter, University Würzburg
MEF_MIZ1$^{\Delta POZ/BTB}$	mouse embryonic fibroblast cell line; depletion of the MIZ1-POZ/BTB-domain [294]	Elmar Wolf, Biocenter, University Würzburg

2.1.2.1 Media for mammalian cell culture

Table 7: Culture conditions of the respective cell lines

Cell line	Medium	Supplements
HeLa, HEK293T	'culture medium': Dulbecco's Modified Eagle Medium (DMEM);	10 % Fetal Calf Serum (FCS), inactivation at 56 °C for 30 minutes required before usage; 1 % Penicillin/Streptomcyin;
	'transfection medium': DMEM	2 % FCS
	'freezing medium':	90 % FCS; 10 % Dimethylsulfoxide (DMSO);
MEF MIZ1$^{\Delta POZ/BTB}$	'culture medium': DMEM	10 % FCS; 1 % Penicillin/Streptomcyin; 1 % non-essential amino acids (NEAA); 2 µl β-mercaptoethanol;
	'freezing medium': DMEM	40 % FCS; 10 % DMSO

2.2 Primers

Oligonucleotides for cloning (Restriction-free (RF) cloning, see 3.1.1; site-directed mutagenesis (SDM), see 3.1.2) and sequencing were obtained from Sigma-Aldrich. The purification grade of the lyophilized oligonucleotides was 'Desalt'. The lyophilizate was dissolved in the specified amount of ddH$_2$O to obtain a 100 µM stock solution and was diluted to 10 µM for further use.

Table 8: List of primers used for RF cloning, SDM and sequencing in this study (F, fw, Fwd: Forward; R, Rev: Reverse)

Primer name	Sequence (5´ → 3´)	Application
HUWE1		
HUWEC_H3874A_Fwd	GAAAGCCATGATCAGGCTGCGGTGCTGGTGC	SDM
HUWEC_H3874A_Rev	GCACCAGCACCGCAGCCTGATCATGGCTTTC	SDM
HUWEC_L3877A_Fwd1	CAGCATGCGGTGGCAGTGCTACAGC	SDM
HUWEC_L3877A_Rev1	GCTGTAGCACTGCCACCGCATGCTG	SDM
HU1_L3877P_F1	CAGCATGCGGTGCCGGTGCTACAGCCTG	SDM
HU1_L3877P_R1	CAGGCTGTAGCACCGGCACCGCATGCTG	SDM

Primer name	Sequence (5´→ 3´)	Application
L3879A F	GGTGCTAGTGGCACAGCCTGC	SDM
L3879A R	GCAGGCTGTGCCACTAGCACC	SDM
V3883A F	GCTACAGCCTGCTGCCGAGGCCTTCTTTC	SDM
V3883A R	GAAAGAAGGCCTCGGCAGCAGGCTGTAGC	SDM
F3886A F	GCTGTCGAGGCCGCCTTTCTGGTCC	SDM
F3886A R	GGACCAGAAAGGCGGCCTCGACAGC	SDM
HUWEC_F3887A_Fwd4	GCTGTCGAGGCCTTCGCTCTGGTCCATGCCAC	SDM
HUWEC_F3887A_Rev4	GTGGCATGGACCAGAGCGAAGGCCTCGACAGC	SDM
HU1_F3887P_F1	GTCGAGGCCTTCCCGCTGGTCCATGC	SDM
HU1_F3887P_R1	GCATGGACCAGCGGGAAGGCCTCGAC	SDM
HU1_delta3870-90_F1	GGAGTGTCTAAAGGAACTAGAGGAAGCCACAGAGCGGGAGAGCAAGCCTCC	Deletion of aa 3870-90 in dN-HUWE1 (aa 2474-4374) by PCR2 (RF cloning)
HU1_delta3870-90_R1	GGAGGCTTGCTCTCCCGCTCTGTGGCTTCCTCTAGTTCCTTTAGACACTCC	
dNHU1_ab3843_F1	CCATACGATGTTCCAGATTACGCTAGCGGATCCGAGTTACCCCTGCTCAGCGAGCAGCTGAGTTTGGAC	Shortening of dN-HUWE1 (aa 2474-4374) to HUWE1[AS] (aa 3843-4374) by using the SDM protocol
dNHU1_ab3843_R1	GTCCAAACTCAGCTGCTCGCTGAGCAGGGGTAACTCGGATCCGCTAGCGTAATCTGGAACATCGTATGG	
pM41_C2_F	CGAGAATCTTTATTTTCAGGGCGCCATGGACTCCCATGACCAGCATGCGGTG	RF cloning: Amplification of AS[C] (HUWE1 aa 3870-3890) for insertion into pETM41 encoding a N-terminal MBP- and C-terminal His6-tag
pM41_C2_R	GGATCTCAGTGGTGGTGGTGGTGGTGATGGACCAGAAAGAAGGCCTCGAC	
HA_2364-3665_F1	CGGCCGCCAGTGTGCTGGAATTCACCATGGCATACCCATACGATGTTCCAGATTACGCTAGCGGATCTAACAGTACAATTATAGTGAGCAGAAGTGGAG	RF cloning: Amplification of HUWE1 aa 2364-3665 from Fl-HUWE1 (pCMV) for insertion into pcDNA3ΔBam (empty vector #692 Eilers/Wolf laboratory)
HA_2364-3665_R1	CCAATGTGAAACCCTCTCTCCTGATGGCTAATAATCTAGAGGGCCCTATTCTATAGTGTCACC	
HU1delta2960-75_F1	CCTTCAACAAGCAGTGAAGAAGAAGATCCCCTTCTGCCTGATGACATCCGTCGGGAAGTTCTACAGAACCAGC	Deletion of aa 2960-75 in HUWE1 2364-3665 by PCR2 (RF cloning) to generate HUWE1 2364-3665 ΔBS1
HU1delta2960-75_R1	GCTGGTTCTGTAGAACTTCCCGACGGATGTCATCAGGCAGAAGGGGATCTTCTTCTTCACTGCTTGTTGAAGG	

Primer name	Sequence (5´→ 3´)	Application
HU1delta3023-36_F1	GGTGTGACTGAAGTGAGCCCTGAGTTTCTGCA GAGAGCTGAGCAGCAGCGACGAGAACTAGC	Deletion of aa 3032-36 in HUWE1 2364-3665 by PCR2 (RF cloning) to generate HUWE1 2364-3665 ΔBS2
HU1delta3023-36_R1	GCTAGTTCTCGTCGCTGCTGCTCAGCTCTCTGC AGAAACTCAGGGCTCACTTCAGTCACACC	
HU1delta3324-50_F1 (primer miss labeling; correction: HU1delta3323-49_F1)	GCATGCAAGCGGTGGCTCCACCGTCCACTTCA CACAGCAGCGGACCAAAGAAACAAACTGTGAG	Deletion of aa 3323-49 in HUWE1 2364-3665 by PCR2 (RF cloning) to generate HUWE1 2364-3665 ΔBS3
HU1delta3324-50_R1 (primer miss labeling; correction: HU1delta3323-49_R1)	CTCACAGTTTGTTTCTTTGGTCCGCTGCTGTGT GAAGTGGACGGTGGAGCCACCGCTTGCATGC	
dNHU1_del3x_F1	CCTAGAAGAGCCGTTGCCTTCAACAAGC	RF cloning: Amplification of an HUWE1 insert from HUWE1 aa 2364-3665 ΔBS1 ΔBS2 ΔBS3 to generate dN-HUWE1 ΔAS^C ΔBS1 ΔBS2 ΔBS3
dNHU1_del3x_R1	GAGGACTGTGAGGAGCATGGGCTACAGG	
delBS1_600bpInsert_F1	GACGGCTGTCAGCAGTCAGCTAGAAGG	RF cloning: Amplification of an about 600 bp HUWE1 insert with Δaa 2960-2975 (BS1) to generate dN-HUWE1 ΔAS^C ΔBS1 ΔBS2 ΔBS3
delBS1_600bpInsert_R1	CACACTGTCCTCCATATCCTCTAGGACAC	
HU1_aa3661_F1	CTCTCTCCTGATGGCCTGCCTGAGGAGCAG	Insert amplification of dNHUWE1 mutants to transfer into Fl-HUWE1 by RF cloning
HU1_aa4105_R1	GCTGAGGTGGTTGGGGTTGCAGTGGGAAGATG G	

Primer name	Sequence (5´→ 3´)	Application
MIZ1		
MizPOZ pLIP F	CCTGTACTTCCAGGGTGGATCCATGGCTATGGACTTTCCCCAGCACAGC	RF cloning: aa 1-115 of MIZ1[BTB] from pET23 (N-terminal cloning overhang: GGSMAS) into pLip(NHis)-vector (N-terminal cloning overhang GGSMA)
MizPOZ pLIP R	CCTTTCGGGCTTTGTTAGCAGCCGGATCTTAAGCAAGTGACTTGAGGGCATGG	
pCCA_POZ1-115_Fwd3	GCTCACAGAGAACAGATTGGTGGGATGGACTTTCCCCAGCACAGCCAG	RF cloning: aa 1-115 of MIZ1[BTB] from pLip(NHis)-vector into pCCA vector to remove N-terminal cloning overhang GGSMA
pCCA_POZ1-115_Rev3	AGGCCTGCATTCGATGAGGTGGTATTAAGCAAGTGACTTGAGGGCATGG	
Mizmono_F	CACAGAGAACAGATTGGTGGG	Amplification gBlock MIZ1[BTB] dimer interface variant, see 2.2.1, by RF cloning, PCR1
Mizmono_R	CCTGCATTCGATGAGGTGC	
pLIP-POZ_FlAsH_N F	CACCGGCGAAAACCTGTACTTCCAGGGTTGCTGTCCGGGTTGTTGCATGG	N-terminal insertion of (G)CCPGCCMA to MIZ1[BTB] (aa 1-115) in pLip(NHis)-vector by RF cloning, for fluorescent labeling with FlAsH-EDT$_2$
pLIP-POZ_FlAsH_N R	GCTGTGCTGGGGAAAGTCCATAGCCATGCAACAACCCGGACAGCAACC	
MIZ1_POZ_F28A_Fwd2	GTGACTGCACCGCTGTGGTGGACG	SDM
MIZ1_POZ_F28A_Rev2	CGTCCACCACAGCGGTGCAGTCAC	SDM
MIZ1_POZ_L52A_Fwd3	CGAGTACTTCAAGATGGCCTTCGTGGACCAGAAGG	SDM
MIZ1_POZ_L52A_Rev3	CCTTCTGGTCCACGAAGGCCATCTTGAAGTACTCG	SDM
MIZ1_POZ_F53A_Fwd3	GAGTACTTCAAGATGCTCGCCGTGGACCAGAAGGACG	SDM
MIZ1_POZ_F53A_Rev3	CGTCCTTCTGGTCCACGGCGAGCATCTTGAAGTACTC	SDM
MIZ1_POZ_V60P_Fwd3	GACCAGAAGGACGTGCCGCACCTGGACATCAG	SDM
MIZ1_POZ_V60P_Rev3	CTGATGTCCAGGTGCGGCACGTCCTTCTGGTC	SDM
MIZ1_POZ_H61A_Fwd3	CCAGAAGGACGTGGTGGCCCTGGACATCAGTAACG	SDM

Primer name	Sequence (5´→ 3´)	Application
MIZ1_POZ_H61A_Rev3	CGTTACTGATGTCCAGGGCCACCACGTCCTTCTGG	SDM
MIZ1_POZ_L62A_Fwd1	GACGTGGTGCACGCCGACATCAGTAACG	SDM
MIZ1_POZ_L62A_Rev1	CGTTACTGATGTCGGCGTGCACCACGTC	SDM
MIZ1_POZ_I64A_Fwd1	GTGCACCTGGACGCCAGTAACGCGG	SDM
MIZ1_POZ_I64A_Rev1	CCGCGTTACTGGCGTCCAGGTGCAC	SDM
MIZ1Cterm3xFlag_F1	CTGAATGTCCCCCGCCTGCCGAGGACTACAAAGACCATGACGGT	Amplification of Flag-tag for insertion at the C-terminus of Fl-MIZ1 in the pcDNA3 and pUHD vector (#691b and #647, from E. Wolf) by RF cloning
MIZ1Cterm3xFlag_pcDNA3_R1	GTGACACTATAGAATAGGGCCCTCTAGATCACTTGTCGTCATCGTCTTTGTAGTC	
MIZ1Cterm3xFlag_pUHD_R1	CTCATCAATGTATCTTATCATGTCTGGATCCTCTAGATCACTTGTCGTCATCGTCTTTGTAGTC	
FlMIZ1_1xFlag_HzuD_F	GGACTACAAAGACGATGACGACAAGTG	SDM
FlMIZ1_1xFlag_HzuD_R	CACTTGTCGTCATCGTCTTTGTAGTCC	SDM
lenti_POZ_Rf_F1	GAGTCGGCCGGTGGATCCACCGGTATGGACTTTCCCCAGCACAGCCAGCATGTC	Amplification of MIZ1^{BTB} single mutant variants from Fl-MIZ1 (pcDNA3 vector (#691b, from E. Wolf) for insertion into lentiviral pRRL vectors encoding Fl-MIZ1 WT (D. Solvie, Eilers laboratory) by RF cloning
lenti_POZ_Rf_R1	AGCAAGTGACTTGAGGGCATGGCAGGCCGTGATGATGTCCTGCATTTGGAGG	
Sequencing		
pBAD F	ATGCCATAGCATTTTTATCG	Sequencing plasmids with pBAD promoter
pBAD R	GATTTAATCTGTATCAGG	
180725_Seq_HUWEC_R	CGAAGGAACTTCTGTGTGTCAG	Reverse sequencing of HUWE1 starting from aa 3956
pM41 Seq fw	GTGTCGATGAAGCCCTGAAAGACGCGCAGAC	Sequencing pETM41 vectors encoding MBP-AS^C-His$_6$ and MBP-MIZ1$^{1-282}$-HA-His$_6$
T7_Fwd_Seq	TAATACGACTCACTATAGGG	Sequencing plasmids with T7 promoter
T7_Rev_Seq	GCTAGTTATTGCTCAGCGG	

50

Primer name	Sequence (5´→ 3´)	Application
CMV_Fwd	CGCAAATGGGCGGTAGGCGTG	Sequencing plasmids with CMV promoters
CMV_Rev	AGTAGGAAAGTCCCGTAAGG	
BGH_Rev	TAGAAGGCACAGTCGAGG	Sequencing pcDNA3 (ΔBam) vector (encoding Fl-MIZ1; plasmid #691b from E. Wolf)
EBV_Rev	GTGGTTTGTCCAAACTCATC	Sequencing pUHD vector (encoding MIZ1$^{\Delta POZ/BTB}$; plasmid #647 from E. Wolf)
MIZ1_Cterminus_Fwd	GCACTGGTCATGTTCCAGACAGACG	Sequencing C-terminus of pUHD vector (#647, from E. Wolf) encoding MIZ1$^{\Delta POZ/BTB}$, and pcDNA3 ΔBam vector (#691b, from E. Wolf) encoding Fl-MIZ1
MIZ1deltaPOZ_Nterm_ Rev	GCTCCTCCTTGAGGTCCCTGCTG	Sequencing N-terminus of pUHD vector (#647, from E. Wolf) encoding MIZ1$^{\Delta POZ/BTB}$
pRRL_SFFV_Fwd_Seq	CTTCTGCTTCCCGAGCTCTA	Sequencing lentiviral vectors, from D. Solvie (Eilers laboratory), K. Wiese
pRRL_IREShygRn_Rev _Seq	CAGACCTTGCATTCCTTTGG	
Others		
Nac1_F1	TGCCCTCAAGTCACTTGCTCGCTCCGGTGGCG GGTCGAGC	Amplification gBlock by PCR1 (RF cloning) to generate MIZ1^{BTB}-NAC1^{BTB} heterodimer, see 2.2.1
Nac1_R1	GCATTCGATGAGGTGGTATTATCAACTACTTAC CTTCAG	

Primer name	Sequence (5′→ 3′)	Application
pCCA_Kaiso+HA_F1	GCTGAGTTAGGAGTTCCTCTTTCACAGTACCCATACGATGTTCCAGATTACGCTTGATAATACCACCTCATCGAATGC	Insertion of C-terminal HA-tag to KAISO^{BTB} (aa 1-122, pCCA vector) with SDM protocol
pCCA_Kaiso+HA_R1	GCATTCGATGAGGTGGTATTATCAAGCGTAATCTGGAACATCGTATGGGTACTGTGAAAGAGGAACTCCTAACTCAGC	

2.2.1 Double-stranded DNA fragments (gBlocks)

The double-stranded DNA fragments (gBlocks) were purchased from Integrated DNA Technologies (IDT).

MIZ1^{BTB} dimer interface variant (V10D/L14D/Q17D/V41K)

CACAGAGAACAGATTGGTGGGATGGATTTCCCGCAGCAGCATTCGCAGCATGATTTAGAGCAAGAACAACCAGGACCGTCAGTTGGGCTTACTGTGCGATTGTACGTTCGTTGTCGATGGAGTCCATTTTAAGGCACATAAAGCTAAGTTAGCAGCGTGCTCTGAGTACTTTAAGATGCTTTTTGTGGACCAAAAAGACGTAGTACACTTAGACATTTCCAATGCGGCGGGACTGGGTCAGGTTTTAGAGTTCATGTACACCGCCAAGTTGTCCTTATCGCCTGAAAATGTCGATGACGTGTTAGCAGTGGCAACTTTTCTGCAGATGCAAGACATCATCACCGCATGTCATGCGTTAAAAAGTTTGGCGTAATAGGCACCTCATCGAATGCAGG

Due to the incorrectly inserted nucleotide 'G' in the gBlock, the MIZ1^{BTB} dimer interface insert was amplified with the respective primers (see 2.2) by following the PCR1 protocol for RF cloning (see 3.1.1), prior to PCR2 of RF cloning to finally insert the quadruple mutant of MIZ1^{BTB} (aa 1-115 with two stop codons; V10D/L14D/Q17D/V41K) into the pCCA vector.

MIZ1^{BTB}-BCL6^{BTB} heterodimer

TGCCCTCAAGTCACTTGCTCGTAGTGGTGGCGGGTCGAGCGGGGGGTTCCGGTACCGCAGATTCTTGCATCCAATTTACACGTCATGCGTCTGACGTTCTGTTGAACCTTAATCGCTTACGCTCTCGCGACATTCTTACAGACGTTGTGATCGTCGTCTCTCGCGAGCAGTTTCGCGCACATAAGACTGTTTTGATGGCCTGCTCAGGATTATTCTACTCTATTTTCACTGATCAATTGAAATGCAACCTGTCGGTGATTAATCTTGATCCGGAGATCAATCCTGAGGGGTTCTGCATCTTACTTGATTTCATGTACACATCTCGTTTGAACCTTCGTGAGGGTAATATCATGGCGGTCATGGCTACCGCCATGTATTTACAAATGGAGCACGTCGTGGACACCTGCCGTAAGTTTATTAAAGCCTCCGAATGATAATACCACCTCATCGAATGC

MIZ1^{BTB} (aa 110-115) served as cloning overhang to attach BCL6^{BTB} (aa 5-129 with stop codon) to the C-terminus of MIZ1^{BTB} through connection by a Gly/Ser-linker in the pCCA vector encoding MIZ1^{BTB} (aa 1-115) by using the PCR2 protocol of RF-cloning (see 3.1.1).

MIZ1^BTB-NAC1^BTB heterodimer

TGCCCTCAAGTCACTTGCTCGCTCCGGTGGCGGGTCGAGCGGAGGAAGCGGGACAGCACAG
ACTTTGCAGATGGAGATTCCTAACTTTGGAAATTCTATCCTTGAATGCCTGAATGAGCAACGCT
TACAGGGGTTATACTGTGACGTTTCGGTTGTTGTGAAGGGTCATGCCTTCAAGGCTCATCGCG
CCGTATTGGCGGCCTCGAGTTCGTACTTCCGCGATCTTTTTAATAATTCTCGTAGTGCTGTAGT
GGAACTGCCAGCGGCAGTACAACCTCAGTCTTTTCAGCAGATTCTGTCATTCTGTTATACAGG
TCGCTTAAGCATGAACGTCGGGGATCAAGATTTACTGATGTACACTGCCGGTTTCTTGCAGAT
CCAAGAAATCATGGAGAAAGGTACGGAATTCTTCCTGAAGGTAAGTAGTTGATAATACCACCT
CATCGAATGC

MIZ1^BTB (aa 110-115) served as cloning overhang to attach NAC1^BTB (aa 2-125 with stop codon) to the C-terminus of MIZ1^BTB through connection by a Gly/Ser-linker in the pCCA vector encoding MIZ1^BTB (aa 1-115). Due to low concentration and volume of the ordered gBlock, the insert was first amplified by using the PCR1 protocol of RF cloning (see 3.1.1) with the respective primers (see 2.2). Afterwards, the purified insert was cloned into the pCCA vector encoding MIZ1^BTB (aa 1-115) by the PCR2 protocol of RF-cloning (see 3.1.1).

KAISO^BTB (aa 1-122)

CACAGAGAACAGATTGGTGGGATGGAATCGCGTAAATTGATCTCGGCGACAGATATTCAGTAT
TCGGGGTCTCTGCTTAATTCGCTGAATGAACAACGTGGTCATGGCTTATTTTGTGACGTGACT
GTAATCGTAGAAGACCGCAAGTTCCGCGCACATAAAAACATTTTGAGCGCGTCCTCAACCTAC
TTTCACCAGTTATTTAGTGTAGCTGGGCAGGTGGTGGAGTTATCCTTCATCCGTGCAGAAATTT
TCGCTGAAATTCTGAACTACATTTACTCCAGTAAGATCGTTCGCGTCCGTAGTGACCTTCTGGA
TGAACTGATTAAATCCGGACAGTTACTTGGGGTAAAATTCATCGCTGAGTTAGGAGTTCCTCTT
TCACAGTGATAATACCACCTCATCGAATGC

KAISO^BTB (aa 1-122 with stop codon; based on PDB: 3M4T) was inserted into the pCCA vector by following the PCR2 protocol of RF cloning (see 3.1.1).

2.3 Plasmids

Table 9: List of vectors used in this study with the respective encoded gene and specifying tag, cleavage site and selection marker (only WT genes are listed but respective variants were cloned into the same vector backbone).

Vector	Gene	Tag	Cleavage site	Resistance	Source
Protein expression in bacterial cells					
pBADM11	HUWE1^{AS} aa 3843-4374 HUWE1^{D} aa 3896-4374 HUWE1$^{D, min}$ aa 3951-4374	N^{term} His$_6$	TEV	Ampicillin	empty vector: EMBL Heidelberg, modified; vector with insert cloned by B. Sander (Lorenz laboratory)
pSKB2	HUWE1^{HECT} aa 3993-4374	N^{term} His$_6$	3C	Kanamycin	empty vector: modified pSKB2-backbone, derived from pET28a (Merck); vector with insert cloned by B. Sander (Lorenz laboratory)
	AS aa 3843-3890 AS^{N} aa 3843-3869 AS^{C} aa 3870-3890	N^{term} lipoyl-domain (*) and C^{term} His$_6$	TEV (to cleave lipoyl-domain)	Kanamycin	
pETM41	MBP- AS^{C} aa 3870-3890	N^{term} MBP; C^{term} His$_6$	TEV (to cleave MBP)	Kanamycin	empty vector: provided by B. Sander (Lorenz laboratory)
pETM41	MIZ1$^{1-282}$ aa 1-282	N^{term} MBP; C^{term} HA-His$_6$	TEV (to cleave MBP)	Kanamycin	cloned by B. Sander (Lorenz laboratory)
pET23	MIZ1^{BTB} aa 1-115, N^{term} cloning overhang after TEV cleavage: GGSMAS	N^{term} His$_6$ and lipoyl-domain (*)	TEV	Kanamycin	provided by B. Sander (Lorenz laboratory); used for crystallization only
pLip(NHis)	MIZ1^{BTB} aa 1-115, N^{term} cloning overhang after TEV cleavage: GGSMA	N^{term} His$_6$ and lipoyl-domain (*)	TEV	Kanamycin	empty vector: provided by B. Sander (Lorenz laboratory)

Vector	Gene	Tag	Cleavage site	Resistance	Source
pCCA (pET-28, modified)	MIZ1^{BTB} aa 1-115; dimer-interface variant V10D/L14D/Q17D/V41K	N^{term} His$_6$ and SUMO	ULP1	Kanamycin	empty vector: Merck
	MIZ1^{BTB}-BCL6^{BTB} aa 1-115 + aa 5-129				empty vector: Merck; insert based on [386]
	MIZ1^{BTB}-NAC1^{BTB} aa 1-115 + aa 2-125				
	KAISO^{BTB} aa 1-122				empty vector: Merck
pET-28a	UBCH5A aa 1-147	N^{term} His$_6$	ULP1	Kanamycin	[50]; modified
	UBCH5B aa 1-147	N^{term} His$_6$	ULP1		
	UBCH5C aa 1-147	N^{term} His$_6$	TEV		provided by M. Rape; modified
	UBCH7 aa 1-154	N^{term} His$_6$	3C		
pET-30a	Ubiquitin aa 1-76	-	-	Kanamycin	provided by S. Lorenz; [100]
pRK793	TEV aa 1-303	N^{term} His$_6$	-	Ampicillin	provided by J. Kuriyan
pFGET19	ULP1 aa 403-621	N^{term} His$_6$	-	Kanamycin	
pET-24d	3C aa 1-401	C^{term} His$_6$	-	Kanamycin	provided by F. Sauer (Kisker laboratory)
Protein expression in insect cells					
pFASTBac	UBA1	N^{term} His$_6$	-	Ampicillin, Gentamicin	provided by M. Rape
Protein expression in mammalian cells					
pCMV	Fl-HUWE1 aa 1-4374	N^{term} HA		Ampicillin	provided by M. Kurokawa
	dN-HUWE1 aa 2474-4374				provided by S. Peter (Eilers laboratory)/ K. Helin
	HUWE1^{AS} aa 3843-4374				modified from dN-HUWE1
pcDNA3 ΔBam	HUWE1 aa 2364-3665	N^{term} HA		Ampicillin	empty vector: #692 from Eilers/Wolf laboratory

Vector	Gene	Tag	Cleavage site	Resistance	Source
pcDNA3 ΔBam	Fl-MIZ1 aa 1-803	C^{term} 1xFlag		Ampicillin	modified vector #691b from Eilers/Wolf laboratory
pUHD	MIZ1 aa 105-803	C^{term} 1xFlag		Ampicillin	modified vector #647 from Eilers/Wolf laboratory
pBABE-H2B	GFP			Ampicillin	provided by Eilers laboratory

(*) Lipoyl-domain tag: residues 2–85 of branched-chain alpha-keto acid dehydrogenase subunit E2 from *Geobacillus stearothermophilus* [403].

2.4 Synthetic peptides

Table 10: List of synthetic HUWE1 peptides used for crystallization and fluorescence polarization experiments

	Application	Supplier
HUWE1-derived peptide AS^C aa 3870-3897	crystallization	Elim Biopharm
fluorescently labeled HUWE1-peptide 5-FAM-AS^N aa 3843-3869	fluorescence polarization	
fluorescently labeled HUWE1-peptide AS^C-Lys-5-FAM aa 3870-3894		
fluorescently labeled HUWE1-peptide HUWE1-Lys-5-FAM aa 3283-3310		

2.5 Antibodies

Table 11: List of antibodies used in this study

Antibody	Specification	Dilution	Application	Supplier
Primary antibodies				
HA	mouse, monoclonal	2 µg/IP	IP	Sigma-Aldrich, H9658
Flag	mouse, monoclonal	2 µg/IP	IP	Sigma-Aldrich, F3165
IgG	mouse, polyclonal	2 µg/IP	IP	Merck, 12-371
HUWE1	rabbit, polyclonal	5 µg/IP	IP	Bethyl Laboratories, A300-486A
		1:1000	WB (FI-HUWE1)	
HA	rabbit, polyclonal	1:5000	WB	Abcam, ab9110
HA	rabbit, monoclonal	1:1000	WB	CellSignaling, #3724
Actin	mouse, monoclonal	1:2000	WB	Sigma-Aldrich, A1978
MIZ1	goat, polyclonal	1:500	WB	R&D, AF3760
HUWE1	rabbit, polyclonal	1:1000	WB	Sigma-Aldrich, SAB2900746
Secondary antibodies				
Anti-goat IgG-HRP		1:10000	WB	Santa Cruz Technology, sc-2354
Anti-mouse IgG-HRP				Cell Signaling Technology, 7076S
Anti-rabbit IgG-HRP				Cell Signaling Technology, 7074S
Horseradish peroxidase (HRP) conjugated primary antibodies				
HA-HRP	Mouse, monoclonal	1:4000	WB	Sigma-Aldrich, H6533
Flag-HRP	Mouse, monoclonal	1:1000, 1:6000 (co-IP FI-HUWE1/ FI-MIZ1)	WB	Sigma-Aldrich, A8592
Actin-HRP	Mouse, monoclonal	1:100000	WB	Sigma-Aldrich, A3854

2.6 Kits, enzymes, standards

2.6.1 Kits

Table 12: Kits

Kit	Supplier
NucleoSpin Gel and PCR Clean-up Kit	Macherey & Nagel
NucleoSpin Plasmid, Mini kit for plasmid DNA	Macherey & Nagel
NucleoBond Xtra Midi/Maxi	Macherey & Nagel
Pierce BCA Protein Assay Kit	Thermo Fisher Scientific

2.6.2 Enzymes, commercial buffers, reagents

Table 13: Enzymes, commercial buffers and reagents purchased from the specified supplier

	Supplier
Enzymes	
Benzonase Nuclease	Merck
Q5 High-Fidelity DNA Polymerase	New England Biolabs (NEB)
DpnI	New England Biolabs
DNase I	AppliChem
Commerical buffers	
Q5 Reaction Buffer	New England Biolabs
Q5 High GC Enhancer	New England Biolabs
NuPAGE MES SDS Running Buffer	Thermo Fisher Scientific
Reagents	
Midori Green Advance DNA stain	Nippon Genetics Europe
SignalFire ECL Reagent	Cell Signaling Technology
Pierce ECL Western Blotting Substrate	Thermo Fisher Scientific
Pierce ECL Plus Western Blotting Substrate	Thermo Fisher Scientific

2.6.3 Standards

Table 14: Standards for gel electrophoresis

Standard	Supplier
PageRuler Plus Prestained Protein Ladder	Thermo Fisher Scientific
1kb DNA Ladder	New England Biolabs
100 bp DNA Ladder	New England Biolabs

2.7 Crystallization screens

Table 15: Commerically available crystallization screens used for crystal trials with the 'Analytic Honey Bee 963' (Digilab) robot

Crystallization screen	Supplier
Additive Screen	Hampton Research
Crystal Screen, Crystal Screen 2	Hampton Research
Index Screen HT	Hampton Research
JCSG+	Molecular Dimensions
Nextal PEG Suite	Qiagen
Nucleix Suite	Qiagen
Optimix 3	Fluidigm
Optimix PEG	Fluidigm
PEGs Suite, PEGs II Suite	Qiagen
pH Clear Suite, pH Clear II Suite	Qiagen
Protein Complex Suite	Qiagen
Silver Bullets Bio	Hampton Research
Wizard 1+2, Wizard 3+4	Emerald BioSystems

2.8 Chemicals

Table 16: List of chemicals, including biochemical and cell biological substances

Substance	Supplier
2'-Deoxyadenosine 5'-triphosphate (dATP), sodium salt solution	New England Biolabs
2'-Deoxycytidine 5'-triphosphate (dCTP), sodium salt solution	
2'-Deoxyguanosine 5'-triphosphate (dGTP), sodium salt solution	
2'-Deoxythymidine 5'-triphosphate (dTTP), sodium salt solution	
2-Propanol (Isopropanol)	Carl Roth
4-(2-hydroxyethyl)-1-piperazineethanesulfonic acid (HEPES)	
Acetic acid	
Adenosin-5'-triphosphate disodium salt (ATP)	
Agar-Agar	
Agarose NEEO ultra quality	
Albumin fraction V (BSA)	
Ammonium persulfate (APS)	
Ampicillin sodium salt	
L(+)-Arabinose	
Beta-mercapthoethanol (β-ME)	Sigma-Aldrich
Bis-acrylamide 29:1	Fisher Bioreagents
Chloramphenicol	Carl Roth
cOmplete EDTA-free protease inhibitor tablets	Roche

Substance	Supplier
Coomassie Brilliant Blue R-250	Carl Roth
Cycloheximide	Enzo Life Sciences
Dimethylsulfoxide	Carl Roth
Disodium hydrogen phosphate (Na$_2$HPO$_4$)	
Dithiothreitol (DTT)	
Dulbecco´s Modified Eagle Medium (DMEM)	Sigma-Aldrich
Ethanol	
Ethylenediaminetetraacetic acid (EDTA)	
Fetal calf serum (FCS)	Capricorn Scientific
Glycerol	Carl Roth
Glycine	
Hydrochloric acide (HCl)	
IGEPAL CA-630 (NP-40)	Sigma-Aldrich
Imidazole	
Isopropyl-β-D-thiogalactopyranoside (IPTG)	
Kanamycin sulfate	
Lysogeny broth (LB) medium	
Magnesium chloride hexahydrate	
Methanol	
MG-132	Enzo Life Sciences
Milk powder	Carl Roth
Non-essential amino acids (NEAA)	Gibco
Nickel(II) sulfate hexahydrate	Carl Roth
Penicillin/Streptomycin (100x)	Capricorn
Polyethylenglycol (PEG) 3350	Sigma-Aldrich
Polyethylenglycol (PEG) 4000	Sigma-Aldrich
Polyethylenimine (PEI)	Sigma-Aldrich
Potassium dihydrogen phosphate (KH$_2$PO$_4$)	Carl Roth
Ponceau S	Sigma-Aldrich
Protease-and phosphatase inhbitor cocktail	Sigma-Aldrich
Sodium acetate	Carl Roth
Sodium chloride (NaCl)	Carl Roth
Sodium dodecyl sulfate (SDS)	Sigma-Aldrich
Sodium hydroxide (NaOH)	Carl Roth
Tetramethylethylenediamin (TEMED)	Carl Roth
Tris-(2-carboxyethyl)-phosphine (TCEP)	Carl Roth
Tris-(hydroxymethyl)-aminoethane (TRIS)	Carl Roth
TritonTM X-100	Sigma-Aldrich
Tween 20	Sigma-Aldrich

2.9 Buffers and solutions

Table 17: List of buffers and solutions used in this study

Buffer or solution	Composition
Analytical gel filtration buffer	20 mM HEPES pH 8 100 mM NaCl 1 mM EDTA 5 mM DTT
Blocking solution (Western blot)	5 % BSA or milk powder in TBS-T or PBS-T
Coomassie staining solution	0.2 % Coomassie Brilliant Blue R250 1.5 % acetic acid 50 % ethanol
Coomassie destaining solution	20 % ethanol 10 % acetic acid
Dialysis buffer (recombinant protein purification)	20 mM HEPES pH 8 150 mM NaCl 5 or 10 mM imidazole
Elution buffer B (Ni-affinity chromatography)	80 mM HEPES pH 8 500 mM NaCl 10 % glycerol 1 M imidazole 5 mM β-mercaptoethanol (β-ME)
Fluorescence polarization (FP) buffer	20 mM HEPES pH 8 150 mM NaCl 1 mM EDTA 5 mM DTT 0.01 % Triton X-100
Gel filtration buffer (recombinant protein purification)	20 mM HEPES pH 8 150 mM NaCl 1 mM EDTA
Immunoprecipitation (IP) buffer (low salt)	20 mM HEPES pH 7.9 200 mM NaCl 0.2 % NP-40 0.5 mM EDTA 10 % glycerol
Immunoprecipitation (IP) buffer (high salt)	20 mM HEPES pH 7.9 450 mM NaCl 0.2 % NP-40 0.5 mM EDTA 10 % glycerol
IP buffer (for co-IP with Fl-HUWE1)	50 mM HEPES 150 mM NaCl 1 % Triton X-100 1.5 mM $MgCl_2$
Isothermal titration calorimetry (ITC) buffer	20 mM HEPES pH 8 100 mM NaCl 1 mM EDTA 5 mM DTT

Buffer or solution	Composition
Lysis buffer A (Ni-affinity chromatography)	80 mM HEPES pH 8 500 mM NaCl 10 % glycerol 5 or 20 mM imidazole 5 mM β-mercaptoethanol (β-ME)
Phosphate buffered saline (PBS), 10x	137 mM NaCl 2.7 mM KCl 10 mM Na_2HPO_4 1.8 mM KH_2PO_4
PBS-T (Western blot)	1x PBS buffer, supplemented with 0.05 % Tween-20
Stripping buffer (Western blot)	200 mM glycine 0.1 % SDS 1 % Tween-20 pH 2.3 adjusted with HCl
Protein dilution buffer (Activity assay)	25 mM HEPES pH 7.4 100 mM NaCl 1 mM DTT; 50 mM HEPES pH 8 50 mM NaCl 100 µM DTT (activity assay with Fl-HUWE1)
Reaction buffer (Activity assay)	25 mM HEPES pH 7.4; 50 mM HEPES pH 8 (activity assay with Fl-HUWE1)
SDS running buffer	25 mM TRIS 192 mM glycine 0.1 % SDS
SDS stacking gel (4 %)	125 mM TRIS pH 6.8 0.1 % SDS 4 % bis-acrylamide 0.05 % APS 0.1 % TEMED
SDS separating gel (10/12/15 %)	375 mM TRIS pH 8.8 0.1 % SDS 10/12/15 % bis-acrylamide 0.05 % APS 0.05 % TEMED
TAE-buffer (Agarose gel electrophoresis)	40 mM TRIS pH 8 20 mM acetic acid 1 mM EDTA
TBS-T (Western blot)	20 mM TRIS pH 7.5 150 mM NaCl 0.05 % Tween-20
Transfer buffer (Western blot)	25 mM TRIS 192 mM glycine 20 % methanol

2.10 Consumables

Table 18: List of specialized consumables used in this study

Consumable	Specification	Supplier
BCA assay		
96-well polystyrene plates, corner notch	clear, flat bottom	Thermo Fisher Scientific
Sealing tape	pre-cut, pressure sensitive	Thermo Fisher Scientific
Crystallization		
96-well sitting-drop crystallization plates	CrystalQuick 1 square well, flat bottom, low profile	Greiner Bio-One
96-well sitting drop crystallization plates	CrystalQuick, 3 drops/well	Greiner Bio-One
24-well hanging-drop crystallization plates	Crystalgen SuperClear Plate	Jena Bioscience
Cover slides (22 mm)	siliconised	Jena Bioscience
Optical quality sealing foil	VIEWseal	Greiner Bio-One
Fluorescence polarization		
384-well microplate	black, non-binding, flat bottom	Greiner Bio-One
Immunoprecipitation		
Dynabeads Protein A	superparamagentic beads	Thermo Fisher Scientific
Dynabeads Protein G	superparamagentic beads	Thermo Fisher Scientific
Isothermal titration calorimetry (ITC)		
Dialysis Kit	Pur-A-Lyzer Midi 3500	Sigma-Aldrich
Recombinant protein expression and purification		
Disposable cuvettes	UVette	Eppendorf
Dialysis membranes	Spectra/Por	Spectrum Laboratories
Ultrafiltration units	Amicon MWCO 3-30 kDa, 0.5-20 mL	Merck Millipore
SDS-PAGE		
6 %, 8 %, 4-20 %	Tris-Glycine Mini Gels, WedgeWell	Thermo Fisher Scientific
4-12 %, 12 %	Bis-Tris Gels	Thermo Fisher Scientific
Western blot		
Filter paper	Whatman Blotting Paper	Sigma-Aldrich
PVDF membrane	Roti-PVDF	Carl Roth
Others		
Pipette tips	10 µl, 200 µl, 1000 µl	StarLab
Syringe	30 mL, 12 mL, 5 mL, 3 mL, 1 mL	Braun
Syringe attachment filter	0.22 µm or 0.45 µm	Carl Roth

2.11 Equipment and instrumentation

Table 19: List of equipment and devices used in this study

Device	Specification	Supplier
Affinity chromatography column	HisTrap HP 5 mL	GE Healthcare
	MBP Trap HP 5 mL	
Agarose gel electrophoresis system	Mini-Sub Cell GT System	BioRad
Analytical SEC column	SD75 10/300 GL Increase	GE Healthcare
	SD200 10/300 GL Increase	
	SD200 3.2/300 Increase	
Autoclave	V-150	Systec
Balances	LE225D	Sartorius
	TE412	
Calorimeter	Microcal iTC200	GE Healthcare
Cell counter (Eilers laboratory)	CASY cell counter	Innovatis
Cell culture incubator (Eilers laboratory)	BBD 6220	Heraeus
Cell disruption system	Microfluidizer M-110P	Microfluidics
Centrifuges	Avanti J-26 XP	Beckman Coulter
	5415R	Eppendorf
	5804R	
Centrifuge (Eilers laboratory)	Multifuge 1S-R	Heraeus
Centrifuge bottles/tubes	Bottle J-Lite 1000 mL, for JLA 8.1 rotor in Avanti J-26 XP centrifuge	Beckman Coulter
	Polypropylene bottle, screw-cap (29 x 104 mm, 50 mL), for JA25.50 rotor in Avanti J-26 XP centrifuge	
Chemiluminescence imaging	FluorChem Q Imaging System	Alpha Innotech
Crystallization tools	CrystalCap Magnetic, CryoVial, CrystalWand Magnetic, CryoLoop	Hampton Research
Crystallization robot	Analytic Honey Bee 963	Digilab
Crystal storage pucks	SPINE Puck	Jena Bioscience
Gel electrophoresis chamber (SDS-PAGE)	Mini-PROTEAN Tetra Vertical Electrophoresis Cell (handcast SDS gels)	BioRad
	XCell SureLock Mini-Cell (precast SDS gels)	Invitrogen

Device	Specification	Supplier
Handcast systems for SDS-gels	Mini-PROTEAN Casting Frame	BioRad
	Mini-PROTEAN 3 Multi-Casting Chamber	
Liquid handling robot	LISSY 2002	Zinsser Analytik
MALS detector	DAWN 8 + HELEOS II	Wyatt
Microplate reader	CLARIOstar	BMG LABTECH
Microscope	SteREO Discovery.V12	Zeiss
	STEMI 2000	
Microscope: Camera	AxioCam MRC	Zeiss
Microscope: Light source	KL 2500 LCD	Zeiss
Microscope (Eilers laboratory)	Axiovert 40CFL	Zeiss
PCR Cycler	C1000 Touch Thermal Cycler	BioRad
pH Meter	EL20	Mettler Toledo
Power supply (gel electrophoresis)	PowerPac Basic	BioRad
Preparative SEC columns	SD75 16/600	GE Healthcare
	SD200 16/600	
Robotic sealing unit for microplates	RoboSeal	HJ-BIOANALYTIC
Rotor for Avanti J-26 XP	JA 25.50	Beckman Coulter
	JLA 8.1	
Scanner (SDS gels)	Odyssey	LI-COR
Shaker	LabTherm	Kühner
	LabTherm LT-X	
	ISF-1-W	
	ISF-1-X	
Semi-dry Blotting System (Western Blot)	Trans-Blot Turbo Transfer-System	BioRad
Sonicator	Labsonic	B. Braun Biotech International
Sonicator (Eilers laboratory)	Digital Sonifier W-250 D	Branson
Spectrophotometer	Bio-Photometer Plus	Eppendorf
	NanoDrop ND 2000c	Thermo Fisher Scientific
Thermomixer	Comfort	Eppendorf
UV imaging system (Agarose gels)	Gel Doc XR System	BioRad
Wet Blotting System (Western Blot)	Mini Trans-Blot Cell	BioRad

65

2.12 Softwares, servers, databases

Table 20: List of softwares, servers and databases used in this study

Name	Supplier/Reference
Acrobat Professional	Adobe Systems
AIMLESS	[404]
AlphaView	Alpha Innotech
Ape - A plasmid Editor	http://biologylabs.utah.edu/jorgensen/wayned/ape/
Astra VI	Wyatt Technology
AxioVision	ZEISS
CCP4	[405]
ChemDraw	PerkinElmer
COOT	[406]
Clustal Omega	[407]-[409]
ExPASy ProtParam tool	[410]
ExPASy Translate tool	[410]
Image Studio Lite Software	LI-COR Biosciences
MARS	BMG LABTECH
Microsoft Excel	Microsoft Corporation
Microsoft Power Point	Microsoft Corporation
Microsoft Word	Microsoft Corporation
NITPIC	[411]
ODYSSEY	LI-COR
OriginPro 9.4	OriginLab Corporation
PDB Databank	[412]
PHASER	[413]
Phenix	[414]
Photoshop	Adobe Systems, Inc.
PrimerX	Lapid, 2003
PyMOL 1.7.6	DeLano Scientific LLC
Pubmed	[415]
Quantity One	Bio-Rad
RF-cloning.org	[416]
STARANISO	[417]
UNICORN	GE Healthcare
XDS	[418]
XSCALE	[418]

3 Methods

Several of the reported methods in this thesis have been described in my publication 'Identification of an atypical interaction site in the BTB domain of the MYC-interacting zinc-finger protein 1', which presents the main findings of this thesis. Therefore, parts of the methods section are original excerpts that were extended or adapted as required.

3.1 Molecular biological methods

3.1.1 Restriction-free (RF) cloning

Restriction-free cloning is based on two polymerase chain reactions (PCR) and can be performed without the help of any restriction enzyme or ligase. In the first PCR the insert is amplified from a vector carrying the desired insert by using primers with a nucleotide overhang complementary to the target vector of at least 20 nucleotides and an overlap of about 20 nucleotides with the insert to be amplified. The amplified insert furtherone serves as 'mega-primer' in the second PCR, in which the single-stranded overhangs anneal with the complementary sequence in the target vector and the double-stranded insert can be looped into this vector [419]. Following this strategy, the web-service tool RF-Cloning.org was used to design the appropriate primers [416]. The composition and reaction conditions of the individual PCRs are summarized in **Table 21** and **Table 22**. After confirming the success of insert amplification by agarose gel electrophoresis (see 3.1.3), the amplified insert was purified prior to PCR 2 by using the NucleoSpin Gel and PCR Clean-up Kit (Macherey & Nagel) and following the manufacturer´s instructions, except for the elution volume, which was reduced to 25 µl. The DNA concentration was determined with the NanoDrop spectrophotometer, as described in 3.1.7, to calculate the required amount of amplified insert for the PCR 2. After removing methylated template DNA by incubating the product of PCR 2 with DpnI for at least 3 hours at 37 °C, the reaction mixture was transformed into competent *E. coli* cells (see 3.1.4). The success of RF cloning was validated after analytical preparation of plasmid DNA from bacteria (see 3.1.5) by DNA Sanger sequencing, performed by LGC Genomics or Microsynth Seqlab.

Table 21: Composition of the PCR mixtures in the context of RF cloning

	PCR 1	PCR 2
5x Q5-buffer	14 µl	4 µl
vector (20-50 ng/µl)	1.4 µl	1 µl
dNTP (10 mM)	1.4 µl	0.4 µl
primer forward (10 µM)	3.5 µl	
primer reverse (10 µM)	3.5 µl	
insert (20x molar excess)		1 µl
H_2O	45.5 µl	13.4 µl
Q5-Polymerase	0.7 µl	0.2 µl

The reaction mixture was divided, with one part incubated at 60 °C and the other at 72 °C during hybridization, in PCR 1 as well as in PCR 2 (see **Table 22**).

Table 22: PCR program for RF cloning

PCR 1	A (1x)	initial denaturation	2 min	98 °C
	B (30x)	denaturation	20 sec	98 °C
		hybridisation	30 sec	60/72 °C
		polymerisation	30 sec	72 °C
	C (1x)	extension	5 min	72 °C
	D		∞	4 °C
PCR 2	A (1x)	initial denaturation	2 min	98 °C
	B (35x)	denaturation	20 sec	98 °C
		hybridisation	30 sec	60/72 °C
		polymerisation	8 min (*)	72 °C (30 s/kb)
	C (1x)	extension	5 min	72 °C
	D		∞	4 °C

(*) Depending on the size of vector and insert the extension time was chosen as 4, 8, or 12 minutes.

3.1.2 Site-directed mutagenesis

Appropriate complementary primer pairs carrying the desired mutation were designed with the online program PrimerX (Carlo Lapid, 2003). When designing the primers, it was ensured that the mutation was located in the middle of the primer sequence and the total length of the primer was between 20 and 40 nucleotides and contained 2 G or C bases in the last three nucleotides at each side. The composition of the PCR and the PCR programs are summarized in **Table 23** and **Table 25**. PCR 1, in which forward and reverse primer were incubated separately with the reaction mixture, was performed to ensure sufficient annealing of the primers to the complementary sequence in the target vector, prior

to the actual PCR 2, by following the pipetting scheme shown in **Table 24**. By varying the buffer (Q5/GC-rich buffer, see 2.6.2, **Table 13**) as well as the temperature during annealing (60 °C or 72 °C) increases the chance to find at least one appropriate condition for the corresponding primers in one round of experiment. After removing methylated template DNA by incubating the products of PCR 2 with DpnI for at least 3 hours at 37 °C, the reaction mixture was transformed into competent *E. coli* cells (see 3.1.4). The successful introduction of a point mutation, the deletion or insertion of certain amino acids was validated after analytical preparation of plasmid DNA from bacteria (see 3.1.5) by DNA Sanger sequencing, performed by LGC Genomics or Microsynth Seqlab.

Table 23: Composition of the PCR mixtures for site-directed mutagenesis

	mixture 1	**mixture 2 (with GC-buffer)**
5x Q5 buffer	12 µl	12 µl
5x GC-rich buffer	-	12 µl
vector (30-40 ng/µl)	1.2 µl	1.2 µl
dNTP (10 mM)	1.2 µl	1.2 µl
H$_2$O	42 µl	30 µl
Q5-Polymerase	0.6 µl	0.6 µl

Table 24: Pipetting scheme for site-directed mutagenesis

	I Mixture 1 + primer F	**II** Mixture 1 + primer R	**III** Mixture 2 + primer F	**IV** Mixture 2 + primer R
Mixture 1 (see **Table 23**)	19 µl	19 µl		
Mixture 2 (see **Table 23**)			19 µl	19 µl
primer forward (F) (10 µM)	1 µl		1 µl	
primer reverse (R) (10 µM)		1 µl		1 µl

I, II, III and IV were divided into two Eppendorf tubes with 10 µl each, incubated either at 60 °C or 72 °C during hybridisation; after PCR 1, I and II incubated at 60 °C were combined and PCR 2 was started. The same was done for I and II incubated at 72 °C, III and IV incubated at 60 °C and III and IV incubated at 72 °C.

Table 25: PCR program for site-directed mutagenesis

PCR 1				
	A (1x)	*initial denaturation*	2 min	98 °C
	B (8x)	*denaturation*	20 sec	98 °C
		hybridisation	30 sec	60/72 °C
		polymerisation	12 min	72 °C
	C (1x)	*extension*	5 min	72 °C
	D		∞	4 °C
PCR 2				
	A (1x)	*initial denaturation*	2 min	98 °C
	B (27x)	*denaturation*	20 sec	98 °C
		hybridisation	30 sec	60/72 °C
		polymerisation	12 min (*)	72 °C (30 s/kb)
	C (1x)	*extension*	5 min	72 °C
	D		∞	4 °C

(*) Depending on the size of vector and insert the extension time varied between 4/8/12 minutes.

3.1.3 Agarose gel electrophoresis

Intermediate products during cloning procedures (e. g., amplified inserts during RF cloning, see 3.1.1) were analyzed by agarose gel electrophoresis. Therefore, 0.4 g agarose was dissolved in 50 mL 1x TAE buffer (see 2.9) by heating, this corresponds to a 0.8 % agarose gel. The lukewarm solution was supplement with 2.5 µl Midori Green Advance (MG04, NIPPON Genetics EUROPE), that intercalates into DNA and allows the detection of fluorescent DNA-fragments by UV-light. The solution was poured into a gel chamber containing an appropriate comb. 3 µl PCR product were diluted with 2 µl double-distilled water (ddH$_2$O) and 1 µl 6x Gel Loading Dye Purple (#B7025S, New England Biolabs) was added. The total 6 µl were loaded onto the agarose gel as well as an appropriate DNA ladder (see 2.6.3, **Table 14**) depending on the size of the fragments to be analyzed. After applying 120 V for 35 minutes to the agarose gel, which was stored in 1x TAE buffer, in the horizontal gel apparatus, the negatively charged DNA-fragments moved to the positively charged electrode and are thereby separated based on their size, with shorter DNA-fragments moving faster than longer DNA-fragments. Finally, the fluorescent DNA-fragments were visualized with the Molecular Imager Gel Doc XR system (BioRad).

3.1.4 Transformation of *E. coli* cells with plasmid DNA

Depending on the purpose appropriate competent cells (cloning: One Shot Top10 Competent Cells; cloning with lentiviral vectors: NEB Stable Competent *E. coli* cells; recombinant protein expression: LOBSTR-BL21(DE3)-RIL, see 2.1.1, **Table 3**) were selected and thawn on ice for 10-15 minutes. Afterwards, the whole reaction mixture of the PCR after the final DpnI digestion (10 µl PCR product + 1 µl DpnI; see 3.1.1 or 3.1.2), or in case of recombinant protein expression 0.3-0.5 µl of the plasmid encoding the desired protein, were added to the competent cells, and incubated on ice for 15 minutes (recombinant protein expression) or 1 h (cloning). After incubation at 42 °C (or 30 °C for NEB Stable Competent *E. coli* cells) for 45 sec in a water bath, the cells were incubated for another 10´ (recombinant protein expression) or 30´ (cloning) on ice, before 800 µl of LB-medium was added and the mixture was kept for shaking for 60´ (recombinant protein expression) or 90´ (cloning) at 37 °C (or 30 °C for NEB Stable Competent *E. coli* cells). After centrifugation (2000 g, 2 min, RT) the cell pellet was resuspended in about 30-50 µl of remaining LB-medium from the supernatant and plated onto an agar-plate with the corresponding antibiotic encoded by the plasmid. The plate was kept at 37 °C (or 30 °C for NEB Stable Competent *E. coli* cells) overnight.

3.1.5 Analytical preparation of plasmid DNA from bacteria (MiniPrep)

After transformation of *E. coli* cells (see 3.1.4) with the respective plasmid DNA a single colony from the agar plate was inoculated in 5 mL LB-medium with the appropriate antibiotic encoded by the plasmid and shaked at 200 rpm at 37 °C (or 30 °C in case the transformation was performed with NEB Stable Competent *E. coli* cells) for at least 7 hours or overnight. Afterwards the bacterial cells were pelleted by centrifugation (4000 rpm, 10 minutes, 4 °C). Isolation of the plasmid DNA was performed with the NucleoSpin Plasmid Kit (Macherey & Nagel) following the manufacture´s instructions. The plasmid DNA was finally eluted in 35 µl ddH$_2$O and analyzed by DNA Sanger sequencing, performed by LGC Genomics or Microsynth Seqlab.

3.1.6 Preparative preparation of plasmid DNA from bacteria (MidiPrep)

After transformation of *E. coli* cells (see 3.1.4) with the respective plasmid DNA a single colony from the agar plate was inoculated in 5 mL LB-medium with the appropriate antibiotic encoded by the plasmid and shaked at 200 rpm at 37 °C (or 30 °C in case the transformation was performed with NEB Stable Competent *E. coli* cells) for about 8 hours. Afterwards at least 100 µl of the bacterial culture was transferred into 100 mL LB-medium with the corresponding antibiotic and shaked at 200 rpm for 12-16 h at 37 °C (or 30 °C in case the transformation was performed with NEB Stable Competent *E. coli* cells*).* The bacterial cells were pelleted (4000 g, 20 minutes, 4 °C) and the plasmid DNA was isolated with the NucleoBond Xtra Midi/Maxi Kit (Macherey & Nagel) according to the manufacture´s instructions. The plasmid DNA was finally eluted in 100 µl ddH$_2$O and further diluted to a stock concentration of 1000 µg/µl.

3.1.7 Determination of DNA concentrations

The concentration of plasmid DNA was determined by measuring the absorbance at 260 nm with a spectrophotometer (NanoDrop, ND2000c, Peqlab). Calculation of the 260/280 ratio as well as the 260/230 ratio by the software provides information about the purity of the DNA, with 260/280 ~ 1.8 and 260/230 ~ 1.8 – 2.2 indicating pure DNA. My DNA samples typically displayed 260/280 ratios of 1.8-1.9 and 260/230 ratios of 1.7-2.2.

3.2 Cell biological methods

3.2.1 Cultivation of mammalian cells

Mammalian cells were cultivated at 37 °C, 5 % CO$_2$ and a relative humidity of 95 %. Cell cultures were maintained by using a sterile workbench.

3.2.1.1 Passaging of cells

Depending on the doubling time of the respective cell line adherent cell cultures were passaged several times per week before they reached confluence. Therefore, cells were washed with PBS. Upon addition of trypsin and possibly incubation at RT for a few minutes depending on the cell line, cells could be detached from the cell culture dish. Trypsin activity was stopped by adding 4 times

the volume of FCS-(fetal calf serum) containing DMEM-(Dulbecco´s Modified Eagle´s Medium) medium (see 2.1.2.1, **Table 7**). By up and down pipetting of the cell suspension, cells were isolated and a certain volume required for the desired density was transferred to a new cell culture dish. In case a specific cell number was required to perform an experiment, cells were centrifugated (1000 g, 4 min, RT) after trypsination, the pellet was resuspended in fresh DMEM-medium, the cell number was determined with the CASY cell counter (Innovatis), and the required volume for the desired cell number was calculated.

3.2.1.2 Freezing and thawing cells

For long-term storage of cells in liquid nitrogen, 80 % confluent cells were washed with PBS, trypsinated and centrifugated as described in 3.2.1.1. Afterwards the pellet was resuspended in freezing medium (see 2.1.2.1, **Table 7**) containing dimethylsulfoxide (DMSO) as cryoprotective agent. The cell suspension was splitted into several cryo vials which were stored in a freezing container (Mr. Frosty, Nalgene) at -80 °C, prior to long-term storage in liquid nitrogen, to reduce ice formation and preserve cell viability, by slowly cooling down with 1 °C/minute.

In contrast to slow freezing cells were quickly thawn at 37 °C in a water bath and transferred into a falcon with fresh culture medium. Upon centrifugation (1000 g, 4 minutes, RT) and resupension of the pellet in fresh culture medium, to remove the DMSO of the freezing medium, the cell suspension was plated on a new cell culture dish.

3.2.2 Transfection of plasmid DNA with polyethylenimine (PEI)

Depending on the cell line, cells were seeded either one (5 Mio. HEK293T cells/10cm-dish) or two days (600000 HeLa cells/10cm-dish) prior to the transfection of plasmid DNA with PEI. The DMEM 'culture medium', supplemented with 10 % FCS and 1 % Penicillin/Streptomcyin was replaced by DMEM 'tranfection medium' supplemented with 2 % FCS only (see 2.1.2.1). For the transfection of plasmid DNA with PEI two separate Eppendorf tubes with 250 µl OptiMem-medium each were prepared. To one of them the plasmid DNA (4 µg Fl-MIZ1, 8 µg HUWE1[AS] or dN-HUWE1 or 16 µg Fl-HUWE1, 2 µg GFP, or the respective empty vector in case a single component was transfected) was

added, while 30 µl PEI were added to the second vial. Both were incubated at RT for 5 minutes. Afterwards 250 µl of the OptiMem/PEI-mixture was added to the OptiMem/DNA-mixture and incubated for another 15 minutes at RT. Inbetween the Eppendorf tube was inverted several times, before the mixture was added to the cell culture dish containing 5 mL DMEM 'transfection medium'. After 6-7 h the DMEM 'transfection medium' was replaced by 10 mL DMEM 'culture medium'. 24 h post transfection the cells were harvested, as described in 3.3.12 and 3.3.13.

3.2.3 Lentivirus production in HEK293T cells

One day prior to the transfection 5 Mio. cells/10cm-dish were seeded. The transfection was performed analogously to the protocol described in 3.2.2. Only the composition of the OptiMem/PEI- and OptiMem/DNA-mixture varied: 500 µl OptiMem were supplemented with 10 µl of a lentiviral vector carrying the protein of interest, 10 µl of PAX2 (packaging plasmid) and 2.5 µl of pMD2G (VSV-G envelope expressing plasmid) with each plasmid having a stock-concentration of 1 µg/µl. The OptiMem/PEI-mixture was made up of 500 µl OptiMem and 30 µl PEI. 8 h post transfection 6 mL fresh 'culture medium' was added to the cells. Afterwards, supernatant was collected every 12 h and replaced by 6 mL of fresh medium (three times). Finally, the collected supernatant was combined, filtered and either stored at -80 °C or used directly for infection (see 3.2.4).

3.2.4 Lentiviral transduction and selection

Freshly passaged MEF$^{\Delta BTB}$ cells (see 2.1.2) were treated with a 1:1 mixture of culture medium and produced lentivirus (see 3.2.3), supplemented with 1:500 polybrene. After 24 h the medium was changed.

For selection, infected MEF$^{\Delta BTB}$ cells were treated with 200 µg/mL hygromycin for at least three days. To monitor the selection GFP-expressing cells lacking a plasmid carrying a hygromycin selection marker were also treated with hygromycin and the death of these cells confirmed the successful selection.

3.2.5 Cycloheximide (CHX) assay after lentiviral transduction of Fl-MIZ1 WT or variants thereof in MEF$^{\Delta BTB}$ cells

At day one, 75000 MEF$^{\Delta BTB}$ cells stably expressing Fl-MIZ1 WT or variants thereof were seeded per 6-well. At day 4, cells were treated with either ethanol (EtOH; as control), 50 µg/mL cycloheximide (in EtOH) for 9 h or with 10 µM MG-132 (in

EtOH) for 6 h. Cells were harvested in 50 mM HEPES, 150 mM sodium chloride, 1.5 mM $MgCl_2$ and 1 % Triton X-100, supplemented with a Protease- and Phosphatase-Inhibitor Cocktail (Sigma-Aldrich, PPC1010; 1:1000) and Benzonase (Merck, 70746; 1:1000), using 100 µl buffer/6-well. Further details of cell lysis and sample preparation for Western blot analysis are described in 3.3.12.

3.3 Protein biochemical and biophysical methods

3.3.1 Recombinant protein expression, harvesting and cell lysis (*E. coli* cells)

3.3.1.1 Recombinant protein expression in *E. coli*

After transformation of LOBSTR-BL21(DE3)-RIL cells (see 2.1.1 and 3.1.4) with the respective plasmid DNA several colonies from the agar plate were inoculated in 50 mL LB-medium with the appropriate antibiotic encdoded by the plasmid and shaked at 200 rpm at 37 °C for about 4 hours. Based on the optical density of the bacterial cell culture at 600 nm (OD_{600}) the required volume of the pre-culture for an initial OD_{600} of 0.02 in the 2 l main culture was calculated and transferred into 2 l LB-medium with the appropriate antibiotics which was then shaked for about 3 h at 200 rpm at 37 °C. At OD_{600} ~ 0.8-1.0 the protein expression was induced by adding 0.05 % L-arabinose or 0.5 mM IPTG (see 2.1.1.3) depending on the respective plasmid. Afterwards the temperature was lowered to 15 °C and the bacterial cell culture was shaked for 16-18 h at 200 rpm.

3.3.1.2 Harvesting and cell lysis of *E. coli* cells

After the protein expression, as described in 3.3.1.1, the bacterial cells were harvested by centrifugation (6000 g, 12 minutes, 4 °C; Fixed angle rotor JLA-8.1, Beckman Coulter). Afterwards the bacterial cell pellet was either stored at -80 °C or directly lysed. Therefore, the cell pellet was homogenized in ~ 75 mL lysis buffer A (see 2.9) and was supplemented with a spatula tip DNase I (AppliChem), ¼ cOmplete, EDTA-free Protease Inhibitor tablet (ROCHE) and 5 mM β-mercaptoethanol (Sigma-Aldrich) prior to the actual cell lysis by sonication with the Labsonic Sonicator from B. Braun Biotech International. Sonication ('cycle': 0.5; 'amplitude': 70) was done on ice 10-times 1 minute with a one-minute break between each sonication round to prevent heating of the cell suspension.

Thereafter, the cell lysate was cleared by centrifugation (57750 g, 1 h, 4 °C, Fixed angle rotor JA 25.50, Beckman Coulter).

3.3.2 Recombinant protein purification (*E. coli* cells)

In the following, I grouped the protein preparation protocols according to the molecular weight, the protease used, and the tag of the respective construct.

$HUWE1^{D, min}$, $HUWE1^{D}$ and $HUWE1^{AS}$ were cloned into a modified pBADM11 vector (EMBL Heidelberg) encoding a TEV (Tobacco etch virus)-cleavable N-terminal His_6-tag (see 2.3). Accordingly, as previously described by Sander et al. [136], the cleared cell lysate (see 3.3.1.2) was first purified by Nickel-nitrilotriacetic acid (Ni-NTA) affinity chromatography, followed by overnight dialysis at 4 °C to remove the N-terminal His_6-tag by incubation of the eluted peak fractions with the TEV-protease (for lysis buffer A, elution buffer B and dialysis buffer see 2.9). After applying a reverse Nickel affinity chromatography by using the dialysis buffer to remove remaining uncleaved protein and the protease, the untagged and concentrated protein was finally injected onto a preparative gel filtration column (Superdex 200 16/600, GE Healthcare) and eluted in gel filtration buffer (for buffer compositions see 2.9). The chromatograms for the individual purification steps for all proteins are provided in the Appendix (7.1.2).

The HUWE1 constructs AS, AS^{N} and AS^{C} were purified by following a similar protocol, but without any tag-cleavage and therefore neither overnight dialysis nor inverse Ni-NTA. Instead, the eluted peak fractions after the Ni-NTA were concentrated and directly injected onto the preparative gel filtration column Superdex 75 16/600 (GE Healthcare), due to the smaller size compared to the previous constructs. $MBP-AS^{C}$ (pETM41 vector; N-terminal MBP-tag, C-terminal His_6-tag; see 2.3) was purified analogously to AS, AS^{N} and AS^{C}, also without tag cleavage, but using the SD200 16/600 gel filtration column due to the higher molecular weight caused by the remaining MBP-tag.

$MIZ1^{BTB}$ and its variants, containing an TEV-cleavable N-terminal His_6 and lipoyl-domain-tag (see 2.3), were purified according to the protocol described for $HUWE1^{D, min}$, $HUWE1^{D}$ and $HUWE1^{AS}$. Only the imidazole concentration in the dialysis buffer to remove the N-terminal His_6- and lipoyl-domain-tag by TEV-cleavage was lowered from 10 mM to 5 mM (see 2.9 for buffer composition) and

the preparative Superdex 200 16/600 gel filtration column was replaced by the preparative Superdex 75 16/600 gel filtration column.

This protocol, described for MIZ1^{BTB}, was maintained for the purification of MIZ1^{BTB} (without cloning overhang), its variants (dimer-interface variant, MIZ1-BCL6 heterodimer, MIZ1-NAC1 heterodimer) as well as KAISO^{BTB}, which were cloned into the pCCA vector [100] (see 2.3). Only the dialysis procedure varied due to the fact that the pCCA vector encodes a Ubiquitin-like-specific protease 1 (ULP1)-cleavable N-terminal His$_6$-tag. To improve the cleavage efficiency of ULP1 the eluted peak fractions were dialysed for 2-2.5 h without the protease to lower the sodium chloride concentration (500 mM in lysis buffer A and elution buffer B; 150 mM in dialysis buffer; see 2.9). After 2-2.5 h the dialysis bag was transferred into a beaker with fresh dialysis buffer and ULP1 was added to the protein fractions in the dialysis bag. The dialysis was kept at 4 °C overnight. After removal of the cleaved tag and uncleaved protein by inverse Ni-NTA, the concentrated protein was injected onto the preparative Superdex 75 16/600 gel filtration column (for the corresponding chromatograms and the purity of the eluted peak fractions, see Appendix 7.1.2).

MIZ1$^{1-282}$ and its variants were cloned into a pETM41 vector encoding a N-terminal TEV-cleavable MBP-tag and a C-terminal HA-His$_6$-tag. Here, the imidazole concentration was kept constantly at 5 mM in all buffers during affinity chromatography and dialysis. After cell lysis, MIZ1$^{1-282}$ was purified by Nickel affinity chromatography, followed by overnight dialysis at 4 °C to remove the N-terminal MBP-tag by incubation with the TEV-protease. The next day, uncleaved protein and cleaved MBP-tag were captured by a MBP Trap HP column (GE Healthcare) while the flow through containing the cleaved protein was collected, concentrated and injected onto the preparative Superdex 200 16/600 gel filtration column.

The recombinant, human E1 UBA1 was purified by Sonja Lorenz from insect cells, as described in Orth et al. The E2 enzymes used (UBCH5A, UBCH5B, UBCH5C, UBCH7), ubiquitin and HUWE1^{HECT} as well as the proteases (TEV, ULP1) were mainly purified by Julia Haubenreißer, following standard purification protocols, some of which have been described previously [136], [100], or were kindly provided by other lab members (UBCH5C, Jonas Düring, Lorenz laboratory).

3.3.3 Determination of protein concentrations

3.3.3.1 NanoDrop

Protein concentrations were determined by measuring the absorbance at 280 nm with a spectrophotometer (NanoDrop, ND2000c, Peqlab). Nucleic acid impurities could be monitored by the 260/280 ratio, provided by the software, which should be ideally < 0.6. My protein samples typically displayed 260/280 ratios of ~ 0.5.

3.3.3.2 Bicinchoninic acid (BCA) assay

The BCA assay was performed to determine the amount of total protein in cell lysates from mammalian cells (see 3.3.12) by using the Pierce BCA Protein Assay Kit (Thermo Fisher Scientific) following the manufacturer´s instructions for the 'microplate procedure'. The cell lysate sample was diluted 1:2 with the respective lysis buffer (12.5 µl cell lysate + 12.5 µl lysis buffer; see 3.3.12 or 2.9, respectively) to stay in the working range. The absorbance at 562 nm was measured using a CLARIOstar microplate reader (BMG LABTECH). The standard curve was generated with a serial dilution of BSA (Bovine serum albumin).

3.3.4 Analytical size exclusion chromatography

For interaction studies between C-terminal HUWE1-fragments, 150 µM of AS^N, AS^C, AS (all contain a N-terminal lipoyl-domain-tag and a C-terminal His_6-tag), $HUWE1^D$ or $HUWE1^{AS}$, respectively, and 300 µM of $MIZ1^{BTB}$ (with N-terminal cloning overhang) were injected separately or as a mixture onto a Superdex 200 Increase 3.2/300 column (GE Healthcare) in 20 mM HEPES, pH 8.0, 100 mM NaCl, 1 mM EDTA, and 5 mM DTT at 4 °C. The eluted protein fractions were analyzed by SDS-PAGE.

To study the interaction between Fl-HUWE1 (with C-terminal Strep-tag; provided by David Haselbach, IMP Vienna) and $MIZ1^{BTB}$ (without cloning overhang), 3.45 µM of Fl-HUWE1 and 70 µM of $MIZ1^{BTB}$ (corresponding to a 20-fold molar excess over the Fl-HUWE1 concentration) in 50 mM HEPES pH 8.0, 150 mM NaCl, 1 mM DTT at 4 °C were injected onto a Superdex 200 Increase 3.2/300 column (GE Healthcare). The eluted protein fractions were analyzed by SDS-PAGE and Coomassie staining or Western blot.

To compare the oligomerization states of $MIZ1^{BTB}$ WT, mutated variants thereof, and the fusion constructs, respectively, the proteins were injected onto a

Superdex 75 10/300 GL Increase column (GE Healthcare) at a concentration of 100 µM. In the case of HUWE1^D, HUWE1^{AS} WT, and mutated variants thereof, a protein concentration of 50 µM and a Superdex 200 10/300 GL Increase column (GE Healthcare) was used.

3.3.5 SEC-coupled multi-angle light scattering (SEC-MALS)

300 µM of AS^C (N-terminal lipoyl-domain-tag and C-terminal His$_6$-tag) and 500 µM of MIZ1^{BTB} (with cloning overhang), respectively, were injected onto a Superdex 200 10/300 GL column (GE Healthcare) in 20 mM HEPES, pH 8.0, 150 mM NaCl, 1 mM EDTA, and 5 mM DTT at RT. The column was coupled to a Dawn 8+ MALS detector and an Optilab T-rEX refractive index detector (Wyatt Technology; Santa Barbara, CA, USA). Molecular weights were determined at the absorbance peak tips with ASTRA 6 (Wyatt Technology).

3.3.6 Fluorescent labeling of tetracysteine tagged proteins with Fluorescein Arsenical Hairpin (FlAsH)

To not restrict fluorescence polarization measurements to fluorescently labeled synthetic peptides only, but further expand it to interaction studies between two recombinantly expressed proteins, a *tetracysteine sequence* (G(TEV-cleavage overhang)-*CCPGCC*-MA(spacer)-Met1(of MIZ1^{BTB})) was N-terminally attached to MIZ1^{BTB} that can react with FlAsH-EDT$_2$ (Cayman Chemical, ItemNo. 20704). Excitation and emission wavelengths for FlAsH-EDT$_2$ are described with 508 nm and 528 nm. The fluorescence polarization experiment with the FlAsH-labeled MIZ1^{BTB} by using a CLARIOstar microplate reader (BMG LABTECH), was performed using excitation and emission wavelengths of 540 nm and 590 nm, analogously to the measurements with 5-FAM labeled synthetic peptides (see 3.3.7).

After buffer exchange of the MIZ1^{BTB} protein into 20 mM HEPES pH 7.2, 150 mM sodium chloride, 5 % glycerol, 1 mM TCEP with Zeba Spin Desalting Columns (Thermo Fisher Scientific), the labeling reaction was set up with the final concentrations of 0.015 mM MIZ1^{BTB} and 0.15 mM FlAsH-EDT$_2$ in a final volume of 1 mL. The reaction mixture was incubated for 90 minutes at room temperature under exclusion of light. After overnight dialysis at 4 °C in 20 mM HEPES pH 7.2, 150 mM NaCl and 5 % glycerol, the protein was centrifugated (16000 g,

10 minutes, 4 °C) and injected onto a HiPrep 26/10 Desalting column to remove the remaining free FlAsH-EDT$_2$. After concentrating the eluted protein fractions of FlAsH-labeled MIZ1^{BTB} the concentration could be determined by measuring the absorption at 515 nm with a spectrophotometer (NanoDrop, ND2000c, Peqlab) and FlAsH-labeled MIZ1^{BTB} could be used for interaction studies by performing fluorescence polarization experiments, as described in 3.3.7.
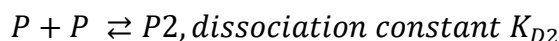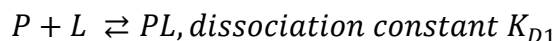
3.3.7 Fluorescence polarization (FP)

FP measurements were performed in black, non-binding, flat-bottom, 384-well microplates (Greiner Bio-One, Frickenhausen, Germany) at 30 °C, using a CLARIOstar microplate reader (BMG LABTECH) with excitation and emission wavelengths of 540 and 590 nm, respectively. All proteins and 5-FAM-labeled peptides were in 20 mM HEPES, pH 8.0, 150 mM NaCl, 1 mM EDTA, 5 mM DTT, and 0.01 % Triton X-100 with a constant peptide concentration of 1 µM. To derive a dissociation constant, K$_D$, for the MIZ1^{BTB}-AS^C interaction, averaged binding curves from three independent experiments were fitted to a single-site binding model with OriginPro 9.4 (OriginLab Corporation):

$$FP = FP_f + \left(\left(\frac{FP_b - FP_f}{2L}\right)\right) \cdot \left((L + c + K_D) - \sqrt{(L + c + K_D)^2 - 4 \cdot L \cdot c}\right)$$

where FP = fluorescence polarization, FP$_b$ = fluorescence polarization for the bound state, FP$_f$ = fluorescence polarization for the unbound state, and L = concentration of fluorophore-labeled peptide.

To analyze the interaction of the HUWE1$^{D, min}$ protein with the AS^N-ligand, the averaged binding curves from three independent experiments were fitted to a competition model that accounts for both protein-ligand binding and protein dimerization (in collaboration with Prof. Dr. Andreas Möglich, University Bayreuth):

$$P + L \rightleftarrows PL, dissociation\ constant\ K_{D1}$$

$$P + P \rightleftarrows P2, dissociation\ constant\ K_{D2}$$

where P = unbound protein monomer, P2 = unbound protein dimer, L = unbound ligand, and PL = protein-ligand complex.

This reaction scheme gives rise to a third-order polynomial for P (unbound protein):

$$P^3 + P^2 \cdot \left(1 + 2 \cdot \frac{K_{D1}}{K_{D2}}\right) \cdot \frac{K_{D2}}{2} + P \cdot (K_{D1} + L_0 - P_0) \cdot \frac{K_{D2}}{2} - K_{D1}P_0 \cdot \frac{K_{D2}}{2} = 0$$

The only real third root of the polynomial was calculated using Cardano´s formula (IN et al., 2001). With the knowledge of P, the values of P2, L, and PL can be determined. The fluorescence polarization signal was then fitted with Fit-o-mat [420] to

$$FP = L/L_0 \times FP_f + PL/L_0 \times FP_b$$

where L_0 is the total concentration of the fluorophore-labeled peptide.

To analyze the interaction between HUWE1^{AS} (or MBP-AS^{C} as control) and FlAsH-labeled MIZ1^{BTB} (see 3.3.6) the concentration of FlAsH-labeled MIZ1^{BTB} was constantly kept at 550 nM, with increasing concentrations of HUWE1^{AS} (0-250 µM; 25 µM-steps) or MBP-AS^{C} (0-100 µM; lower protein concentration was sufficient to reach saturation due to the increased binding affinity). K$_D$-values were determined based on averaged binding curves of three independent experiments, fitted to a single-site binding model with OriginPro 9.4 (OriginLab Corporation), see the formula above.

3.3.8 Isothermal titration calorimetry (ITC)

ITC was performed with a Microcal ITC$_{200}$ calorimeter (GE Healthcare) at 37 °C. The proteins were dialyzed into 20 mM HEPES, pH 8.0, 100 mM NaCl, 1 mM EDTA, and 1 mM β-mercaptoethanol over night. 60 µM MIZ1^{BTB} (with N-terminal cloning overhang) was applied to the sample cell and 810 µM AS^{C} (with N-terminal lipoyl-domain-tag and C-terminal His$_6$-tag) to the syringe of the calorimeter. The reference cell was filled with buffer. Titration experiments included 15 injections of 2.7 µl in 240-second intervals. The reference cell power was set to 6 µcal/sec and the stirring speed to 300 rpm. The data were fitted to a single-site binding model with the NITPIC [411], yielding the changes in the free energy (ΔG), enthalpy (ΔH), entropy (ΔS), as well as the dissociation constant (K$_D$) and the stoichiometry (n).

3.3.9 Activity Assays

0.2 µM UBA1, 5 µM UBCH7 (or UBCH5A, or UBCH5C), 5 µM HUWE1^{AS} (WT or mutated variant), 100 µM ubiquitin, 12 µM MIZ1$^{1-282}$ (WT or mutated variant) were incubated with 3 mM ATP and 8 mM MgCl$_2$ in 25 mM HEPES, pH 7.4 at 37 °C for 20 minutes.

The optimal reaction time of 20 minutes was determined based on a time course with reaction times of 10, 20, 40 and 60 minutes (**Figure 34A**).

MIZ1[1-282] was used because the BTB domain of MIZ1 is not ubiquitinated [421], as confirmed by the above-mentioned protein concentrations and assay conditions (**Figure 20A**).

While comparing UBCH5A and UBCH7 (each 5 µM) in MIZ1[1-282] ubiquitination assays with HUWE1[AS] WT, the assay was performed for 30 and 60 minutes.

All the reactions were quenched by the addition of reducing loading dye and analyzed by SDS-PAGE and Western blotting. If shown, the input and reaction products were quantified with the Image Studio Lite Software (Li-COR Biosciences). The mean and standard deviations from three independent experiments were plotted. Additional details are provided in the corresponding figure legends.

To analyze the MIZ1[1-282] ubiquitination by Fl-HUWE1 (C-terminal Strep-tag; provided by Irina Grishkovskaya and David Haselbach, IMP Vienna), the above-mentioned reaction conditions were largely maintained; only the buffer was adapted to that, in which Fl-HUWE1 was stored (50 mM HEPES pH 7.5). The final concentration of Fl-HUWE1 in the reaction was 1.8 µM due to overall material limitations as well as a low Fl-HUWE1 stock concentration. To compare the E2s UBCH5B and UBCH7 in this context, the reaction was initially incubated for 30 minutes at 37 °C (**Figure 37A**). Later on, a time course with reaction times of 5, 10 and 15 minutes was performed (**Figure 37B**).

3.3.10 SDS-polyacrylamide gel electrophoresis (SDS-PAGE)

SDS-polyacrylamide gel electrophoresis allows the separation of proteins depending on their molecular weight, with small molecules migrating faster than proteins of higher molecular weight. To analyze for example peak fractions of eluted proteins, to monitor ubiquitination reactions or to study protein-protein interactions by co-Immunopreciptiation protein samples were prepared with reducing SDS-loading dye and boiled 3-10 minutes at 95 °C to ensure complete denaturation and facilitate sample loading into the pockets of the SDS-gel. While SDS-gels with a higher percentage of polyacrylamide better resolve small proteins, a lower percentage of polyacrylamide is recommended for larger proteins. According to this, suitable gels of 6 %, 8 % (Thermo Fisher Scientific), 10 %, 12 %

or 15 % or even commercially available gradient gels of 4-12 % and 4-20 % (Thermo Fisher Scientific) were selected, depending on the molecular weight of the protein to be analyzed. As size standard the Page Ruler Plus Prestained Protein Ladder (Thermo Fisher Scientific) was loaded onto the SDS-gel. The applied voltage mostly varied between 165 V and 225 V and the time was adjusted as required, ranging from 35 minutes up to 1 h. The SDS-gel was stained with Coomassie staining solution (see 2.9). Therefore, the SDS-gel was incubated for at least 10 minutes or overnight in staining solution (optional: heating for 10-15 seconds in the microwave; accelerates staining). Afterwards, the staining solution was discarded, the SDS-gel was rinsed with ddH$_2$O and incubated in destaining solution (see 2.9) for at least 10 minutes or overnight. To improve and accelerate the destaining procedure the destaining solution can be replaced by fresh destaining solution after 10 minutes, prior to overnight incubation. Finally, the SDS-gel was stored in ddH$_2$O and scanned by using the LI-COR Odyssey system.

3.3.11 Western blot

Analyzing specific proteins at low concentrations can be facilitated by Western blotting after protein separation by SDS-PAGE (see 3.3.10). Therefore, the protein bands were transferred from the SDS-gel onto a PVDF (Polyvinylidine Fluoride) membrane by applying 100 V for 1 h at 4 °C to a sandwich comprising two sponges on the outside, followed by two Whatman papers towards the inside, while the SDS-gel and the PVDF-membrane directly faced each other internally. Everything was incubated in transfer buffer (see 2.9) prior to the described assembly and the PVDF-membrane was incubated in 100 % methanol for 30 seconds to improve its hydrophilicity and increase its protein-binding capacity before it was soaked with transfer buffer. The whole transfer chamber was filled with transfer buffer and contained a cool pack. After transfer and disassembly, the membrane was shaken in 5 % BSA in 1x TBS-T, or 5 % milk in 1x TBS-T (Flag-HRP antibody, Sigma-Aldrich) or in 1x PBS-T (HA-HRP antibody, Sigma-Aldrich) (see 2.9), depending on the respective antibody, for 1 h at RT to block unspecific binding sites. Afterwards, the membrane was incubated at 4 °C overnight with the primary antibody that recognizes the desired protein. According to the manufacturer´s instructions, the primary antibody was diluted (see 2.5, **Table 11**) in 5 % BSA in 1x TBS-T (1 % BSA in 1x PBS-T for HA-HRP, Sigma-Aldrich;

1x TBS-T for Flag-HRP, Sigma-Aldrich). On the next day, the membrane was incubated three times for 5 minutes with 1x TBS-T (or 1x PBS-T) while shaking in order to remove unspecifically bound antibodies. Thereafter, the membrane was incubated for 1 h at RT with the respective secondary antibody, which was diluted 1:10000 in 5 % BSA in 1x TBS-T. Finally, the membrane was again washed three times for 5 minutes with 1x TBS-T while shaking. By applying a HRP substrate to the membrane (for ECL Reagents used, see 2.6.2, **Table 13**), protein bands could be detected with a FluorChem Q Imaging System (Alpha Innotech) due to the reaction of the HRP-coupled secondary antibodies (or the HRP conjugated primary antibodies) with the HRP substrate, which induces chemiluminescence.

3.3.11.1 Stripping of the PVDF-membrane

To detect several proteins on the same membrane, the respective membrane can be cut according to the molecular weight of the protein to be analyzed and the membrane strips can be separately incubated with the respective primary antibody. In case two proteins of interest have a similar molecular weight, they can also be visualized sequentially. To this end, the PVDF-membrane was reactivated by incubation in 100 % methanol for 30 seconds, three times rinsed with ddH$_2$O and incubated for 2 h at RT in stripping buffer (see 2.9) while shaking. Thereafter, the membrane was washed three times for 5 minutes with 1x TBS-T, followed by blocking and primary and secondary antibody incubation, as described in 3.3.11.

3.3.12 Co-Immunoprecipitation (co-IP) from mammalian cell lysates

Co-Immunoprecipitations were performed as previously described [422]. In short, cells were washed twice with ice-cold phosphate-buffered saline (PBS) and harvested in 20 mM Hepes pH 7.9, 200 mM NaCl, 0.5 mM EDTA, 10 % glycerol and 0.2 % NP40 (IP buffer), supplemented with a Protease- and Phosphatase-Inhibitor Cocktail (Sigma-Aldrich, PPC1010; 1:1000). After sonication with a Branson Digital Sonifier W-250D for 4 times 5 seconds with 10-second breaks and 20 % output power, the lysates were incubated on a rotating wheel at 4 °C for 30 minutes and cleared by centrifugation (21000 g, 10 minutes, 4 °C) thereafter. 20 µl of a Dynabeads A/G mixture (Thermo Fisher Scientific) were pre-incubated with 2 µg (Flag-M2-antibody, F3165, Sigma-Aldrich; HA-antibody, clone HA-7, H9658, Sigma-Aldrich; IgG-antibody, 12-371, Merck) or 5 µg (Lasu1/Ureb1

antibody, A300-486A, Bethyl Laboratories) and 5 g/l BSA in 1x PBS on a rotating wheel at 4 °C overnight. After washing the beads three times with 5 g/l BSA in 1x PBS, 20 µl dynabeads A/G mixture was added to the lysate (500 µg or 1000 µg for the Fl-MIZ1 mutants with HUWE1 aa 2364-3665 (**Figure 45**), respectively) and incubated on a rotating wheel at 4 °C for 6 hours. The resin was then washed four times with IP buffer (low salt, see 2.9) and two-times with the same buffer, but containing an increased sodium chloride concentration of 450 mM (IP buffer, high salt; see 2.9) to reduce unspecific binding. Proteins were eluted by addition of 50 µl of 1.5x SDS-loading dye and the samples were heated for 5 minutes at 95 °C before 15 µl of eluate were loaded on a suitable SDS-gel (4-20 % gel (Thermo Fisher Scientific) in the context of HUWE1^{AS}; 8 % gel (Thermo Fisher Scientific) in the context of dN-HUWE1), followed by Western blot analysis (see 3.3.11).

The co-Immunoprecipitation protocol for Fl-HUWE1 and its variants with Fl-MIZ1 and variants thereof (**Figure 42** and **Figure 44**) was slightly adapted to ensure a good signal for the 482 kDa Fl-HUWE1 protein in the final Western blot with as little unspecific binding as possible. Therefore, the IP buffer was replaced by an IP buffer containing 50 mM HEPES, 150 mM sodium chloride, 1.5 mM MgCl$_2$ and 1 % Triton X-100, supplemented with a Protease- and Phosphatase-Inhibitor Cocktail (Sigma-Aldrich, PPC1010; 1:1000) and Benzonase (Merck, 70746; 1:1000). Prior to the actual IP, a pre-clearing step was added, in which the cell lysate (whole 10 cm-dish of transfected HEK293T cells harvested in 500 µl IP buffer) was incubated with 25 µl of a Dynabeads A/G mixture with 5 g/l BSA in PBS for 1 h at 4 °C on a rotating wheel. Afterwards, the lysate was transferred into a new eppendorf tube and incubated with 2 µg of the Flag-M2-antibody (F3165, Sigma-Aldrich) for 1 h at 4 °C on a rotating wheel. Thereafter, 25 µl of a Dynabeads A/G mixture with 5 g/l BSA in 1x PBS were added and the mixture was incubated for another hour at 4 °C on the rotating wheel. Then the beads were washed three times with IP buffer, prior to elution in 35 µl 1.5x SDS-loading dye and boiling at 95 °C for 10 minutes. The whole eluate was loaded on a 6 % SDS-gel, followed by Western blot analysis (see 3.3.11).

3.3.13 Generation of whole cell protein extracts from mammalian cells

To monitor steady-state levels of MIZ1 in HeLa cells upon transient transfection (see 3.2.2) as shown in **Figure 48**, cells were washed twice with ice-cold phosphate-buffered saline (PBS) and harvested in 500 µl 1x PBS. After centrifugation (1000 g, 10 minutes, 4 °C) the supernatant was discarded and the pellet was stored at -80 °C. For the Western blot analysis, the cell pellet was thawed on ice and resupended in 500 µl 20 mM Hepes pH 7.9, 200 mM NaCl, 0.5 mM EDTA, 10 % glycerol, and 0.2 % NP-40, supplemented with a Protease- and Phosphatase-Inhibitor Cocktail (Sigma-Aldrich, PPC1010; 1:1000). After incubation for 30 minutes at 4 °C on a rotating wheel and centrifugation (16000 g, 10 minutes, 4 °C) the supernatant was transferred into a new eppendorf tube. 90 µl of the cleared cell lysate were added with 30 µl of 4x SDS-loading dye and boiled for 5 minutes at 95 °C. Finally, 15 µl were loaded onto an 8 % SDS-gel for Western blot analysis (see 3.3.11).

To monitor the protein stability of MIZ1 WT and variants thereof in a cycloheximide assay in MIZ1^{BTB}-depleted MEF cells (see 2.1.2) upon lentiviral transduction (see 3.2.3 or 3.2.4, respectively, and **Figure 49**) the described protocol above was slightly adapted: Cells were washed with ice-cold phosphate-buffered saline (PBS) and harvested in 100 µl (6-well) of 50 mM HEPES, 150 mM sodium chloride, 1 % Triton X-100 and 1.5 mM magnesium chloride, supplemented with a Protease- and Phosphatase-Inhibitor Cocktail (Sigma-Aldrich, PPC1010; 1:1000) and Benzonase (Merck, 70746; 1:1000). After centrifugation (16000 g, 10 minutes, 4 °C) 37.5 µl of the cleared cell lysate were added with 12.5 µl of 4x SDS-loading dye and boiled for 5 minutes at 95 °C. Finally, 15 µl were loaded onto an 8 % SDS-gel for Western blot analysis (see 3.3.11).

3.4 Protein crystallization and structure determination

MIZ1[BTB] *apo* crystals grew at 4.9 mg/mL and 20 °C in hanging drops containing 0.1 mM sodium acetate and 8 % PEG4000, pH 4.6. The same conditions including 26.7 % glycerol were used for cryo-protection. Diffraction data were collected at beamline P13 of the PETRA III storage ring at DESY (Hamburg, Germany) [423]. Data processing was performed with XDS [418] and molecular replacement with Phaser [413], as implemented in CCP4 [405], using PDB 3M52 [343] as a search model.

MIZ1[BTB] *apo* crystals grown at 4.9, 7 or 9.5 mg/mL and 20 °C in hanging drops containing 75/100/125 mM sodium acetate pH 4.6 and 4/6/7/8/10 % PEG4000 were used for 1/5/10 minutes or 1.5/19/25 h soaking with AS[C]-peptides of different length (aa 3870-3890 in 100 % DMSO; 3870-3897 in 1x gelfiltration buffer (see 2.9)) at 20 °C or at RT. The final AS[C]-peptide concentration for soaking varied: for AS[C] (aa 3870-3890) between 381 µM/763 µM/1.14 mM/3.45 mM with 30 % glycerol as cryoprotectant; for AS[C] (aa 3870-3897) 1.3 mM in the presence of 22.5 % glycerol or 4.7 mM with 16.7 % or 26.7 % glycerol. Diffraction data were collected at beamLine P13 of the PETRA III storage ring at DESY (Hamburg, Germany) [423]. Data processing was performed with XDS [418] and molecular replacement with Phaser [413], as implemented in CCP4 [405], using PDB 3M52 [343] as a search model. Seven datasets with a resolution of 2.1-2.6 Å were indexed all of which were MIZ1[BTB] *apo* crystals.

Crystals of the MIZ1[BTB]-AS[C]-peptide complex grew in hanging drops and two similar conditions: (i) 3 mg/mL MIZ1[BTB] with a 1.2-fold excess of AS[C] in 125 mM sodium acetate and 6 % PEG4000, pH 4.6. (ii) 5 mg/mL MIZ1[BTB] with a 1.2-fold excess of AS[C] in or 100 mM sodium acetate and 4 % PEG4000, pH 4.6. For cryo-protection, 30 % glycerol and 1.3 mM AS[C] (corresponding to a 2.5-fold molar excess over the MIZ1[BTB] concentration) were included in the respective mother liquor. Diffraction data were collected at beamLine ID30A-3 of the ESRF (Grenoble, France). Two data sets obtained from crystals grown in either condition were processed with XDS, merged with XSCALE [418], and analyzed with STARANISO [417]. Molecular replacement was performed with Phaser, as implemented in Phenix [414], using PDB 3M52 [343] as a search model. The use of STARANISO resulted in weak reflections being excluded, and thus a reduced

number of reflections was used during the refinement (see **Table S1**). All structures (PDB: 7AZW, 7AZX; as well as the crystal structures that were not deposited in the PDB) were refined with phenix.refine [414] using individual B-factors; model building was performed in Coot) [406]. All structural representations were created with PyMOL (open source, V1.7.6; DeLano Scientific LLC).

Crystals of the MIZ1^{BTB}-AS^C-peptide complex, with the data sets of which the peptide orientation could not be clearly determined (see section 4.3), grew at 7 mg/mL and 20 °C in hanging drops containing 100 mM Na$_2$HPO$_4$, 5 % PEG1000, pH 4.2 and 40 % reagent alcohol, in the presence of AS^C with a 1.2-fold excess. The same conditions including 30 % glycerol and 2.3 mM AS^C (corresponding to a 4.4-fold molar excess over the MIZ1^{BTB} concentration) were used for cryo-protection. Diffraction data were collected at beamLine ID30A-3 of the ESRF (Grenoble, France) and at beamLine BL14.X (X=[1,2,3]) at the BESSY II electron storage ring operated by the Helmholtz-Zentrum Berlin [424]. Processing, molecular replacement and refinement was performed as described above.

3.5 Quantification and statistical analysis

Quantification of Western blots was done from three replicates using the Image Studio Lite Software (Li-COR, Biosciences). The mean and standard deviations were plotted. Additional details are provided in the corresponding figure legends. The data points in the FP analysis represent the mean of three independent experiments and SDs are shown.

4 Results and Discussion

4.1 MIZ1$^{1\text{-}282}$ is polyubiquitinated by HUWE1^{AS} *in vitro*.

In 2005 Adhikary et al. showed that MIZ1 interacts with an N-terminally truncated HUWE1 construct (aa 2474-4374) *in vitro* and that this interaction is mediated by the BTB domain of MIZ1 [228]. Based on these results I set out to identify the binding site for MIZ1^{BTB} in HUWE1. Since HUWE1 - a 4374 amino acid ligase with a molecular weight of 482 kDa - was structurally poorly characterized in 2017 when I started to address this question, I initially focused on the C-terminal part of HUWE1 in my *in vitro* studies. I monitored MIZ1 ubiquitination *in vitro* using C-terminal constructs of HUWE1 with variable lengths (**Figure 18**). These constructs originated from studies by Sander et al. [136] and allowed for recombinant expression in *E. coli* and purification to sufficient yields (~ 30 mg/l of AS, AS^N, AS^C; ~ 60 mg/l of HUWE1^{AS}, HUWE1^D; ~ 200 mg/l of HUWE1$^{D,\,min}$) and purity, as required for biophysical analyses (for purification protocols, see 3.3.1 or 3.3.2, respectively; for the corresponding chromatograms and the purity of the eluted peak fractions, see Appendix 7.1.2).
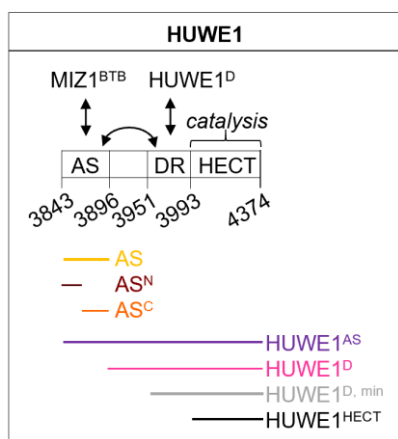

Figure 18: Schematic representation of C-terminal HUWE1 constructs used in this project for *in vitro* experiments
C-terminal HUWE1 constructs were stepwise extended towards the N-terminus, from the isolated catalytic HECT domain (HUWE1^{HECT}, aa 3993-4374), to HUWE1$^{D,\,min}$ (aa 3951-4374), to HUWE1^D (aa 3896-4374), to HUWE1^{AS} (aa 3843-4374). HUWE1$^{D,\,min}$ and HUWE1^D (additional unstructured and uncharacterized region: aa 3896-3951), both contain a dimerization region (DR) that induces dimer formation, while the activation segment (AS, aa 3843-3896) in HUWE1^{AS} prevents dimerization and keeps HUWE1^{AS} monomeric due to an intramolecular interaction with DR. AS contains the binding site for MIZ1^{BTB} in the context of these C-terminal HUWE1 constructs and was divided into AS^N (N-terminal part of AS) and AS^C (C-terminal part of AS) for further interaction studies.

The reported ubiquitination sites of MIZ1 are outside of the BTB domain (Lys135, Lys332, Lys341, Lys350, Lys360, Lys406, Lys462; according to PhosphoSitePlus (v6.5.9.3) [421]). In line with this, MIZ1^{BTB} is not ubiquitinated by HUWE1^{AS} (**Figure 19A**). We thus performed all MIZ1 ubiquitination assays with an elongated construct, MIZ1$^{1\text{-}282}$, which contains Lys135 as a ubiquitination site. All *in vitro*

binding assays were perfomed with MIZ1^{BTB} (**Figure 19B**), since this is more stable than MIZ1$^{1-282}$ and sufficient for binding to HUWE1 (see [228]) (for purification protocols, see 3.3.1 or 3.3.2, respectively; for the corresponding chromatograms and the purity of the eluted peak fractions, see Appendix 7.1.2).
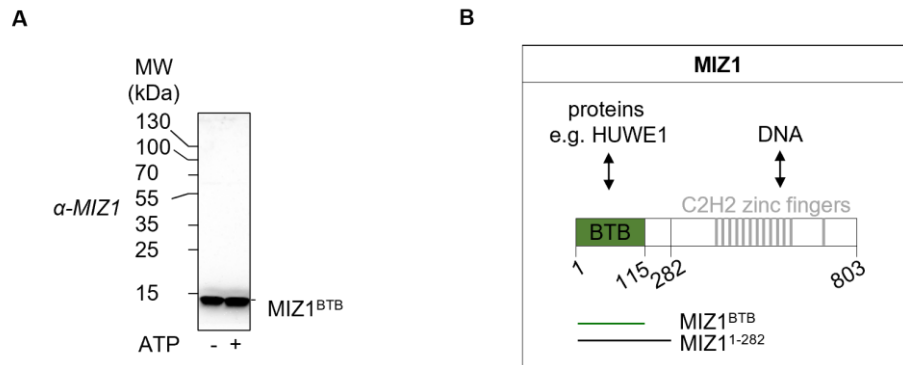
Figure 19: MIZ1^{BTB} (aa 1-115) is not ubiquitinated by HUWE1^{AS} (aa 3843-4374).
(A) MIZ1^{BTB} ubiquitination assay containing MIZ1^{BTB}, UBA1 (E1), UBCH7 (E2), HUWE1^{AS} (E3), ubiquitin, and MgCl$_2$ in the absence or presence of ATP at 37 °C. After 20 minutes the reaction was stopped by adding SDS-loading dye. The samples were loaded on SDS-PAGE, followed by anti-MIZ1 Western blot. (B) Domain organization of MIZ1: the N-terminal BTB domain mediates protein-protein interactions, including HUWE1; the thirtheen C2H2 zinc fingers in the C-terminal region are involved in DNA-binding. In this study, interaction assays were perfomed with MIZ1^{BTB}; MIZ1$^{1-282}$ was used for ubiquitination assays.

When using MIZ1 ubiquitination as a read out for the ubiquitination activity of three different N-terminally truncated HUWE1 constructs (HUWE1^{HECT} (aa 3993-4374), HUWE1^{D} (aa 3896-4374), HUWE1^{AS} (aa 3843-4374)), I observed enhanced chain formation on MIZ1$^{1-282}$ with the longest construct, HUWE1^{AS} (aa 3843-4374) (**Figure 20**). Compared to HUWE1^{D}, HUWE1^{AS} includes an additional region (aa 3843-3896), known as the activation segment, which prevents the formation of an auto-inhibitory, dimeric state that was observed in the context of HUWE1^{D} and HUWE1$^{D, min}$ [136] (for details see 1.5.4). This enhanced activity of HUWE1^{AS} toward MIZ1$^{1-282}$ indicates that the activation segment promotes binding of HUWE1^{AS} to MIZ1$^{1-282}$. Note that the anti-HUWE1 Western blot in **Figure 20A** served as a loading control for the amount of E3 input in each reaction. At the same time it shows the auto-ubiquitinaton capacity of the different HUWE1 constructs, which varies with the number and accessilibity of lysine residues, amongst other factors, and was studied in detail by Sander et al. [136].
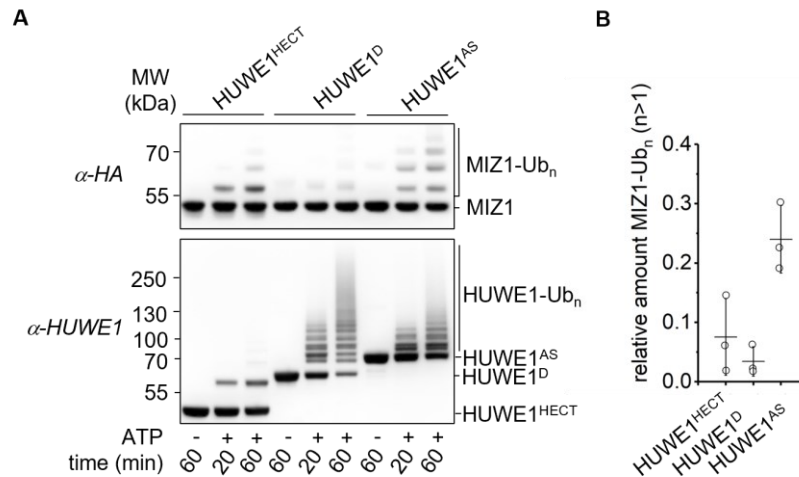
Figure 20: HUWE1^{AS} promotes polyubiquitination of MIZ1$^{1-282}$.
(A) Analysis of MIZ1$^{1-282}$ (aa 1-282, C-terminal HA-His$_6$-tag) ubiquitination by three different N-terminally truncated HUWE1 constructs (HUWE1^{HECT}: aa 3993-4374, HUWE1^D: aa 3896-4374, HUWE1^{AS}: aa 3843-4374). MIZ1$^{1-282}$ and the indicated HUWE1 construct were incubated at 37 °C with UBA1 (E1), UBCH7 (E2), ubiquitin, MgCl$_2$, with or without ATP. The reaction was stopped with SDS-loading dye after 20 and 60 minutes, respectively. Samples were subjected to SDS-PAGE, followed by anti-HA Western blot (for MIZ1$^{1-282}$) and anti-HUWE1 Western blot. The latter blot served as an E3 loading control (for an analysis of the different levels of auto-ubiquitination of the HUWE1 constructs used, see [136]). (B) Quantification of MIZ1$^{1-282}$ polyubiquitination at 60 minutes from three independent experiments, normalized to the HUWE1-level (-ATP).

It should be noted that Pao et al. reported UBCH5B to be favored over UBCH7 as an E2 for HUWE1. However, I did not detect any difference between UBCH5A, UBCH5C and UBCH7 in MIZ1-directed ubiquitination assays with HUWE1^{AS} (**Figure 21**). Although I did not test UBCH5B itself, I did not expect a difference between the different members of the UBCH5 family, due to their high sequence identity (97 % between UBCH5B and UBCH5C [168]). Therefore, all ubiquitination assays in the context of HUWE1^{AS} and MIZ1$^{1-282}$ were performed with UBCH7 to allow for comparison of my results with previous, related studies [136].
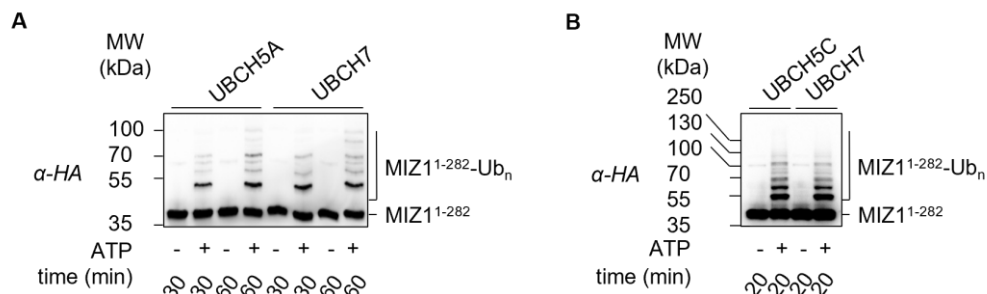

Figure 21: HUWE1^{AS} activity toward MIZ1$^{1-282}$ is similar with different E2s.
(A) HUWE1^{AS}, MIZ1$^{1-282}$, UBA1 (E1), UBCH5A or UBCH7 (E2), ubiquitin, MgCl$_2$ in the presence or absence of ATP were incubated at 37 °C for 30 and 60 minutes, respectively. The reaction was stopped with SDS-loading dye at the indicated time points. Samples were analyzed by SDS-PAGE, followed by anti-HA Western blot (for MIZ1$^{1-282}$). (B) The ubiquitination assay was performed in the same way as in (A), but with 20-minute time points, and UBCH5A was substituted with UBCH5C.

4.2 MIZ1^{BTB} interacts with the C-terminal part of the HUWE1 activation segment *in vitro*.

Based on the finding that polyubiquitination of MIZ1$^{1-282}$ is enhanced in the presence of the activation segment (aa 3843-3896) of HUWE1 (as described in section 4.1) I investigated whether an interaction between MIZ1^{BTB} and the activation segment of HUWE1 is detectable by size-exclusion chromatography (SEC). Indeed, analytical SEC analyses, combined with SDS-PAGE, showed coelution of MIZ1^{BTB} and AS (**Figure 22**).
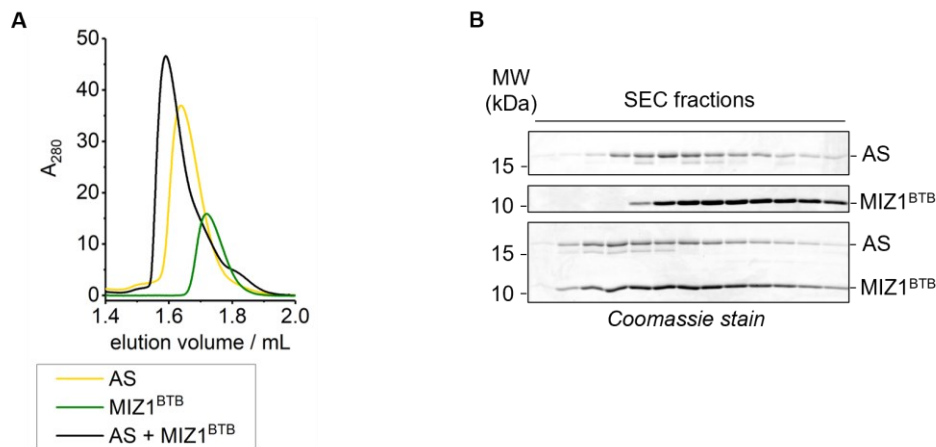
Figure 22: MIZ1^{BTB} interacts with the activation segment (AS) of HUWE1 *in vitro*.
(A) Analytical SEC of MIZ1^{BTB} (aa 1-115, N-terminal cloning overhang) and AS of HUWE1 (aa 3843-3890, N-terminal lipoyl-domain-tag and C-terminal His$_6$-tag). The figure shows a superposition of the elution profiles of the single components (AS = yellow; MIZ1^{BTB} = green) and the mixture (AS + MIZ1^{BTB} = black). (B) SDS-PAGE with Coomassie staining of the elution fractions from the analytical SEC analyses in (A). Equivalent fractions of the three runs were aligned with each other.

To further narrow down the relevant region within the HUWE1 activation segment that mediates the interaction with MIZ1^{BTB} I used secondary structure predictions to divide the activation segment into two parts, AS^N (aa 3843-3869) and AS^C (aa 3870-3890) (**Figure 23**).
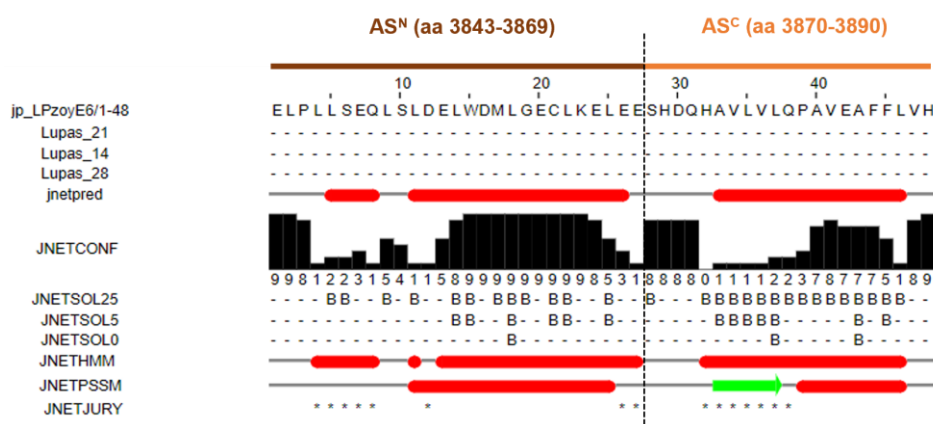
Figure 23: The activation segment is predicted to be mostly α-helical with an unstructured 4-amino-acid stretch (aa 3870-3874) in the middle that was used to subdivide AS into AS^N (aa 3843-3869) and AS^C (aa 3870-3890).
Secondary structure prediction for the activation segment of HUWE1 was performed with JPred4 [425]. Red bars indicate helices; green arrows represent β-strands; Lupas_21, Lupas_14, Lupas_28: Coiled-coil predictions for the sequence. These are binary predictions for each location; JNetPRED: The consensus prediction; JNetCONF: The confidence estimated for the prediction. High values reflect high confidence; JNETSOL25, JNETSOL5, JNETSOL0: Solvent accessibility predictions, binary predictions of 25 %, 5 % or 0 % solvent accessibility. 'B' indicates buried secondary structure, '-' indicates exposed secondary structure; JNetHMM: HMM (Hidden Markov Model)-profile based prediction; JNETPSSM: PSSM (Position Specific Scoring Matrix)-based prediction; JNETJURY: '*' indicates that the JNETJURY was invoked to rationalize significantly different primary predictions.

Analytical SEC analyses revealed an interaction of MIZ1^{BTB} with AS^C, but not with AS^N (**Figure 24A and B**). This result could be confirmed by an alternative method, fluorescence polarization (FP), where AS^N and AS^C were labeled with a fluorophore (5-FAM) and changes in FP measured with varying concentrations of MIZ1^{BTB}. The physical basis for this readout is that complex formation of AS^C with MIZ1^{BTB} leads to a decrease in the molecular rotation rate compared to the unbound form, which results in an increase in FP and allows for the determination of a K$_D$-value. For the interaction of AS^C with MIZ1^{BTB}, a K$_D$-value of 10.0 ± 0.9 μM was derived. In contrast, no K$_D$-value could be determined for AS^N and MIZ1^{BTB}. The associated FP was low over the entire concentration range tested, reflecting a lack of (measureable) complex formation (**Figure 24C**). Instead, I found that AS^N mediates interactions with the dimerization region (DR, aa 3951-3993) in HUWE1$^{D, min}$ (aa 3951-4374) with a binding affinity of 4.9 ± 0.8 μM (**Figure 24D**). AS^C, however, displays only weak affinity for the dimerization region, with a K$_D$-value of 322 ± 46 μM (**Figure 24D**). In sum, these data suggest that AS^N and AS^C mediate distinct interactions in the context of C-terminal constructs of HUWE1.
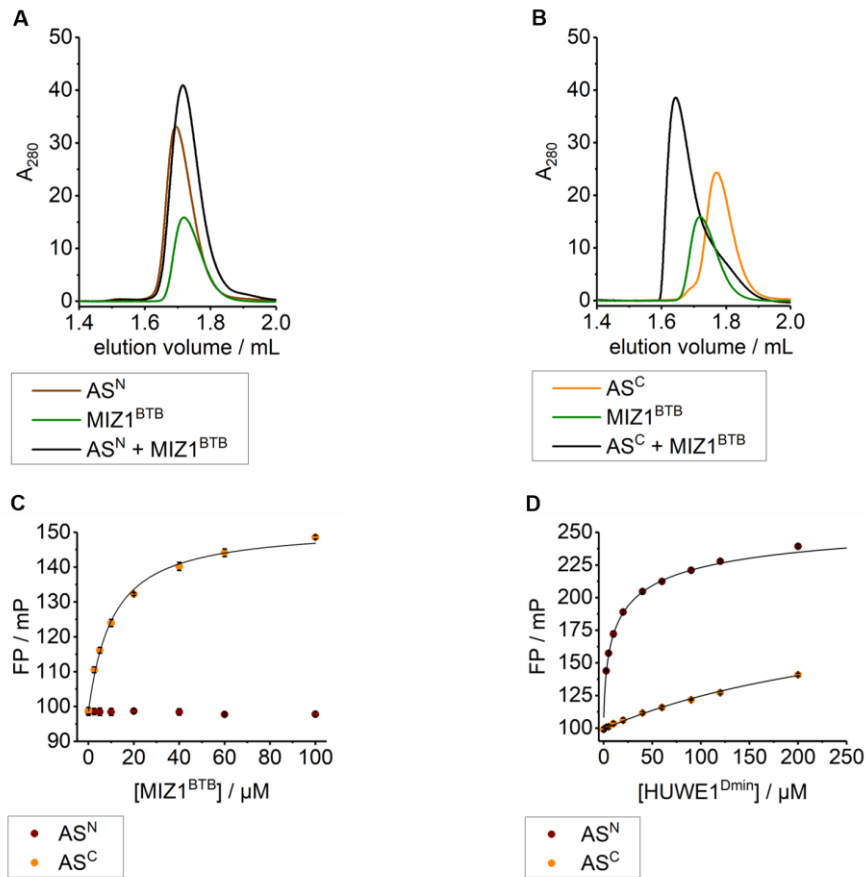
Figure 24: AS^C of HUWE1 mediates interactions with MIZ1^{BTB}, while AS^N mediates interactions with the dimerization region.
(A) Analytical SEC of MIZ1^{BTB} (aa 1-115, N-terminal cloning overhang) and AS^N of HUWE1 (aa 3843-3869, N-terminal lipoyl-domain-tag and C-terminal His$_6$-tag). The figure shows a superposition of chromatograms of the single components (AS^N = brown; MIZ1^{BTB} = green) and the mixture (AS^N + MIZ1^{BTB} = black). (B) Analytical SEC of MIZ1^{BTB} (aa 1-115, N-terminal cloning overhang) and AS^C of HUWE1 (aa 3870-3890, N-terminal lipoyl-domain-tag and C-terminal His$_6$-tag). The figure shows a superposition of chromatograms of the single components (AS^C = orange; MIZ1^{BTB} = green) and the mixture (AS^C + MIZ1^{BTB} = black). (C) FP analysis of the interaction between MIZ1^{BTB} (aa 1-115, N-terminal cloning overhang) and the 5-FAM-labeled AS^N (aa 3843-3869, N-terminal 5-FAM) and AS^C (aa 3870-3894, C-terminal 5-FAM with an additional Lys-residue after aa 3894) peptides, respectively. The data points represent the mean and standard deviations (SDs) of three independent experiments. The data for AS^C were fitted to a single-site binding model; for the K$_D$-value, see Table S2. The data for AS^N could not be fitted. (D) FP analysis of the interaction between HUWE1$^{D, min}$ (aa 3951-4374; minimal dimerizing C-terminal HUWE1 fragment) and the 5-FAM-labeled AS^N and AS^C peptides used in (C), respectively. The mean and SD of three independent experiments were fitted to a competition model (for details, see methods 3.3.7) that accounts for protein-ligand binding and protein dimerization; the corresponding K$_D$-values are 4.9 ± 0.8 µM and 322 ± 46 µM for AS^N and AS^C, respectively.

Building on my analyses of AS^C as the smallest HUWE1 fragment to show binding to MIZ1^{BTB}, I sought to confirm the HUWE1-MIZ1^{BTB} interaction in the context of extended HUWE1 constructs, as used in the ubiquitination assays (**Figure 20**). Therefore, I performed analytical SEC analyses comparing the binding of MIZ1^{BTB} to active, monomeric HUWE1^{AS} and inactive, dimeric HUWE1^D, respectively. In

line with the results of the activity assays (**Figure 20**), an interaction of MIZ1^{BTB} with HUWE1^D was not detected, which can be explained by the fact that HUWE1^D lacks the activation segment. In contrast, I observed a weak interaction of MIZ1^{BTB} with HUWE1^{AS} (**Figure 25**).
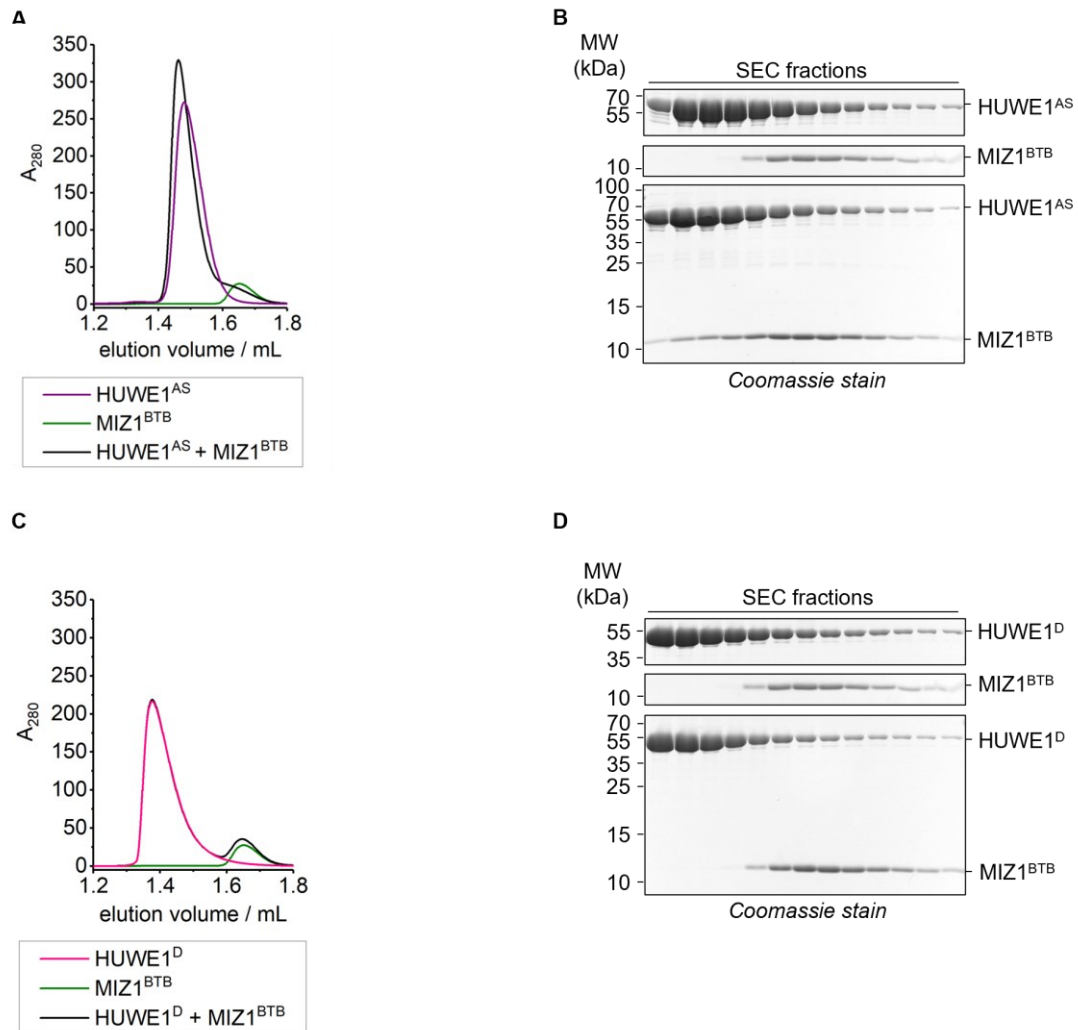
Figure 25: The binding of MIZ1^{BTB} to the C-terminal region of HUWE1 requires the activation segment.
(A) Analytical SEC of MIZ1^{BTB} (aa 1-115, N-terminal cloning overhang) and HUWE1^{AS} (aa 3843-4374). The figure shows a superposition of chromatograms of the single components (HUWE1^{AS} = purple; MIZ1^{BTB} = green) and the mixture (black). (B) SDS-PAGE with Coomassie staining of the elution fractions from the analytical SEC in (A), representing the individual runs HUWE1^{AS} and MIZ1^{BTB} as well as the HUWE1^{AS}-MIZ1^{BTB} mixture. Equivalent fractions were aligned with each other. (C) Analytical SEC of MIZ1^{BTB} (aa 1-115, N-terminal cloning overhang) and HUWE1^D (aa 3896-4374). The figure shows a superposition of chromatograms of the single components (HUWE1^D = pink; MIZ1^{BTB} = green) and the mixture (black). (D) SDS-PAGE with Coomassie staining of the elution fractions from the analytical SEC in (C), representing the individual runs (HUWE1^D and MIZ1^{BTB}, respectively) and the HUWE1^D-MIZ1^{BTB} mixture. Equivalent fractions were aligned with each other.

To quantitatively compare the interactions of AS^C and HUWE1^{AS}, respectively, with MIZ1^{BTB}, I labeled MIZ1^{BTB} with FlAsH (Fluorescein Arsenical Helix binder; for details see 3.3.6). In this case, an MBP rather than lipoyl domain-tagged version of AS^C was used to ensure a sufficiently large molecular weight difference between AS^C and MIZ1^{BTB} (MIZ1^{BTB}-dimer: ~ 27 kDa; lipoyl domain-tagged AS^C: ~ 15 kDa; MBP-tagged AS^C: ~ 46 kDa). My measurements show that the HUWE1^{AS}-MIZ1^{BTB} interaction (K$_D$ = 70.5 ± 0.7 µM, **Figure 26A**) is significantly weaker than the AS^C-MIZ1^{BTB} interaction (K$_D$ = 8.3 ± 0.6 µM, **Figure 26B**). This may be explained by the intramolecular interaction between the N-terminal part of the AS and the dimerization region (**Figure 24D**) that is expected to counteract the AS^C-MIZ1^{BTB} interaction.
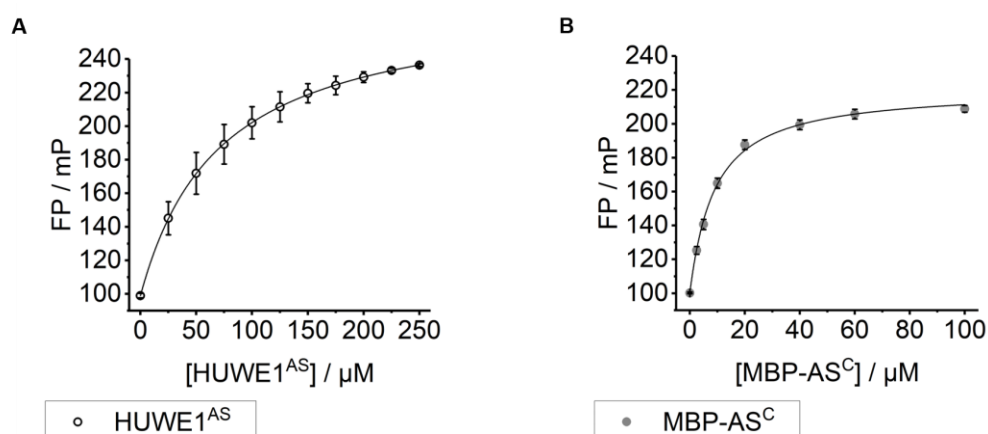
Figure 26: The interaction of MIZ1^{BTB} with HUWE1^{AS} is weaker than its interaction with AS^C.
(A) FP analysis of the interaction between FlAsH-labeled MIZ1^{BTB} (N-terminal FlAsH recognition sequence (GCCPGCCMA) + aa 1-115) and HUWE1^{AS} (aa 3843-4374). The mean and SDs of three independent experiments were fitted to a single-site binding model. A K$_D$-value of 70.5 ± 0.7 µM could be determined. (B) FP analysis of the interaction between FlAsH-labeled MIZ1^{BTB} (aa 1-115, with N-terminal FlAsH recognition sequence as shown in (A)) and N-terminally MBP-tagged AS^C (aa 3870-3890). The mean and SDs of three independent experiments were fitted to a single-site binding model. A K$_D$-value of 8.3 ± 0.6 µM could be determined.

4.3 The dimeric BTB domain of MIZ1 interacts with the HUWE1-AS^C peptide in an atypical mode compared to BCL6^{BTB}-peptide ligand complexes.

Based on the results described in 4.1 and 4.2 I used mixtures of the HUWE1-AS^C peptide and the MIZ1^{BTB} domain for crystallization trials. I initially obtained *apo* MIZ1^{BTB} crystals and determined a structure at 2.1 Å resolution (**Figure 27A and B**; PDB: 7AZW; **Table S1**). In principle BTB domains of the BTB-ZF-finger family are dimeric and show a butterfly-like architecture with an alpha-helical core from each subunit. This alpha-helical core is flanked by β-sheet-extensions at the lower and the upper part (**Figure 27B**). Superposition with an available *apo* MIZ1^{BTB} crystal structure by Stogios et al. (PDB: 3M52 [343]) showed high similarity, with a root-mean-square deviation (RMSD) of 1.21 Å in the positions of the Cα/backbone atoms, indicating an overall similar or almost identical fold of two *apo* MIZ1^{BTB} crystal structures with different space groups and different resolution (**Figure 27C**). In both crystal structures MIZ1^{BTB} forms a domain-swapped dimer that is characteristic for BTB-ZF proteins (see 1.6.2). However, unlike some other BTB domains, MIZ1^{BTB} lacks an N-terminal extension that typically forms a domain-swapped β-strand (β1). MIZ1^{BTB} thus does not inherently form a domain-swapped, lower β-sheet (see PDB: 3M52) [343] (see 1.6.2). Notably, however the 6-amino acids cloning overhang (β1'-mimic) at the N-terminus that is present in my crystallization construct extends the domain-swapped region, resulting, at least in one subunit, in a lower, mixed β-sheet, which is similar to that seen in other BTB domains. (**Figure 27B**).
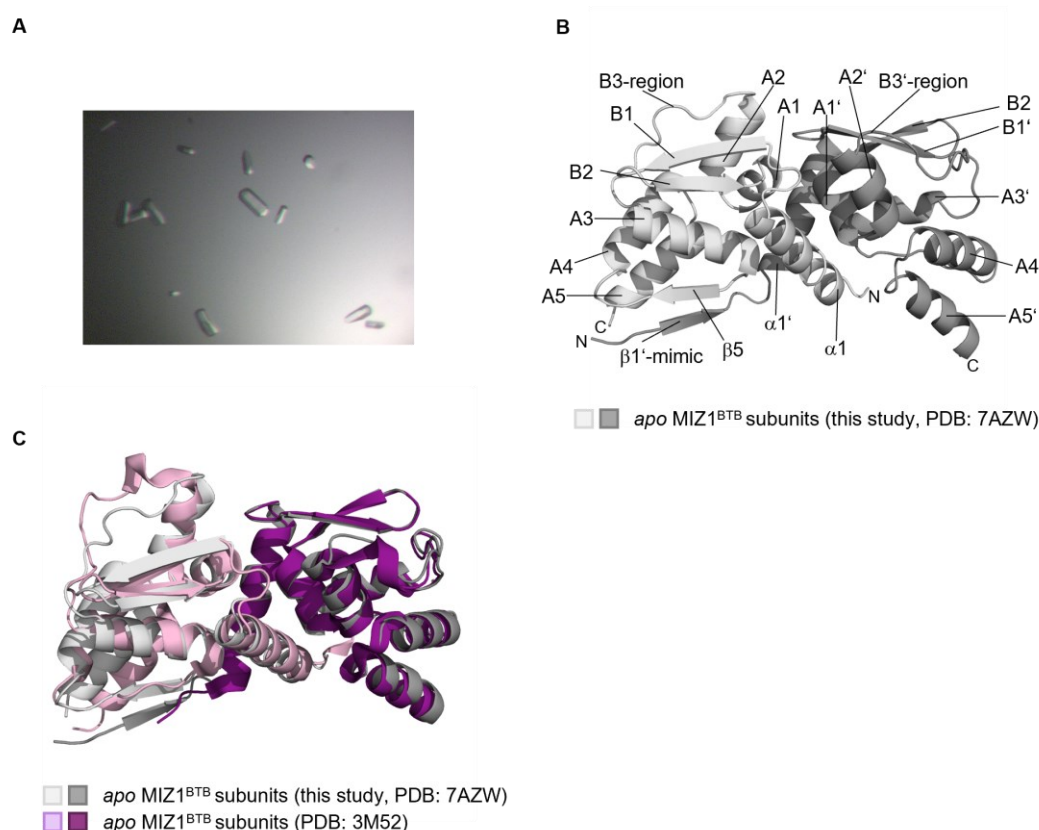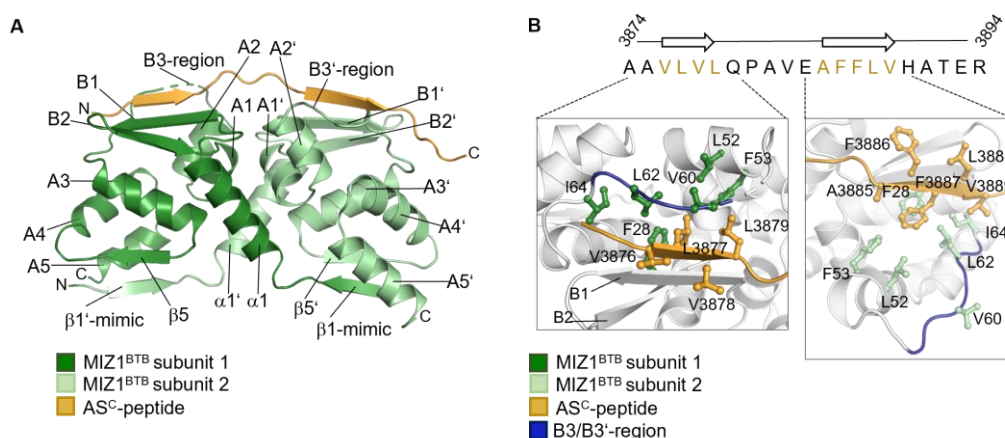
Figure 27: Crystal structure of apo MIZ1^{BTB}

(A) Crystals of *apo* MIZ1^{BTB}, generated in this study, grown in 100 mM sodium acetate pH 4.6, 8 % PEG4000 at 20 °C with a protein concentration of 4.9 mg/mL (for details, see 3.4). (B) Crystal structure of *apo* MIZ1^{BTB} (aa 1-115; 6-residue N-terminal cloning overhang; subunit 1: light grey; subunit 2: grey; PDB: 7AZW (this study)). The secondary structure elements are labeled according to Stogios et al. (for details, see 1.6.2) with capital Latin letters for the BTB core and small Greek letters for N- and C-terminal extensions [319]. The apostrophe indicates elements of subunit 2. The β´-mimic is due to a 6-residue N-terminal cloning overhang (GGSMAS), which is not part of the MIZ1^{BTB} sequence. (C) Superposition of two *apo* MIZ1^{BTB} crystal structures: PDB: 7AZW (this study) in grey; PDB: 3M52 in purple. Subunit 1 and 2 of the MIZ1^{BTB} homodimer are coloured in light grey/grey (this study, PDB: 7AZW) and light purple/purple (PDB: 3M52). The RMSD could be determined to 1.21 Å. For data collection and refinement statistics see Table S1.

The crystallization condition (100 mM sodium acetate pH 4.6, 8 % PEG4000), which yielded my crystals (**Figure 27A**), was similar to the one reported by Stogios et al. (75 mM zinc acetate pH 4.6) [343]. Since the *apo* MIZ1^{BTB} crystals diffracted well and formed in 1 to 2 days, I used this crystal form for soaking experiments with the HUWE1-AS^C peptide and for co-crystallization. Soaking for different time points (1, 5, and 10 minutes and 1.5, 19, and 25 hours) and temperatures (20 °C and RT) yielded additional *apo* MIZ1^{BTB}-structures with resolutions between 2.1 to 2.6 Å, but no density for the peptide. However, co-crystallization of the HUWE1-AS^C-peptide and MIZ1^{BTB} was successful, and a crystal structure with a resolution

of 2.25 Å could be determined (PDB: 7AZX; **Figure 28**, **Table S1**). The crystal morphology was the same as the one seen for *apo* MIZ1^{BTB} (**Figure 27A**).

Figure 28: The flexibility of the B3-region in MIZ1^{BTB} allows for an atypical binding mode of HUWE1-AS^C.
(A) Crystal structure of the homodimeric MIZ1-BTB-domain (aa 1-115; 6-residue N-terminal cloning overhang; subunit 1: green; subunit 2: pale green; PDB: 7AZX (this study)) in complex with the HUWE1-AS^C-peptide (orange; aa 3870-3897; peripheral residues are not resolved). The secondary structure elements are labeled according to Stogios et al. (for details, see 1.6.2) with capital Latin letters for the BTB core and small Greek letters for N- and C-terminal extensions [319]. The apostrophe indicates elements of subunit 2. The β1/β′-mimic is due to a 6-residue N-terminal cloning overhang (GGSMAS), which is not part of the MIZ1^{BTB} sequence. (B) Detail of the MIZ1^{BTB}-HUWE1-AS^C interface from the crystal structure in (A). The HUWE1-AS^C peptide sequence is shown at the top, with those residues highlighted in orange that are part of the β-strands and represented as balls and sticks in the structure below. Those hydrophobic residues in the BTB domain that contact the highlighted hydrophobic residues of the peptide are also represented as balls and sticks. The B3-region in MIZ1^{BTB} subunit 1 and the B3′-region in MIZ1^{BTB} subunit 2 are highlighted in blue; note that the latter region is tilted outward.

Another condition in which the AS^C peptide-MIZ1^{BTB} complex crystallized contained 100 mM Na$_2$HPO$_4$, 5 % PEG1000, and 40 % reagent alcohol, pH 4.2. Those crystals are shown in **Figure 29**. Six datasets recorded for these crystals were merged with XSCALE [418] and subjected to STARANISO [417], resulting in a resolution of 1.6 Å.
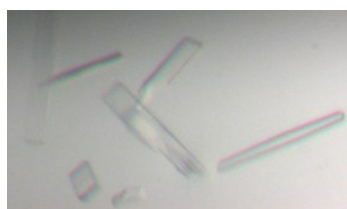
Figure 29: Co-crystals of MIZ1^{BTB} with the HUWE1-derived AS^C peptide
The crystals grew in 100 mM Na$_2$HPO$_4$, 5 % PEG1000, and 40 % reagent alcohol, pH 4.2, at 20 °C with a protein concentration of 7 mg/mL and a 1.2-fold molar excess of the HUWE1-AS^C peptide (for additional details, see 3.4).

In my deposited structure (PDB: 7AZX, **Figure 28**) the HUWE1-AS^C-peptide could be assigned one orientation across the MIZ1^{BTB} dimer. In contrast, it was not

possible to unequivocally determine an orientation and the amino acid register for the HUWE1-AS^C-peptide in the second crystallization condition (**Figure 29**; data not shown). Nevertheless, the peptide was found to bind to the same position in MIZ1^{BTB} in the second, unfinished structure. Because the orientation of the HUWE1-AS^C-peptide could not be determined and the overall fold of the MIZ1-BTB-domain does not differ from that presented in PDB: 7AZW and PDB: 7AZX, the crystal structure obtained from the crystals shown in **Figure 29** is not shown here. It is conceivable that the peptide binds to the binding site in MIZ1^{BTB} in more than one mode or register, due to its largely hydrophobic nature. To evaluate such alternative binding modes in solution requires further investigation, e.g., by NMR spectroscopy. It is possible, however, that a distinct binding mode is used in the context of the full-length proteins, based on additional, yet uncharacterized protein-protein interactions. Importantly, the HUWE1-AS^C peptide was found to bind to the same region of MIZ1^{BTB} in both crystallization conditions and this region differs from the canonical peptide binding site observed in previous crystal structures of BTB domains (see 1.6.3). The HUWE1-AS^C peptide extends the two-fold β-sheet at the upper end of the domain to a three-fold β-sheet, adding an antiparallel β-strand in the one, and a parallel β-sheet in the other subunit (**Figure 28A**). **Figure 28B** illustrates that the resulting interface is hydrophobic on either side, but asymmetric. In one BTB domain subunit, the flexible B3-region is oriented parallel to the β-strand of the HUWE1-peptide, while the same region is tilted outward in the other subunit. These alternative arrangements imply that a given amino acid may be involved in peptide binding in one subunit but not in the other.

Why this binding mode may be exclusive for the BTB domain of MIZ1 becomes evident from comparing the MIZ1^{BTB}-AS^C crystal structure (PDB: 7AZX) with that of the BCL6^{BTB} domain bound to a SMRT-derived peptide (PDB: 1R2B), as shown in the superposition in **Figure 30A**. MIZ1^{BTB} differs from other BTB domains in the number of β-strands at the upper part of the domain: While many other BTB domains, such as BCL6, contain a three-stranded β-sheet, MIZ1^{BTB} has only a two-stranded β-sheet. This is due to an atypical flexibility of the B3-region in MIZ1^{BTB} and allows the AS^C ligand to bind in lieu of a third β-strand. In BCL6, the peptide ligand instead positions its C-terminal part into a 'lateral groove' and extends toward the lower end of the domain (see also 1.6.3; **Figure 30A**). As a

consequence, the dimeric MIZ1^{BTB}-domain binds one HUWE1 peptide, thus displaying a 2:1 stoichiometry, while the dimeric BCL6^{BTB}-domain binds one SMRT peptide per subunit, yielding a 1:1 stoichiometry (**Figure 30A**).

Notably, not only the crystal structures of MIZ1^{BTB} determined in this study show conformational flexibility of the B3-region (**Figure 30B**): 5 out of 6 subunits seen in three previous crystal structures of *apo* MIZ1^{BTB} also show plasticity in the B3-region, while one subunit contains a B3-strand. In this case, however, the β-strand is induced by lattice contacts within a crystallographic tetramer, which neither others nor I could detect in solution [343], [426] (**Figure 30C**).
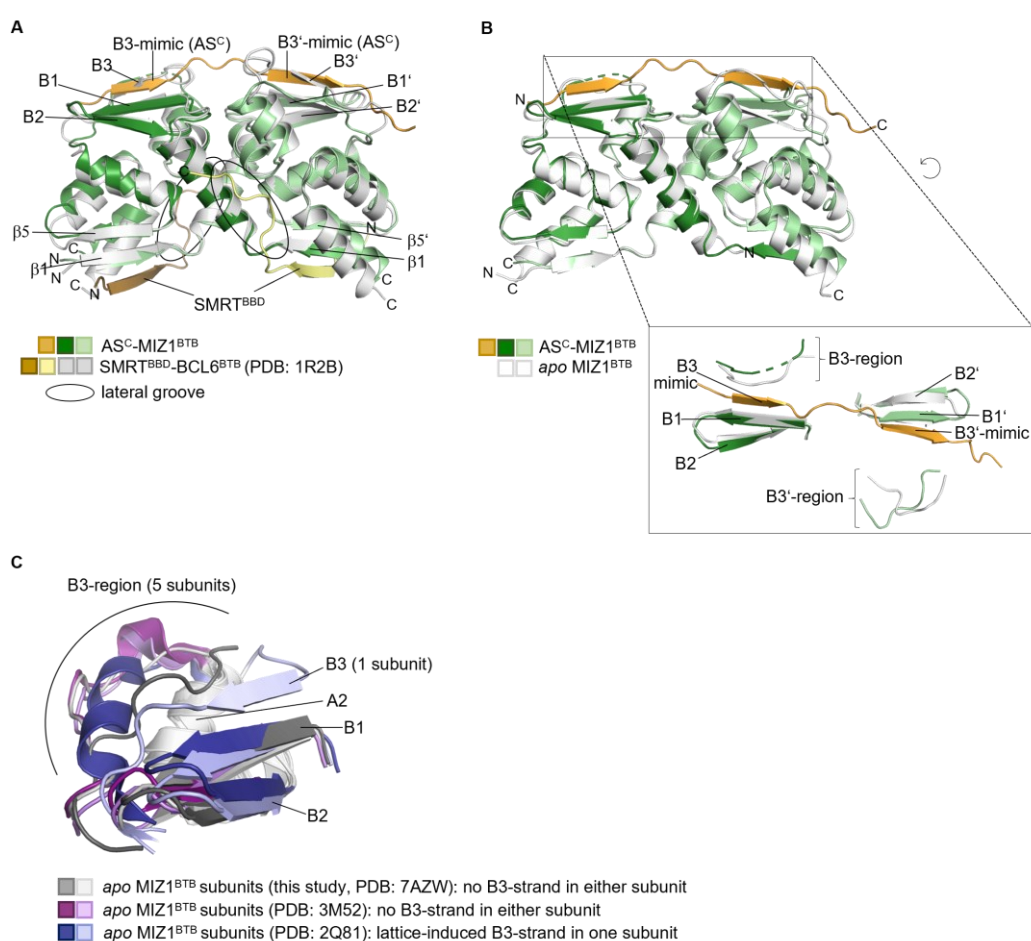
Figure 30: The lack of a pre-formed B3-strand in MIZ1^{BTB} allows for the atypical binding of HUWE1-AS^C.
(A) Superposition of the crystal structures of the MIZ1^{BTB}-AS^C complex in green/orange (this study, PDB: 7AZX, see FigureA) and BCL6^{BTB} in complex with a SMRT-derived peptide in grey/brown/ochre (PDB: 1R2B, [346]), with BBD denoting 'BCL6-binding domain'. The lateral groove is encircled in black. Each BCL6^{BTB} subunit binds to one SMRT-peptide, coloured in brown and ochre. The individual β-strands of the β-sheets that are extended by the peptide ligands are labeled, following the nomenclature from Stogios et al. with capital Latin letters for the BTB-core and small Greek letters for N- and C-terminal extensions. Apostrophe indicate elements of subunit 2 [343]. (B) Superposition of the crystal structures of the MIZ1^{BTB}-AS^C complex in green/orange (this study, PDB: 7AZX, see FigureA) and *apo* MIZ1^{BTB} in grey (this study; PDB: 7AZW). Detail of

the upper B1-B2-sheet, B3-region, and peptide ligand, extracted from the surrounding protein for clarity (box). In all panels, visible protein N- and C-termini are labeled. (C) Superposition of 6 individual MIZ1^{BTB} subunits, extracted from the BTB domain dimers seen in the indicated three crystal structures. For ease of comparison, only the upper parts of the BTB domains, comprising residues 24 to 37 and 54 to 67, is displayed.

4.4 The binding stoichiometry observed in the crystal structure of the MIZ1^{BTB}-AS^C complex also applies in solution.

SEC-coupled multi-angle light scattering (MALS) analyses of MIZ1^{BTB} and AS^C (with a N-terminal lipoyl-domain-tag and a C-terminal His$_6$-tag) showed that MIZ1^{BTB} forms a dimer (as shown previously [343]) and that this dimer likely interacts with one AS^C molecule in solution (**Figure 31A, Table 26**). It should be noted, however, that the determination of the stoichiometry was somewhat ambiguous in this experiment, since the instrument calibration turned out to be insufficient. The calculation of the molecular weight for the indivual binding partners yielded 22.6 ± 0.4 kDa for MIZ1^{BTB} (theoretical MW: 26.6 kDa (dimer)) and 12.5 ± 0.3 kDa for AS^C (theoretical MW: 14.6 kDa), respectively. The data-derived molecular weight for the complex is 22.6 + 12.5 kDa, which fits a 2:1 stoichiometry of MIZ1^{BTB} over AS^C, based on the data-derived individual molecular weights. Yet, the weight would rather reflect a 1:1 stoichiometry based on the theoretical molecular weights of the components. To eliminate this ambuiguity additional calibration of the instrument, e.g., with BSA, would have been necessary. For technical reasons, I instead performed isothermal titration calorimetry (ITC). The MIZ1^{BTB} protein was placed into the cell and AS^C of HUWE1 was applied to the syringe and titrated into the cell (for details, see 3.3.8). A K$_D$-value of 3.1 ± 0.7 μM could be determined for the MIZ1^{BTB}-AS^C interaction and n = 0.41 ± 0.02, in line with the 2:1 stoichiometry seen crystallographically (**Figure 31B**).
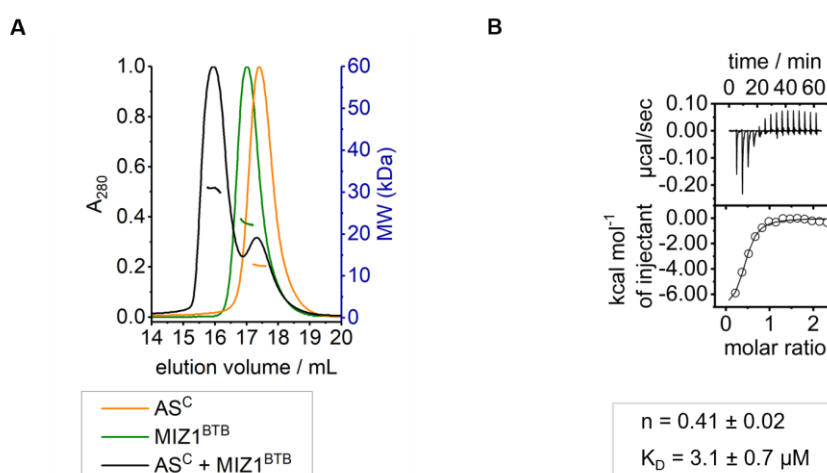
Figure 31: The stoichiometry of the MIZ1^{BTB}-AS^C interaction is 2:1 in solution, in line with the crystal structure.
(A) SEC-MALS analysis of MIZ1^{BTB} (aa 1-115, with N-terminal cloning overhang; elution profile of the individual run shown in green) yielding a molecular weight (MW) of 22.6 ± 0.4 kDa; and of AS^C (aa 3870-3890; N-terminal lipoyl-domain-tag and C-terminal His$_6$-tag; single run shown in orange) yielding a MW of 12.5 ± 0.3 kDa; and of the complex (shown in black), yielding a MW of 31.1 ± 0.4 kDa. For details of the theoretical MWs, see Table 26. The absorbance peak heights were normalized to 1. The UV data (left y-axis) are shown continuously; the MALS data (right y-axis; converted to MW) are only displayed for the region across the tip of each absorbance peak, as used for the determination of the MW. (B) Isothermal titration calorimetry analysis of the HUWE1-AS^C (aa 3870-3890; N-terminal lipoyl-domain-tag and C-terminal His$_6$-tag)-MIZ1^{BTB} (aa 1-115, with N-terminal cloning overhang) interaction. The determined stoichiometry, n, and dissociation constant, K$_D$, are indicated.

Table 26: Calculated and determined molecular weights (MWs) analysing the interaction between MIZ1^{BTB} and HUWE1-AS^C by SEC-MALS analysis (see FigureA)

	determined MW	calculated MW
MIZ1^{BTB}	22.6 ± 0.4 kDa	26.6 kDa (dimer)
Lipoyl-AS^C-His$_6$	12.5 ± 0.3 kDa	14.6 kDa
MIZ1^{BTB}-AS^C-complex	31.1 ± 0.4 kDa	41.2 kDa

4.5 *In vitro* binding and activity assays support the interaction mode observed crystallographically.

To confirm the atypical mode observed crystallographically for the interaction of the MIZ1^{BTB} domain with the HUWE1-derived peptide AS^C we introduced point mutations in the MIZ1^{BTB}-AS^C interface (**Figure 28B**). A key residue that I selected was Phe 28 of MIZ1 that forms hydrophobic interactions with Leu 3877 of AS^C in one BTB subunit and Phe 3887 in the other subunit (**Figure 28B**). I also chose to

interrogate several hydrophobic residues in the flexible B3-region, including Val 60, His 61, Leu 62 and Ile 64, since they make contacts with at least one part of the AS^C peptide at the asymmetric interface. Moreover, I decided to replace Val 60 by a proline with the intention of perturbing the conformational space accessible to the B3-region. Finally, I also selected Leu 52 and Phe 53 in MIZ1^{BTB} for mutagenesis, both of which point towards the interface, despite being positioned more peripherally than the other residues I analyzed. In AS^C I mutated Leu 3877 and Phe 3887, as described above. Val 3883, which is not involved in the interface seen crystallographically, served as a negative control. A few more surrounding residues, His 3874, Phe 3886 and Leu 3879, were expected to be WT-like or show only minor effects due to the, if at all, only peripheral contribution to the interface seen crystallographically.

I first analyzed the effect of the mutations on the affinity of the MIZ1^{BTB}-AS^C interaction by FP. To this end the HUWE1-AS^C peptide was fluorescently labeled and the FP signal detected with increasing concentration of MIZ1^{BTB} (for details, see 2.4 or 3.3.7, respectively). This yielded a K_D-value of 10.0 ± 0.9 µM for MIZ1^{BTB} WT and AS^C WT. This result is in good agreement with the K_D-value of 8.3 ± 0.6 µM that I had previously determined for MBP-tagged AS^C (with C-terminal His$_6$-tag) and FlAsH-labeled MIZ1^{BTB} by FP (**Figure 26B**) and the K_D-value of 3.1 ± 0.7 µM for MIZ1^{BTB} and AS^C (N-terminal lipoyl-domain-tag and C-terminal His$_6$-tag), determined by ITC (**Figure 31B**). The most drastic effects of mutations in *MIZ1^{BTB}* were observed for F28A, V60P, L62A and I64A, resulting in K_D-values of over 60 µM; L52A, F53A and H61A showed only minor effects, with WT-like K_D-values ranging from 9 to 17 µM (**Figure 32A**, **Table S2**). To ascertain that the introduced point mutations did not affect the dimerization of MIZ1^{BTB}, I employed analytical SEC, showing that all MIZ1^{BTB} variants eluted at a similar volume compared to MIZ1^{BTB} WT. In contrast, a quadruple mutant (V10D/L14D/Q17D/V41K) of MIZ1^{BTB}, that I had designed to disrupt dimerization based on a dimerization-defective SPOP variant [427], showed an increase in the elution volume, thus corroborating my interpretation of the SEC analyses (**Figure 32B**). I also performed a control experiment interrogating the N-terminal cloning overhang of the MIZ1^{BTB} construct I had crystallized. As described above (section 1.6.2), this cloning overhang mimics a N-terminal β1/β1′-strand, which is formed in several other BTB domains and induces a domain-swapped antiparallel

β-sheet (β1-β5´) at the lower part of the domain, **Figure 13B** and **Figure 30A**), but is not present in MIZ1. As shown in **Figure 32C**, the overhang-induced β1´-mimic interacts with the AS^C-peptide bound to a symmetry-related molecule (subunit 2) in my crystal structure of the $MIZ1^{BTB}$-AS^C complex. To exclude the possibility that the overhang induces a similar binding of the AS^C-peptide at the upper β-sheet of $MIZ1^{BTB}$ in solution, I conductded additional FP analyses upon removal of the overhang from $MIZ1^{BTB}$. Encouragingly, $MIZ1^{BTB}$ with and without cloning overhang bound to the AS^C-peptide with similar K_D-values of ~ 10 µM (**Figure 32D**, **Table S2**). This indicates that the cloning overhang does not induce the binding of AS^C to $MIZ1^{BTB}$ nor does it affect the dimerization of $MIZ1^{BTB}$ (**Figure 32B**).

In addition, I performed the FP assays with variants of HUWE1-AS^C. As expected, based on the crystal structure, L3877A and F3887A showed reduced binding affinities for $MIZ1^{BTB}$ (**Figure 33**). The interaction with $MIZ1^{BTB}$ was completely abolished by the double mutation L3877A/F3887A. L3879A also showed reduced affinity for $MIZ1^{BTB}$ with a K_D-value of 33.2 ± 1.6 µM, yet the effect is weaker than for L3877A and F3887A. Somewhat surprisingly, F3886A also led to a drastic reduction in binding, similar to L3877A (**Figure 33**), despite F3886A pointing away from the $MIZ1^{BTB}$-AS^C interface formed in the crystal structure (**Figure 28B**). This may be due to binding of the peptide ligand in a different register, as possibly enabled by the overall hydrophobic nature of the binding sequence, as discussed in section 4.3. Moreover, it is conceivable that conformational rearrangements of the B3-region alter the peptide binding mode in solution compared to the crystal structure.
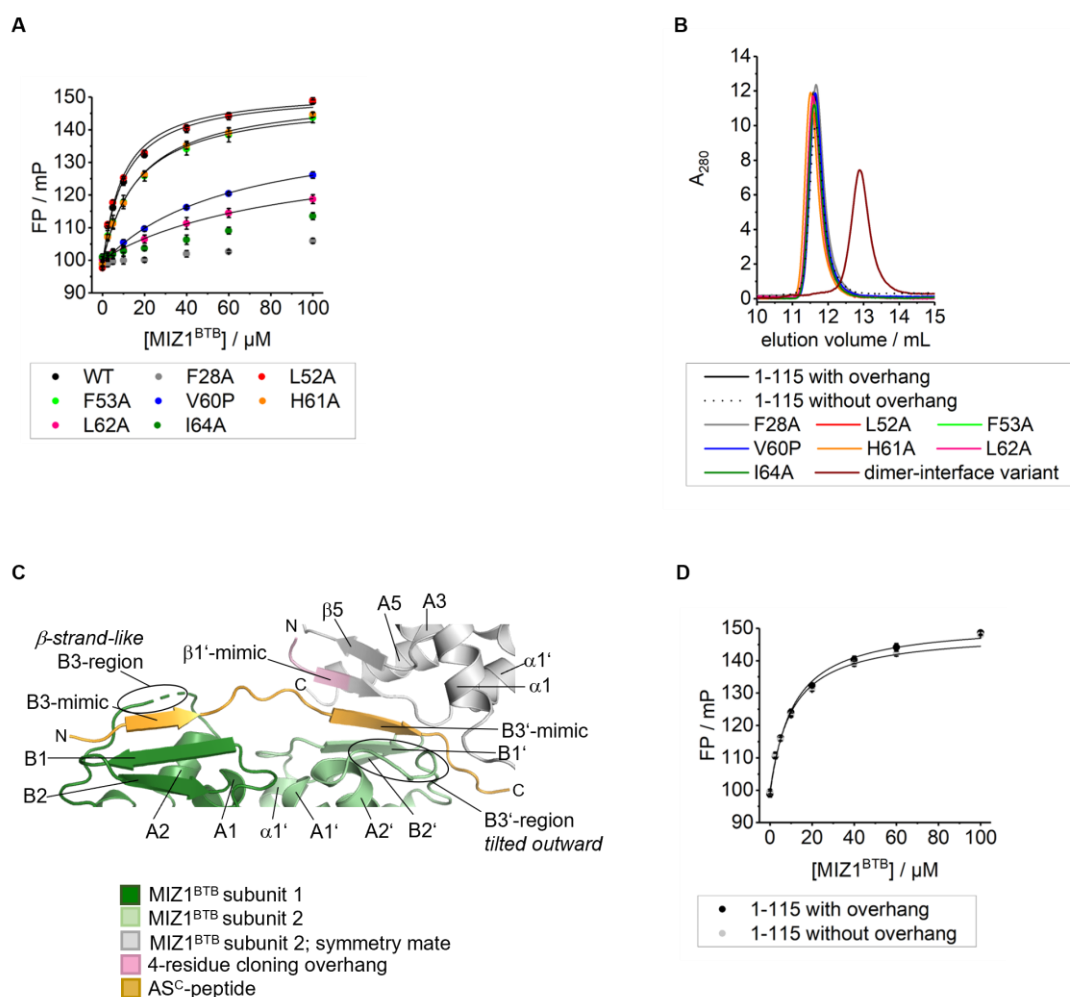
Figure 32: Structure-guided mutagenesis of MIZ1^BTB in combination with binding assays support the atypical peptide binding mode between MIZ1^BTB and AS^C observed crystallographically.
(A) FP analysis of the interaction between MIZ1^BTB WT (aa 1-115, with a N-terminal cloning overhang) or mutated variants and the C-terminally 5-FAM-labeled HUWE1-AS^C peptide (aa 3870-3894; additional Lys residue inserted after aa 3894 prior to 5-FAM). The mean and SDs of three independent experiments were fitted to a single-site binding model, where possible; for the corresponding K_D-values, see Table S2. (B) Analytical SEC of MIZ1^BTB and variants thereof. All MIZ1^BTB variants contain a N-terminal cloning overhang, except for the dimer interface variant (V10D/L14D/Q17D/V41K), which was designed to disrupt dimerization, based on Zhuang et al. [427]. (C) Detailed view of lattice contacts of subunit 2 of the crystallographic dimer in the structure of the MIZ1^BTB-AS^C complex (this study; PDB: 7AZX). Secondary structure elements of subunit 1 are labeled without an apostrophe, those of subunit 2 with an apostrophe (see FigureA). The 4 modeled residues of the cloning overhang (pink) form a β-strand that mimics a strand-exchanged β1-strand found in certain other BTB domains, but not in MIZ1. This β1'-mimic of subunit 2 interacts with the AS^C-peptide that is bound to the upper B1-B2 sheet of a symmetry mate of subunit 2 (symmetry operation in fractional space relative to the position given in PDB 7AZX: -y,x-y+1,z+1/3). The B3-region of subunit 2 is tilted outward. In subunit 1, the equivalent position of the β1-mimic is occupied by a portion of the B3-region, which adopts a β-strand-like conformation. (D) FP analysis of the interaction between the C-terminally 5-FAM-labeled HUWE1-AS^C peptide (aa 3870-3894; additional Lys residue inserted after aa 3894 prior to 5-FAM) and MIZ1^BTB (aa 1-115) with or without a N-terminal cloning overhang. The mean and SDs of three independent experiments were fitted to a single-site binding model, where possible; for the corresponding K_D-values, see Table S2.

106
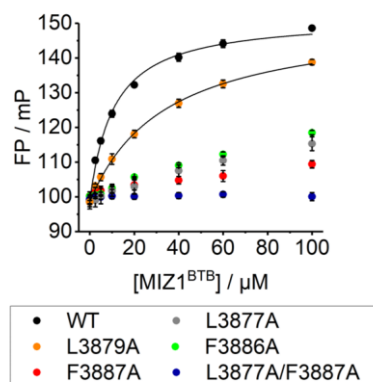
Figure 33: Structure-guided mutagenesis of the HUWE1-AS^C peptide is overall consistent with the atypical binding mode characterized crystallographically.
FP analysis of the interaction between MIZ1^{BTB} WT (aa 1-115, with a N-terminal cloning overhang) and the C-terminally 5-FAM-labeled HUWE1-AS^C peptide (WT sequence) or variants thereof (aa 3870-3894; additional Lys residue inserted after aa 3894 prior to 5-FAM). The mean and SDs of three independent experiments were fitted to a single-site binding model, where possible; for the corresponding K_D-values, see Table S2.

Having analyzed the effect of structure-guided mutations in both - *MIZ1^{BTB}* and *HUWE1-AS^C* – on binding (**Figure 32A** and **Figure 33**), I turned to investigate their effect on the ubiquitination of MIZ1 by HUWE1. I monitored MIZ1-ubiquitination using the same set up as in **Figure 20**. MIZ1$^{1-282}$, containing one ubiquitination site (Lys 135) served as a substrate and the HUWE1-AS^C peptide extended C-terminally to include the catalytic HECT domain, as required for ligase activity. I first tested the F28A variant of MIZ1$^{1-282}$ and L3877A/F3887A of HUWE1^{AS}, because these two protein variants showed the strongest effect in the binding assays (**Figure 32A** and **Figure 33**). I monitored the HA-His$_6$-tagged MIZ1$^{1-282}$ ubiquitination by Western blotting against the HA-tag at 10, 20, 40 and 60 minutes in order to identify a time point at which the difference between WT and protein variant was most pronounced. (**Figure 34A**). Based on this experiment, I decided for a 20-minute endpoint assay and performed triplicate experiments for all protein variants at 37 °C. One representative blot comparing the MIZ1$^{1-282}$ variants is shown in **Figure 34B**, the associated quantification in **Figure 34C**. This data shows that the F28A, V60P, L62A and I64A mutations have the strongest effects on MIZ1$^{1-282}$ ubiquitination, in line with the FP-based effects on binding (**Figure 32A**) and the crystal structure (**Figure 28**). The H61A variant is ubiquitinated to a similar degree as the WT, wheres L52A and F53A are modestly affected, once again in agreement with my binding assays (**Figure 32A**).

All mutations that were tested in the context of the AS^C-peptide (**Figure 33**) were also analyzed for their MIZ1$^{1-282}$ ubiquitination activity in the context of HUWE1^{AS}, in addition to H3874A and V3883A (negative controls). As shown in **Figure 35A**, all HUWE1^{AS} variants are still monomeric, like HUWE1^{AS} WT, indicating that point mutations in HUWE1^{AS} do not affect the oligomerization state. The dimerizing construct HUWE1^D is shown for comparison. Furthermore, the anti-HUWE1 Western blot in **Figure 35B** demonstrates that the introduced point mutations do not reduce the ligase activity of HUWE1^{AS} *per se* and their effects can therefore be interpreted in terms of the HUWE1-MIZ1 interaction.

Anti-HA Western blots monitoring MIZ1$^{1-282}$ ubiquitination, along with their quantification (**Figure 35B and C**), showed over 60 % reduction in the activity of HUWE1^{AS} F3886A, F3887A and L3877A/F3887A. Furthermore, the L3877A and L3879A variants of HUWE1^{AS} were comprised in MIZ1$^{1-282}$ ubiquitination (60 % or 80 % of the WT activity, respectively). As I had anticipated, HUWE1^{AS} V3883A showed WT-like activity, while the H3874A variant was mildly compromised in its activity toward MIZ1$^{1-282}$, resulting in 70 to 80 % of the WT activity. In sum, these results confirm those obtained in the binding assays (**Figure 33**) and support the notion that the crystal structure (**Figure 28**) highlights a relevant interface between AS^C and MIZ1^{BTB}.
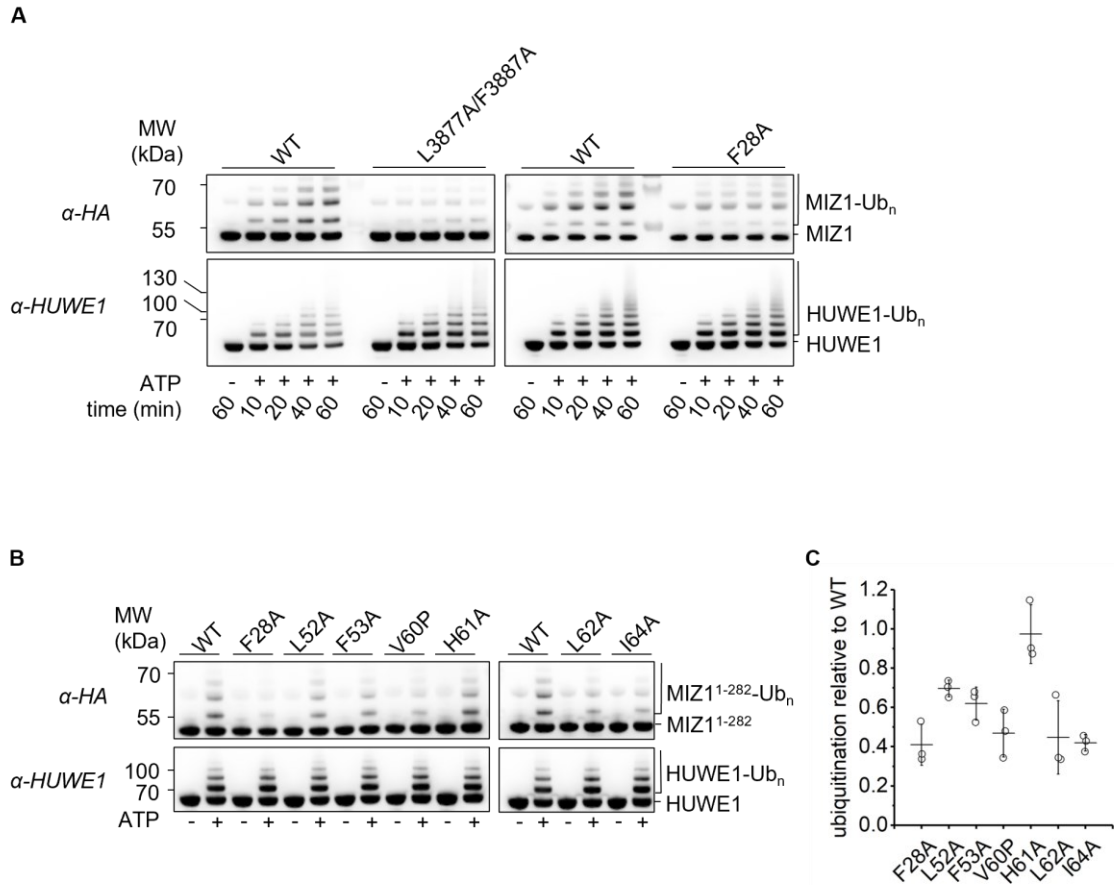
Figure 34: Structure-guided mutagenesis of MIZ1$^{1-282}$ reduces its ubiquitination by HUWE1^{AS}, in line with the atypical peptide binding mode observed crystallographically.
(A) Analysis of MIZ1$^{1-282}$ (aa 1-282, HA-His$_6$-tag at the C-terminus) ubiquitination by HUWE1^{AS} (aa 3843-4374). MIZ1$^{1-282}$ (WT or variants thereof) and HUWE1^{AS} (WT or a variant thereof) were incubated at 37 °C with UBA1 (E1), UBCH7 (E2), ubiquitin, MgCl$_2$, with or without ATP. The reaction was stopped with SDS-loading dye at the indicated time point, subjected to SDS-PAGE, followed by anti-HA Western blotting (for MIZ1$^{1-282}$) and anti-HUWE1 Western blot. The latter blot served as a loading control for the input amount (-ATP lane) of HUWE1^{AS}. (B) Analysis of MIZ1$^{1-282}$ ubiquitination by HUWE1^{AS} for MIZ1$^{1-282}$ (WT or variants thereof), analogous to (A), but for a 20-minute endpoint only. (C) Quantification of MIZ1$^{1-282}$ ubiquitination (+ATP lane in (B)) for MIZ1$^{1-282}$ WT and the indicated variants, respectively, from three independent experiments, normalized to the input amount of MIZ1$^{1-282}$ (corresponding -ATP lane in (B)). The ubiquitination efficiency was plotted relative to MIZ1$^{1-282}$ WT (WT = 1.0).
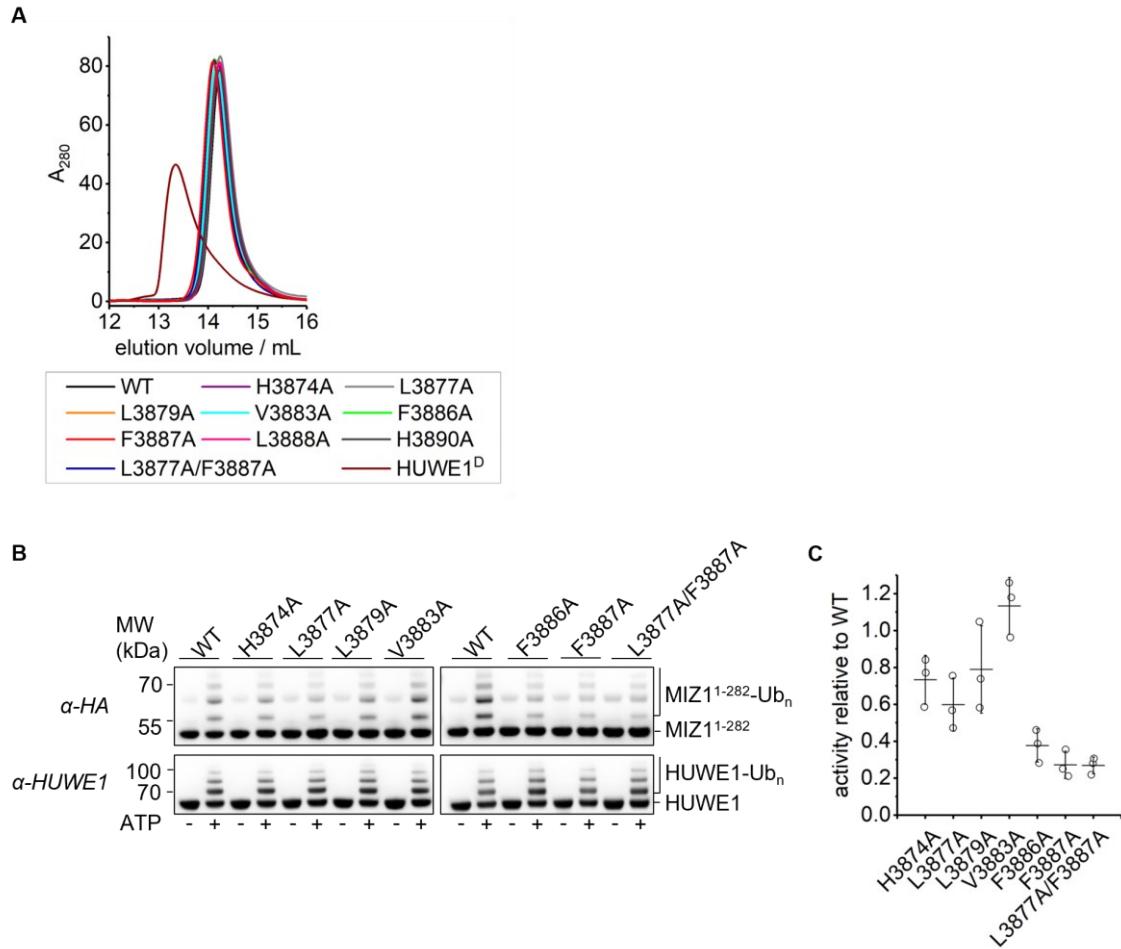
Figure 35: Structure-guided mutagenesis of HUWE1^{AS} reduces MIZ1$^{1-282}$ ubiquitination, in line with the atypical peptide binding mode observed crystallographically.
(A) Analytical SEC of HUWE1^{AS} (aa 3843-4374) and the indicated variants thereof, respectively, in comparison with dimeric HUWE1^D (aa 3896-4374). (B) Analysis of MIZ1$^{1-282}$ (aa 1-282, HA-His$_6$-tag at the C-terminus) ubiquitination by HUWE1^{AS} WT (aa 3843-4374) or variants thereof. MIZ1$^{1-282}$, HUWE1^{AS} WT or variants thereof were incubated at 37 °C with UBA1 (E1), UBCH7 (E2), ubiquitin, MgCl$_2$, with or without ATP. The reaction was stopped with SDS-loading after 20 minutes. Samples were subjected to SDS-PAGE, followed by anti-HA Western blotting (for MIZ1$^{1-282}$) and anti-HUWE1. The latter blot served as a loading control for the input amount (-ATP lane) of HUWE1^{AS}. (C) Quantification of MIZ1$^{1-282}$ ubiquitination (+ATP lane in (B)) by HUWE1^{AS} WT or the indicated variants thereof from three independent experiments, normalized to the input amount of HUWE1^{AS} (corresponding -ATP lane in (B)). The ubiquitination efficiency was plotted relative to HUWE1^{AS} WT (WT = 1.0).

4.6 Preliminary *in vitro* attempts to translate the data on the MIZ^BTB-AS^C/HUWE1^AS interaction into the context of full-length HUWE1

In the following I investigated the interaction between full-length HUWE1 (Fl-HUWE1) and MIZ1^BTB by analytical SEC and activity assays *in vitro*. Fl-HUWE1 was kindly provided by Irina Grishkovskaya and David Haselbach (IMP, Vienna). MIZ1^BTB, Fl-HUWE1, and a 20:1 molar mixture of the two where consecutively analyzed by SEC (for further details, see 3.3.4). A large excess of MIZ1 was chosen to optimize the chance of detecting weak complex formation. Due to limitations of the available amount of Fl-HUWE1, a Fl-HUWE1 concentration of 3.45 µM was used in each run and the fractions were analyzed by anti-MIZ1 and anti-HUWE1 Western blotting. Based on the chromatogram, no interaction was observed (no shift of the HUWE1 elution peak to smaller elution volumes upon addition of MIZ1^BTB nor an increase in absorption) (**Figure 36A**). The Western blot analysis did not yield unambiguous evidence of complex formation, yet: On the one hand, the anti-MIZ1 blot of the SEC containing both proteins shows a weak signal for MIZ1^BTB in the HUWE1-containing fractions, as it would be expected for weak complex formation. On the other hand, such a signal, even if after a longer exposure time, was also observed in an anti-MIZ1 control blot for the SEC in which only Fl-HUWE1 had been injected (**Figure 36B**). This may suggest that the anti-MIZ1 antibody unspecifically recognizes a contaminating band in the Fl-HUWE1 sample. Hence, while this first experiment did not yield evidence for an interaction between Fl-HUWE1 and MIZ1^BTB in this set-up, further investigation will be required, e.g., confirming the identity of the suspected contamination, repeating SEC experiments at higher protein concentrations or using more sensitive biophysical techniques. Given that SEC is accompanied by a dilution of the injected proteins in the course of the run, weak interactions may well escape detection with this technique.
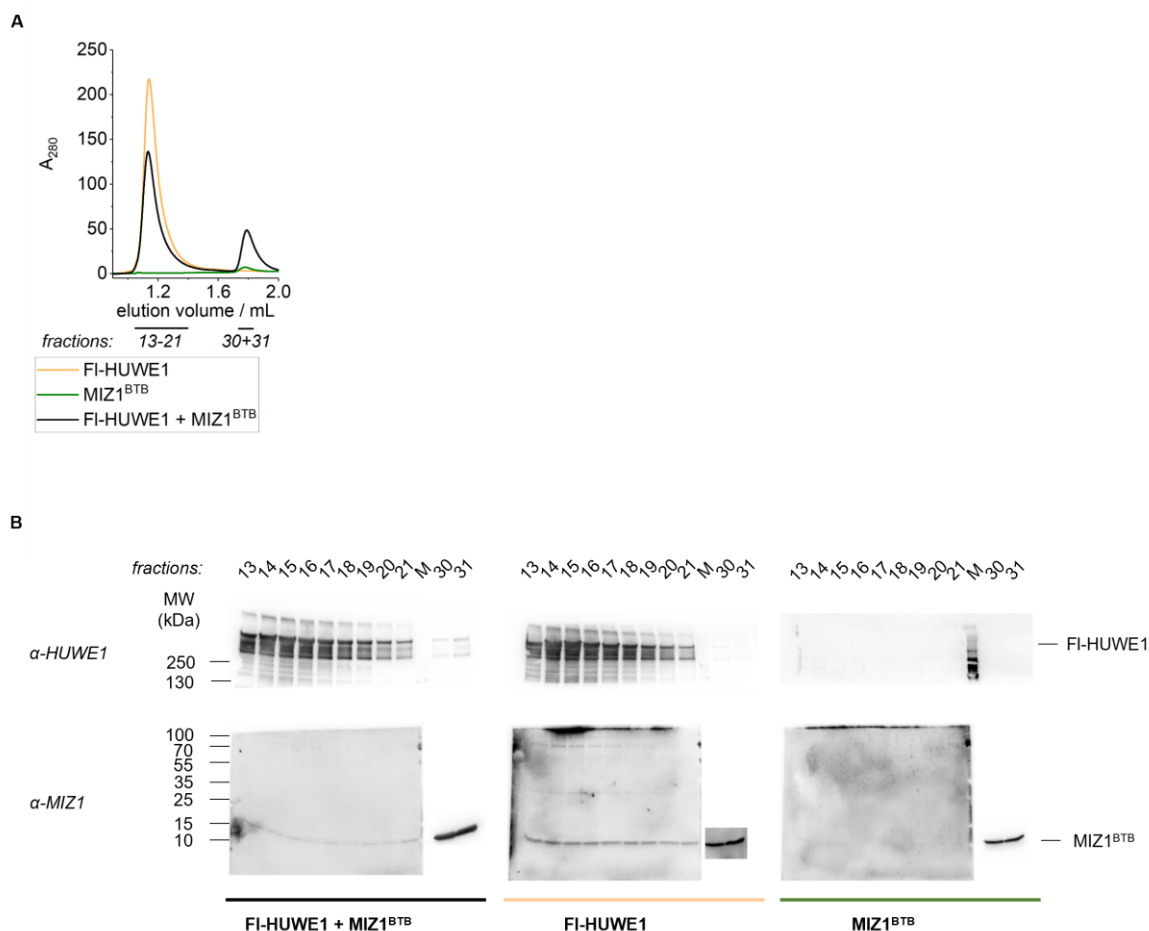
Figure 36: Preliminary, analytical SEC analysis (n=1) of MIZ1^{BTB} and Fl-HUWE1 does not yield unambiguous evidence for an interaction.
(A) Analytical SEC of MIZ1^{BTB} (aa 1-115) and Fl-HUWE1 (C-terminal Strep-tag, provided by Irina Grishkovskaya and David Haselbach, IMP Vienna). The figure shows a superposition of the elution profiles of the single components (Fl-HUWE1 = apricot; MIZ1^{BTB} = green) and a 1:20 molar mixture (Fl-HUWE1 + MIZ1^{BTB} = black). The peak fractions analyzed in (B) by Western blotting are indicated below the chromatogram. (B) anti-HUWE1 and anti-MIZ1 Western blot analysis of the fractions indicated in (A) for the Fl-HUWE1-MIZ1^{BTB} mixture (left), *apo* Fl-HUWE1 (middle) and *apo* MIZ1^{BTB} (right). Fraction numbers are indicated above; M denotes a molecular weight marker.

Nevertheless, I aimed to test whether MIZ1$^{1-282}$ ubiquitination could be detected in the presence of Fl-HUWE1. To this end, I initially compared UBCH7 and UBCH5B to see which E2 enzyme works best with Fl-HUWE1. Although the overall MIZ1$^{1-282}$ ubiquitination by Fl-HUWE1 was weak, I detected slightly higher activity with UBCH5B than UBCH7 (**Figure 37A**), which is in agreement with cell-based reactivity profiles of activity-based probes, based on these two E2s [168]. Therefore, all further MIZ1$^{1-282}$ ubiquitination assays with Fl-HUWE1 were carried out with UBCH5B. In my hands, MIZ1$^{1-282}$ was mainly mono-ubiqutinated by Fl-HUWE1, while additional higher molecular bands orginated, at least in part, from impurities in the Fl-HUWE1 sample (compare with the minus-ATP lane)

rather than multi- or polyubiuitination (**Figure 37B**). Additional analyses of AS^C-binding-deficient variants of MIZ1 (section 4.5), e.g., V60P, with Fl-HUWE1 remained inconclusive, with material availability presenting a major bottleneck for repeating and quantifiying the initial data (**Figure 37B**).
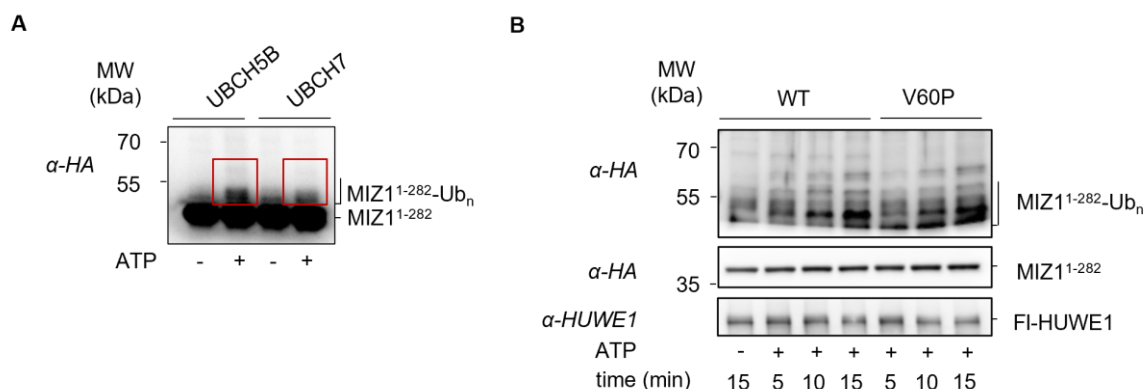
Figure 37: MIZ1$^{1-282}$ is mainly monoubiquitinated by Fl-HUWE1.
(A) Analysis of the MIZ1$^{1-282}$ (aa 1-282, C-terminal HA-His$_6$-tag) ubiquitination by Fl-HUWE1 (C-terminal Strep-tag; provided by I. Grishkovskaya and D. Haselbach, IMP Vienna). MIZ1$^{1-282}$ and Fl-HUWE1 were incubated at 37 °C with UBA1 (E1 enzyme), UBCH5B or UBCH7 (E2 enzyme), ubiquitin, MgCl$_2$ and with or without ATP. The reaction was stopped with SDS-loading after 30′. Samples were loaded on SDS-PAGE, followed by anti-HA Western blot (for MIZ1$^{1-282}$). (B) Analysis of the MIZ1$^{1-282}$ WT or V60P (aa 1-282, C-terminal HA-His$_6$-tag) ubiquitination by Fl-HUWE1 (C-terminal Strep-tag; provided by I. Grishkovskaya and D. Haselbach, IMP Vienna), following the protocol as described in (A) with some optimization (with UBCH5B as E2; incubation at 37 °C for the indicated endpoints; Western blots for MIZ1$^{1-282}$ input and MIZ1$^{1-282}$-Ub$_n$ were developed separately). Samples were loaded on SDS-PAGE, followed by anti-HA Western blot (for MIZ1$^{1-282}$) and anti-HUWE1 Western blot.

A plausible explanation for the rather weak ubiquitination activity of Fl-HUWE1 was the presence of a C-terminal Strep-tag in this construct. C-terminal tagging of HECT domains has previously shown to be inactivating [118]. Furthermore, I used a C-terminally truncated MIZ1 construct (aa 1-282) rather than full-length MIZ1 as a substrate, which contains only one, and potentially suboptimal, ubiquitination site (K135). While I chose the truncated MIZ1 construct for ease of preparation, future studies should test the full-length protein. Additionally, the affinities of MIZ1$^{1-282}$ and full-length MIZ1, respectively, for Fl-HUWE1 ought to be compared. Finally, it should be noted that all previous studies reporting interactions between full-length MIZ1 and N-terminally truncated HUWE1 (aa 2474-4374) or Fl-HUWE1 relied on cell-based methods, leaving open the possibility that third factors stabilize the interaction in the cell [228], [230]. The lack of such factors in my *in vitro*

experiments may also account for the difficulty to observe an interaction in my preliminary SEC analysis (**Figure 36**).

I thus set out to (i) monitor the interaction of full-length MIZ1 with different truncated HUWE1 constructs and Fl-HUWE1 in cell-based studies; (ii) clarify, whether their cellular interaction is mediated by the MIZ1-BTB-domain, as shown in my *in vitro* studies and previous studies [228]; and (iii) interrogate the effect of structure-guided mutations (section 4.5) in $MIZ1^{BTB}$ and AS^C in the context of the cell. These studies will be described in the following sections.

4.7 The HUWE1-MIZ1 interaction is detectable in cells and mediated by the MIZ1-BTB-domain.

To confirm that the HUWE1-MIZ1 interaction observed crystallographically (**Figure 28A**) exists in the cellular context I performed co-Immunoprecipitation (co-IP) experiments with HUWE1^{AS} and full-length MIZ1 (Fl-MIZ1). Upon transient transfection of HA-HUWE1^{AS} and with Flag-tagged Fl-MIZ1 in HeLa cells, HUWE1^{AS} co-immunoprecipitated with Fl-MIZ1 (**Figure 38A**) (for details, see 3.2.2 or 3.3.12, respectively). In contrast, no binding was observed when using a N-terminally truncated MIZ1 construct (aa 105-803) that lacks the BTB domain, confirming that the BTB domain is required for the MIZ1-HUWE1^{AS} interaction (**Figure 38A**). Next, I used a N-terminally extended HUWE1 construct, known as deltaN (dN)-HUWE1 (aa 2474-4374) [228]. Before the Fl-HUWE1 structure was published [129], dN-HUWE1 had been used in lieu of Fl-HUWE1, since it showed better exogenous expression levels [228]. However, considering the newly-discovered capacity of Fl-HUWE1 to form a ring-shaped structure, the boundary of the dN-HUWE1 construct appears problematic. Therefore, the following experiments performed with dN-HUWE1 may not present the properties of Fl-HUWE1 and have thus to be treated with caution.

The Western blot (**Figure 38B**) confirmed the interaction between dN-HUWE1 and Fl-MIZ1, and revealed that this interaction is mediated predominantly by the BTB domain of MIZ1 (**Figure 38C**), as shown previously [228]. It should be noted, however, that a small amount of dN-HUWE1 co-precipitates with MIZ1$^{\Delta BTB}$. Co-IP analyses of Fl-HUWE1 and MIZ1$^{\Delta BTB}$ also showed a reduced binding compared to Fl-MIZ1, but only to ~ 50 % (preliminary experiment with n = 1; **Figure 38D**). This

114

indicates that the BTB domain is important for the interaction of MIZ1 with Fl-HUWE1, but there are either other regions of MIZ1 involved in the interaction or the interaction is stabilized by an additional BTB domain-independent protein in the cell. It is conceivable, for instance, that MYC may have such a stabilizing function, since it interacts with both HUWE1 and the zinc-finger region of MIZ1. To investigate such a scenario and identify the set of overlapping interaction partners of HUWE1 and MIZ1, interaction-proteomic analyses would be required.
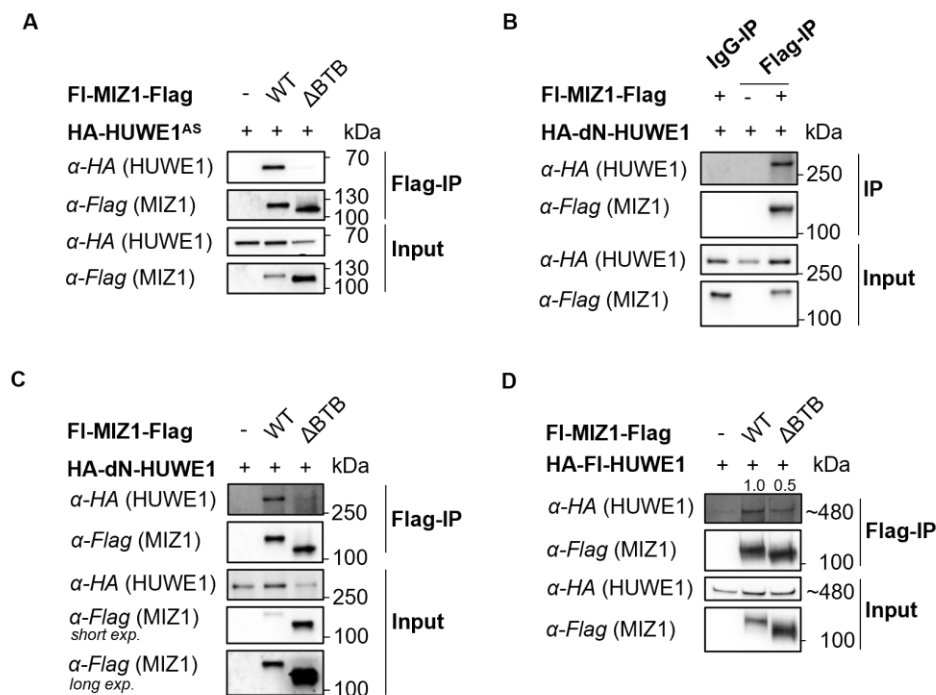
Figure 38: An interaction between Fl-MIZ1 and N-terminally truncated HUWE1 constructs or Fl-HUWE1 is confirmed by co-Immunoprecipitation in mammalian cells and depends on the BTB domain of MIZ1.
(A) Co-IP analyses of transiently transfected Fl-MIZ1 (C-terminal Flag-tag) or MIZ1$^{\Delta BTB}$ (aa 105-803, C-terminal Flag-tag) with HUWE1^{AS} (aa 3843-4374, N-terminal HA-tag) in HeLa cells, monitored by anti-Flag (for MIZ1) or anti-HA (for HUWE1) Western blotting. The first lane with only HA-HUWE1^{AS} overexpressed serves tests for unspecific binding. (B) Co-IP perfomed as in (A), reporting on the interaction between Fl-MIZ1 and HA-dN-HUWE1 (aa 2474-4374, N-terminal HA-tag). An IP with IgG served as a negative control. (C) Co-IP performed as in (A), reporting on the interaction between Fl-MIZ1 or MIZ1$^{\Delta BTB}$ (aa 105-803, C-terminal Flag-tag) and HA-dN-HUWE1 (aa 2474-4374, N-terminal HA-tag). (D) Co-IP performed as in (A), but in HEK293T cells, and HA-HUWE1^{AS} was substituted by HA-Fl-HUWE1 (N-terminal HA-tag).

By performing the co-IP *vice versa*, i.e. pull-down of HA-dN-HUWE1 or HA-Fl-HUWE1, followed by anti-Flag Western blotting to detect Fl-MIZ1, a HUWE1-MIZ1 interaction was also confirmed (**Figure 39A and B**). In addition, exogenously expressed Fl-MIZ1 could be detected after pull-down of endogenous

HUWE1 (**Figure 39C**). Since I aimed to test protein variants of MIZ1 and HUWE1, I focused on transient transfection (rather than monitoring endogenous protein) in the following experiments and on Flag-IP rather than HA-IP for it had proved more efficient in my hands.

Figure 39: An interaction between Fl-MIZ1 and dN-HUWE1 or Fl-HUWE1 is confirmed by co-IP of transiently transfected Fl-MIZ1 with endogenous HUWE1.
(A) Co-IP analyses of transiently transfected Fl-MIZ1 (C-terminal Flag-tag) with HA-dN-HUWE1 (aa 2474-4374, N-terminal HA-tag) in HeLa cells, monitored by anti-Flag (for MIZ1) or anti-HA (for HUWE1) Western blotting. The first lane with only HA-dN-HUWE1 overexpressed serves tests for unspecific binding. (B) Co-IP perfomed as in (A), but in HEK293T cells, and HA-HUWE1^{AS} was substituted with HA-Fl-HUWE1 (N-terminal HA-tag). (C) Co-IP analyses of transiently transfected Fl-MIZ1 (C-terminal Flag-tag) with endogenous HUWE1 in HEK293T, monitored by anti-Flag (for MIZ1) or anti-HUWE1 Western blotting.

4.8 Cell-based studies in the context of HUWE1^{AS} and Fl-MIZ1 support the novel interaction mode observed crystallographically.

To validate the atypical binding mode seen crystallographically (**Figure 28A**, sections 4.3-4.5) in the context of Fl-MIZ1 and HUWE1^{AS} in the cell, co-IP experiments were performed with the previously analyzed single-mutant variants (see section 4.5). **Figure 40A and B** show a representative experiment and quantification. Reduced binding of HUWE1^{AS} is observed for the Fl-MIZ1 variants F28A, L62A and I64A and minor effects (~ 80 % binding compared to the WT) for the F53A and V60P variants. Except for F53A, these are the same MIZ1 variants that showed reduced binding to the AS^C-peptide in the context of MIZ1^{BTB} (**Figure 32A**) and less MIZ1$^{1-282}$ ubiquitination by HUWE1^{AS} *in vitro* (**Figure 34B and C**). The L52A and H61A variants behave similarly to the WT in co-IP analyses, which is also in line with my previous *in vitro* results. Co-IP experiments using variants of HUWE1^{AS} are also in line with the *in vitro* studies (**Figure 33, Figure 35**, section 4.5): The HUWE1^{AS} single-mutant variants L3877A and F3887A show reduced binding to Fl-MIZ1 (~ 60 %) compared to the WT. For

the double mutant, HUWE1[AS] L3877A/F3887A, the interaction with Fl-MIZ1 is completely abolished, whereas HUWE1[AS] V3883A (the negative control) resembles the WT (**Figure 40C and D**). Therefore, these results confirm the atypical peptide binding mode that I had observed crystallographically and validated *in vitro,* in the context of the cells. They further show that the identified binding interface is relevant in the context of Fl-MIZ1, which was not analyzed *in vitro*.
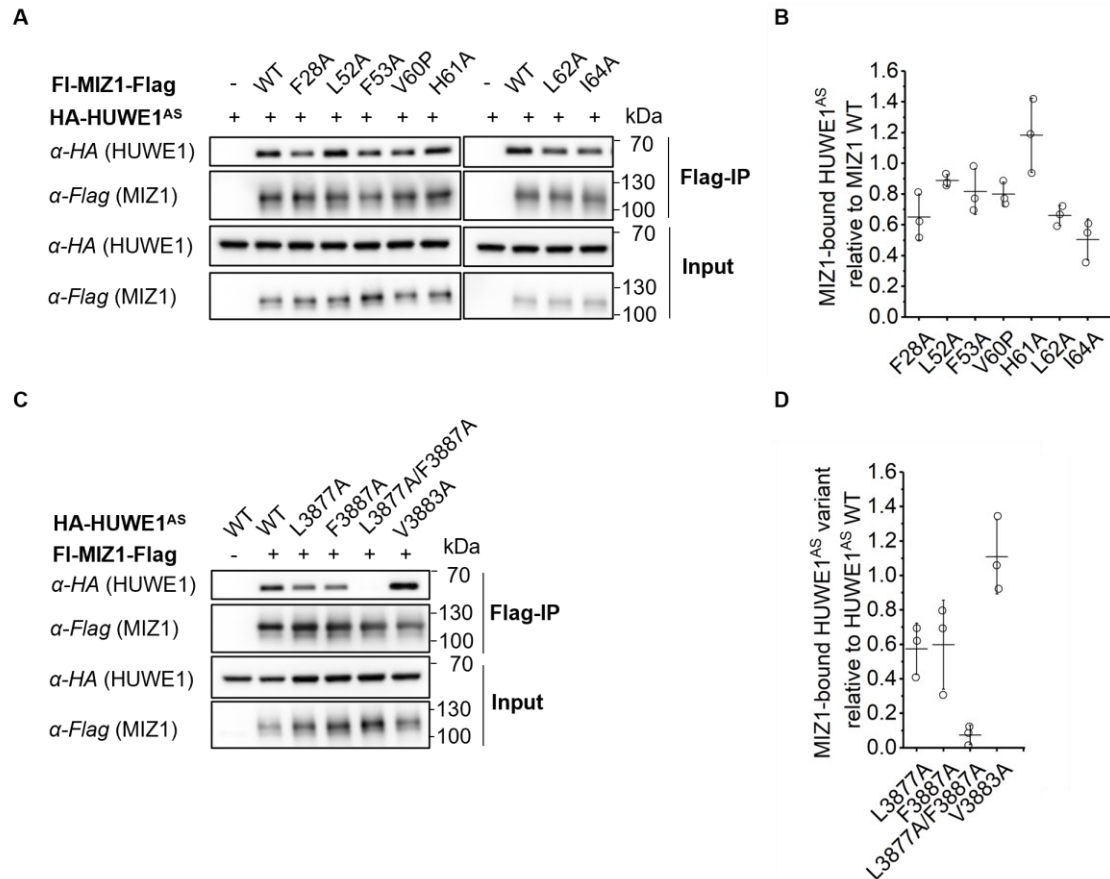
Figure 40: Cell-based co-IP experiments with HUWE1[AS] and Fl-MIZ1 support the atypical binding mode observed crystallographically.
(A) Co-IP of transiently transfected HA-HUWE1[AS] (aa 3843-4374, N-terminal HA-tag) with Fl-MIZ1 WT (C-terminal Flag-tag) or a single mutant variant thereof in HeLa cells, monitored by anti-Flag (for MIZ1) or anti-HA (for HUWE1) Western blotting. The first lane with only HA-HUWE1[AS] overexpressed serves tests for unspecific binding. (B) Quantification of co-IPed HA-HUWE1[AS], normalized to IPed Fl-MIZ1-Flag. The mean and SDs of three independent experiments are represented. The efficiency of co-IP was plotted relative to Fl-MIZ1-Flag WT (i. e., WT = 1). (C) Co-IP performed as in (A) but upon overexpression of different HA-HUWE1[AS] variants instead of Fl-MIZ1-Flag variants. (D) Quantification and representation of the mean and SDs, as described in (B), based on three independent experiments, normalized to HA-HUWE1[AS] WT = 1.

4.9 The interaction of Fl-MIZ1 with dN-HUWE1 or Fl-HUWE1 in cells is in line with the atypical binding site in MIZ1 observed crystallographically.

I next investigated whether the identified binding site in the BTB domain of MIZ1 holds in the context of Fl-MIZ1 and dN-HUWE1 (aa 2474-4374) or Fl-HUWE1 in the cell. To this end, I conducted co-IP experiments, as described in section 4.8, with these N-terminally extended HUWE1 constructs. These studies show that the Fl-MIZ1 variants F28A, L62A and I64A have reduced binding to dN-HUWE1 (< 80 %) compared to the WT (**Figure 41**), in line with previous results (section 4.5 and 4.8). Interestingly, the V60P variant showed less than ~ 30 % binding to dN-HUWE1 compared to the WT. Moreover, the L52A, F53A and H61A variants showed less than ~ 60 % binding to dN-HUWE1 compared to the WT (**Figure 41**), even though they showed WT-like behavior in my *in vitro* assays. This indicates that dN-HUWE1 binds at the upper β-sheet of MIZ1^{BTB}, as observed previously, and is therefore sensitive to mutations at this site. However, in the context of Fl-MIZ1 and the cellular environment, additional regions appear to become relevant for the interaction. It is likely that the contribution of the activation segment to binding of MIZ1^{BTB} changes in the context of dN-HUWE1 compared to HUWE1^{AS}. It is also possible that dN-HUWE1 contains an additional hydrophobic sequence which binds to the upper β-sheet of the MIZ1^{BTB}-domain, but in a distinct way from the activation segment. These hypotheses can be evaluated in detail when the structure of full-length HUWE1 [129] will be released.

Finally, I tested binding of the Fl-MIZ1 variants F28A and V60P to Fl-HUWE1 (**Figure 42**). Indeed, both variants showed reduced binding, indicating that the interaction requires the upper β-sheet of the MIZ1-BTB-domain, in line with all previous assays. Which additional interfaces between HUWE1 and MIZ1 stabilize this interaction requires further investigation.
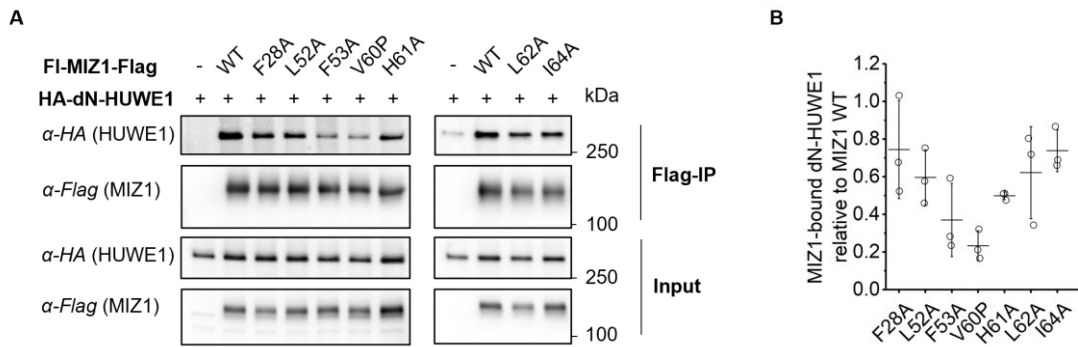
Figure 41: Cell-based co-IP experiments with dN-HUWE1 and Fl-MIZ1 or variants thereof support the atypical binding site in MIZ1^BTB observed crystallographically.
(A) Co-IP analyses of transiently transfected HA-dN-HUWE1 (aa 2474-4374, N-terminal HA-tag) with Fl-MIZ1 WT (C-terminal Flag-tag) or a single mutant variant thereof in HeLa cells, monitored by anti-Flag (for MIZ1) or anti-HA (for HUWE1) Western blotting. The first lane with only HA-dN-HUWE1 overexpressed serves tests for unspecific binding. (B) Quantification of co-IPed HA-dN-HUWE1, normalized to IPed Fl-MIZ1-Flag. The mean and SDs of three independent experiments are represented. The efficiency of co-IP was plotted relative to Fl-MIZ1-Flag WT (i. e., WT = 1).

Figure 42: Cell-based co-IP experiments with Fl-HUWE1 and Fl-MIZ1 or variants thereof support the atypical binding site in MIZ1^BTB observed crystallographically.
(A) Co-IP analyses of transiently transfected HA-Fl-HUWE1 (N-terminal HA-tag) with Fl-MIZ1 WT (C-terminal Flag-tag) or a single mutant variant thereof in HEK293T cells, monitored by anti-Flag (for MIZ1) or anti-HA (for HUWE1) Western blotting. The first lane with only HA-Fl-HUWE1 overexpressed serves tests for unspecific binding. (B) Quantification of co-IPed HA-Fl-HUWE1, normalized to IPed Fl-MIZ1-Flag. The mean and SDs of three independent experiments are represented. The efficiency of co-IP was plotted relative to Fl-MIZ1-Flag WT (i. e., WT = 1).

4.10 dN-HUWE1 and Fl-HUWE1 likely contain several binding sites for MIZ1.

Besides the MIZ1 variants described above, I also analyzed the interactions of dN-HUWE1 (aa 2474-4374) and Fl-HUWE1 variants in cell-based co-IP experiments. **Figure 43** summarizes these results: Although a small reduction in binding of the L3877A and L3877A/F3887A variants to Fl-MIZ1 compared to the WT was seen in certain individual experiments (**Figure 43A**), this effect was no longer supported upon replication and quantification of the data (**Figure 43B**).

Moreover, the L3877P/F3887P variant, designed to disrupt the β-strands seen for the isolated AS, binds to Fl-MIZ1 with the same efficiency as the WT. Finally, the deletion of AS^C (aa 3870-3890) in the context of dN-HUWE1 did not disrupt the interaction with Fl-MIZ1 (**Figure 43C and D**).
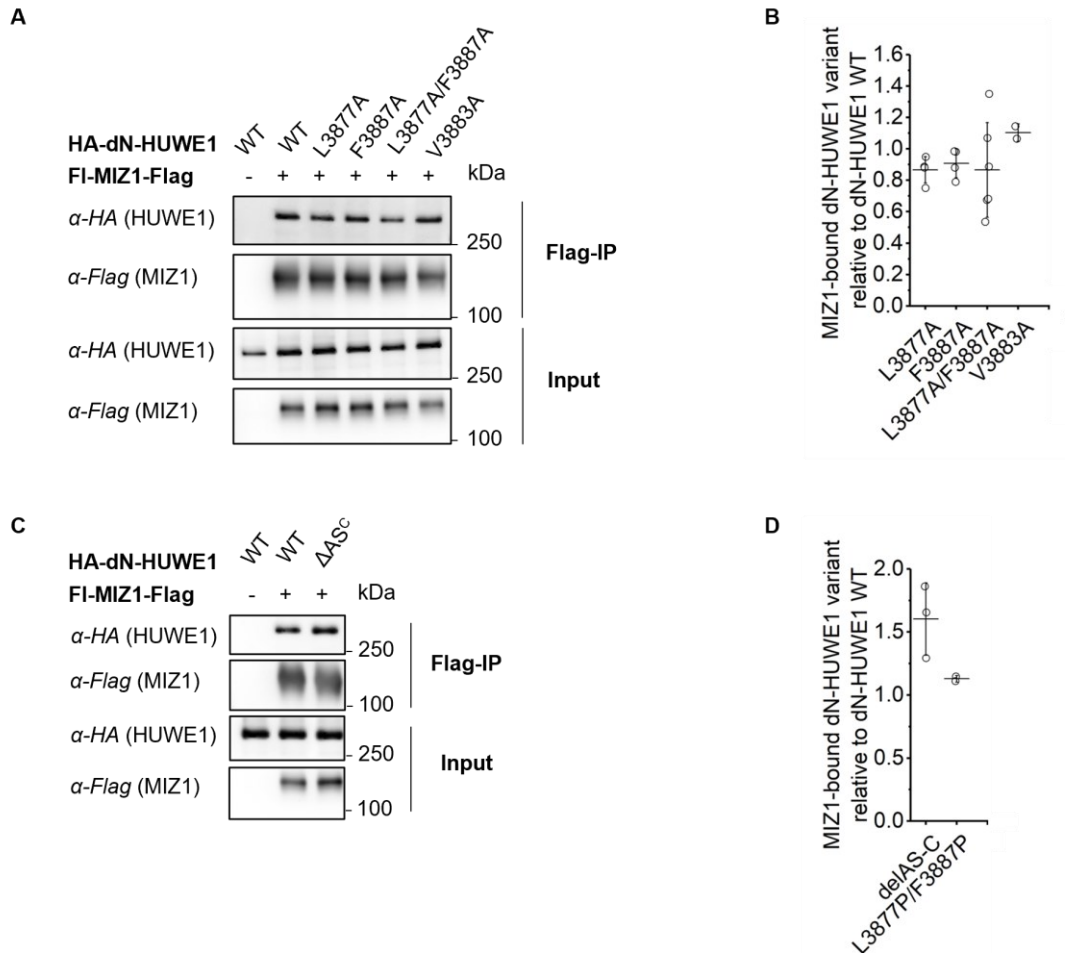
Figure 43: In the context of dN-HUWE1, the activation segment does not appear to mediate the interaction with Fl-MIZ1.
(A) Co-IP analyses of transiently transfected HA-dN-HUWE1 WT (aa 2474-4374, N-terminal HA-tag) or variants thereof with Fl-MIZ1 WT (C-terminal Flag-tag) in HeLa cells, monitored by anti-Flag (for MIZ1) or anti-HA (for HUWE1) Western blotting. The first lane with only HA-dN-HUWE1 overexpressed serves tests for unspecific binding. (B) Quantification of co-IPed HA-dN-HUWE1 WT or a single mutant variant, respectively, normalized to IPed Fl-MIZ1-Flag. The mean and SDs of three independent experiments are represented. The efficiency of co-IP was plotted relative to HA-dN-HUWE1 WT (i. e., WT = 1). (C) Co-IP performed as in (A), reporting on the interaction between Fl-MIZ1 and HA-dN-HUWE1 or a deletion variant thereof, HA-dN-HUWE1 ΔAS^C (aa 2474-4374 Δ3870-3890, N-terminal HA-tag). (D) Quantification of co-IPed HA-dN-HUWE1 WT or a mutant variant or deletion variant thereof, normalized to IPed Fl-MIZ1-Flag. The mean and SDs of three independent experiments are represented. The efficiency of co-IP was plotted relative to HA-dN-HUWE1 WT (i. e., WT = 1). For HA-dN-HUWE1 L3877P/F3887P, only the quantification without the corresponding Western blot is shown due to other, unrelated samples being analyzed in the respective Western blot.

120

The L3877A, L3877A/F3887A variants, V3883A as a negative control, and the deletion construct ΔAS^C (Δ aa 3870-3890) of Fl-HUWE1 also did not show any reduction in binding to Fl-MIZ1 (preliminary experiment with n = 1; **Figure 44**). These results are somewhat not surprising in the light of the recently published Fl-HUWE1 structure [129]. Based on this, it is conceivable that mutations or deletion of the AS may disrupt the structural integrity of HUWE1, thereby resulting in a dysfunctional protein. However, such disruption of the fold may also expose hydrophobic regions, rendering the protein 'sticky' and giving rise to unspecific binding. My mutational analyses of Fl-HUWE1 are therefore hard to interpret at this point. It is important to note, however, that my analyses are in line with an important aspect that Hunkeler et al. propose [129]: They envision HUWE1 to utilize several alternative, weak binding sites to recruit substrates rather than a distinct binding site for each. Building on this idea, it is possible that the BTB domain of MIZ1 binds to HUWE1 via the upper β-sheet, as identified by my studies, while also utilizing additional regions to strengthen the interaction. This would explain my observation that additional residues of MIZ1 become relevant in the context of the full-length proteins in the cell, while only the upper β-sheet is required when studying protein fragments *in vitro*. If and how parts of the AS contribute to such an interaction requires further inspection. This will be particularly interesting since Hunkeler et al. have observed large conformational flexibility in Fl-HUWE1, with a ring-shaped structure co-existing with open/extended forms. The factors regulating these conformational dynamics and the relevance of distinct states for the interaction and modification of MIZ1 will be an exciting area of future study.
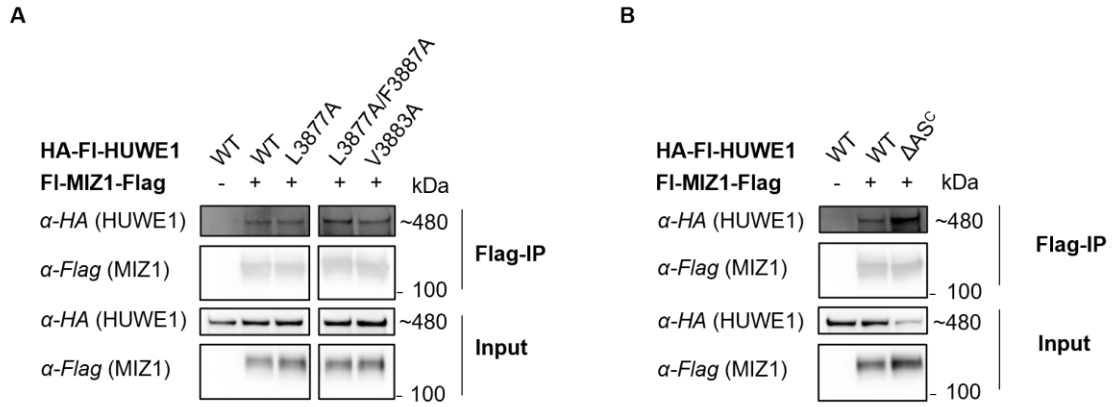
Figure 44: Preliminary experiment (n=1) indicates that the activation segment does not mediate the interaction with Fl-MIZ1 in the context of Fl-HUWE1.
(A) Co-IP analyses of transiently transfected HA-Fl-HUWE1 (N-terminal HA-tag) or a mutant variant thereof with Fl-MIZ1 WT (C-terminal Flag-tag) in HEK293T cells, monitored by anti-Flag (for MIZ1) or anti-HA (for HUWE1) Western blotting. The first lane with only HA-Fl-HUWE1 overexpressed serves tests for unspecific binding. HA-Fl-HUWE1 WT and variants thereof were analyzed on the same Western blot. An unrelated sample loaded in the middle was removed. Therefore, HA-Fl-HUWE1 L3877A/F3887A and V3883A are shown as separate panels. (B) Co-IP performed as in (A), reporting on the interaction between Fl-MIZ1 and HA-Fl-HUWE1 or a deletion variant thereof, HA-Fl-HUWE1 ΔAS^C (aa 1-4374 Δ3870-3890, N-terminal HA-tag).

4.11 Preliminary search for other putative MIZ1 binding sites in HUWE1

As neither the single-mutant variants nor the deletion of the activation segment (aa 3870-3890) showed an effect on the interaction of MIZ1 with dN-HUWE1 (aa 2474-4374) and Fl-HUWE1, respectively, in cells (section 4.10), I started a preliminary search for other MIZ1 binding sites N-terminally to the activation segment. Note, that these studies were based on secondary structure predictions before the cryo-EM structure of Fl-HUWE1 was published [129, 428]. My previous observation that the HUWE1^{AS} variants showed a reduction, but not an abrogation of binding to MIZ1 (section 4.5 and 4.8) suggested that the additional N-terminal sequence (aa 2474-3842) of dN-HUWE1 (aa 2474-4374) compared to HUWE1^{AS} (aa 3843-4374) might include a MIZ1 binding site. Yi et al. showed that a HUWE1 fragment comprising aa 2364-3665 can be exogenously expressed in mammalian cells [275]. Since this construct covered most of the sequence I was interested in, I decided to use it for further analyses. Notably, however, the fragment contains large unstructured regions (~ 50 %), so the data I obtained for this construct ought to be treated with caution. Based on the available full-length HUWE1 structure, these unstructured regions serve as linker to connect the 'tower' (aa 2641-2696) of the 'WWE module' with 'UB module 2' (aa 2951-3100) and this with the N-terminal

part of ARLD4 (aa 3179-4374) [129]. HUWE1 aa 2364-3665 could be coIPed with Fl-MIZ1, but not Fl-MIZ1$^{\Delta BTB}$, indicating that this interaction depends on the MIZ1-BTB-domain. To investigate whether this interaction also involves the upper β-sheet of MIZ1^{BTB} (see **Figure 28A**), I tested the structure-based mutations in *MIZ1* I had previously characterized (section 4.5). Indeed, reduced binding is observed for F28A, V60P, H61A, (L62A), and I64A (**Figure 45**), which were also required for the MIZ1^{BTB}-AS^C-peptide interaction. Moreover, L52A and F53A showed WT-like binding (**Figure 45**), which is also in line with my previous results.
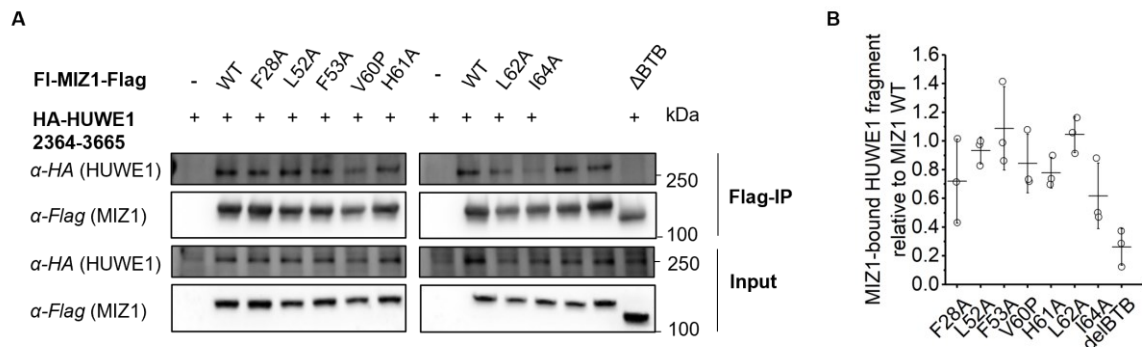
Figure 45: Fl-MIZ1 appears to bind to aa 2364-3665 of HUWE1 via the BTB domain.
(A) Co-IP analyses of transiently transfected HA-HUWE1 (aa 2364-3665, N-terminal HA-tag) with Fl-MIZ1 WT (C-terminal Flag-tag) or a single mutant variant thereof in HeLa cells, monitored by anti-Flag (for MIZ1) or anti-HA (for HUWE1) Western blotting. The first lane with only HA-HUWE1 (aa 2364-3665) overexpressed serves tests for unspecific binding. The two unlabeled lanes in the right panel include variants that are not relevant in this context and therefore are not discussed. (B) Quantification of co-IPed HA-HUWE1 (aa 2364-3665), normalized to IPed Fl-MIZ1-Flag. The mean and SDs of three independent experiments are represented. The efficiency of co-IP was plotted relative to HA-HUWE1 (aa 2364-3665) (WT = 1).

Assuming that parts of the HUWE1 fragment containing aa 2364 to 3665 interact with the upper β-sheet of MIZ1^{BTB} as seen in the crystal structure of the MIZ1^{BTB}-AS^C complex (**Figure 28A**), I searched for a sequence between aa 2364 and 3665 that adopts a similar binding mode as AS^C. Based on a sequence aligment of AS^C (aa 3870-3890) with HUWE1 aa 2364-3665, I noticed that a stretch comprising amino acids 2960 to 2975 (unstructured region connecting 'tower' and 'UB module 2' in the full-length HUWE1 cryo-EM structure [129]) resembles AS^C in terms of charge distribution and hydrophobicity. For example, both regions have two hydrophobic residues separated by 9 residues, which may allow for the interaction with Phe 28 in the two subunits of the MIZ1^{BTB} dimer (see **Figure 28A and B**). To test the hypothesis, I mutated these two residues,

Ile 2962 and Phe 2972, which are at homologous positions to Leu 3877 and Phe 3887 in AS^C, to alanine and tested their binding capacity to Fl-MIZ1 by co-IP experiments in HeLa cells. However, neither in the context of aa 2364-3665 nor in dN-HUWE1 did these variants show impaired binding to Fl-MIZ1; both, a double-mutant (I2962A/F2972A) and a quadruple-mutant variant (I2962A/F2972A/L3877A/F3887A) were tested (**Figure 46**).
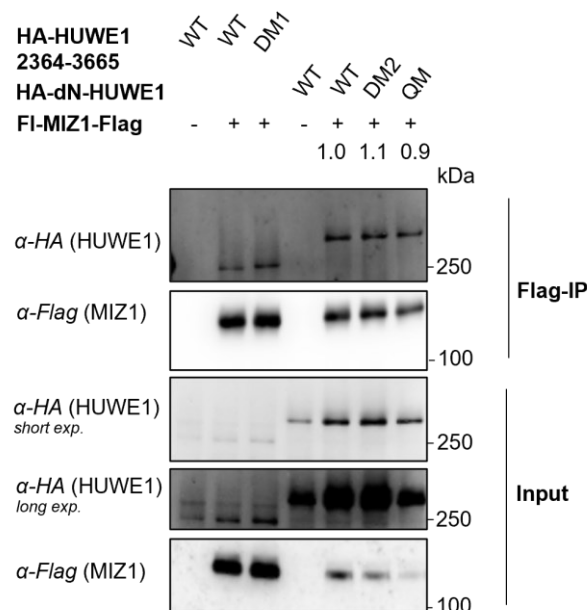
Figure 46: Ile 2962 and Phe 2972 are not necessary for the interaction of HA-HUWE1 (aa 2364-3665) to Fl-MIZ1.
Co-IP analyses of transiently transfected HA-HUWE1 (aa 2364-3665, N-terminal HA-tag) and mutant variants thereof (DM1: I2962A/F2972A) or HA-dN-HUWE1 (aa 2474-4374, N-terminal HA-tag) and mutant variants thereof (DM2: L3877A/F3887A; QM: I2962A/F2972A/L3877A/F3887A) with Fl-MIZ1 WT (C-terminal Flag-tag) in HeLa cells, monitored by anti-Flag (for MIZ1) or anti-HA (for HUWE1) Western blotting. The lanes with only HA-HUWE1 (aa 2364-3665) or dN-HUWE1 (aa 2474-4374) overexpressed serve tests for unspecific binding; 'exp.' denotes exposure time; the indicated values at the top show the quantification of co-IPed HA-dN-HUWE1, normalized to immunoprecipitated Fl-MIZ1-Flag, relative to HA-dN-HUWE1 (WT = 1).

I next performed an alignment excluding aa 2960-2975 of HUWE1 (aa 2364-3665), which led me to identify an additional region (aa 3323-3349; a region that is part of ARLD4 (aa 3179-4374) in the full-length HUWE1 cryo-EM structure [129]) with resemblance to AS^C, based on the above-mentioned criteria. Subsequent alignments excluding both aa 2960-2975 and aa 3323-3349, identified yet another putative MIZ1-binding region, comprising aa 3023 to 3036 (part of UB module 2 in the full-length HUWE1 cryo-EM structure [129]). I then deleted these three regions in the context of the HUWE1 (aa 2364-3665) construct, either

individually, in pairs, or simultaneously, but found that all constructs still interacted with Fl-MIZ1 by co-IP (**Figure 47A**). To rule out that the observed interaction is unspecific due to the putative 'sticky' nature of HUWE1 (aa 2364-3665), the same deletions were introduced into dN-HUWE1 with or without additional deletion of the activation segment. Yet, neither deletion impaired the binding of dN-HUWE1 to Fl-MIZ1 (**Figure 47B**). This likely indicates that the tested segments are not required for MIZ1 binding. As mentioned above, it is important to note, however, that all analyses performed in the context of dN-HUWE1 are comprised by the inability of this fragment to adopt a native, ring-shaped structure, which may be essential for native interactions and activity of Fl-HUWE1.
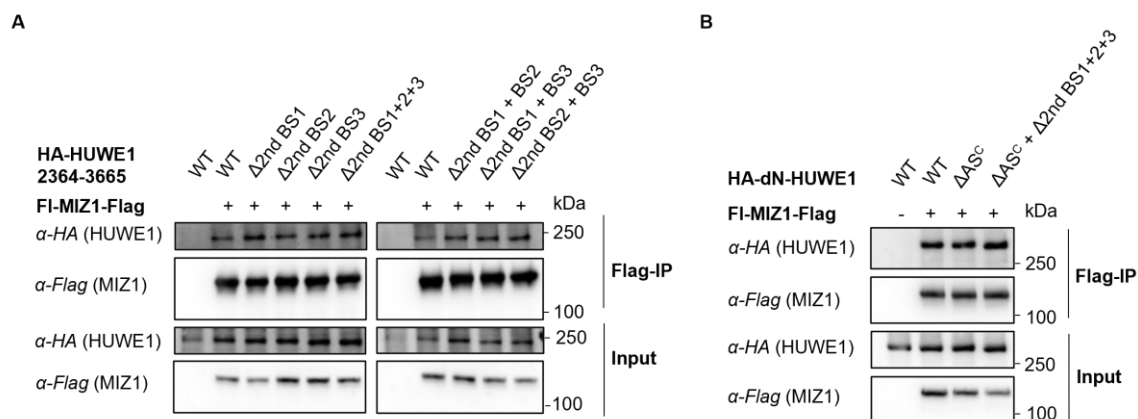
Figure 47: Depletion of predicted MIZ1-binding sites in HUWE1 aa 2364-3665 with sequence similarity to AS^C do not diminish binding to Fl-MIZ1.
(A) Co-IP analyses of transiently transfected HA-HUWE1 (aa 2364-3665, N-terminal HA-tag) and deletion variants thereof with Fl-MIZ1 WT (C-terminal Flag-tag) in HeLa cells, monitored by anti-Flag (for MIZ1) or anti-HA (for HUWE1) Western blotting. The lanes with only HA-HUWE1 (aa 2364-3665) overexpressed serve tests for unspecific binding; '2nd' denotes the interrogation of a predicted, secondary binding site other than AS^C (aa 3870-3890); BS1: aa 2960-2975; BS2: aa 3023-3036; BS3: aa 3323-3349. (B) Co-IP performed as in (A), but in the context of HA-dN-HUWE1 (aa 2474-4374, N-terminal HA-tag).

4.12 Stability of the MIZ1 variants compared to MIZ1 WT in the cell

MIZ1 was reported to be ubiquitinated and targeted for proteasomal degradation by HUWE1 [230]. As a consequence, disrupting the HUWE1-MIZ1 interaction is expected to lead to a stabiliziation of MIZ1 in the cell. In initial, preliminary studies I exogenously expressed Fl-MIZ1 and monitored the MIZ1 levels in the presence and absence of dN-HUWE1. In the presence of dN-HUWE1 a reduction of the MIZ1 level dropped to ~ 60 % and can be rescued by the catalytically inactive

dN-HUWE1 variant C4341S (**Figure 48**). As the FI-MIZ1 variant V60P bound less than 30 % of dN-HUWE1 compared to the WT in co-IPs (**Figure 41**) I expected FI-MIZ1 V60P would be more stable than the WT. However, FI-MIZ1 V60P protein levels were comparable to the WT upon HUWE1 overexpression (**Figure 48**). Moreover, overexpression of the dN-HUWE1 variant L3877A/F3887A did not trigger MIZ1 stabilization (**Figure 48**, 3rd lane). The latter observation, however, is in line with the analyses discussed in section 4.10.
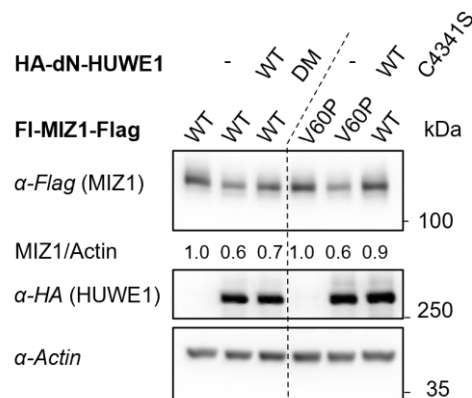
Figure 48: Structure-guided mutagenesis of FI-MIZ1 or dN-HUWE1 does not increase steady-state levels of MIZ1 in HeLa cells upon transient transfection.
Western blot monitoring FI-MIZ1-Flag WT or the single mutant variant V60P and HA-dN-HUWE1 (aa 2474-4374) WT, DM (L3877A/F3887A) or the catalytic inactive variant (C4341S) upon transient transfection in HeLa cells. Actin serves as loading control. MIZ1 levels were quantified and normalized to the corresponding actin amount.

To eliminate the background interaction of endogenous HUWE1 and MIZ1, I made use of MIZ1 knockout mouse embryonic fibroblasts (MEFs) stably expressing a BTB domain-deletion mutant of MIZ1 (kindly provided by Elmar Wolf (Biocenter, University Würzburg)) [294]. By lentiviral transduction we introduced FI-MIZ1 WT and the variants F28A, V60P and I64A, respectively, into these MEFs (in collaboration with Jessica Schwarz and Elmar Wolf; both Biocenter, University Würzburg). To analyze the effect of the mutations on MIZ1 stability in the presence of endogenous HUWE1 I performed a cycloheximide chase assay. A previous experiment with exogenous FI-MIZ1 and dN-HUWE1 yielded a half-life of approximately 9 hours for MIZ1 WT (see also [429]). To reduce the number of samples to be analyzed, I initially focused on a 9-hour time point. (**Figure 49**). This experiment revealed markedly different starting concentrations of the various MIZ1 variants, which may indicate differences in the efficiency of lentiviral transduction (rather than differences in protein stability). Taking the different input levels of the MIZ1 variants into account, I was not able to observe a difference in protein

stability during the cycloheximide chase. However, to make a robust statement, more time points and/or replicates would be required. In the light of more pressing analyses of full-length HUWE1, I decided not to pursue these analyses further.
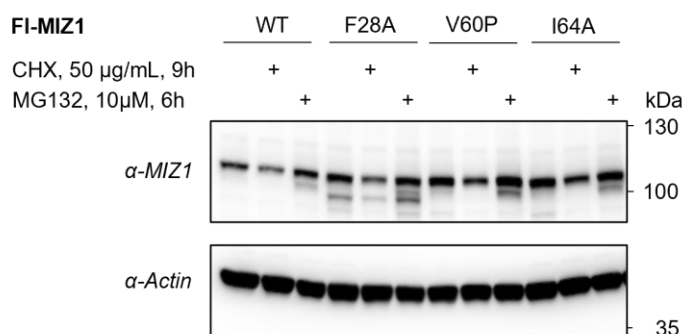
Figure 49: Preliminary experiment (n=1) analyzing the effect of mutations in the BTB domain of MIZ1 on protein stability in MEFs
Fl-MIZ1 WT or a single mutant variant thereof was expressed via lentiviral transduction in MIZ1^{BTB}-depleted MEF cells. 9h prior to harvesting, cells were treated with 50 µg/mL cycloheximide (CHX) or ethanol (first lane of WT or single mutant variant) or 6h prior harvesting, with 10 µM of the proteasome inhibitor MG-132. Total cell lysates were analyzed by anti-MIZ1 and anti-actin Western blot. Actin served as loading control.

4.13 HUWE1 AS^C-peptide selectively binds to the MIZ1 homodimer over heterodimers or a monomer *in vitro*.

Finally, I wanted to understand how the oligomerization state of MIZ1 affects the atypical peptide mode I had characterized. In other words, I addressed the question of how binding specificity is induced by the atypical conformational flexibility of the B3-region in MIZ1^{BTB}. The HUWE1 AS^C-peptide serves as an example to address this question rather than as a means to study the biological relevance of this particular interaction.

As other members of the BTB-ZF family, MIZ1 does not only form homodimers, but also heterodimers (section 1.6.4), e.g., with BCL6 and NAC1. By genetically fusing the C-terminus of MIZ1^{BTB} to the N-terminus of BCL6^{BTB} and NAC1^{BTB}, respectively by a Gly/Ser-rich linker the crystal structures of these heterodimers were solved (PDB: 4U2M, 4U2N) [386] (section 1.6.4). I used the same strategy to generate BTB domain heterodimers of MIZ1^{BTB} with BCL6^{BTB} and NAC1^{BTB}, respectively, and purified the two fusion proteins (for purification protocols, see 3.3.1 or 3.3.2, respectively; for the corresponding chromatograms and the purity of the eluted peak fractions, see Appendix 7.1.2). In addition, I generated a MIZ1^{BTB}

monomer by introducing four mutations (V10D/L14D/Q17D/V41K) at the dimer interface, analogously to a previously reported dimer-defective SPOP variant (L186D/L190D/L193D/I217K) [427]. Based on these protein variants I analyzed whether an intact homodimer is needed for binding to the AS^C peptide. Analytical SEC (**Figure 50A**) confirmed the dimeric state of the two heterodimers, which eluted similarly to homodimeric $MIZ1^{BTB}$. In contrast, the quadruple mutant of $MIZ1^{BTB}$ elutes later, confirming that the disruption of the dimer interface worked. (**Figure 50A**). Note that the different extinction coefficients of the different protein variants cause differences in the absorbance and, hence, the elution peak height, although equal protein amounts had been injected onto the column. In the next step, I tested the binding of the HUWE1-AS^C-peptide to the two heterodimers and the $MIZ1^{BTB}$-monomer by fluorescence polarization. I observed that the binding affinities for the heterodimers for the peptide are reduced to K_D-values of > 120 µM compared to the $MIZ1^{BTB}$ homodimer with a K_D-value of 10 ± 0.9 µM (**Figure 50B**, **Table S2**). This indicates that the peptide selects for the $MIZ1^{BTB}$ homodimer over heterodimers. On a structural level, this can be explained by the fact that the heterodimers contain a pre-formed B3-strand in the BCL6- or NAC1 subunit, which may interfere with peptide binding to the upper β-sheet of the BTB domain; the binding site in the MIZ1 homodimer may be more accessible (see **Figure 15** and **Figure 28A**) because it has a flexible B3-region in both subunits.
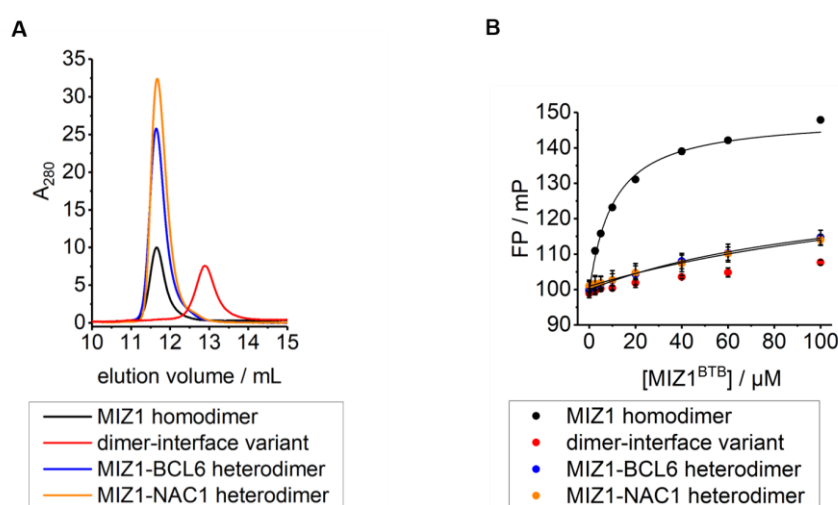
Figure 50: The HUWE1-AS^C-peptide selects for the $MIZ1^{BTB}$ homodimer over a monomer or heterodimers. For detailed figure legend see next page.

(A) SEC analysis to confirm the oligomerization state of the homodimeric MIZ1^{BTB} protein (aa 1-115, without N-terminal cloning overhang) and the MIZ1^{BTB}-BCL6^{BTB} (aa 2-115 of MIZ1^{BTB} and aa 5-129 of BCL6^{BTB})- and MIZ1^{BTB}-NAC1^{BTB} (aa 2-115 of MIZ1^{BTB} and aa 2-125 of NAC1^{BTB}) heterodimers as well as the monomeric dimer-interface variant (V10D/L14D/Q17D/V41K). The peak areas vary due to differences in the respective extinction coefficients, despite loading of equal amounts. (B) FP analysis of the interaction between the MIZ1^{BTB} variants analyzed in (A) and a C-terminally 5-FAM-labeled HUWE1-AS^C-peptide (aa 3870-3894, additional Lys residue inserted after aa 3894 prior to 5-FAM). The mean and SD of three independent experiments were fitted to a single-site binding model, where possible; for the corresponding K_D-values, see Table S2.

For the same reason, I expected that the HUWE1-peptide would not bind to the homodimeric, canonical KAISO^{BTB}-domain either, as analyzed in the following paragraph. The BTB-ZF protein KAISO was reported as substrate of HUWE1 (see 1.7) [390], [391], [392]. The available crystal structure of KAISO^{BTB} (PDB: 3M4T) shows pre-formed B3-strands in both subunits. I thus selected it as an additional test of my hypothesis on the selectivity of the newly identified binding mode. I cloned and purified the BTB domain of KAISO (for purification protocols, see 3.3.1 or 3.3.2, respectively; for the corresponding chromatograms and the purity of the eluted peak fractions, see Appendix 7.1.2) and confirmed that it forms a dimer by analytical SEC (**Figure 51A**). As expected, FP assays showed no interaction between KAISO^{BTB} and the HUWE1-AS^C-peptide (**Figure 51B**). In line with this, HUWE1^{AS} did not stimulate ubiquitination of KAISO^{BTB} *in vitro* over shorter HECT constructs (**Figure 51C**). Of note, the latter experiment only served as a control and does not have implications for the HUWE1-KAISO interplay in the cell, since the mutual interaction sites on either protein are unknown and the analyzed constructs are truncated.
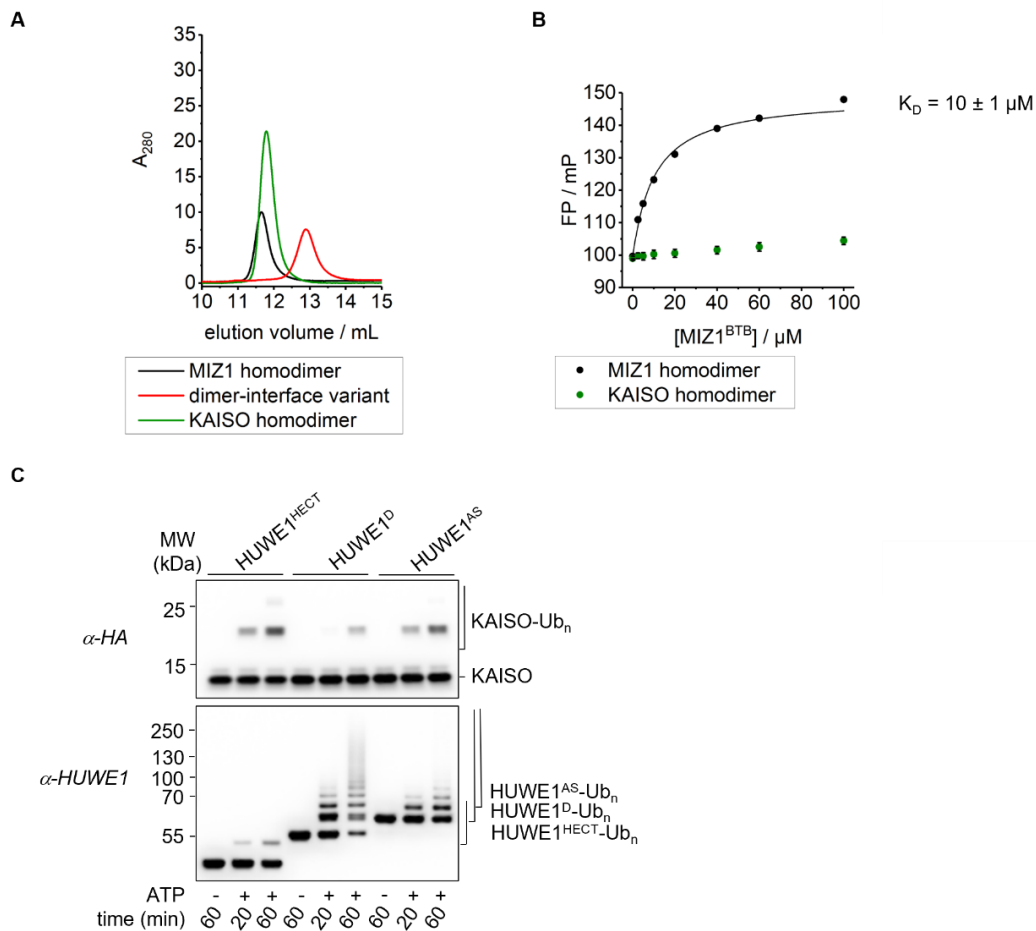
Figure 51: The KAISO^{BTB} homodimer does not interact with the HUWE1-AS^C-peptide.
(A) SEC analysis to confirm the oligomerization state of homodimeric KAISO^{BTB} (aa 1-122; based on PDB: 3M4T) relative to the MIZ1^{BTB} homodimer and the monomeric variant (V10D/L14D/Q17D/V41K). The peak areas vary due to differences in the respective extinction coefficients. (B) FP analysis of the interaction between the homodimeric MIZ1^{BTB} or KAISO^{BTB} (as described in (A)) and a C-terminally 5-FAM-labeled HUWE1-AS^C-peptide (aa 3870-3894, additional Lys residue inserted after aa 3894 prior to 5-FAM). The mean and SD of three independent experiments were fitted to a single-site binding model for MIZ1^{BTB} with a K_D-value of 10 ± 1 μM. The data for KAISO^{BTB} could not be fitted. (C) Analysis of KAISO^{BTB} (aa 1-122, C-terminal HA-tag) ubiquitination by three different N-terminally truncated HUWE1 constructs (HUWE1^{HECT}: aa 3993-4374, HUWE1^D: aa 3896-4374, HUWE1^{AS}: aa 3843-4374). KAISO^{BTB} and the indicated HUWE1 construct were incubated with UBA1 (E1-enzyme), UBCH7 (E2-enzyme), ubiquitin, MgCl$_2$ and with or without ATP. The reaction was stopped with SDS-loading dye after 20′ or 60′. Samples were loaded on SDS-PAGE, followed by anti-HA Western blot (for KAISO^{BTB}) or anti-HUWE1 Western blot, which served as loading control for the HUWE1-constructs used (analysis of the different levels of HUWE1 auto-ubiquitination depending on the extend of N-terminal truncation was part of another study, see [136]).

Taken together, the selectivity of the HUWE1-AS[C] peptide for the MIZ1 homodimer over heterodimers is likely enabled by the flexible B3-region. Whether this selectivity is part of a dimerization quality control system, as described by Michael Rape and colleagues for the E3-ligase SCF[FBXL17] (see 1.8) requires further investigation [401], [402]. To this end, it would be necessary to test my findings in the cellular context and determine under which conditions a selective destabilization of MIZ1 homodimers may be beneficial (see 5.2).

5 Conclusion and future perspectives

5.1 Peptide-induced upper β-sheet extension in MIZ1^{BTB} may offer opportunities toward the development of peptidomimetics or small-molecule inhibitors targeting MIZ1.

The cartoon shown in **Figure 52** finally summarizes the key result of this thesis. The functionally validated crystal structure of the homodimeric BTB domain of MIZ1 with a HUWE1-derived peptide revealed an atypical binding mode (**Figure 52A**). The mode is atypical in the sense that the peptide extends the upper β-sheet of MIZ1^{BTB}, which is likely facilitated by flexibility in the B3-region. In contrast, crystal structures of other BTB domains of BTB-ZF proteins show a pre-formed B3-strand at this position. This strand is mimicked by the peptide ligand in the MIZ1^{BTB} complex. Crystal structures of the canonical BTB domain of BCL6, however, have peptide ligands positioned at the lateral groove and extending toward the lower β-sheet that contains a β1-strand. (**Figure 52B**). Notably, this β1-strand is largely missing in MIZ1 (PDB: 3M52) [343] (even though part of it is mimicked by a cloning overhang in my crystal structures: PDB: 7AZW, PDB: 7AZX).
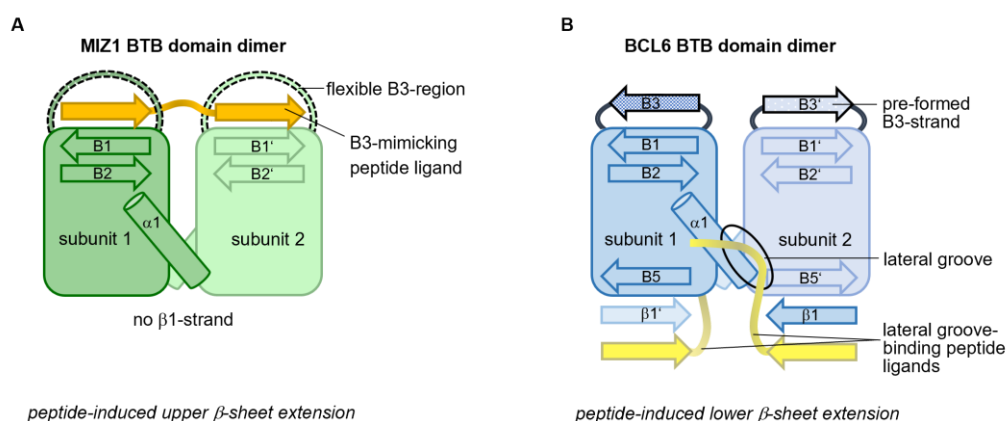
Figure 52: Flexible B3-region in MIZ1^{BTB} allows atypical peptide binding mode selective for the MIZ1^{BTB} homodimer.
(A) Cartoon representation of the the MIZ1^{BTB}-AS^C complex (this study, PDB: 7AZX). The homodimeric MIZ1-BTB-domain is represented in green (subunit 1) and palegreen (subunit 2). Secondary structure nomenclature according to Stogios et al. [343]. The orange HUWE1-AS^C-peptide mimics the pre-formed B3-strand observed in other BTB-domains (see (B)) and extends the upper B1/B2-β-sheet in the MIZ1^{BTB} homodimer (2:1 stoichiometry). (B) Cartoon representation of the BCL6^{BTB} homodimer in complex with co-repressor peptides (e.g. SMRT, BCoR, F1324; PDB: 1R2B, 3BIM, 5H7G, 5H7H) [346], [378], [379]. The homodimeric BCL6-BTB-domain is represented in blue (subunit 1) and light blue (subunit 2). Secondary structure nomenclature according to Stogios et al. [343]. The yellow co-repressor peptides extend the lower domain-swapped β-sheet with one peptide binding per subunit (1:1 stoichiometry) and bind to the lateral groove.

If such a binding mode holds in the context of full-length MIZ1, it may be specific for MIZ1, since neither MIZ1^{BTB} heterodimers, nor the monomeric MIZ1-BTB-domain or the KAISO^{BTB} homodimer could substitute the MIZ1^{BTB} homodimer with a similar binding affinity in my *in vitro* experiments. The relevance and specificity of the interface remains to be investigated in future cell-based studies. Yet, it is intriguing to think that the HUWE1-AS^C-peptide complex I determined may serve as an entry point for drug design to specifically interrupt interactions of MIZ1. As discussed above, it remains to be evaluated whether the identified binding site is relevant for the binding to HUWE1 based on the full-length structure of HUWE1 (which has not been released at this point in time) and its dynamics. Independently of HUWE1, however, the identified binding site may also serve as a docking site for other interaction partners of MIZ1. This could be assessed by a combination of mutagenesis with cell-based proteomics. Also, it may be possible to design peptides that block the atypical binding site of MIZ1^{BTB}, analogously to studies on BCL6. An inhibitory peptide that occupies the lateral groove of BCL6 was found to abrogate BCL6-mediated transcriptional repression and chromatin silencing and reactivate BCL6 target genes, thus disrupting the biological function of BCL6 in B cells [344]. Building on this finding, a large number of small-molecule inhibitors targeting the lateral groove were designed (see section 1.6.3) Peptide-based inhibitors of the upper binding site in MIZ1^{BTB} could be turned into small-molecule inhibitors. Such compounds would be highly useful to explore the question of whether this site is used by interaction partners of MIZ1 in the cell. Based on my crystal structure, it may also be interesting to search for peptide stretches in the human proteome that resemble the HUWE1-derived AS^C peptide and predict possible binders. If several different proteins were to use the binding site on MIZ1 that I discovered, it would be interesting to study how the binding of these alternative partners is regulated and under which conditions it would be possible to interfere with one partner selectively, while leaving other functions of MIZ1 intact.

5.2 What may be the biological function of peptide selectivity for MIZ1^{BTB} homodimers over heterodimers?

In the next section I would like to take up a question introduced in section 4.13: My *in vitro* binding assays showed that the HUWE1-AS^C-peptide selects for the MIZ1 homodimer over heterodimers (**Figure 50**). Assuming, that HUWE1 actually binds to MIZ1 via the identified site (which requires careful validation in the full-length context) and acts as a degradative E3 toward MIZ1, the selective recognition of MIZ1 homodimers over heterodimers would result in a stabilization of heterodimers. What may be the biological function of such selectivity? One hypothetical scenario is described in the following. Yi et al. showed that CUL4B targets HUWE1 for proteasomal degradation upon DNA-damage [275]. This highlights that HUWE1 does not regulate a broad range of substrates and controls their levels, but that HUWE1 itself underlies tight control. Under non-stress conditions, the cell may contain high HUWE1 levels and, therefore, low levels of MIZ1 homodimers, with MIZ1 heterodimers accumulating. MIZ1 heterodimers are known to bind to the same promoters as MIZ1 homodimers, but instead of activating target gene expression, they inhibit it, for example the *p21* gene, *CDKN1A*, (see 1.6.4), which induces cell cycle arrest. In contrast, upon DNA-damage, it would be desirable if p21 excerted cell cycle arrest. My hypothesis is that *p21* expression may be regulated by the relative concentrations of MIZ1 homo- and heterodimers. Upon DNA-damage, HUWE1 is degraded by CUL4B [275] and as a consequence, MIZ1 homodimers may be stabilized, resulting in increased MIZ1-target gene expression, e.g., that of *p21*. p21 may thus induce cell cycle arrest, allowing for DNA-repair mechanisms to take effect. To test this hypothesis, it would be necessary to compare the relative concentrations of homo- and heterodimers of MIZ1 under stress and non-stress conditions. To this end, one may analyze two MIZ1^{BTB} constructs with different tags and a BCL6^{BTB} construct carrying the same tag as one of the MIZ1^{BTB} constructs. In one condition, the two monomeric MIZ1^{BTB} constructs would be transfected and in a second condition one MIZ1^{BTB} construct would be substituted by BCL6^{BTB}, followed by co-IPs under non-stress and stress condition. If this experiment would support the hypothesis I outlined above, one may repeat the experiment in the absence of CUL4B. Finally, it would be interesting to perform ChIP-seq to evaluate whether more heterodimers can indeed be detected at MIZ1 target gene promoters under

non-stress than stressed conditions. Notably, such experiments would be particularly interesting in the light of the recent finding that the AS is part of a critical, yet highly dynamic intramolecular interface. Independently of the precise role and dynamical features of the AS, it is possible that other binding partners utilize the atypical binding site I discovered in the BTB domain of MIZ1 in a similar manner.

5.3 Searching for an additional/another MIZ1 binding site with sequence similarity to the HUWE1-AS^C-peptide

Deletion of the AS^C (aa 3870-3890) in various, mostly N-terminally, truncated HUWE1-fragments, as well as preliminary experiments in the context of the full-length protein, (see section 4.9 and 4.10) did not abrogate the binding of MIZ1 to HUWE1. As mentioned above, these experiments may indicate that the AS^C does not represent the MIZ1 binding site in the context of Fl-HUWE1. However, this interpretation is complicated by the fact that deletion of AS^C likely causes perturbances of the structural integrity of HUWE1 (which could not be predicted at the time, due to the lack of the full-length structure). Interestingly, I detected binding of MIZ1 to a partially structured HUWE1 fragment comprising residues 2364 to 3665 in the cell, but was unable to map the binding site within this region more precisely (see section 4.11). As mentioned in section 4.11, I can not exclude that the identified binding site is an unspecific one, due to the low secondary structure predicted for the used construct and the typical problems associated with studying truncated fragments of unknown conformation. The so far limited available structural information of the Fl-HUWE1 cryo-EM structure also indicates that this HUWE1 fragment is only partially structured. Because the HUWE1 fragment comprising residues 2364 to 3665 does not completely cover the N-terminal extension (aa 2474-3843) in dN-HUWE1 (aa 2474-4374) compared to HUWE1^{AS} (aa 3843-4374), I were interested in analyzing, whether aa 3666-3842 might contain a sequence stretch with similarity to AS^C (aa 3870-3890) (**Figure 53A**). If so, this might explain why binding of MIZ1 is diminished by site-directed mutagenesis in AS^C in the context of HUWE1^{AS}, but depletion of AS^C in dN-HUWE1 or Fl-HUWE1 does not abrogate the binding of Fl-MIZ1 (see 4.10).

Figure 53B shows a sequence alignment, revealing a ~ 20 aa region (aa 3706-3726) within HUWE1 aa 3666-3842 that contains the same key hydrophobic residues (Leu 3713 and Phe 3723), separated by nine amino acids, as the HUWE1-AS^C-peptide (Leu 3877 and Phe 3887). In the Fl-HUWE1 cryo-EM structure, the sequence comprising residues 3666 to 3842 is part of ARLD4, located near the catalytic HECT domain [129] (see 1.5.4). Therefore, it would be worthwhile to generate a HUWE1-fragment that comprises both the catalytic HECT domain and ARLD4 (aa 3179-3989) and investigate whether the binding of MIZ1 is abolished upon depletion of AS^C (aa 3870-3890) and the potential additional MIZ1-binding site (aa 3706-3726) in this context. Once again, this would be done assuming that a truncated construct is still active and the closed ring-structure not necessary for HUWE1 activity toward all substrates.

Secondary structure predictions of HUWE1 aa 3666-3842 (**Figure 54**) suggest another potential MIZ1 binding site, which is not obvious from the sequence alignment (**Figure 53B**). While aa 3706-3726 is predicted to be α-helical, a region comprising aa 3675-3694 is predicted to contain two β-strands, separated by an unstructured region, similar to the HUWE1-AS^C-peptide. Each of these β-strands contains at least two hydrophobic residues, where Met 3680 (potentially analogous to Leu 3877 in AS^C) in one strand is separated by nine amino acids from Val 3690 (potentially analogous to Phe 3887 in AS^C) in the other. Therefore, it may be interesting to delete aa 3675-3694 in the context of HUWE1 aa 3179-4374 (possibly also in combination with deletion of aa 3706-3726 and AS^C) to analyze whether MIZ1 binding to HUWE1 is diminished in this context. The upcoming release of the HUWE1 structure [129] will facilitate evaluating these and additional predictions regarding MIZ1 binding to HUWE1. In the light of the corresponding study, it is possible that the solenoid architecture of HUWE1 contains multiple binding sites for a given substrate. Binding may thus be mediated by combinatorial, low-affinity interactions, as previously observed in RING-type E3s [129], [430], [431]. Therefore, it is also conceivable that HUWE1 contains more than one MIZ1 binding site. In my preliminary search for putative MIZ1 binding sites in HUWE1 (section 4.11), I focused on regions with similarity to the AS^C-peptide, based on the assumption that AS^C may not be accessible in full-length HUWE1 and MIZ1-binding may thus be mediated by another, similar site. It would be worthwhile to search for other putative MIZ1 binding sites in

HUWE1 without the restraint of similarity to the AS^C-peptide. Such site may enable MIZ1 binding to HUWE1 in a synergistic way. In line with such a model, I observed that MIZ1$^{\Delta BTB}$ retained 50 % binding capacity of MIZ1 WT to HUWE1 (**Figure 38D**; preliminary experiment with n = 1). Finally, it can not be excluded that PTMs of MIZ1 modulate its interactions with HUWE1, analogously to phosphorylation of DDIT4 [129].
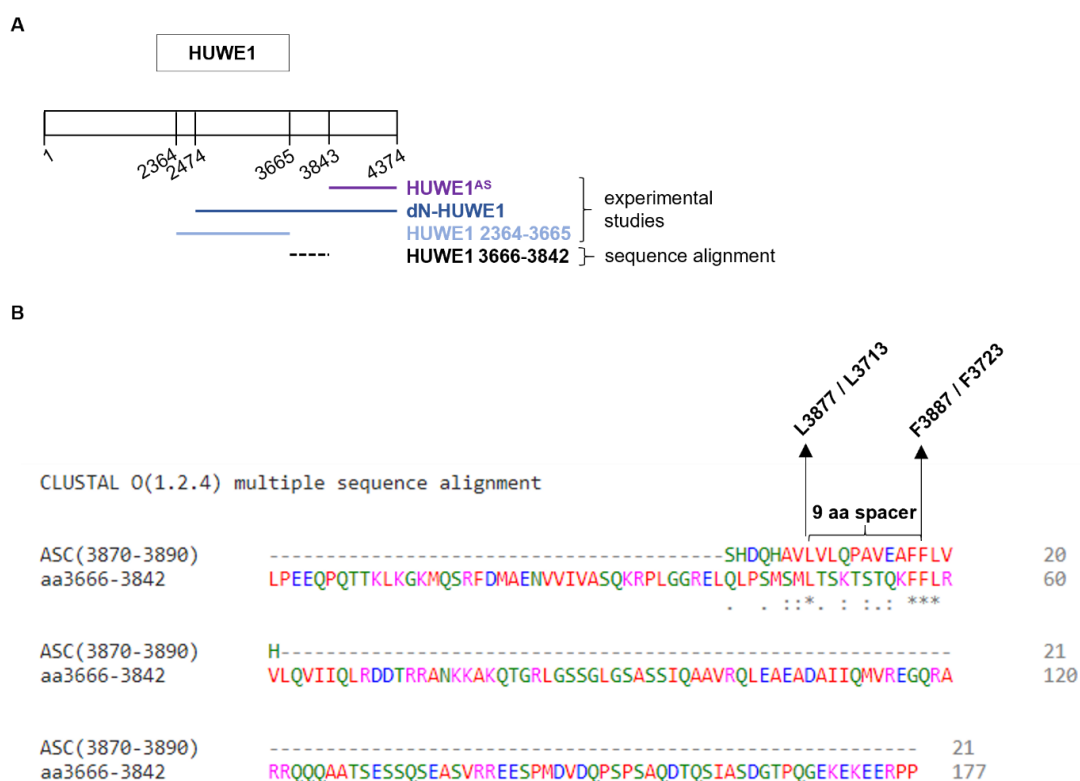
Figure 53: Sequence similarity of HUWE1 aa 3706-3726 and the HUWE1-AS^C-peptide (aa 3870-3890) based on two key hydrophobic residues (leucine and phenylalanine) separated by nine amino acids
(A) Overview of selected C-terminal HUWE1 constructs used in experimental studies (HUWE1^AS: aa 3843-4374; dN-HUWE1: aa 2474-4374; HUWE1 aa 2364-3665) or analyzed by sequence alignment only (HUWE1 aa 3666-3842). (B) Sequence alignment of the HUWE1-AS^C-peptide and HUWE1 aa 3666-3842, performed with Clustal Omega (1.2.4) [408], shows sequence similarity of the HUWE1-AS^C-peptide and HUWE1 aa 3706-3726 (box). (*) indicates a conserved residue; (:) indicates side chains with strong similarity; (.) indicates side chains with weak similarity; red: small and hydrophobic side chains (AVFPMILW); blue: acidic side chains (DE); magenta: basic side chains (RHK); green: side chains with hydroxyl-/sulfhydryl-groups and/or amines (STYHCNGQ). The two key hydrophobic residues, either in AS^C or in aa 3666-3842 are labeled.
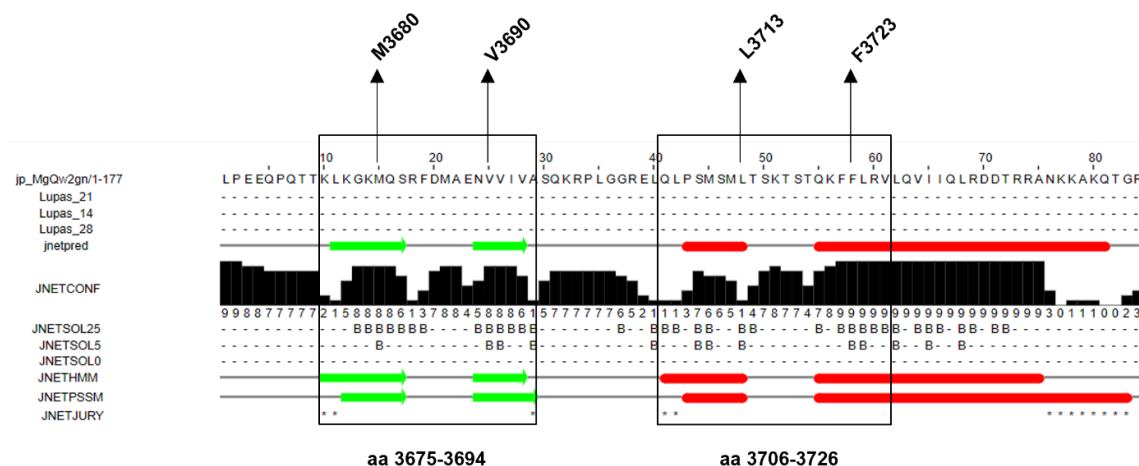
Figure 54: HUWE1 aa 3666-3842 contains two potential MIZ1 binding sites with similarity to HUWE1-AS^C, predicted to contain β-strands (aa 3675-3694) and one predicted to be mostly α-helical (aa 3706-3726).
Secondary structure prediction for HUWE1 aa 3666-3842 (only aa 3666-3749 is shown), performed with JPred4 [425]. Red tubes indicate helices; green arrows represent β-strands; Lupas_21, Lupas_14, Lupas_28: Coiled-coil predictions for the sequence. These are binary predictions for each location; JNetPRED: The consensus prediction; JNetCONF: The confidence estimated for the prediction. High values mean high confidence; JNETSOL25, JNETSOL5, JNETSOL0: Solvent accessibility predictions, binary predictions of 25 %, 5 % or 0 % solvent accessibility. B indicates buried secondary structure, - indicates exposed secondary structure; JNetHMM: HMM (Hidden Markov Model)-profile based prediction; JNETPSSM: PSSM (Position Specific Scoring Matrix)-based prediction; JNETJURY: A * in this annotation indicates that the JNETJURY was invoked to rationalize significantly different primary predictions.

5.4 Does MIZ1 mainly function as an adaptor protein or part of a multiprotein complex rather than a substrate of HUWE1?

My *in vitro* binding and activity assays showed impaired interactions of MIZ1 variants with N-terminally truncated HUWE1, in line with the crystal structure of the homodimeric MIZ1^{BTB} domain with the HUWE1-derived AS^C peptide (section 4.5). This could be confirmed in cell-based assays, notably also in the context of both full-length HUWE1 and full-length MIZ1 (section 4.8 and 4.9). However, my preliminary results showed no robust effects of structure-guided mutations in *MIZ1^{BTB}* on MIZ1 stability (section 4.12) (**Figure 48** and **Figure 49**). While these experiments require consolidation, I speculate that MIZ1 might not predominantly act as degradative substrate of HUWE1 under the conditions used, but may rather be an interaction partner, e.g., for the recruitment of other HUWE1 substrates. Such substrates may include MYC, which is known to interact with both HUWE1 and MIZ1 [288], [228]. It should be noted however, that MIZ1 was reported to be

modified with K48-linked ubiquitin chains by HUWE1 upon TNFα stimulation in HEK293 cells. [230]. Unfortunately, I was unable to reproduce this effect. *In vitro*, however, HUWE1^{AS} catalyzed polyubiquitination of MIZ1$^{1\text{-}282}$ (**Figure 20**) at rather high protein concentrations. Worthwhile future experiments to understand the HUWE1-MIZ1-MYC interplay will include co-IPs from suitable cell lines and conditions in combination with mass spectrometry, possibly also applying crosslinking approaches. These experiments should be performed with both catalytically active and dead HUWE1 variants to assess the influence of HUWE1-mediated ubiquitination on the interaction. Also, the HUWE1-targeted ubiquitination sites on MIZ1 and MYC could be mutated to evaluate whether their modification as HUWE1-substrates impact their mutual binding properties. Systematic interactome analyses would also shed light on the possibility that a third partner/substrate stabilizes or modulates the HUWE1-MIZ1 interaction in the cell. This scenario may provide an explanation for why the analytical SEC for MIZ1^{BTB} and Fl-HUWE1 showed only weak (if any) coelution. It is also possible that more than one region of full-length HUWE1 contribute to binding of MIZ1 in the cell, which may explain why the co-IP of Fl-HUWE1 and Fl-MIZ1$^{\Delta BTB}$ only showed a reduction in binding by about 50 % (**Figure 38D**).

In sum, it will be necessary to clarify whether a third interaction partner contributes or modulates the MIZ1/HUWE1-interaction and then embark on structural analyses of the minimal macromolecular complex needed to yield a stable complex. Notably, to study Fl-MIZ1 in this context will require the presence of DNA to stabilize the extended ZF region. To pursue these studies will require the use of insect or mammalian cell expression systems. Structural information of Fl-HUWE1 in complex with MIZ1 would finally bring light into the darkness surrounding their mutual binding mode and potentially offer new therapeutic opportunities by structure-guided design of compounds to disrupt the interaction. All these aspects show that the topic stays challenging and interesting at the same time and needs further investigation.

While my work could not unambiguously uncover the molecular basis of the HUWE1-MIZ1 interaction, it opens avenues to new, exciting lines of research regarding the biology of HUWE1 and MIZ1. Importantly, the new peptide binding mode I observed in MIZ1^{BTB} highlights an outstanding ability of MIZ1 to recruit potential interaction partners in a way that is atypical within the family of

BTB-ZF proteins. I envision that this specificity may be exploited for the design of inhibitory peptides or small-molecule inhibitors that do not target the well-studied lateral groove not the dimer BTB interface, and thus provide specific probe for the study of MIZ1. In the best case, such probes may ultimately provide starting points for therapeutic interference with MIZ1 signaling in cancer.

6 References

[1]   K. D. Wilkinson, **1987**, Protein ubiquitination: a regulatory post-translational modification, Anticancer Drug Des, *2*, 211-29.

[2]   D. Komander and M. Rape, **2012**, The ubiquitin code, Annu Rev Biochem, *81*, 203-29.

[3]   A. J. McClellan, S. H. Laugesen, and L. Ellgaard, **2019**, Cellular functions and molecular mechanisms of non-lysine ubiquitination, Open Biol, *9*, 190147.

[4]   K. Kliza and K. Husnjak, **2020**, Resolving the Complexity of Ubiquitin Networks, Front Mol Biosci, *7*, 21.

[5]   A. Ciechanover and R. Ben-Saadon, **2004**, N-terminal ubiquitination: more protein substrates join in, Trends Cell Biol, *14*, 103-6.

[6]   V. Akimov *et al.*, **2018**, UbiSite approach for comprehensive mapping of lysine and N-terminal ubiquitination sites, Nat Struct Mol Biol, *25*, 631-640.

[7]   G. Goldstein, M. Scheid, U. Hammerling, D. H. Schlesinger, H. D. Niall, and E. A. Boyse, **1975**, Isolation of a polypeptide that has lymphocyte-differentiating properties and is probably represented universally in living cells, Proceedings of the National Academy of Sciences of the United States of America, *72*, 11-15.

[8]   I. L. Goldknopf and H. Busch, **1977**, Isopeptide linkage between nonhistone and histone 2A polypeptides of chromosomal conjugate-protein A24, Proc Natl Acad Sci U S A, *74*, 864-8.

[9]   L. Deng, T. Meng, L. Chen, W. Wei, and P. Wang, **2020**, The role of ubiquitination in tumorigenesis and targeted drug discovery, Signal Transduct Target Ther, *5*, 11.

[10]   G. A. Khoury, R. C. Baliban, and C. A. Floudas, **2011**, Proteome-wide post-translational modification statistics: frequency analysis and curation of the swiss-prot database, Sci Rep, *1*,

[11]   K. N. Swatek and D. Komander, **2016**, Ubiquitin modifications, Cell Res, *26*, 399-422.

[12]   M. J. Clague, C. Heride, and S. Urbé, **2015**, The demographics of the ubiquitin system, Trends Cell Biol, *25*, 417-26.

[13]   A. Lilienbaum, **2013**, Relationship between the proteasomal system and autophagy, Int J Biochem Mol Biol, *4*, 1-26.

[14]   N. M. Kocaturk and D. Gozuacik, **2018**, Crosstalk Between Mammalian Autophagy and the Ubiquitin-Proteasome System, Frontiers in Cell and Developmental Biology, *6*,

[15]   D. Popovic, D. Vucic, and I. Dikic, **2014**, Ubiquitination in disease pathogenesis and treatment, Nat Med, *20*, 1242-53.

[16]   C. Grabbe, K. Husnjak, and I. Dikic, **2011**, The spatial and temporal organization of ubiquitin networks, Nat Rev Mol Cell Biol, *12*, 295-307.

[17]   P. J. Kraulis, **1991**, Similarity of protein G and ubiquitin, Science, *254*, 581.

[18]   J. P. Overington, **1992**, Comparison of three-dimensional structures of homologous proteins, Curr Opin Struct Biol, *2*, 394-401.

[19]   A. G. Murzin, **1992**, Familiar strangers, Nature, *360*, 635.

[20]   A. M. Burroughs, S. Balaji, L. M. Iyer, and L. Aravind, **2007**, Small but versatile: the extraordinary functional and structural diversity of the beta-grasp fold, Biol Direct, *2*, 18.

[21] A. M. Burroughs, S. Balaji, L. M. Iyer, and L. Aravind, **2007**, A novel superfamily containing the beta-grasp fold involved in binding diverse soluble ligands, Biol Direct, *2*, 4.

[22] S. Vijay-Kumar, C. E. Bugg, and W. J. Cook, **1987**, Structure of ubiquitin refined at 1.8 A resolution, J Mol Biol, *194*, 531-44.

[23] O. F. Lange *et al.*, **2008**, Recognition dynamics up to microseconds revealed from an RDC-derived ubiquitin ensemble in solution, Science, *320*, 1471-5.

[24] S. E. Jackson, **2006**, Ubiquitin: a small protein folding paradigm, Organic & Biomolecular Chemistry, *4*, 1845-1853.

[25] M. Hu *et al.*, **2002**, Crystal structure of a UBP-family deubiquitinating enzyme in isolation and in complex with ubiquitin aldehyde, Cell, *111*, 1041-54.

[26] S. Rahighi *et al.*, **2009**, Specific recognition of linear ubiquitin chains by NEMO is important for NF-kappaB activation, Cell, *136*, 1098-109.

[27] K. E. Sloper-Mould, J. C. Jemc, C. M. Pickart, and L. Hicke, **2001**, Distinct functional surface regions on ubiquitin, J Biol Chem, *276*, 30483-9.

[28] F. E. Reyes-Turcu, J. R. Horton, J. E. Mullally, A. Heroux, X. Cheng, and K. D. Wilkinson, **2006**, The ubiquitin binding domain ZnF UBP recognizes the C-terminal diglycine motif of unanchored ubiquitin, Cell, *124*, 1197-208.

[29] H. B. Kamadurai *et al.*, **2009**, Insights into ubiquitin transfer cascades from a structure of a UbcH5B approximately ubiquitin-HECT(NEDD4L) complex, Mol Cell, *36*, 1095-102.

[30] I. Dikic, S. Wakatsuki, and K. J. Walters, **2009**, Ubiquitin-binding domains - from structures to functions, Nat Rev Mol Cell Biol, *10*, 659-71.

[31] S. C. Shih, K. E. Sloper-Mould, and L. Hicke, **2000**, Monoubiquitin carries a novel internalization signal that is appended to activated receptors, Embo j, *19*, 187-98.

[32] L. Jin, A. Williamson, S. Banerjee, I. Philipp, and M. Rape, **2008**, Mechanism of ubiquitin-chain formation by the human anaphase-promoting complex, Cell, *133*, 653-65.

[33] M. L. Matsumoto *et al.*, **2010**, K11-linked polyubiquitination in cell cycle control revealed by a K11 linkage-specific antibody, Mol Cell, *39*, 477-84.

[34] A. Williamson, K. E. Wickliffe, B. G. Mellone, L. Song, G. H. Karpen, and M. Rape, **2009**, Identification of a physiological E2 module for the human anaphase-promoting complex, Proc Natl Acad Sci U S A, *106*, 18213-8.

[35] E. S. Johnson, P. C. Ma, I. M. Ota, and A. Varshavsky, **1995**, A proteolytic pathway that recognizes ubiquitin as a degradation signal, J Biol Chem, *270*, 17442-56.

[36] Y. Saeki *et al.*, **2009**, Lysine 63-linked polyubiquitin chain may serve as a targeting signal for the 26S proteasome, Embo j, *28*, 359-71.

[37] D. S. Kirkpatrick *et al.*, **2006**, Quantitative analysis of in vitro ubiquitinated cyclin B1 reveals complex chain topology, Nat Cell Biol, *8*, 700-10.

[38] F. Ohtake, H. Tsuchiya, Y. Saeki, and K. Tanaka, **2018**, K63 ubiquitylation triggers proteasomal degradation by seeding branched ubiquitin chains, Proc Natl Acad Sci U S A, *115*, E1401-e1408.

[39] Z. J. Chen and L. J. Sun, **2009**, Nonproteolytic Functions of Ubiquitin in Cell Signaling, Molecular Cell, *33*, 275-286.

[40] F. Koyano *et al.*, **2014**, Ubiquitin is phosphorylated by PINK1 to activate parkin, Nature, *510*, 162-6.

[41] L. A. Kane *et al.*, **2014**, PINK1 phosphorylates ubiquitin to activate Parkin E3 ubiquitin ligase activity, J Cell Biol, *205,* 143-53.

[42] A. Kazlauskaite *et al.*, **2014**, Parkin is activated by PINK1-dependent phosphorylation of ubiquitin at Ser65, Biochem J, *460,* 127-39.

[43] A. Kazlauskaite *et al.*, **2015**, Binding to serine 65-phosphorylated ubiquitin primes Parkin for optimal PINK1-dependent phosphorylation and activation, EMBO Rep, *16,* 939-54.

[44] T. Wauer *et al.*, **2015**, Ubiquitin Ser65 phosphorylation affects ubiquitin structure, chain assembly and hydrolysis, Embo j, *34,* 307-25.

[45] Y. Ye and M. Rape, **2009**, Building ubiquitin chains: E2 enzymes at work, Nat Rev Mol Cell Biol, *10,* 755-64.

[46] B. A. Schulman and J. W. Harper, **2009**, Ubiquitin-like protein activation by E1 enzymes: the apex for downstream signalling pathways, Nat Rev Mol Cell Biol, *10,* 319-31.

[47] N. Zheng and N. Shabek, **2017**, Ubiquitin Ligases: Structure, Function, and Regulation, Annu Rev Biochem, *86,* 129-157.

[48] P. M. Handley, M. Mueckler, N. R. Siegel, A. Ciechanover, and A. L. Schwartz, **1991**, Molecular cloning, sequence, and tissue distribution of the human ubiquitin-activating enzyme E1, Proc Natl Acad Sci U S A, *88,* 258-62.

[49] Y. H. Chiu, Q. Sun, and Z. J. Chen, **2007**, E1-L2 activates both ubiquitin and FAT10, Mol Cell, *27,* 1014-23.

[50] J. Jin, X. Li, S. P. Gygi, and J. W. Harper, **2007**, Dual E1 activation systems for ubiquitin differentially regulate E2 enzyme charging, Nature, *447,* 1135-8.

[51] C. Pelzer *et al.*, **2007**, UBE1L2, a novel E1 enzyme specific for ubiquitin, J Biol Chem, *282,* 23010-4.

[52] Z. S. Hann *et al.*, **2019**, Structural basis for adenylation and thioester bond formation in the ubiquitin E1, Proc Natl Acad Sci U S A, *116,* 15475-15484.

[53] A. L. Haas and I. A. Rose, **1982**, The mechanism of ubiquitin activating enzyme. A kinetic and equilibrium analysis, J Biol Chem, *257,* 10329-37.

[54] A. L. Haas, J. V. Warms, A. Hershko, and I. A. Rose, **1982**, Ubiquitin-activating enzyme. Mechanism and role in protein-ubiquitin conjugation, J Biol Chem, *257,* 2543-8.

[55] C. M. Pickart, E. M. Kasperek, R. Beal, and A. Kim, **1994**, Substrate properties of site-specific mutant ubiquitin protein (G76A) reveal unexpected mechanistic features of ubiquitin-activating enzyme (E1), J Biol Chem, *269,* 7115-23.

[56] C. Michelle, P. Vourc'h, L. Mignon, and C. R. Andres, **2009**, What was the set of ubiquitin and ubiquitin-like conjugating enzymes in the eukaryote common ancestor?, J Mol Evol, *68,* 616-28.

[57] R. J. Deshaies and C. A. Joazeiro, **2009**, RING domain E3 ubiquitin ligases, Annu Rev Biochem, *78,* 399-434.

[58] M. B. Metzger, J. N. Pruneda, R. E. Klevit, and A. M. Weissman, **2014**, RING-type E3 ligases: master manipulators of E2 ubiquitin-conjugating enzymes and ubiquitination, Biochim Biophys Acta, *1843,* 47-60.

[59] J. M. Huibregtse, M. Scheffner, S. Beaudenon, and P. M. Howley, **1995**, A family of proteins structurally and functionally related to the E6-AP ubiquitin-protein ligase, Proc Natl Acad Sci U S A, *92,* 2563-7.

[60] M. Scheffner, U. Nuber, and J. M. Huibregtse, **1995**, Protein ubiquitination involving an E1-E2-E3 enzyme ubiquitin thioester cascade, Nature, *373*, 81-3.

[61] H. Walden and K. Rittinger, **2018**, RBR ligase-mediated ubiquitin transfer: a tale with many twists and turns, Nat Struct Mol Biol, *25*, 440-445.

[62] D. M. Wenzel, A. Lissounov, P. S. Brzovic, and R. E. Klevit, **2011**, UBCH7 reactivity profile reveals parkin and HHARI to be RING/HECT hybrids, Nature, *474*, 105-8.

[63] B. E. Riley *et al.*, **2013**, Structure and function of Parkin E3 ubiquitin ligase reveals aspects of RING and HECT ligases, Nat Commun, *4*, 1982.

[64] W. Li *et al.*, **2008**, Genome-wide and functional annotation of human E3 ubiquitin ligases identifies MULAN, a mitochondrial E3 that regulates the organelle's dynamics and signaling, PLoS One, *3*, e1487.

[65] J. Weber, S. Polo, and E. Maspero, **2019**, HECT E3 Ligases: A Tale With Multiple Facets, Front Physiol, *10*, 370.

[66] S. Lorenz, **2018**, Structural mechanisms of HECT-type ubiquitin ligases, Biol Chem, *399*, 127-145.

[67] K. K. Dove and R. E. Klevit, **2017**, RING-Between-RING E3 Ligases: Emerging Themes amid the Variations, J Mol Biol, *429*, 3363-3375.

[68] A. P. VanDemark, R. M. Hofmann, C. Tsui, C. M. Pickart, and C. Wolberger, **2001**, Molecular insights into polyubiquitin chain assembly: crystal structure of the Mms2/Ubc13 heterodimer, Cell, *105*, 711-20.

[69] M. J. Eddins, C. M. Carlile, K. M. Gomez, C. M. Pickart, and C. Wolberger, **2006**, Mms2-Ubc13 covalently bound to ubiquitin reveals the structural basis of linkage-specific polyubiquitin chain formation, Nat Struct Mol Biol, *13*, 915-20.

[70] M. Hochstrasser, **2006**, Lingering mysteries of ubiquitin-chain assembly, Cell, *124*, 27-34.

[71] W. Li, D. Tu, A. T. Brunger, and Y. Ye, **2007**, A ubiquitin ligase transfers preformed polyubiquitin chains from a conjugating enzyme to a substrate, Nature, *446*, 333-7.

[72] M. Rape, S. K. Reddy, and M. W. Kirschner, **2006**, The processivity of multiubiquitination by the APC determines the order of substrate degradation, Cell, *124*, 89-103.

[73] R. Verma, R. M. Feldman, and R. J. Deshaies, **1997**, SIC1 is ubiquitinated in vitro by a pathway that requires CDC4, CDC34, and cyclin/CDK activities, Mol Biol Cell, *8*, 1427-37.

[74] M. D. Petroski and R. J. Deshaies, **2005**, Mechanism of lysine 48-linked ubiquitin-chain synthesis by the cullin-RING ubiquitin-ligase complex SCF-Cdc34, Cell, *123*, 1107-20.

[75] S. Gazdoiu, K. Yamoah, K. Wu, and Z. Q. Pan, **2007**, Human Cdc34 employs distinct sites to coordinate attachment of ubiquitin to a substrate and assembly of polyubiquitin chains, Mol Cell Biol, *27*, 7041-52.

[76] M. J. Clague, S. Urbé, and D. Komander, **2019**, Breaking the chains: deubiquitylating enzyme specificity begets function, Nat Rev Mol Cell Biol, *20*, 338-352.

[77] D. Komander, M. J. Clague, and S. Urbé, **2009**, Breaking the chains: structure and function of the deubiquitinases, Nat Rev Mol Cell Biol, *10*, 550-63.

[78] M. J. Clague, I. Barsukov, J. M. Coulson, H. Liu, D. J. Rigden, and S. Urbé, **2013**, Deubiquitylases from genes to organism, Physiol Rev, *93*, 1289-315.

[79]   T. E. T. Mevissen and D. Komander, **2017**, Mechanisms of Deubiquitinase Specificity and Regulation, Annu Rev Biochem, *86*, 159-192.

[80]   E. Ozkaynak, D. Finley, and A. Varshavsky, **1984**, The yeast ubiquitin gene: head-to-tail repeats encoding a polyubiquitin precursor protein, Nature, *312*, 663-6.

[81]   D. Finley, B. Bartel, and A. Varshavsky, **1989**, The tails of ubiquitin precursors are ribosomal proteins whose fusion to ubiquitin facilitates ribosome biogenesis, Nature, *338*, 394-401.

[82]   C. P. Grou, M. P. Pinto, A. V. Mendes, P. Domingues, and J. E. Azevedo, **2015**, The de novo synthesis of ubiquitin: identification of deubiquitinases acting on ubiquitin precursors, Sci Rep, *5*, 12836.

[83]   T. Yao and R. E. Cohen, **2002**, A cryptic protease couples deubiquitination and degradation by the proteasome, Nature, *419*, 403-7.

[84]   E. J. Worden, C. Padovani, and A. Martin, **2014**, Structure of the Rpn11-Rpn8 dimer reveals mechanisms of substrate deubiquitination during proteasomal degradation, Nat Struct Mol Biol, *21*, 220-7.

[85]   D. Finley, **2009**, Recognition and processing of ubiquitin-protein conjugates by the proteasome, Annu Rev Biochem, *78*, 477-513.

[86]   G. L. Grice and J. A. Nathan, **2016**, The recognition of ubiquitinated proteins by the proteasome, Cell Mol Life Sci, *73*, 3497-506.

[87]   P. D. Mace *et al.*, **2008**, Structures of the cIAP2 RING domain reveal conformational changes associated with ubiquitin-conjugating enzyme (E2) recruitment, J Biol Chem, *283*, 31633-40.

[88]   C. W. Liew, H. Sun, T. Hunter, and C. L. Day, **2010**, RING domain dimerization is essential for RNF4 function, Biochem J, *431*, 23-9.

[89]   H. Dou, L. Buetow, G. J. Sibbet, K. Cameron, and D. T. Huang, **2012**, BIRC7-E2 ubiquitin conjugate structure reveals the mechanism of ubiquitin transfer by a RING dimer, Nat Struct Mol Biol, *19*, 876-83.

[90]   Z. Xu, E. Kohli, K. I. Devlin, M. Bold, J. C. Nix, and S. Misra, **2008**, Interactions between the quality control ubiquitin ligase CHIP and ubiquitin conjugating enzymes, BMC Struct Biol, *8*, 26.

[91]   K. Linke, P. D. Mace, C. A. Smith, D. L. Vaux, J. Silke, and C. L. Day, **2008**, Structure of the MDM2/MDMX RING domain heterodimer reveals dimerization is required for their ubiquitylation in trans, Cell Death Differ, *15*, 841-8.

[92]   P. S. Brzovic, P. Rajagopal, D. W. Hoyt, M. C. King, and R. E. Klevit, **2001**, Structure of a BRCA1-BARD1 heterodimeric RING-RING complex, Nat Struct Biol, *8*, 833-7.

[93]   S. Iyappan *et al.*, **2010**, Turning the RING domain protein MdmX into an active ubiquitin-protein ligase, J Biol Chem, *285*, 33065-33072.

[94]   M. D. Petroski and R. J. Deshaies, **2005**, Function and regulation of cullin-RING ubiquitin ligases, Nat Rev Mol Cell Biol, *6*, 9-20.

[95]   F. Bassermann, R. Eichner, and M. Pagano, **2014**, The ubiquitin proteasome system - implications for cell cycle control and the targeted treatment of cancer, Biochim Biophys Acta, *1843*, 150-62.

[96]   C. Penas, V. Ramachandran, and N. G. Ayad, **2011**, The APC/C Ubiquitin Ligase: From Cell Biology to Tumorigenesis, Front Oncol, *1*, 60.

[97]   E. R. Watson, N. G. Brown, J. M. Peters, H. Stark, and B. A. Schulman, **2019**, Posing the APC/C E3 Ubiquitin Ligase to Orchestrate Cell Division, Trends Cell Biol, *29*, 117-134.

[98] W. Liu, G. Wu, W. Li, D. Lobur, and Y. Wan, **2007**, Cdh1-anaphase-promoting complex targets Skp2 for destruction in transforming growth factor beta-induced growth inhibition, Mol Cell Biol, *27*, 2967-79.

[99] E. Branigan, J. Carlos Penedo, and R. T. Hay, **2020**, Ubiquitin transfer by a RING E3 ligase occurs from a closed E2~ubiquitin conformation, Nat Commun, *11*, 2846.

[100] Katherine E. Wickliffe, S. Lorenz, David E. Wemmer, J. Kuriyan, and M. Rape, **2011**, The Mechanism of Linkage-Specific Ubiquitin Chain Elongation by a Single-Subunit E2, Cell, *144*, 769-781.

[101] A. Plechanovová, E. G. Jaffray, M. H. Tatham, J. H. Naismith, and R. T. Hay, **2012**, Structure of a RING E3 ligase and ubiquitin-loaded E2 primed for catalysis, Nature, *489*, 115-20.

[102] J. N. Pruneda *et al.*, **2012**, Structure of an E3:E2~Ub complex reveals an allosteric mechanism shared among RING/U-box ligases, Mol Cell, *47*, 933-42.

[103] L. Buetow *et al.*, **2015**, Activation of a primed RING E3-E2-ubiquitin complex by non-covalent ubiquitin, Mol Cell, *58*, 297-310.

[104] J. M. Huibregtse, M. Scheffner, and P. M. Howley, **1993**, Cloning and expression of the cDNA for E6-AP, a protein that mediates the interaction of the human papillomavirus E6 oncoprotein with p53, Mol Cell Biol, *13*, 775-84.

[105] L. Huang *et al.*, **1999**, Structure of an E6AP-UbcH7 complex: insights into ubiquitination by the E2-E3 enzyme cascade, Science, *286*, 1321-6.

[106] Y. Masuda *et al.*, **2019**, Stepwise multipolyubiquitination of p53 by the E6AP-E6 ubiquitin ligase complex, J Biol Chem, *294*, 14860-14875.

[107] K. Wolyniec *et al.*, **2012**, E6AP ubiquitin ligase regulates PML-induced senescence in Myc-driven lymphomagenesis, Blood, *120*, 822-32.

[108] S. Srinivasan and Z. Nawaz, **2011**, E3 ubiquitin protein ligase, E6-associated protein (E6-AP) regulates PI3K-Akt signaling and prostate cell growth, Biochim Biophys Acta, *1809*, 119-27.

[109] S. Ramamoorthy *et al.*, **2012**, Overexpression of ligase defective E6-associated protein, E6-AP, results in mammary tumorigenesis, Breast Cancer Res Treat, *132*, 97-108.

[110] C. Gamell *et al.*, **2017**, Reduced abundance of the E3 ubiquitin ligase E6AP contributes to decreased expression of the INK4/ARF locus in non-small cell lung cancer, Sci Signal, *10*,

[111] G. R. Buel *et al.*, **2020**, Structure of E3 ligase E6AP with a proteasome-binding site provided by substrate receptor hRpn10, Nat Commun, *11*, 1291.

[112] A. D. Jacobson, A. MacFadden, Z. Wu, J. Peng, and C. W. Liu, **2014**, Autoregulation of the 26S proteasome by in situ ubiquitination, Mol Biol Cell, *25*, 1824-35.

[113] H. C. Kim, A. M. Steffen, M. L. Oldham, J. Chen, and J. M. Huibregtse, **2011**, Structure and function of a HECT domain ubiquitin-binding site, EMBO Rep, *12*, 334-41.

[114] E. Maspero *et al.*, **2011**, Structure of the HECT:ubiquitin complex and its role in ubiquitin chain elongation, EMBO Rep, *12*, 342-9.

[115] E. Maspero *et al.*, **2013**, Structure of a ubiquitin-loaded HECT ligase reveals the molecular basis for catalytic priming, Nat Struct Mol Biol, *20*, 696-701.

[116] M. A. Verdecia *et al.*, **2003**, Conformational flexibility underlies ubiquitin ligation mediated by the WWP1 HECT domain E3 ligase, Mol Cell, *11*, 249-59.

[117] S. Lorenz, A. J. Cantor, M. Rape, and J. Kuriyan, **2013**, Macromolecular juggling by ubiquitylation enzymes, BMC Biol, *11*, 65.

[118] C. Salvat, G. Wang, A. Dastur, N. Lyon, and J. M. Huibregtse, **2004**, The -4 phenylalanine is required for substrate ubiquitination catalyzed by HECT ubiquitin ligases, J Biol Chem, *279*, 18935-43.

[119] M. Scheffner and S. Kumar, **2014**, Mammalian HECT ubiquitin-protein ligases: biological and pathophysiological aspects, Biochim Biophys Acta, *1843*, 61-74.

[120] N. A. Boase and S. Kumar, **2015**, NEDD4: The founding member of a family of ubiquitin-protein ligases, Gene, *557*, 113-22.

[121] R. Dunn, D. A. Klos, A. S. Adler, and L. Hicke, **2004**, The C2 domain of the Rsp5 ubiquitin ligase binds membrane phosphoinositides and directs ubiquitination of endosomal cargo, J Cell Biol, *165*, 135-44.

[122] P. Bork and M. Sudol, **1994**, The WW domain: a signalling site in dystrophin?, Trends Biochem Sci, *19*, 531-3.

[123] M. Sudol, H. I. Chen, C. Bougeret, A. Einbond, and P. Bork, **1995**, Characterization of a novel protein-binding module--the WW domain, FEBS Lett, *369*, 67-71.

[124] J. García-Cano, A. Martinez-Martinez, J. Sala-Gaston, L. Pedrazza, and J. L. Rosa, **2019**, HERCing: Structural and Functional Relevance of the Large HERC Ubiquitin Ligases, Front Physiol, *10*, 1014.

[125] J. Sala-Gaston *et al.*, **2020**, HERC Ubiquitin Ligases in Cancer, Cancers (Basel), *12*,

[126] S. Sánchez-Tena, M. Cubillos-Rojas, T. Schneider, and J. L. Rosa, **2016**, Functional and pathological relevance of HERC family proteins: a decade later, Cell Mol Life Sci, *73*, 1955-68.

[127] X. Mao, G. Sethi, Z. Zhang, and Q. Wang, **2018**, The Emerging Roles of the HERC Ubiquitin Ligases in Cancer, Curr Pharm Des, *24*, 1676-1681.

[128] L. Renault, J. Kuhlmann, A. Henkel, and A. Wittinghofer, **2001**, Structural basis for guanine nucleotide exchange on Ran by the regulator of chromosome condensation (RCC1), Cell, *105*, 245-55.

[129] M. Hunkeler *et al.*, **2021**, Solenoid architecture of HUWE1 contributes to ligase activity and substrate recognition, Molecular Cell,

[130] D. B. Grabarczyk *et al.*, **2021**, HUWE1 employs a giant substrate-binding ring to feed and regulate its HECT E3 domain, Nature Chemical Biology,

[131] S. Wiesner *et al.*, **2007**, Autoinhibition of the HECT-type ubiquitin ligase Smurf2 through its C2 domain, Cell, *130*, 651-62.

[132] S. Mari *et al.*, **2014**, Structural and functional framework for the autoinhibition of Nedd4-family ubiquitin ligases, Structure, *22*, 1639-49.

[133] C. Riling *et al.*, **2015**, Itch WW Domains Inhibit Its E3 Ubiquitin Ligase Activity by Blocking E2-E3 Ligase Trans-thiolation, J Biol Chem, *290*, 23875-87.

[134] Z. Chen *et al.*, **2017**, A Tunable Brake for HECT Ubiquitin Ligases, Mol Cell, *66*, 345-357.e6.

[135] K. Zhu *et al.*, **2017**, Allosteric auto-inhibition and activation of the Nedd4 family E3 ligase Itch, EMBO Rep, *18*, 1618-1630.

[136] B. Sander, W. Xu, M. Eilers, N. Popov, and S. Lorenz, **2017**, A conformational switch regulates the ubiquitin ligase HUWE1, Elife, *6*, e21036.

[137] V. P. Ronchi, J. M. Klein, D. J. Edwards, and A. L. Haas, **2014**, The active form of E6-associated protein (E6AP)/UBE3A ubiquitin ligase is an oligomer, J Biol Chem, *289*, 1033-48.

[138] D. Martinez-Zapien *et al.*, **2016**, Structure of the E6/E6AP/p53 complex required for HPV-mediated degradation of p53, Nature, *529*, 541-5.

[139] S. Kühnle *et al.*, **2011**, Physical and functional interaction of the HECT ubiquitin-protein ligases E6AP and HERC2, J Biol Chem, *286*, 19410-6.

[140] E. Gallagher, M. Gao, Y. C. Liu, and M. Karin, **2006**, Activation of the E3 ubiquitin ligase Itch through a phosphorylation-induced conformational change, Proc Natl Acad Sci U S A, *103*, 1717-22.

[141] A. L. Chan *et al.*, **2013**, c-Abl phosphorylates E6AP and regulates its E3 ubiquitin ligase activity, Biochemistry, *52*, 3119-29.

[142] R. D. Finn *et al.*, **2017**, InterPro in 2017-beyond protein family and domain annotations, Nucleic Acids Res, *45*, D190-d199.

[143] I. Marín, J. I. Lucas, A. C. Gradilla, and A. Ferrús, **2004**, Parkin and relatives: the RBR family of ubiquitin ligases, Physiol Genomics, *17*, 253-63.

[144] A. M. Pickrell and R. J. Youle, **2015**, The roles of PINK1, parkin, and mitochondrial fidelity in Parkinson's disease, Neuron, *85*, 257-73.

[145] A. Eiyama and K. Okamoto, **2015**, PINK1/Parkin-mediated mitophagy in mammalian cells, Curr Opin Cell Biol, *33*, 95-101.

[146] H. Matsumine *et al.*, **1997**, Localization of a gene for an autosomal recessive form of juvenile Parkinsonism to chromosome 6q25.2-27, Am J Hum Genet, *60*, 588-96.

[147] T. Kitada *et al.*, **1998**, Mutations in the parkin gene cause autosomal recessive juvenile parkinsonism, Nature, *392*, 605-8.

[148] M. Aguilera, M. Oliveros, M. Martínez-Padrón, J. A. Barbas, and A. Ferrús, **2000**, Ariadne-1: a vital Drosophila gene is required in development and defines a new conserved family of ring-finger proteins, Genetics, *155*, 1231-44.

[149] N. G. Tan, H. C. Ardley, G. B. Scott, S. A. Rose, A. F. Markham, and P. A. Robinson, **2003**, Human homologue of ariadne promotes the ubiquitylation of translation initiation factor 4E homologous protein, 4EHP, FEBS Lett, *554*, 501-4.

[150] X. Qiu and D. S. Fay, **2006**, ARI-1, an RBR family ubiquitin-ligase, functions with UBC-18 to regulate pharyngeal development in C. elegans, Dev Biol, *291*, 239-52.

[151] F. Elmehdawi *et al.*, **2013**, Human Homolog of Drosophila Ariadne (HHARI) is a marker of cellular proliferation associated with nuclear bodies, Exp Cell Res, *319*, 161-72.

[152] D. C. Scott *et al.*, **2016**, Two Distinct Types of E3 Ligases Work in Unison to Regulate Substrate Ubiquitylation, Cell, *166*, 1198-1214.e24.

[153] I. R. Kelsall *et al.*, **2013**, TRIAD1 and HHARI bind to and are activated by distinct neddylated Cullin-RING ligase complexes, Embo j, *32*, 2848-60.

[154] K. K. Dove *et al.*, **2017**, Two functionally distinct E2/E3 pairs coordinate sequential ubiquitination of a common substrate in Caenorhabditis elegans development, Proc Natl Acad Sci U S A, *114*, E6576-e6584.

[155] T. Kirisako *et al.*, **2006**, A ubiquitin ligase complex assembles linear polyubiquitin chains, Embo j, *25*, 4877-87.

[156] B. Boisson *et al.*, **2015**, Human HOIP and LUBAC deficiency underlies autoinflammation, immunodeficiency, amylopectinosis, and lymphangiectasia, J Exp Med, *212*, 939-51.

[157] Y. Fuseya *et al.*, **2020**, The HOIL-1L ligase modulates immune signalling and cell death via monoubiquitination of LUBAC, Nat Cell Biol, *22*, 663-673.

[158] F. Tokunaga *et al.*, **2011**, SHARPIN is a component of the NF-κB-activating linear ubiquitin chain assembly complex, Nature, *471*, 633-6.

[159] F. Ikeda *et al.*, **2011**, SHARPIN forms a linear ubiquitin ligase complex regulating NF-κB activity and apoptosis, Nature, *471*, 637-641.

[160] F. Tokunaga and K. Iwai, **2009**, [Involvement of LUBAC-mediated linear polyubiquitination of NEMO in NF-kappaB activation], Tanpakushitsu Kakusan Koso, *54*, 635-42.

[161] T. L. Haas *et al.*, **2009**, Recruitment of the linear ubiquitin chain assembly complex stabilizes the TNF-R1 signaling complex and is required for TNF-mediated gene induction, Mol Cell, *36*, 831-44.

[162] K. Rittinger and F. Ikeda, **2017**, Linear ubiquitin chains: enzymes, mechanisms and biology, Open Biol, *7*,

[163] T. R. Cotton and B. C. Lechtenberg, **2020**, Chain reactions: molecular mechanisms of RBR ubiquitin ligases, Biochem Soc Trans, *48*, 1737-1750.

[164] D. M. Duda *et al.*, **2013**, Structure of HHARI, a RING-IBR-RING ubiquitin ligase: autoinhibition of an Ariadne-family E3 and insights into ligation mechanism, Structure, *21*, 1030-41.

[165] J. F. Trempe *et al.*, **2013**, Structure of parkin reveals mechanisms for ubiquitin ligase activation, Science, *340*, 1451-5.

[166] T. Wauer, M. Simicek, A. Schubert, and D. Komander, **2015**, Mechanism of phospho-ubiquitin-induced PARKIN activation, Nature, *524*, 370-4.

[167] B. Stieglitz, A. C. Morris-Davies, M. G. Koliopoulos, E. Christodoulou, and K. Rittinger, **2012**, LUBAC synthesizes linear ubiquitin chains via a thioester intermediate, EMBO Rep, *13*, 840-6.

[168] K.-C. Pao *et al.*, **2018**, Activity-based E3 ligase profiling uncovers an E3 ligase with esterification activity, Nature, *556*, 381-385.

[169] E. G. Otten *et al.*, **2021**, Ubiquitylation of lipopolysaccharide by RNF213 during bacterial infection, Nature, *594*, 111-116.

[170] J. Ahel *et al.*, **2020**, Moyamoya disease factor RNF213 is a giant E3 ligase with a dynein-like core and a distinct ubiquitin-transfer mechanism, Elife, *9*,

[171] J. Ahel *et al.*, **2021**, E3 ubiquitin ligase RNF213 employs a non-canonical zinc finger active site and is allosterically regulated by ATP, bioRxiv, 2021.05.10.443411.

[172] A. L. Schwartz and A. Ciechanover, **2009**, Targeting proteins for destruction by the ubiquitin system: implications for human pathobiology, Annu Rev Pharmacol Toxicol, *49*, 73-96.

[173] D. Hoeller and I. Dikic, **2009**, Targeting the ubiquitin system in cancer therapy, Nature, *458*, 438-44.

[174] T. C. Kouroukis, F. G. Baldassarre, A. E. Haynes, K. Imrie, D. E. Reece, and M. C. Cheung, **2014**, Bortezomib in multiple myeloma: systematic review and clinical considerations, Curr Oncol, *21*, e573-603.

[175] E. E. Manasanch and R. Z. Orlowski, **2017**, Proteasome inhibitors in cancer therapy, Nat Rev Clin Oncol, *14*, 417-433.

[176] D. J. Sherman and J. Li, **2020**, Proteasome Inhibitors: Harnessing Proteostasis to Combat Disease, Molecules, *25*,

[177] S. H. Barghout and A. D. Schimmer, **2021**, E1 Enzymes as Therapeutic Targets in Cancer, Pharmacol Rev, *73*, 1-58.

[178] M. L. Hyer *et al.*, **2018**, A small-molecule inhibitor of the ubiquitin activating enzyme for cancer treatment, Nat Med, *24*, 186-193.

[179] T. A. Soucy *et al.*, **2009**, An inhibitor of NEDD8-activating enzyme as a new approach to treat cancer, Nature, *458*, 732-6.

[180] S. Tsukamoto *et al.*, **2008**, Leucettamol A: a new inhibitor of Ubc13-Uev1A interaction isolated from a marine sponge, Leucetta aff. microrhaphis, Bioorg Med Chem Lett, *18*, 6319-20.

[181] S. Ushiyama *et al.*, **2012**, Manadosterols A and B, sulfonated sterol dimers inhibiting the Ubc13-Uev1A interaction, isolated from the marine sponge Lissodendryx fibrosa, J Nat Prod, *75*, 1495-9.

[182] D. F. Ceccarelli *et al.*, **2011**, An allosteric inhibitor of the human Cdc34 ubiquitin-conjugating enzyme, Cell, *145*, 1075-87.

[183] C. D. Hodge, L. Spyracopoulos, and J. N. Glover, **2016**, Ubc13: the Lys63 ubiquitin chain building machine, Oncotarget, *7*, 64471-64504.

[184] A. Laine, I. Topisirovic, D. Zhai, J. C. Reed, K. L. Borden, and Z. Ronai, **2006**, Regulation of p53 localization and activity by Ubc13, Mol Cell Biol, *26*, 8901-13.

[185] M. A. Mansour, **2018**, Ubiquitination: Friend and foe in cancer, Int J Biochem Cell Biol, *101*, 80-93.

[186] S. H. Kao, H. T. Wu, and K. J. Wu, **2018**, Ubiquitination by HUWE1 in tumorigenesis and beyond, J Biomed Sci, *25*, 67.

[187] L. T. Vassilev *et al.*, **2004**, In vivo activation of the p53 pathway by small-molecule antagonists of MDM2, Science, *303*, 844-8.

[188] B. Vu *et al.*, **2013**, Discovery of RG7112: A Small-Molecule MDM2 Inhibitor in Clinical Development, ACS Med Chem Lett, *4*, 466-9.

[189] N. Issaeva *et al.*, **2004**, Small molecule RITA binds to p53, blocks p53-HDM-2 interaction and activates p53 function in tumors, Nat Med, *10*, 1321-8.

[190] E. S. Fischer *et al.*, **2014**, Structure of the DDB1-CRBN E3 ubiquitin ligase in complex with thalidomide, Nature, *512*, 49-53.

[191] P. P. Chamberlain *et al.*, **2014**, Structure of the human Cereblon-DDB1-lenalidomide complex reveals basis for responsiveness to thalidomide analogs, Nat Struct Mol Biol, *21*, 803-9.

[192] W. Lenz, R. A. Pfeiffer, W. Kosenow, and D. J. Hayman, **1962**, THALIDOMIDE AND CONGENITAL ABNORMALITIES, The Lancet, *279*, 45-46.

[193] W. G. McBride, **1961**, THALIDOMIDE AND CONGENITAL ABNORMALITIES, The Lancet, *278*, 1358.

[194] M. Melchert and A. List, **2007**, The thalidomide saga, Int J Biochem Cell Biol, *39*, 1489-99.

[195] S. Bhogaraju and I. Dikic, **2014**, A peek into the atomic details of thalidomide's clinical effects, Nat Struct Mol Biol, *21*, 739-40.

[196] Y. Liu *et al.*, **2015**, A novel effect of thalidomide and its analogs: suppression of cereblon ubiquitination enhances ubiquitin ligase function, Faseb j, *29*, 4829-39.

[197] K. M. Sakamoto, K. B. Kim, A. Kumagai, F. Mercurio, C. M. Crews, and R. J. Deshaies, **2001**, Protacs: chimeric molecules that target proteins to the Skp1-Cullin-F box complex for ubiquitination and degradation, Proc Natl Acad Sci U S A, *98*, 8554-9.

[198] M. Konstantinidou *et al.*, **2019**, PROTACs- a game-changing technology, Expert Opin Drug Discov, *14*, 1255-1268.

[199] Y. Wang, X. Jiang, F. Feng, W. Liu, and H. Sun, **2020**, Degradation of proteins by PROTACs and other strategies, Acta Pharmaceutica Sinica B, *10*, 207-238.

[200] T. K. Neklesa, J. D. Winkler, and C. M. Crews, **2017**, Targeted protein degradation by PROTACs, Pharmacol Ther, *174*, 138-144.

[201] J. Lu *et al.*, **2015**, Hijacking the E3 Ubiquitin Ligase Cereblon to Efficiently Target BRD4, Chem Biol, *22*, 755-63.

[202] B. N. Devaiah *et al.*, **2020**, MYC protein stability is negatively regulated by BRD4, Proc Natl Acad Sci U S A, *117*, 13457-13467.

[203] T. Neklesa *et al.*, **2018**, Abstract 5236: ARV-110: An androgen receptor PROTAC degrader for prostate cancer, Cancer Research, *78*, 5236.

[204] T. Neklesa *et al.*, **2019**, ARV-110: An oral androgen receptor PROTAC degrader for prostate cancer, Journal of Clinical Oncology, *37*, 259-259.

[205] **2020**, Proof-of-Concept with PROTACs in Prostate Cancer, Cancer Discov, *10*, 1084.

[206] A. Mullard, **2019**, First targeted protein degrader hits the clinic, Nat Rev Drug Discov,

[207] E. Aleo, C. J. Henderson, A. Fontanini, B. Solazzo, and C. Brancolini, **2006**, Identification of new compounds that trigger apoptosome-independent caspase activation and apoptosis, Cancer Res, *66*, 9235-44.

[208] B. H. Lee *et al.*, **2010**, Enhancement of proteasome activity by a small-molecule inhibitor of USP14, Nature, *467*, 179-84.

[209] D. Chauhan *et al.*, **2012**, A small molecule inhibitor of ubiquitin-specific protease-7 induces apoptosis in multiple myeloma cells and overcomes bortezomib resistance, Cancer Cell, *22*, 345-58.

[210] A. P. Turnbull *et al.*, **2017**, Molecular basis of USP7 inhibition by selective small-molecule inhibitors, Nature, *550*, 481-486.

[211] B. T. Gutierrez-Diaz, W. Gu, and P. Ntziachristos, **2020**, Deubiquitinases: Pro-oncogenic Activity and Therapeutic Targeting in Blood Malignancies, Trends Immunol, *41*, 327-340.

[212] B. Nicholson and K. G. Suresh Kumar, **2011**, The multifaceted roles of USP7: new therapeutic opportunities, Cell Biochem Biophys, *60*, 61-8.

[213] J. A. Harrigan, X. Jacq, N. M. Martin, and S. P. Jackson, **2018**, Deubiquitylating enzymes and drug discovery: emerging opportunities, Nat Rev Drug Discov, *17*, 57-78.

[214] L. Kategaya *et al.*, **2017**, USP7 small-molecule inhibitors interfere with ubiquitin binding, Nature, *550*, 534-538.

[215] M. Altun *et al.*, **2011**, Activity-based chemical proteomics accelerates inhibitor development for deubiquitylating enzymes, Chem Biol, *18*, 1401-12.

[216] F. Wang *et al.*, **2017**, Active site-targeted covalent irreversible inhibitors of USP7 impair the functions of Foxp3+ T-regulatory cells by promoting ubiquitination of Tip60, PLoS One, *12*, e0189744.

[217] I. M. Ghobrial *et al.*, **2019**, Phase I/II trial of the CXCR4 inhibitor plerixafor in combination with bortezomib as a chemosensitization strategy in relapsed/refractory multiple myeloma, Am J Hematol, *94*, 1244-1253.

[218] P. Moreau *et al.*, **2019**, Bortezomib, thalidomide, and dexamethasone with or without daratumumab before and after autologous stem-cell transplantation for newly diagnosed multiple myeloma (CASSIOPEIA): a randomised, open-label, phase 3 study, Lancet, *394*, 29-38.

[219] B. K. Tomlinson *et al.*, **2019**, A phase II study of bortezomib in combination with pegylated liposomal doxorubicin for acute myeloid leukemia, Am J Hematol, *94*, E291-e294.

[220] T. Nagase *et al.*, **1997**, Prediction of the coding sequences of unidentified human genes. VII. The complete sequences of 100 new cDNA clones from brain which can code for large proteins in vitro, DNA Res, *4*, 141-50.

[221] Z. Liu, R. Oughtred, and S. S. Wing, **2005**, Characterization of E3Histone, a novel testis ubiquitin protein ligase which ubiquitinates histones, Mol Cell Biol, *25*, 2819-31.

[222] Q. Zhong, W. Gao, F. Du, and X. Wang, **2005**, Mule/ARF-BP1, a BH3-only E3 ubiquitin ligase, catalyzes the polyubiquitination of Mcl-1 and regulates apoptosis, Cell, *121*, 1085-95.

[223] Y. Xu, D. E. Anderson, and Y. Ye, **2016**, The HECT domain ubiquitin ligase HUWE1 targets unassembled soluble proteins for degradation, Cell Discov, *2*, 16040.

[224] J. L. Parsons *et al.*, **2009**, Ubiquitin ligase ARF-BP1/Mule modulates base excision repair, Embo j, *28*, 3207-15.

[225] Z. Liu, D. Miao, Q. Xia, L. Hermo, and S. S. Wing, **2007**, Regulated expression of the ubiquitin protein ligase, E3(Histone)/LASU1/Mule/ARF-BP1/HUWE1, during spermatogenesis, Dev Dyn, *236*, 2889-98.

[226] A. C. Giles and B. Grill, **2020**, Roles of the HUWE1 ubiquitin ligase in nervous system development, function and disease, Neural Dev, *15*, 6.

[227] M. A. Michel, K. N. Swatek, M. K. Hospenthal, and D. Komander, **2017**, Ubiquitin Linkage-Specific Affimers Reveal Insights into K6-Linked Ubiquitin Signaling, Mol Cell, *68*, 233-246.e5.

[228] S. Adhikary *et al.*, **2005**, The Ubiquitin Ligase HectH9 Regulates Transcriptional Activation by Myc and Is Essential for Tumor Cell Proliferation, Cell, *123*, 409-421.

[229] J. B. Heidelberger *et al.*, **2018**, Proteomic profiling of VCP substrates links VCP to K6-linked ubiquitylation and c-Myc function, EMBO Rep, *19*,

[230] Y. Yang *et al.*, **2010**, E3 ubiquitin ligase Mule ubiquitinates Miz1 and is required for TNFalpha-induced JNK activation, Proc Natl Acad Sci U S A, *107*, 13444-9.

[231] P. R. Elliott, **2016**, Molecular basis for specificity of the Met1-linked polyubiquitin signal, Biochem Soc Trans, *44*, 1581-1602.

[232] R. Filadi, D. Pendin, and P. Pizzo, **2018**, Mitofusin 2: from functions to disease, Cell Death & Disease, *9*, 330.

[233] L. Vaughan *et al.*, **2015**, HUWE1 ubiquitylates and degrades the RAC activator TIAM1 promoting cell-cell adhesion disassembly, migration, and invasion, Cell Rep, *10*, 88-102.

[234] T. Noy, O. Suad, D. Taglicht, and A. Ciechanover, **2012**, HUWE1 ubiquitinates MyoD and targets it for proteasomal degradation, Biochem Biophys Res Commun, *418*, 408-13.

[235] Y. Atsumi *et al.*, **2015**, ATM and SIRT6/SNF2H Mediate Transient H2AX Stabilization When DSBs Form by Blocking HUWE1 to Allow Efficient γH2AX Foci Formation, Cell Rep, *13*, 2728-40.

[236] H. J. Lee *et al.*, **2019**, Non-proteolytic ubiquitination of Hexokinase 2 by HectH9 controls tumor metabolism and cancer stem cell expansion, Nat Commun, *10*, 2625.

[237] Z. Zhao *et al.*, **2018**, Hepatic PPARα function is controlled by polyubiquitination and proteasome-mediated degradation through the coordinated actions of PAQR3 and HUWE1, Hepatology, *68*, 289-303.

[238] L. Li, S. S. Martinez, W. Hu, Z. Liu, and R. Tjian, **2015**, A specific E3 ligase/deubiquitinase pair modulates TBP protein levels during muscle differentiation, Elife, *4*, e08536.

[239] D. D'Arca, X. Zhao, W. Xu, N. C. Ramirez-Martinez, A. Iavarone, and A. Lasorella, **2010**, Huwe1 ubiquitin ligase is essential to synchronize neuronal and glial differentiation in the developing cerebellum, Proc Natl Acad Sci U S A, *107*, 5875-80.

[240] A. Forget *et al.*, **2014**, Shh signaling protects Atoh1 from degradation mediated by the E3 ubiquitin ligase Huwe1 in neural precursors, Dev Cell, *29*, 649-61.

[241] K. N. Choe *et al.*, **2016**, HUWE1 interacts with PCNA to alleviate replication stress, EMBO Rep, *17*, 874-86.

[242] X. Gong, D. Du, Y. Deng, Y. Zhou, L. Sun, and S. Yuan, **2020**, The structure and regulation of the E3 ubiquitin ligase HUWE1 and its biological functions in cancer, Invest New Drugs, *38*, 515-524.

[243] S. S. Vembar and J. L. Brodsky, **2008**, One step at a time: endoplasmic reticulum-associated degradation, Nat Rev Mol Cell Biol, *9*, 944-57.

[244] T. Tasaki, S. M. Sriram, K. S. Park, and Y. T. Kwon, **2012**, The N-end rule pathway, Annu Rev Biochem, *81*, 261-89.

[245] X. Zhao *et al.*, **2009**, The N-Myc-DLL3 cascade is suppressed by the ubiquitin ligase Huwe1 to inhibit proliferation and promote neurogenesis in the developing brain, Dev Cell, *17*, 210-21.

[246] Z. Hao *et al.*, **2012**, The E3 ubiquitin ligase Mule acts through the ATM-p53 axis to maintain B lymphocyte homeostasis, J Exp Med, *209*, 173-86.

[247] N. Kon, J. Zhong, L. Qiang, D. Accili, and W. Gu, **2012**, Inactivation of arf-bp1 induces p53 activation and diabetic phenotypes in mice, The Journal of biological chemistry, *287*, 5102-5111.

[248] **2014**, Comprehensive molecular characterization of gastric adenocarcinoma, Nature, *513*, 202-9.

[249] **2012**, Comprehensive molecular characterization of human colon and rectal cancer, Nature, *487*, 330-7.

[250] T. P. Lin *et al.*, **2018**, R1 Regulates Prostate Tumor Growth and Progression By Transcriptional Suppression of the E3 Ligase HUWE1 to Stabilize c-Myc, Mol Cancer Res, *16*, 1940-1951.

[251] D. Yang *et al.*, **2018**, HUWE1 controls the development of non-small cell lung cancer through down-regulation of p53, Theranostics, *8*, 3517-3529.

[252] B. A. Walker *et al.*, **2018**, Identification of novel mutational drivers reveals oncogene dependencies in multiple myeloma, Blood, *132*, 587-597.

[253] E. Hodis *et al.*, **2012**, A landscape of driver mutations in melanoma, Cell, *150*, 251-63.

[254] G. Froyen *et al.*, **2008**, Submicroscopic duplications of the hydroxysteroid dehydrogenase HSD17B10 and the E3 ubiquitin ligase HUWE1 are associated with mental retardation, Am J Hum Genet, *82*, 432-43.

[255] S. Moortgat *et al.*, **2018**, HUWE1 variants cause dominant X-linked intellectual disability: a clinical study of 21 patients, Eur J Hum Genet, *26*, 64-74.

[256] M. Bosshard *et al.*, **2017**, Impaired oxidative stress response characterizes HUWE1-promoted X-linked intellectual disability, Sci Rep, *7*, 15050.

[257] S. V. Khoronenkova and G. L. Dianov, **2013**, USP7S-dependent inactivation of Mule regulates DNA damage signalling and repair, Nucleic Acids Res, *41*, 1750-6.

[258] C. V. Dang, **2012**, MYC on the path to cancer, Cell, *149*, 22-35.

[259] T. R. Kress, A. Sabò, and B. Amati, **2015**, MYC: connecting selective transcriptional control to global RNA production, Nat Rev Cancer, *15*, 593-607.

[260] X. Zhao *et al.*, **2008**, The HECT-domain ubiquitin ligase Huwe1 controls neural differentiation and proliferation by destabilizing the N-Myc oncoprotein, Nat Cell Biol, *10*, 643-53.

[261] N. von der Lehr *et al.*, **2003**, The F-box protein Skp2 participates in c-Myc proteosomal degradation and acts as a cofactor for c-Myc-regulated transcription, Mol Cell, *11*, 1189-200.

[262] D. Cepeda *et al.*, **2013**, CDK-mediated activation of the SCF(FBXO) (28) ubiquitin ligase promotes MYC-driven transcription and tumourigenesis and predicts poor survival in breast cancer, EMBO Mol Med, *5*, 1067-86.

[263] X. Fang *et al.*, **2017**, Deubiquitinase USP13 maintains glioblastoma stem cells by antagonizing FBXL14-mediated Myc ubiquitination, J Exp Med, *214*, 245-267.

[264] M. Welcker *et al.*, **2004**, The Fbw7 tumor suppressor regulates glycogen synthase kinase 3 phosphorylation-dependent c-Myc protein degradation, Proc Natl Acad Sci U S A, *101*, 9085-90.

[265] S. Xiong, T. Mu, G. Wang, and X. Jiang, **2014**, Mitochondria-mediated apoptosis in mammals, Protein Cell, *5*, 737-49.

[266] D. Chen, N. Kon, M. Li, W. Zhang, J. Qin, and W. Gu, **2005**, ARF-BP1/Mule is a critical mediator of the ARF tumor suppressor, Cell, *121*, 1071-83.

[267] C. F. Qi *et al.*, **2012**, Characterization of ARF-BP1/HUWE1 interactions with CTCF, MYC, ARF and p53 in MYC-driven B cell neoplasms, Int J Mol Sci, *13*, 6204-19.

[268] M. Jasin, **2002**, Homologous repair of DNA damage and tumorigenesis: the BRCA connection, Oncogene, *21*, 8981-93.

[269] X. Xu *et al.*, **1999**, Centrosome amplification and a defective G2-M cell cycle checkpoint induce genetic instability in BRCA1 exon 11 isoform-deficient cells, Mol Cell, *3*, 389-95.

[270] A. R. Venkitaraman, **2002**, Cancer susceptibility and the functions of BRCA1 and BRCA2, Cell, *108*, 171-82.

[271] X. Wang *et al.*, **2014**, HUWE1 interacts with BRCA1 and promotes its degradation in the ubiquitin-proteasome pathway, Biochem Biophys Res Commun, *444*, 290-5.

[272] H. T. Wu *et al.*, **2016**, K63-polyubiquitinated HAUSP deubiquitinates HIF-1α and dictates H3K56 acetylation promoting hypoxia-induced tumour progression, Nat Commun, *7*, 13644.

[273] M. H. Yang *et al.*, **2008**, Direct regulation of TWIST by HIF-1alpha promotes metastasis, Nat Cell Biol, *10*, 295-305.

[274] X. Zhang, F. G. Berger, J. Yang, and X. Lu, **2011**, USP4 inhibits p53 through deubiquitinating and stabilizing ARF-BP1, Embo j, *30*, 2177-89.

[275] J. Yi *et al.*, **2015**, DNA damage-induced activation of CUL4B targets HUWE1 for proteasomal degradation, Nucleic Acids Res, *43*, 4579-90.

[276] G. P. Leboucher *et al.*, **2012**, Stress-induced phosphorylation and proteasomal degradation of mitofusin 2 facilitates mitochondrial fragmentation and apoptosis, Mol Cell, *47*, 547-57.

[277] S. Peter *et al.*, **2014**, Tumor cell-specific inhibition of MYC function using small molecule inhibitors of the HUWE1 ubiquitin ligase, EMBO Mol Med, *6*, 1525-41.

[278] J. Zhang, S. Kan, B. Huang, Z. Hao, T. W. Mak, and Q. Zhong, **2011**, Mule determines the apoptotic response to HDAC inhibitors by targeted ubiquitination and destruction of HDAC2, Genes Dev, *25*, 2610-8.

[279] K. B. Myant *et al.*, **2017**, HUWE1 is a critical colonic tumour suppressor gene that prevents MYC signalling, DNA damage accumulation and tumour initiation, EMBO Mol Med, *9*, 181-197.

[280] S. Inoue *et al.*, **2013**, Mule/Huwe1/Arf-BP1 suppresses Ras-driven tumorigenesis by preventing c-Myc/Miz1-mediated down-regulation of p21 and p15, Genes Dev, *27*, 1101-14.

[281] M. Jäckl *et al.*, **2018**, β-Sheet Augmentation Is a Conserved Mechanism of Priming HECT E3 Ligases for Ubiquitin Ligation, J Mol Biol, *430*, 3218-3233.

[282] R. K. Pandya, J. R. Partridge, K. R. Love, T. U. Schwartz, and H. L. Ploegh, **2010**, A structural element within the HUWE1 HECT domain modulates self-ubiquitination and substrate ubiquitination activities, J Biol Chem, *285*, 5664-73.

[283] M. R. Warr *et al.*, **2005**, BH3-ligand regulates access of MCL-1 to its E3 ligase, FEBS Lett, *579*, 5603-8.

[284] L. Aravind, **2001**, The WWE domain: a common interaction module in protein ubiquitination and ADP ribosylation, Trends Biochem Sci, *26*, 273-5.

[285] D. Godt, J. L. Couderc, S. E. Cramton, and F. A. Laski, **1993**, Pattern formation in the limbs of Drosophila: bric à brac is expressed in both a gradient and a wave-like pattern and is required for specification and proper segmentation of the tarsus, Development, *119*, 799-812.

[286] S. Zollman, D. Godt, G. G. Privé, J. L. Couderc, and F. A. Laski, **1994**, The BTB domain, found primarily in zinc finger proteins, defines an evolutionarily conserved family that includes several developmentally regulated genes in Drosophila, Proc Natl Acad Sci U S A, *91*, 10717-21.

[287] V. J. Bardwell and R. Treisman, **1994**, The POZ domain: a conserved protein-protein interaction motif, Genes Dev, *8*, 1664-77.

[288] K. Peukert, P. Staller, A. Schneider, G. Carmichael, F. Hänel, and M. Eilers, **1997**, An alternative pathway for gene regulation by Myc, Embo j, *16*, 5672-86.

[289] O. Albagli, P. Dhordain, C. Deweindt, G. Lecocq, and D. Leprince, **1995**, The BTB/POZ domain: a new protein-protein interaction motif common to DNA- and actin-binding proteins, Cell Growth Differ, *6*, 1193-1198.

[290] J. Liu, Y. Zhao, M. Eilers, and A. Lin, **2009**, Miz1 is a signal- and pathway-specific modulator or regulator (SMOR) that suppresses TNF-α-induced JNK1 activation, Proceedings of the National Academy of Sciences, pnas.0906328106.

[291] J. Ziegelbauer, B. Shan, D. Yager, C. Larabell, B. Hoffmann, and R. Tjian, **2001**, Transcription factor MIZ-1 is regulated via microtubule association, Mol Cell, *8*, 339-49.

[292] S. Herold *et al.*, **2002**, Negative Regulation of the Mammalian UV Response by Myc through Association with Miz-1, Molecular Cell, *10*, 509-521.

[293] K. E. Wiese *et al.*, **2013**, The role of MIZ-1 in MYC-dependent tumorigenesis, Cold Spring Harb Perspect Med, *3*, a014290.

[294] E. Wolf *et al.*, **2013**, Miz1 is required to maintain autophagic flux, Nature Communications, *4*, 2535.

[295] B. L. Barrilleaux, D. Burow, S. H. Lockwood, A. Yu, D. J. Segal, and P. S. Knoepfler, **2014**, Miz-1 activates gene expression via a novel consensus DNA binding motif, PLoS One, *9*, e101151.

[296] P. Staller *et al.*, **2001**, Repression of p15INK4b expression by Myc through association with Miz-1, Nat Cell Biol, *3*, 392-9.

[297] J. Seoane, C. Pouponnot, P. Staller, M. Schader, M. Eilers, and J. Massagué, **2001**, TGFbeta influences Myc, Miz-1 and Smad to control the CDK inhibitor p15INK4b, Nat Cell Biol, *3*, 400-8.

[298] S. Wu *et al.*, **2003**, Myc represses differentiation-induced p21CIP1 expression via Miz-1-dependent interaction with the p21 core promoter, Oncogene, *22*, 351-60.

[299] S. Adhikary *et al.*, **2003**, Miz1 is required for early embryonic development during gastrulation, Mol Cell Biol, *23*, 7648-57.

[300] J. van Riggelen *et al.*, **2010**, The interaction between Myc and Miz1 is required to antagonize TGFbeta-dependent autocrine signaling during lymphoma formation and maintenance, Genes Dev, *24*, 1281-94.

[301] M. Wanzel, A. C. Russ, D. Kleine-Kohlbrecher, E. Colombo, P. G. Pelicci, and M. Eilers, **2008**, A ribosomal protein L23-nucleophosmin circuit coordinates Mizl function with cell growth, Nat Cell Biol, *10*, 1051-61.

[302] S. E. Salghetti, S. Y. Kim, and W. P. Tansey, **1999**, Destruction of Myc by ubiquitin-mediated proteolysis: cancer-associated and transforming mutations stabilize Myc, Embo j, *18*, 717-26.

[303] C. Brenner *et al.*, **2005**, Myc represses transcription through recruitment of DNA methyltransferase corepressor, Embo j, *24*, 336-46.

[304] J. D. F. Licchesi *et al.*, **2010**, Transcriptional regulation of Wnt inhibitory factor-1 by Miz-1/c-Myc, Oncogene, *29*, 5923-5934.

[305] R. T. Phan, M. Saito, K. Basso, H. Niu, and R. Dalla-Favera, **2005**, BCL6 interacts with the transcription factor Miz-1 to suppress the cyclin-dependent kinase inhibitor p21 and cell cycle arrest in germinal center B cells, Nat Immunol, *6*, 1054-60.

[306] Q. Liu, S. Basu, Y. Qiu, F. Tang, and F. Dong, **2010**, A role of Miz-1 in Gfi-1-mediated transcriptional repression of CDKN1A, Oncogene, *29*, 2843-52.

[307] S. Basu, Q. Liu, Y. Qiu, and F. Dong, **2009**, Gfi-1 represses CDKN2B encoding p15INK4B through interaction with Miz-1, Proc Natl Acad Sci U S A, *106*, 1433-8.

[308] A. Gebhardt *et al.*, **2006**, Myc regulates keratinocyte adhesion and differentiation via complex formation with Miz1, The Journal of cell biology, *172*, 139-149.

[309] B. Herkert *et al.*, **2010**, The Arf tumor suppressor protein inhibits Miz1 to suppress cell adhesion and induce apoptosis, J Cell Biol, *188*, 905-18.

[310] J. H. Patel and S. B. McMahon, **2007**, BCL2 is a downstream effector of MIZ-1 essential for blocking c-MYC-induced apoptosis, J Biol Chem, *282*, 5-13.

[311] T. Möröy, I. Saba, and C. Kosan, **2011**, The role of the transcription factor Miz-1 in lymphocyte development and lymphomagenesis-Binding Myc makes the difference, Semin Immunol, *23*, 379-87.

[312] I. Saba, C. Kosan, L. Vassen, and T. Möröy, **2011**, IL-7R-dependent survival and differentiation of early T-lineage progenitors is regulated by the BTB/POZ domain transcription factor Miz-1, Blood, *117*, 3370-81.

[313] A. Gebhardt *et al.*, **2007**, Miz1 is required for hair follicle structure and hair morphogenesis, J Cell Sci, *120*, 2586-93.

[314] A. Bagchi and A. A. Mills, **2008**, The quest for the 1p36 tumor suppressor, Cancer Res, *68*, 2551-6.

[315] N. Ikegaki *et al.*, **2007**, De novo identification of MIZ-1 (ZBTB17) encoding a MYC-interacting zinc-finger protein as a new favorable neuroblastoma gene, Clin Cancer Res, *13*, 6001-9.

[316] J. Hönnemann, A. Sanz-Moreno, E. Wolf, M. Eilers, and H. P. Elsässer, **2012**, Miz1 is a critical repressor of cdkn1a during skin tumorigenesis, PLoS One, *7*, e34885.

[317] M. Wanzel *et al.*, **2005**, Akt and 14-3-3eta regulate Miz1 to control cell-cycle arrest after DNA damage, Nat Cell Biol, *7*, 30-41.

[318] R. Perez-Torrado, D. Yamada, and P. A. Defossez, **2006**, Born to bind: the BTB protein-protein interaction domain, Bioessays, *28*, 1194-202.

[319] P. J. Stogios, G. S. Downs, J. J. S. Jauhal, S. K. Nandra, and G. G. Privé, **2005**, Sequence and structural analysis of BTB domain proteins, Genome Biology, *6*, R82.

[320] D. L. Minor *et al.*, **2000**, The polar T1 interface is linked to conformational changes that open the voltage-gated potassium channel, Cell, *102*, 657-70.

[321] A. Kreusch, P. J. Pfaffinger, C. F. Stevens, and S. Choe, **1998**, Crystal structure of the tetramerization domain of the Shaker potassium channel, Nature, *392*, 945-8.

[322] M. H. Nanao, W. Zhou, P. J. Pfaffinger, and S. Choe, **2003**, Determining the basis of channel-tetramerization specificity by x-ray crystallography and a sequence-comparison algorithm: Family Values (FamVal), Proceedings of the National Academy of Sciences of the United States of America, *100*, 8670-8675.

[323] C. Strang, S. J. Cushman, D. DeRubeis, D. Peterson, and P. J. Pfaffinger, **2001**, A central role for the T1 domain in voltage-gated potassium channel formation and function, J Biol Chem, *276*, 28493-502.

[324] M. V. Botuyan *et al.*, **2001**, Solution structure and dynamics of yeast elongin C in complex with a von Hippel-Lindau peptide, J Mol Biol, *312*, 177-86.

[325] C. E. Stebbins, W. G. Kaelin, Jr., and N. P. Pavletich, **1999**, Structure of the VHL-ElonginC-ElonginB complex: implications for VHL tumor suppressor function, Science, *284*, 455-61.

[326] J. H. Min, H. Yang, M. Ivan, F. Gertler, W. G. Kaelin, Jr., and N. P. Pavletich, **2002**, Structure of an HIF-1alpha -pVHL complex: hydroxyproline recognition in signaling, Science, *296*, 1886-9.

[327] W. C. Hon *et al.*, **2002**, Structural basis for the recognition of hydroxyproline in HIF-1 alpha by pVHL, Nature, *417*, 975-8.

[328] A. Pause *et al.*, **1997**, The von Hippel-Lindau tumor-suppressor gene product forms a stable complex with human CUL-2, a member of the Cdc53 family of proteins, Proc Natl Acad Sci U S A, *94*, 2156-61.

[329] K. Iwai *et al.*, **1999**, Identification of the von Hippel-lindau tumor-suppressor protein as part of an active E3 ubiquitin ligase complex, Proc Natl Acad Sci U S A, *96*, 12436-41.

[330] J. Lisztwan, G. Imbert, C. Wirbelauer, M. Gstaiger, and W. Krek, **1999**, The von Hippel-Lindau tumor suppressor protein is a component of an E3 ubiquitin-protein ligase activity, Genes Dev, *13*, 1822-33.

[331] M. Ohh *et al.*, **2000**, Ubiquitination of hypoxia-inducible factor requires direct binding to the beta-domain of the von Hippel-Lindau protein, Nat Cell Biol, *2*, 423-7.

[332] N. Zheng *et al.*, **2002**, Structure of the Cul1-Rbx1-Skp1-F boxSkp2 SCF ubiquitin ligase complex, Nature, *416*, 703-9.

[333] M. Furukawa, Y. J. He, C. Borchers, and Y. Xiong, **2003**, Targeting of protein ubiquitination by BTB-Cullin 3-Roc1 ubiquitin ligases, Nat Cell Biol, *5*, 1001-7.

[334] L. Pintard, A. Willems, and M. Peter, **2004**, Cullin-based ubiquitin ligases: Cul3-BTB complexes join the family, Embo j, *23*, 1681-7.

[335] S. van den Heuvel, **2004**, Protein Degradation: CUL-3 and BTB – Partners in Proteolysis, Current Biology, *14*, R59-R61.

[336] P. Canning *et al.*, **2013**, Structural basis for Cul3 protein assembly with the BTB-Kelch family of E3 ubiquitin ligases, J Biol Chem, *288*, 7803-7814.

[337] D. N. Robinson and L. Cooley, **1997**, Drosophila kelch is an oligomeric ring canal actin organizer, J Cell Biol, *138*, 799-810.

[338] C. Lécuyer, J. L. Dacheux, E. Hermand, E. Mazeman, J. Rousseaux, and R. Rousseaux-Prévost, **2000**, Actin-binding properties and colocalization with actin during spermiogenesis of mammalian sperm calicin, Biol Reprod, *63*, 1801-10.

[339] Y. Chen, R. Derin, R. S. Petralia, and M. Li, **2002**, Actinfilin, a brain-specific actin-binding protein in postsynaptic density, J Biol Chem, *277*, 30495-501.

[340] T. Hara, H. Ishida, R. Raziuddin, S. Dorkhom, K. Kamijo, and T. Miki, **2003**, Novel Kelch-like Protein, KLEIP, Is Involved in Actin Assembly at Cell-Cell Contact Sites of Madin-Darby Canine Kidney Cells, Molecular Biology of the Cell, *15*, 1172-1184.

[341] P. J. Stogios and G. G. Privé, **2004**, The BACK domain in BTB-kelch proteins, Trends Biochem Sci, *29*, 634-7.

[342] M. M. Babu, N. M. Luscombe, L. Aravind, M. Gerstein, and S. A. Teichmann, **2004**, Structure and evolution of transcriptional regulatory networks, Curr Opin Struct Biol, *14*, 283-291.

[343] P. J. Stogios, J. A. Cuesta-Seijo, L. Chen, N. C. Pomroy, and G. G. Privé, **2010**, Insights into Strand Exchange in BTB Domain Dimers from the Crystal Structures of FAZF and Miz1, Journal of Molecular Biology, *400*, 983-997.

[344] J. M. Polo *et al.*, **2004**, Specific peptide interference reveals BCL6 transcriptional and oncogenic mechanisms in B-cell lymphoma cells, Nat Med, *10*, 1329-35.

[345] O. Albagli-Curiel, **2003**, Ambivalent role of BCL6 in cell survival and transformation, Oncogene, *22*, 507-516.

[346] K. F. Ahmad *et al.*, **2003**, Mechanism of SMRT corepressor recruitment by the BCL6 BTB domain, Mol Cell, *12*, 1551-64.

[347] J. A. Costoya and P. P. Pandolfi, **2001**, The role of promyelocytic leukemia zinc finger and promyelocytic leukemia in leukemogenesis and development, Curr Opin Hematol, *8*, 212-7.

[348] K. F. Ahmad, C. K. Engel, and G. G. Privé, **1998**, Crystal structure of the BTB domain from PLZF, Proc Natl Acad Sci U S A, *95*, 12123-8.

[349] M. E. Hoatlin *et al.*, **1999**, A novel BTB/POZ transcriptional repressor protein interacts with the Fanconi anemia group C protein and PLZF, Blood, *94*, 3737-47.

[350] M. Takenaga *et al.*, **2003**, Bcl6-dependent transcriptional repression by BAZF, Biochem Biophys Res Commun, *303*, 600-8.

[351] M. A. Stead and S. C. Wright, **2014**, Nac1 interacts with the POZ-domain transcription factor, Miz1, Biosci Rep, *34*,

[352] A. Weber *et al.*, **2008**, Zbtb4 represses transcription of P21CIP1 and controls the cellular response to p53 activation, Embo j, *27*, 1563-74.

[353] B. N. Jeon *et al.*, **2014**, Two ZNF509 (ZBTB49) isoforms induce cell-cycle arrest by activating transcription of p21/CDKN1A and RB upon exposure to genotoxic stress, Nucleic Acids Res, *42*, 11447-61.

[354] M. L. s. Espinás, E. Jiménez-García, A. Vaquero, S. I. Canudas, J. Bernués, and F. Azorín, **1999**, The N-terminal POZ Domain of GAGA Mediates the Formation of Oligomers That Bind DNA with High Affinity and Specificity*, Journal of Biological Chemistry, *274*, 16461-16469.

[355] K. R. Katsani, M. A. Hajibagheri, and C. P. Verrijzer, **1999**, Co-operative DNA binding by GAGA transcription factor requires the conserved BTB/POZ domain and reorganizes promoter topology, Embo j, *18*, 698-708.

[356] K. D. Huynh and V. J. Bardwell, **1998**, The BCL-6 POZ domain and other POZ domains interact with the co-repressors N-CoR and SMRT, Oncogene, *17*, 2473-84.

[357] K. D. Huynh, W. Fischle, E. Verdin, and V. J. Bardwell, **2000**, BCoR, a novel corepressor involved in BCL-6 repression, Genes Dev, *14*, 1810-23.

[358] Y. Liu and D. Eisenberg, **2002**, 3D domain swapping: as domains continue to swap, Protein Sci, *11*, 1285-99.

[359] C. Tremblay, M. Bédard, M. A. Bonin, and P. Lavigne, **2016**, Solution structure of the 13th C2H2 Zinc Finger of Miz-1, Biochem Biophys Res Commun, *473*, 471-5.

[360] M. Bédard, V. Roy, M. Montagne, and P. Lavigne, **2017**, Structural Insights into c-Myc-interacting Zinc Finger Protein-1 (Miz-1) Delineate Domains Required for DNA Scanning and Sequence-specific Binding, J Biol Chem, *292*, 3323-3340.

[361] D. Bernard, M. Bédard, J. Bilodeau, and P. Lavigne, **2013**, Structural and dynamical characterization of the Miz-1 zinc fingers 5-8 by solution-state NMR, J Biomol NMR, *57*, 103-116.

[362] M. Bédard, L. Maltais, M. E. Beaulieu, J. Bilodeau, D. Bernard, and P. Lavigne, **2012**, NMR structure note: solution structure of human Miz-1 zinc fingers 8 to 10, J Biomol NMR, *54*, 317-23.

[363] J. G. Omichinski, P. V. Pedone, G. Felsenfeld, A. M. Gronenborn, and G. M. Clore, **1997**, The solution structure of a specific GAGA factor-DNA complex reveals a modular binding mode, Nat Struct Biol, *4*, 122-32.

[364] L. Zandarashvili *et al.*, **2012**, Asymmetrical roles of zinc fingers in dynamic DNA-scanning process by the inducible transcription factor Egr-1, Proc Natl Acad Sci U S A, *109*, E1724-32.

[365] L. Zandarashvili, A. Esadze, D. Vuzman, C. A. Kemme, Y. Levy, and J. Iwahara, **2015**, Balancing between affinity and speed in target DNA search by zinc-finger proteins via modulation of dynamic conformational ensemble, Proceedings of the National Academy of Sciences, *112*, E5142-E5149.

[366] K. J. Brayer and D. J. Segal, **2008**, Keep your fingers off my DNA: protein-protein interactions mediated by C2H2 zinc finger domains, Cell Biochem Biophys, *50*, 111-31.

[367] R. S. Brown, **2005**, Zinc finger proteins: getting a grip on RNA, Curr Opin Struct Biol, *15*, 94-8.

[368] Y. Ai, L. Hwang, A. D. MacKerell, Jr., A. Melnick, and F. Xue, **2021**, Progress toward B-Cell Lymphoma 6 BTB Domain Inhibitors for the Treatment of Diffuse Large B-Cell Lymphoma and Beyond, J Med Chem, *64*, 4333-4358.

[369] C. Mlynarczyk, L. Fontán, and A. Melnick, **2019**, Germinal center-derived lymphomas: The darkest side of humoral immunity, Immunol Rev, *288*, 214-239.

[370] S. M. Ranuncolo, J. M. Polo, and A. Melnick, **2008**, BCL6 represses CHEK1 and suppresses DNA damage pathways in normal and malignant B-cells, Blood Cells Mol Dis, *41*, 95-9.

[371] R. T. Phan and R. Dalla-Favera, **2004**, The BCL6 proto-oncogene suppresses p53 expression in germinal-centre B cells, Nature, *432*, 635-9.

[372] W. Ci *et al.*, **2009**, The BCL6 transcriptional program features repression of multiple oncogenes in primary B cells and is deregulated in DLBCL, Blood, *113*, 5536-5548.

[373] S. Parekh *et al.*, **2007**, BCL6 programs lymphoma cells for survival and differentiation through distinct biochemical mechanisms, Blood, *110*, 2067-74.

[374] A. L. Shaffer, X. Yu, Y. He, J. Boldrick, E. P. Chan, and L. M. Staudt, **2000**, BCL-6 represses genes that function in lymphocyte differentiation, inflammation, and cell cycle control, Immunity, *13*, 199-212.

[375] S. Parekh, G. Privé, and A. Melnick, **2008**, Therapeutic targeting of the BCL6 oncogene for diffuse large B-cell lymphomas, Leuk Lymphoma, *49*, 874-882.

[376] J. M. Polo *et al.*, **2007**, Transcriptional signature with differential expression of BCL6 target genes accurately identifies BCL6-dependent diffuse large B cell lymphomas, Proc Natl Acad Sci U S A, *104*, 3207-12.

[377] A. Melnick *et al.*, **2002**, Critical residues within the BTB domain of PLZF and Bcl-6 modulate interaction with corepressors, Mol Cell Biol, *22*, 1804-18.

[378] A. F. Ghetu, C. M. Corcoran, L. Cerchietti, V. J. Bardwell, A. Melnick, and G. G. Privé, **2008**, Structure of a BCOR corepressor peptide in complex with the BCL6 BTB domain dimer, Mol Cell, *29*, 384-91.

[379] K. Sakamoto *et al.*, **2017**, Discovery of high-affinity BCL6-binding peptide and its structure-activity relationship, Biochem Biophys Res Commun, *482*, 310-316.

[380] P. J. Stogios, L. Chen, and G. G. Privé, **2007**, Crystal structure of the BTB domain from the LRF/ZBTB7 transcriptional regulator, Protein Sci, *16*, 336-42.

[381] L. C. Cerchietti *et al.*, **2009**, A peptomimetic inhibitor of BCL6 with potent antilymphoma effects in vitro and in vivo, Blood, *113*, 3397-405.

[382] L. C. Cerchietti *et al.*, **2010**, A small-molecule inhibitor of BCL6 kills DLBCL cells in vitro and in vivo, Cancer Cell, *17*, 400-11.

[383] M. Słabicki *et al.*, **2020**, Small-molecule-induced polymerization triggers degradation of BCL6, Nature, *588*, 164-168.

[384] I. Avivi, D. Stroopinsky, and T. Katz, **2013**, Anti-CD20 monoclonal antibodies: beyond B-cells, Blood Rev, *27*, 217-23.

[385] G. Pavlasova and M. Mraz, **2020**, The regulation and function of CD20: an "enigma" of B-cell biology and targeted therapy, Haematologica, *105*, 1494-1506.

[386] M. A. Stead and S. C. Wright, **2014**, Structures of heterodimeric POZ domains of Miz1/BCL6 and Miz1/NAC1, Acta Crystallogr F Struct Biol Commun, *70*, 1591-1596.

[387] X. Y. Cha, R. C. Pierce, P. W. Kalivas, and S. A. Mackler, **1997**, NAC-1, a rat brain mRNA, is increased in the nucleus accumbens three weeks after chronic cocaine self-administration, J Neurosci, *17*, 6864-71.

[388] J. Wang *et al.*, **2006**, A protein interaction network for pluripotency of embryonic stem cells, Nature, *444*, 364-8.

[389] P. H. Wu, S. H. Hung, T. Ren, M. Shih Ie, and Y. Tseng, **2011**, Cell cycle-dependent alteration in NAC1 nuclear body dynamics and morphology, Phys Biol, *8*, 015005.

[390] BioGRID. "HUWE1." https://thebiogrid.org/115385/summary/homo-sapiens/huwe1.html (accessed May 13, 2021.

[391] H. database. "ZBTB33." https://maayanlab.cloud/Harmonizome/gene_set/ZBTB33/ENCODE+Transcription+Factor+Targets (accessed May 13, 2021.

[392] A. D. Rouillard *et al.*, **2016**, The harmonizome: a collection of processed datasets gathered to serve and mine knowledge about genes and proteins, Database (Oxford), *2016*,

[393] P. A. Wade, **2001**, Methyl CpG-binding proteins and transcriptional repression, Bioessays, *23*, 1131-7.

[394] A. Prokhortchouk *et al.*, **2001**, The p120 catenin partner Kaiso is a DNA methylation-dependent transcriptional repressor, Genes Dev, *15*, 1613-8.

[395] J. M. Daniel, C. M. Spring, H. C. Crawford, A. B. Reynolds, and A. Baig, **2002**, The p120(ctn)-binding partner Kaiso is a bi-modal DNA-binding protein that recognizes both a sequence-specific consensus and methylated CpG dinucleotides, Nucleic Acids Res, *30*, 2911-9.

[396] J. M. Daniel and A. B. Reynolds, **1999**, The catenin p120(ctn) interacts with Kaiso, a novel BTB/POZ domain zinc finger transcription factor, Mol Cell Biol, *19*, 3614-23.

[397] F. M. van Roy and P. D. McCrea, **2005**, A role for Kaiso-p120ctn complexes in cancer?, Nat Rev Cancer, *5*, 956-64.

[398] H.-G. Yoon, D. W. Chan, A. B. Reynolds, J. Qin, and J. Wong, **2003**, N-CoR mediates DNA methylation-dependent repression through a methyl CpG binding protein Kaiso, Molecular cell, *12*, 723-734.

[399] D. I. Koh *et al.*, **2014**, KAISO, a critical regulator of p53-mediated transcription of CDKN1A and apoptotic genes, Proc Natl Acad Sci U S A, *111*, 15078-83.

[400] D. Balchin, M. Hayer-Hartl, and F. U. Hartl, **2016**, In vivo aspects of protein folding and quality control, Science, *353*, aac4354.

[401] E. L. Mena *et al.*, **2018**, Dimerization quality control ensures neuronal development and survival, Science, *362*, eaap8236.

[402] E. L. Mena *et al.*, **2020**, Structural basis for dimerization quality control, Nature, *586*, 452-456.

[403] D. S. Hipps *et al.*, **1994**, The peripheral subunit-binding domain of the dihydrolipoyl acetyltransferase component of the pyruvate dehydrogenase complex of Bacillus stearothermophilus: preparation and characterization of its binding to the dihydrolipoyl dehydrogenase component, Biochem J, *297 (Pt 1)*, 137-143.

[404] P. R. Evans, **2011**, An introduction to data reduction: space-group determination, scaling and intensity statistics, Acta Crystallogr D Biol Crystallogr, *67*, 282-92.

[405] M. D. Winn *et al.*, **2011**, Overview of the CCP4 suite and current developments, Acta Crystallogr D Biol Crystallogr, *67*, 235-242.

[406] P. Emsley and K. Cowtan, **2004**, Coot: model-building tools for molecular graphics, Acta Crystallographica Section D, *60*, 2126-2132.

[407] W. Li *et al.*, **2015**, The EMBL-EBI bioinformatics web and programmatic tools framework, Nucleic Acids Res, *43*, W580-4.

[408] H. McWilliam *et al.*, **2013**, Analysis Tool Web Services from the EMBL-EBI, Nucleic Acids Research, *41*, W597-W600.

[409] F. Sievers *et al.*, **2011**, Fast, scalable generation of high-quality protein multiple sequence alignments using Clustal Omega, Mol Syst Biol, *7*, 539.

[410] P. Artimo *et al.*, **2012**, ExPASy: SIB bioinformatics resource portal, Nucleic Acids Res, *40*, W597-603.

[411] S. Keller, C. Vargas, H. Zhao, G. Piszczek, C. A. Brautigam, and P. Schuck, **2012**, High-precision isothermal titration calorimetry with automated peak-shape analysis, Anal Chem, *84*, 5066-5073.

[412] H. M. Berman *et al.*, **2000**, The Protein Data Bank, Nucleic Acids Res, *28*, 235-42.

[413] A. J. McCoy, R. W. Grosse-Kunstleve, P. D. Adams, M. D. Winn, L. C. Storoni, and R. J. Read, **2007**, Phaser crystallographic software, Journal of Applied Crystallography, *40*, 658-674.

[414] P. D. Adams *et al.*, **2010**, PHENIX: a comprehensive Python-based system for macromolecular structure solution, Acta Crystallogr D Biol Crystallogr, *66*, 213-221.

[415] Z. Lu, **2011**, PubMed and beyond: a survey of web tools for searching biomedical literature, Database (Oxford), *2011*, baq036.

[416] S. R. Bond and C. C. Naus, **2012**, RF-Cloning.org: an online tool for the design of restriction-free cloning projects, Nucleic Acids Res, *40*, W209-13.

[417] C. Vonrhein *et al.*, **2018**, Advances in automated data analysis and processing within autoPROC, combined with improved characterisation, mitigation and visualisation of the anisotropy of diffraction limits using STARANISO, Acta Crystallographica Section A, *74*, a360.

[418] W. Kabsch, **2010**, XDS, Acta Crystallographica Section D, *66*, 125-132.

[419] F. van den Ent and J. Löwe, **2006**, RF cloning: A restriction-free method for inserting target genes into plasmids, Journal of Biochemical and Biophysical Methods, *67*, 67-74.

[420] A. Möglich, **2018**, An Open-Source, Cross-Platform Resource for Nonlinear Least-Squares Curve Fitting, Journal of Chemical Education, *95*, 2273-2278.

[421] P. V. Hornbeck, B. Zhang, B. Murray, J. M. Kornhauser, V. Latham, and E. Skrzypek, **2015**, PhosphoSitePlus, 2014: mutations, PTMs and recalibrations, Nucleic Acids Res, *43*, D512-20.

[422] A. Baluapuri *et al.*, **2019**, MYC Recruits SPT5 to RNA Polymerase II to Promote Processive Transcription Elongation, Molecular Cell, *74*, 674-687.e11.

[423] M. Cianci *et al.*, **2017**, P13, the EMBL macromolecular crystallography beamline at the low-emittance PETRA III ring for high- and low-energy phasing with variable beam focusing, Journal of Synchrotron Radiation, *24*, 323-332.

[424] U. Mueller *et al.*, **2015**, The macromolecular crystallography beamlines at BESSY II of the Helmholtz-Zentrum Berlin: Current status and perspectives, The European Physical Journal Plus, *130*, 141.

[425] A. Drozdetskiy, C. Cole, J. Procter, and G. J. Barton, **2015**, JPred4: a protein secondary structure prediction server, Nucleic Acids Research, *43*, W389-W394.

[426] M. A. Stead *et al.*, **2007**, A beta-sheet interaction interface directs the tetramerisation of the Miz-1 POZ domain, J Mol Biol, *373*, 820-6.

[427] M. Zhuang *et al.*, **2009**, Structures of SPOP-substrate complexes: insights into molecular architectures of BTB-Cul3 ubiquitin ligases, Mol Cell, *36*, 39-50.

[428] M. Hunkeler *et al.*, **2020**, Modular HUWE1 architecture serves as hub for degradation of cell-fate decision factors, bioRxiv, 2020.08.19.257352.

[429] S. Herold *et al.*, **2008**, Miz1 and HectH9 regulate the stability of the checkpoint protein, TopBP1, Embo j, *27*, 2851-61.

[430] K. Baek *et al.*, **2020**, NEDD8 nucleates a multivalent cullin-RING-UBE2D ubiquitin ligation assembly, Nature, *578*, 461-466.

[431] D. Horn-Ghetko *et al.*, **2021**, Ubiquitin ligation to F-box protein targets by SCF–RBR E3–E3 super-assembly, Nature, *590*, 671-676.

7 Appendix

7.1 Supplementary Data

7.1.1 Tables

Table S1: X-ray crystallographic data collection and refinement statistics

	MIZ1[BTB]	MIZ1[BTB]-AS[C] complex
PDB	**7AZW**	**7AZX**
data collection		
wavelength (Å)	1.0332	0.968
resolution (Å)	48.05-2.10 (2.16-2.10)	37.72-2.25 (2.40-2.25)
space group	I121	P3121
unit cell parameters		
a b c (Å)	48.79 34.52 172.56	69.11 69.11 97.15
α β γ (°)	90 96.18 90	90 90 120
total reflections	76616 (6616)	308484 (12141)
unique reflections	17046 (1417)	9023 (450)
R_{pim}	0.069 (0.561)	0.066 (0.684)
completeness (%)	99.8 (99.9)	68.0 (18.8)
I/σ(I)	7.4 (1.2)	13.8 (1.5)
multiplicity	4.5 (4.7)	34.2 (27.0)
Wilson B-factor	31.7	60.5
CC 1/2	0.996 (0.789)	0.999 (0.622)
refinement		
resolution (Å)	35.17-2.10 (2.175-2.10)	34.56-2.248 (2.328-2.248)
reflections used	16959 (1684)	9011 (230)
R_{work}/R_{free}	23.92/28.31	22.80/27.97
number of atoms		
protein	1805	1941
ligands	6	-
water	25	16
average B-factors (Å^2)		
protein	46.0	52.4
ligands	44.4	-
water	35.7	35.5
RMSD from ideality		
bond lengths (Å)	0.002	0.003
bond angles (°)	0.47	0.48
Ramachandran statistics		
favored (%)	96.94	97.96
disallowed (%)	0.00	0.00
MolProbity clash score	4.43	4.41

Table S2: Dissociation constants

protein	peptide ligand	K_D / µM	method
MIZ1^{BTB} variant			
WT	AS^C	10.0 ± 0.9	FP
WT	AS^C	3.1 ± 0.7	ITC
F28A	AS^C	n. d.	FP
L52A	AS^C	9 ± 1	FP
F53A	AS^C	15.8 ± 1.5	FP
V60P	AS^C	60 ± 2	FP
H61A	AS^C	16.9 ± 1.2	FP
L62A	AS^C	88.8 ± 8.1	FP
I64A	AS^C	n. d.	FP
WT	AS^C L3877A	n. d.	FP
WT	AS^C L3879A	33.2 ± 1.6	FP
WT	AS^C F3886A	n. d.	FP
WT	AS^C F3887A	n. d.	FP
WT	AS^C L3877A/F3887A	n. d.	FP
WT	AS^N	n. d.	FP
MIZ1^{BTB} variant (without cloning overhang)			
WT (residues 1-115)	AS^C	10 ± 1	FP
V10D/L14D/Q17D/V41K (monomer)	AS^C	n. d.	
MIZ1-BCL6 heterodimer	AS^C	121 ± 22	FP
MIZ1-NAC1 heterodimer	AS^C	187 ± 20	FP

7.1.2 Recombinant protein purifications: chromatograms and corresponding SDS-gels

7.1.2.1 MIZ1 variants
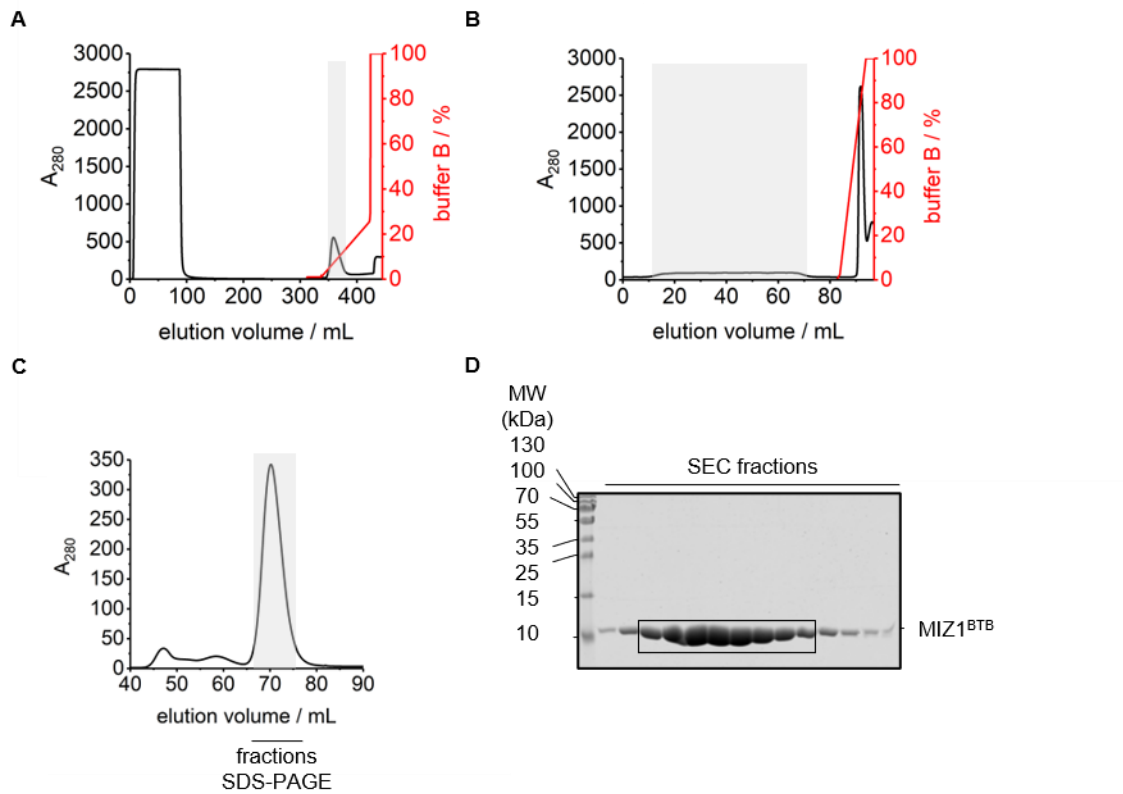
Figure S1: Chromatograms of the individual purification steps during the MIZ1^{BTB} (aa 1-115, with N-terminal GGSMA-cloning overhang) purifications.
(A) Ni-affinity chromatography of His$_6$-lipoyl-MIZ1^{BTB}. The A$_{280}$ signal (left y-axis) is shown in black, the concentration of buffer B in buffer A (right axis in %) is shown in red. (B) Inverse Ni-affinity chromatography after TEV protease-mediated cleavage of the His$_6$-lipoyl-domain-tag during overnight dialysis; colour code as in (A). (C) Preparative SEC with a SD75 16/600 column. The peak fractions analyzed by SDS-PAGE and the pooled fractions (grey box) are indicated. (D) Protein-containing fractions from the SEC shown in (C), analyzed by SDS-PAGE and Coomassie staining.
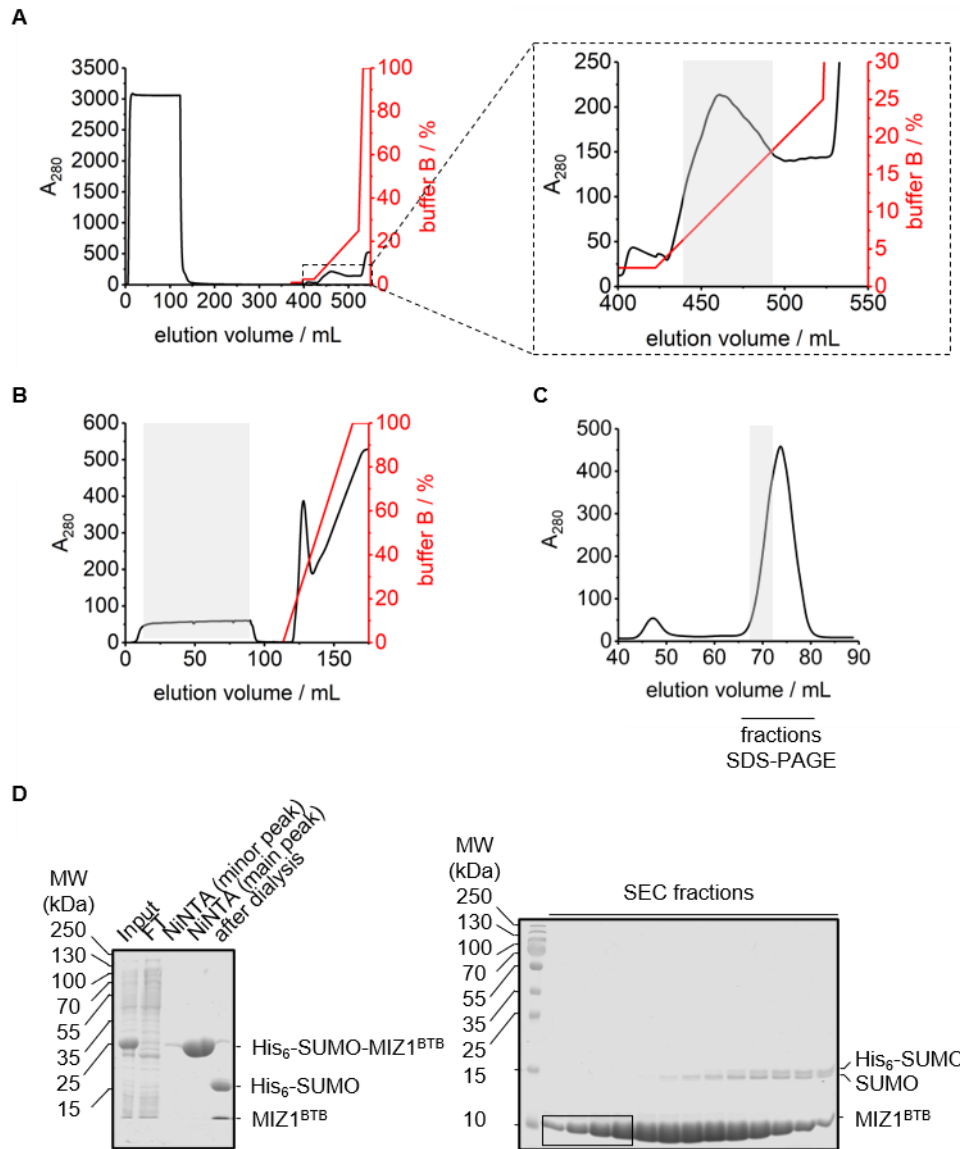
Figure S2: Chromatograms of the individual purification steps during the MIZ1^{BTB} (aa 1-115, without cloning overhang) purifications.
(A) Ni-affinity chromatography of His$_6$-SUMO-MIZ1^{BTB}. The A$_{280}$ signal (left y-axis) is shown in black, the concentration of buffer B in buffer A (right axis in %) is shown in red; detail of the eluted protein peak (dotted box) and the pooled fractions (grey box) are indicated. (B) Inverse Ni-affinity chromatography after ULP1 protease-mediated cleavage of the His$_6$-SUMO-tag during overnight dialysis; colour code as in (A). (C) Preparative SEC with a SD75 16/600 column. The peak fractions analyzed by SDS-PAGE and the pooled fractions (grey box) are indicated. (D) Protein-containing fractions from the Ni-affinity chromatgraphy and the SEC shown in (A) and (C), analyzed by SDS-PAGE and Coomassie staining.

Figure S3: Chromatograms of the individual purification steps during the MIZ1^BTB-BCL6^BTB heterodimer (aa 1-115 of MIZ1, aa 5-129 of BCL6) purifications.
(A) Ni-affinity chromatography of His$_6$-SUMO-MIZ1^{BTB}-BCL6^{BTB}. The A$_{280}$ signal (left y-axis) is shown in black, the concentration of buffer B in buffer A (right axis in %) is shown in red; detail of the eluted protein peak (dotted box) and the pooled fractions (grey box) are indicated. (B) Inverse Ni-affinity chromatography after ULP1 protease-mediated cleavage of the His$_6$-SUMO-tag during overnight dialysis; colour code as in (A). (C) Preparative SEC with a SD75 16/600 column. The peak fractions analyzed by SDS-PAGE and the pooled fractions (grey box) are indicated. (D) Protein-containing fractions from the Ni-affinity chromatgraphy and the SEC shown in (A) and (C), analyzed by SDS-PAGE and Coomassie staining.

Figure S4: Chromatograms of the individual purification steps during the MIZ1^BTB-NAC1^BTB heterodimer (aa 1-115 of MIZ1, aa 2-125 of NAC1) purifications.
(A) Ni-affinity chromatography of His$_6$-SUMO-MIZ1^{BTB}-NAC1^{BTB}. The A$_{280}$ signal (left y-axis) is shown in black, the concentration of buffer B in buffer A (right axis in %) is shown in red; detail of the eluted protein peak (dotted box) and the pooled fractions (grey box) are indicated. (B) Inverse Ni-affinity chromatography after ULP1 protease-mediated cleavage of the His$_6$-SUMO-tag during overnight dialysis; colour code as in (A). (C) Preparative SEC with a SD75 16/600 column. The peak fractions analyzed by SDS-PAGE and the pooled fractions (grey box) are indicated. (D) Protein-containing fractions from the Ni-affinity chromatgraphy and the SEC shown in (A) and (C), analyzed by SDS-PAGE and Coomassie staining.

Figure S5: Chromatograms of the individual purification steps during the MIZ1$^{1\text{-}282}$ (aa 1-282, with C-terminal HA-His$_6$-tag) purifications.

(A) Ni-affinity chromatography of MBP-MIZ1$^{1\text{-}282}$-HA-His$_6$. The A$_{280}$ signal (left y-axis) is shown in black, the concentration of buffer B in buffer A (right axis in %) is shown in red. (B) Inverse Ni-affinity chromatography after TEV protease-mediated cleavage of the MBP-tag by overnight dialysis; colour code as in (A). (C) Preparative SEC with a SD200 16/600 column. The peak fractions analyzed by SDS-PAGE and the pooled fractions (grey box) are indicated. (D) Protein-containing fractions from the SEC shown in (C), analyzed by SDS-PAGE and Coomassie staining.

170

7.1.2.2 HUWE1 variants
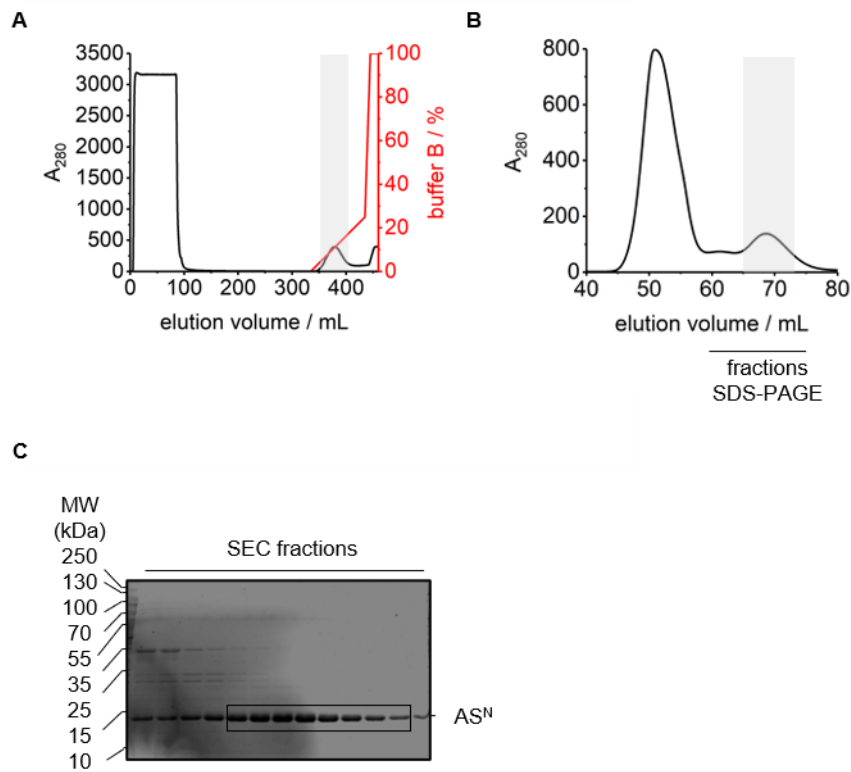
Figure S6: Chromatograms of the individual purification steps during the HUWE1-AS^N (aa 3843-3869, with N-terminal lipoyl domain-tag) purifications.
(A) Ni-affinity chromatography of His$_6$-lipoyl-AS^N. The A$_{280}$ signal (left y-axis) is shown in black, the concentration of buffer B in buffer A (right axis in %) is shown in red; detail of the eluted protein peak (dotted box) and the pooled fractions (grey box) are indicated. (B) Preparative SEC with a SD75 16/600 column. The peak fractions analyzed by SDS-PAGE and the pooled fractions (grey box) are indicated. (C) Protein-containing fractions from the SEC shown in (B), analyzed by SDS-PAGE and Coomassie staining.
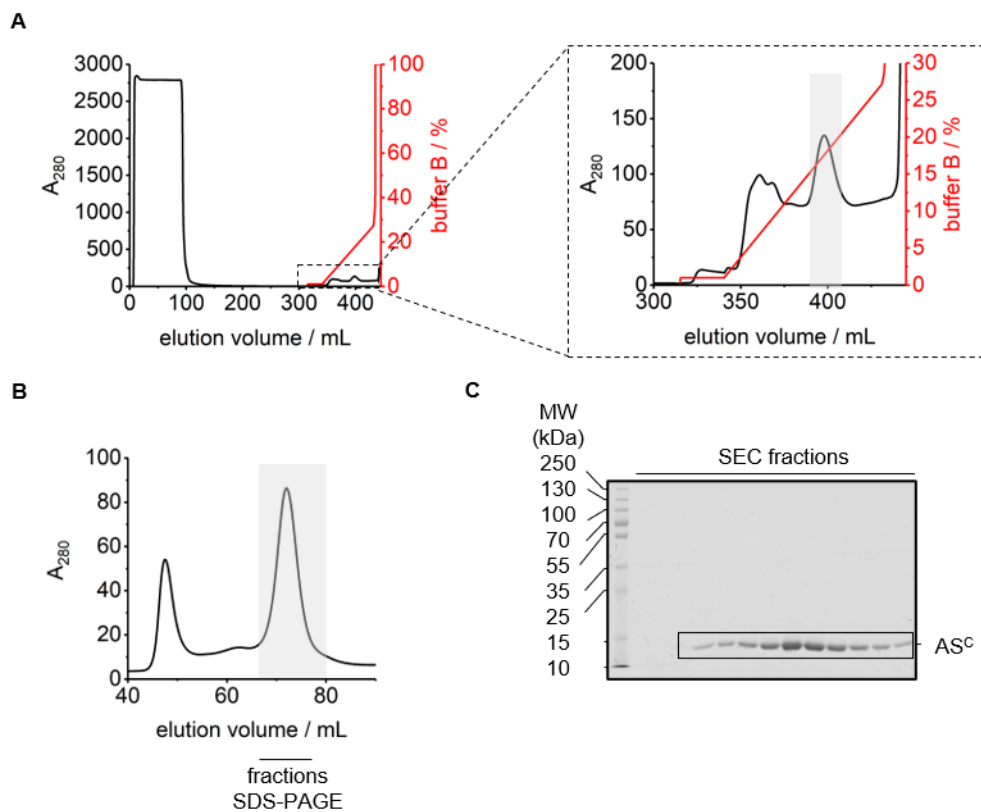
Figure S7: Chromatograms of the individual purification steps during the HUWE1-AS^C (aa 3870-3890, with N-terminal lipoyl domain-tag) purifications.
(A) Ni-affinity chromatography of His$_6$-lipoyl-AS^C. The A$_{280}$ signal (left y-axis) is shown in black, the concentration of buffer B in buffer A (right axis in %) is shown in red; detail of the eluted protein peak (dotted box) and the pooled fractions (grey box) are indicated. (B) Preparative SEC with a SD75 16/600 column. The peak fractions analyzed by SDS-PAGE and the pooled fractions (grey box) are indicated. (C) Protein-containing fractions from the SEC shown in (B), analyzed by SDS-PAGE and Coomassie staining.

172
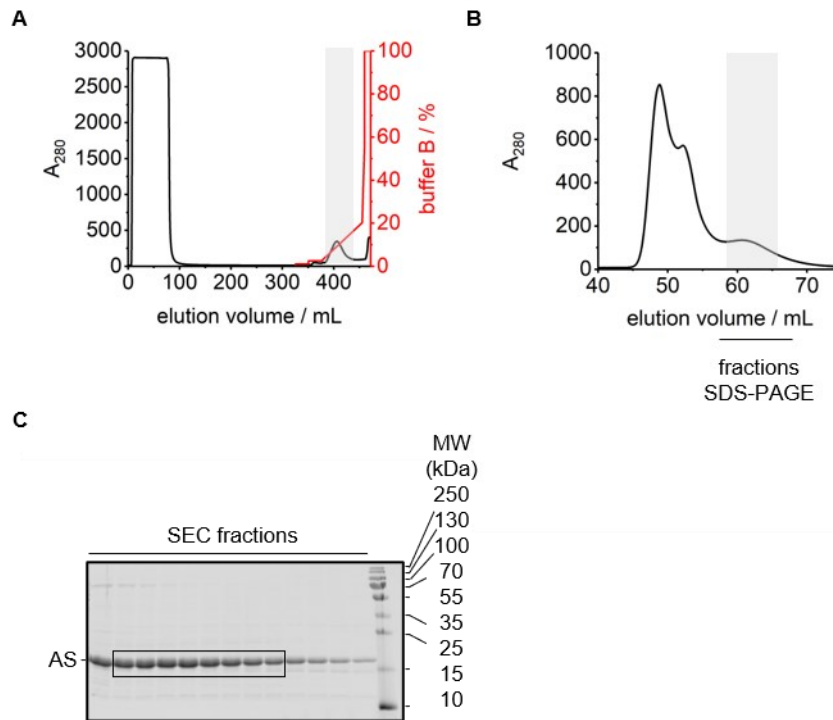
Figure S8: Chromatograms of the individual purification steps during the HUWE1-AS (aa 3843-3890, with N-terminal lipoyl domain-tag) purifications.
(A) Ni-affinity chromatography of His_6-lipoyl-AS. The A_{280} signal (left y-axis) is shown in black, the concentration of buffer B in buffer A (right axis in %) is shown in red; detail of the eluted protein peak (dotted box) and the pooled fractions (grey box) are indicated. (B) Preparative SEC with a SD75 16/600 column. The peak fractions analyzed by SDS-PAGE and the pooled fractions (grey box) are indicated. (C) Protein-containing fractions from the SEC shown in (B), analyzed by SDS-PAGE and Coomassie staining.
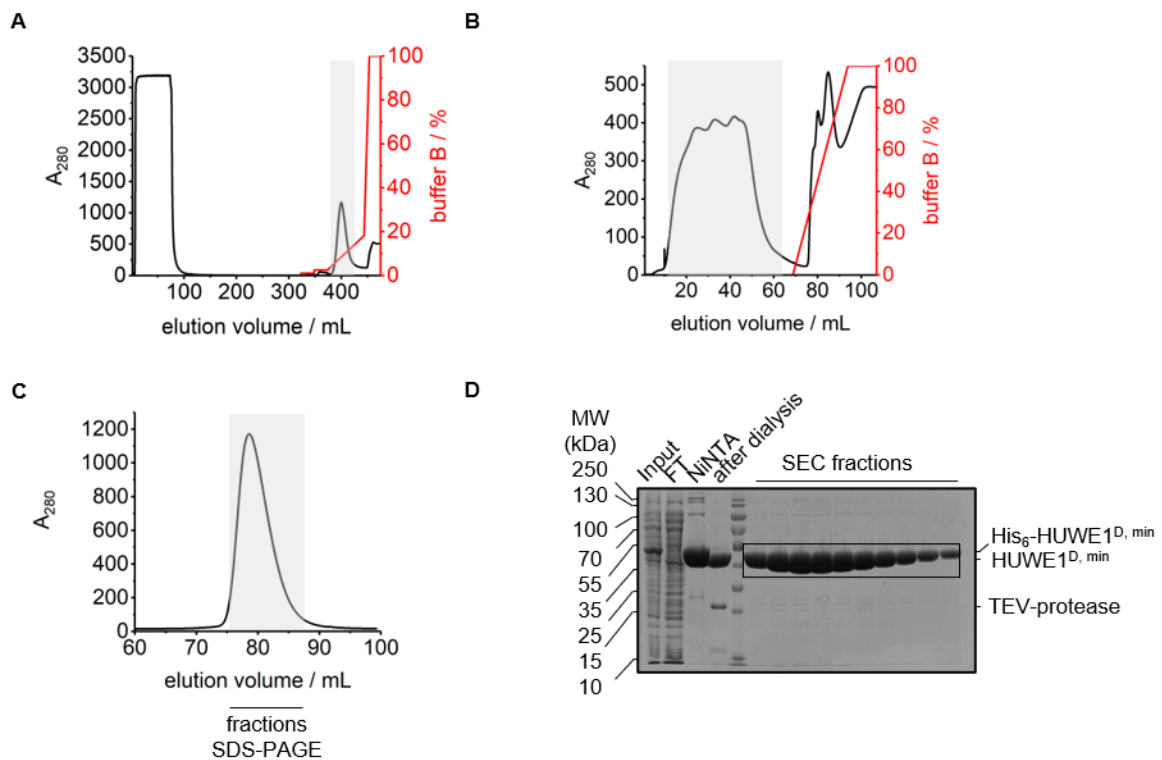
Figure S9: Chromatograms of the individual purification steps during the HUWE1$^{D, min}$ (aa 3951-4374) purifications.

(A) Ni-affinity chromatography of His$_6$-HUWE1$^{D, min}$. The A$_{280}$ signal (left y-axis) is shown in black, the concentration of buffer B in buffer A (right axis in %) is shown in red. (B) Inverse Ni-affinity chromatography after TEV protease-mediated cleavage of the His$_6$-tag during overnight dialysis; colour code as in (A). (C) Preparative SEC with a SD200 16/600 column. The peak fractions analyzed by SDS-PAGE and the pooled fractions (grey box) are indicated. (D) Protein-containing fractions from the Ni-affinity chromatgraphy and the SEC shown in (A) and (C), analyzed by SDS-PAGE and Coomassie staining.
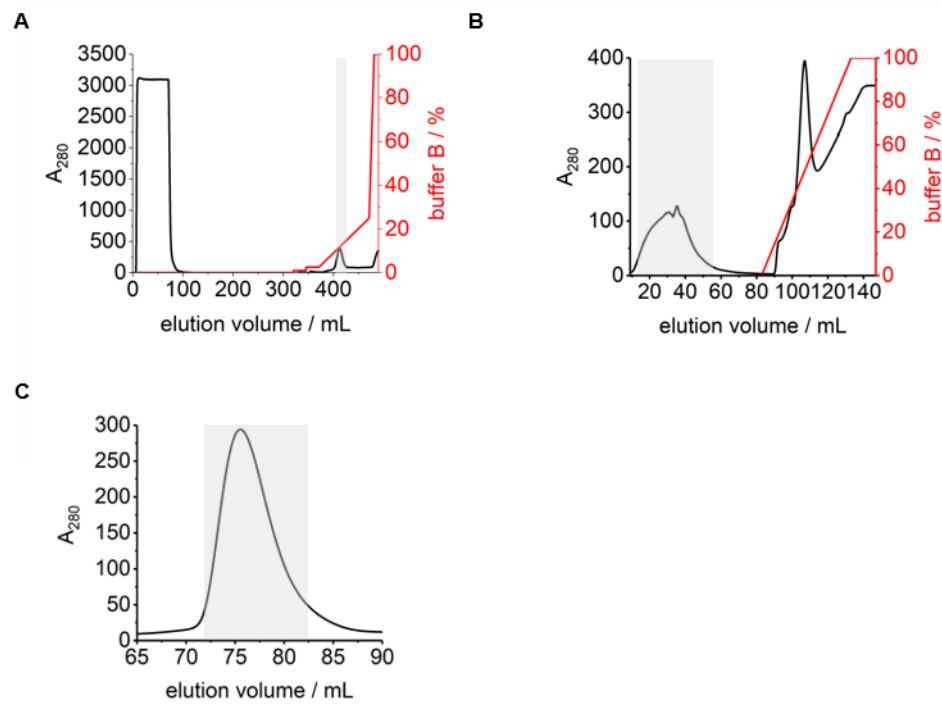
Figure S10: Chromatograms of the individual purification steps during the HUWE1^D (aa 3896-4374) purifications.
(A) Ni-affinity chromatography of His$_6$-HUWE1^D. The A$_{280}$ signal (left y-axis) is shown in black, the concentration of buffer B in buffer A (right axis in %) is shown in red. (B) Inverse Ni-affinity chromatography after TEV protease-mediated cleavage of the His$_6$-tag during overnight; colour code as in (A). (C) Preparative SEC with a SD200 16/600 column. The peak fractions analyzed by SDS-PAGE and the pooled fractions (grey box) are indicated.
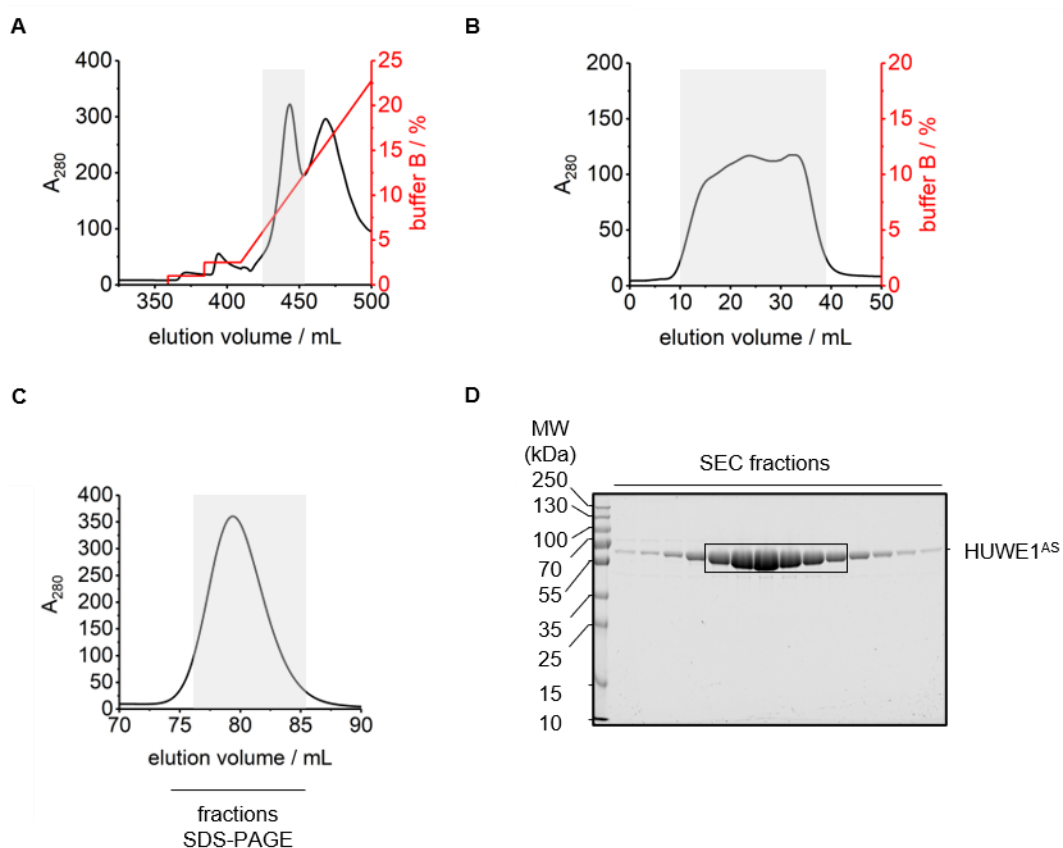
Figure S11: Chromatograms of the individual purification steps during the HUWE1[AS] (aa 3843-4374) purification.
(A) Ni-affinity chromatography of His₆-HUWE1[AS]. The A_{280} signal (left y-axis) is shown in black, the concentration of buffer B in buffer A (right axisin %) is shown in red. (B) Inverse Ni-affinity chromatography after TEV protease-mediated cleavage of the His₆-tag during overnight dialysis; colour code as in (A). (C) Preparative SEC with a SD200 16/600 column. The peak fractions analyzed by SDS-PAGE and the pooled fractions (grey box) are indicated. (D) Protein-containing fractions from the SEC shown in (C), analyzed by SDS-PAGE and Coomassie staining.

7.1.2.3 KAISO^{BTB}
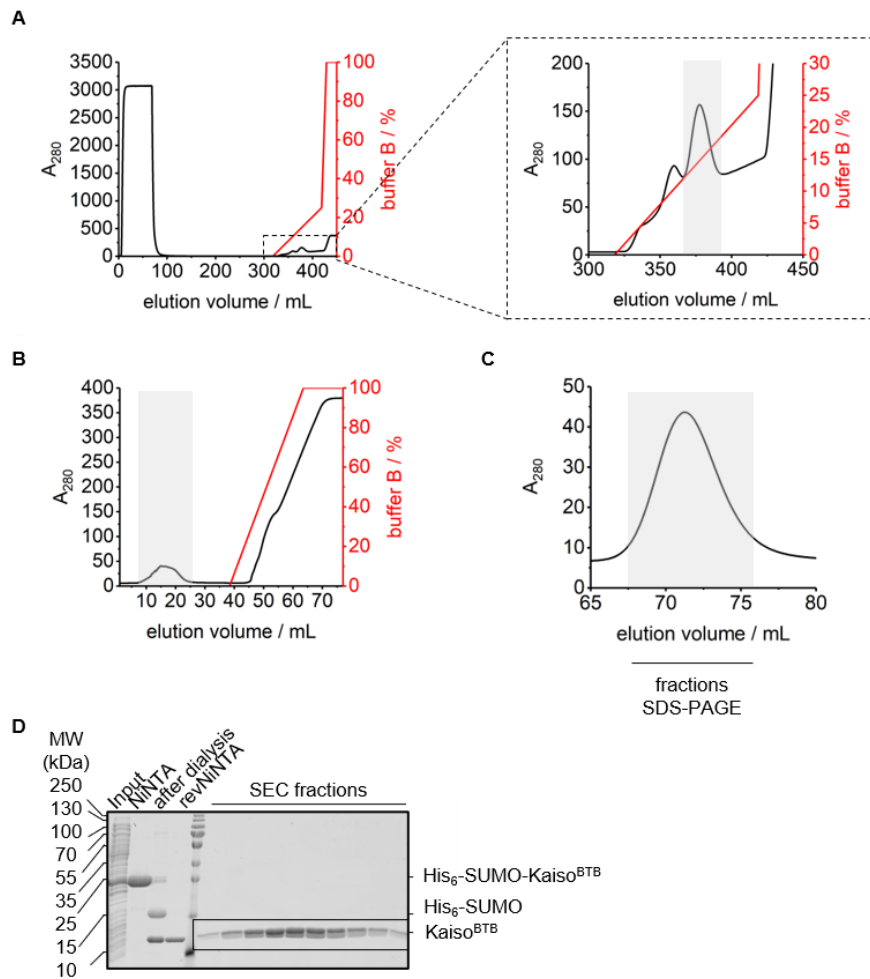
Figure S12: Chromatograms of the individual purification steps during the KAISO^{BTB} (aa 1-122) purifications.
(A) Ni-affinity chromatography of His$_6$-SUMO-KAISO^{BTB}. The A$_{280}$ signal (left y-axis) is shown in black, the concentration of buffer B in buffer A (right axis in %) is shown in red; detail of the eluted protein peak (dotted box) and the pooled fractions (grey box) are indicated. (B) Inverse Ni-affinity chromatography after ULP1 protease-mediated cleavage of the His$_6$-SUMO-tag during overnight dialysis; colour code as in (A). (C) Preparative SEC with a SD75 16/600 column. The peak fractions analyzed by SDS-PAGE and the pooled fractions (grey box) are indicated. (D) Protein-containing fractions from the Ni-affinity chromatgraphy and the SEC shown in (A) and (C), analyzed by SDS-PAGE and Coomassie staining.

Figure S13: Chromatograms of the individual purification steps for the KAISO^BTB-HA (aa 1-122, with C-terminal HA-tag) purifications.

(A) Ni-affinity chromatography of His$_6$-SUMO-KAISO^{BTB}-HA. The A$_{280}$ signal (left y-axis) is shown in black, the concentration of buffer B in buffer A (right axis in %) is shown in red; detail of the eluted protein peak (dotted box) and the pooled fractions (grey box) are indicated. (B) Inverse Ni-affinity chromatography after ULP1 protease-mediated cleavage of the His$_6$-SUMO-tag during overnight dialysis; colour code as in (A). (C) Preparative SEC with a SD75 16/600 column. The peak fractions analyzed by SDS-PAGE and the pooled fractions (grey box) are indicated. (D) Protein-containing fractions from the Ni-affinity chromatgraphy and the SEC shown in (A) and (C), analyzed by SDS-PAGE and Coomassie staining.

7.2 Appreviations

A	Adenine
A	Alanine
A	Helical secondary structure elements, named as in [319]
Å	Ångström
α	Anti; helical secondary structure element
aa	Amino acid
Ac	Acetylation
AMP	Adenosine monophosphate
APC/C	Anaphase-promoting complex/cyclosome
APS	Ammoniumpersulfate
AREL1	Apoptosis-resistant E3 ubiquitin-protein ligase 1
ARF	Alternative Reading Frame (tumor suppressor)
Arg	Arginine
ARLD	Armadillo repeat-like domains
AS	Activation segment
Atoh1	Atonal homolog 1; bHLH tanscription factor
ATP	Adenosine triphosphate
B	Beta-strands as secondary structure element, named as in [319]
b	Base
β	Beta strands as secondary structure element
BACK	BTB and carboxy-terminal kelch
BARD1	BRCA1-associated RING domain protein 1
BAZF	BCL6-associated zinc finger protein
BBD	BCL6 binding domain
BCA	Bicinchoninic acid
BCL	B-cell lymphoma
BCOR	BCL6 corepressor
BESSY	Berlin electron storage ring society for synchrotron radiation
BH	BCL-2 homology (domain)
BIRC7	Baculoviral IAP repeat-containing protein 7
bp	Base pair
BRCA1	Breast Cancer type 1 susceptibility protein
BRD4	Bromodomain-containing protein 4
BS	Binding site
BSA	Bovine serum albumine
BTB	Bric-à-brac, tramtrack and broad complex
C	Cysteine
C	Carboxy (terminus)
C	Cytosine
c	Centi
°C	Degree Celsius
Ca	Calcium
cal	Calorie
Cat#	Catalogue number
CC1/2	Correlation coefficient 1/2
Cdc	Cell division cyle
Cdh1	CDC20-like protein 1; also known as Fzr = Fizzy-related protein homolog
CDKN	Cyclin dependent kinase inhibitor
cDNA	Complementary DNA
CHIP	Carboxyl-terminus of HSC70-interacting protein
CHIP-seq	Chromatin-Immunoprecipitation sequencing
cIAP	Cellular inhibitor of apoptosis protein
CO_2	Carbon dioxide
CRBN	Cereblon
CRL	Cullin-RING-Ligase

CUL	Cullin
D	Aspartic acid
D(, min)	(Minimal) dimerizing (fragment)
Δ	Deletion
Δ(G; H; S)	Change
Da	Dalton
ddH$_2$O	Double-distilled water
DDIT4	DNA damage inducible transcript 4
DESY	Deutsches Elektronen-Synchroton
DLBCL	Diffuse large B-cell lymphoma
DM	Double mutant
DMBA	7,12-dimethylbenz(a)anthracene
DMEM	Dulbecco's modified eagle medium
DMSO	Dimethylsulfoxide
dN	N-terminally truncated construct (here: dN-HUWE1; aa 2474-4374 of HUWE1)
DNA	Deoxyribonucleic acid
DNase	Deoxyribunuclease
dNTP	Deoxyribonucleoside triphosphate (dATP, dCTP, dGTP, dTTP)
DR	Dimerization region
DTT	Dithiothreitol
DUF	Domain of unknown function
Dvl	Dishevelled
E1	Ubiquitin activating enzyme
E2	Ubiquitin conjugating enzyme
E3	Ubiquitin ligase
E6AP	E6-associated protein
E. coli	Escherichia coli
ECL	Enhanced chemiluminescence
EDTA	Ethylendiamintetraacetate deoxyribonucleic acid
e. g.	Exempli gratia (latin); for example
EM	Electron microscopy
EMBL	European molecular biology laboratory
ER	Endoplasmic reticulum
ERAD	ER-associated protein degradation
ESRF	European synchroton radiation facility
Et al	Et alii (latin); and others
EtOH	Ethanol
Exp.	Exposure
F	Phenylalanine
F	Forward
FAM	Fluorescein
FAZF	Fanconi anemia zinc finger protein
FBW7	F-box/WD repeat containing protein 7
FBXL	F-box and leucine rich repeat protein
FBXO28	F-box only protein 28
FCS	Fetal calf serum
Fl	Full-length
Flag	Denotes the octapeptide DYKDDDDK
FP	Fluorescence polarization
fw	Forward
Fwd	Forward
G	Gibbs free energy
G	Guanine
g	Gram; gravitational acceleration
GC	Germinal center
G2E3	G2/M phase-specific E3 ubiquitin-protein ligase
GEF	Guanine nucleotide exchange factor

Gfi-1	Growth factor independent protein 1; zinc finger protein and transcriptional repressor
Gln	Glutamine
H	Helmholtz free energy
H	Histidine
H	Histone
h	Human
h	Hour
H_2O	Water
HA	Human influenza hemagglutinin
HACE1	HECT domain and ankyrin repeat containing E3 ubiquitin protein ligase 1
H2AX	Histone H2A variant
HDAC	Histone deacetylase
HDMX; HDM4	Human homolog of murine double minute X or 4
HECT	Homologous to the E6AP carboxyl-terminus
HECTD	HECT domain E3 ubiquitin protein ligase
HECW	HECT, C2 and WW domain containing E3 ubiquitin protein ligase
HEK293T	Human embryonic kidney cell line
HeLa	Human cervical cancer cell line
HEPES	2-[4-(2-hydroxyethyl)piperazin-1-yl]ethanesulfonic acid
HERC	HECT domain and RCC1-like domain-containing protein
HHARI	Human homolog of Drosophila ariadne
HIF-1α	Hypoxia-inducible factor 1 alpha
His_6	Hexahistidine
HK	Hexokinase 2
HOIL-1L	Heme-oxidized IRP2 ubiquitin ligase 1L
HOIP	HOIL-1L interacting protein
HPV	Human papillomavirus
HRP	Horseradish peroxidase
HUWE1	HECT, UBA and WWE domain-containing protein 1
HWA	HUWE1 WWE module associated (domain)
IBR	In-between-RING
i. e.	Id est (latin); that is
IgG	Immunoglobulin G
IL-7	Interleukin-7
Ile	Isoleucine
IMiD	Immunomodulatory (imide) drug
IMP	Research institute of molecular pathology
INK(4B)	Inhibitor of the cyclin dependent kinase (4B)
IP	Immunoprecipitation; immunoprecipitated
IPTG	Isopropyl β-D-1-thiogalactopyranoside
ITC	Isothermal titration calorimetry
ITCH	E3 ubiquitin protein ligase Itchy homolog
JAMM	JAB1/MPN/MOV34 metalloproteases; also known as MPN+ proteases
JNK	C-JUN N-terminal kinase
K	Lysine
k	Kilo
K_D	Dissociation constant
KIP	Kinase inhibitor protein
KO	Knockout
K_v	Voltage-gated potassium channels
L	Leucine
l	Liter
LB	Lysogeny broth
Leu	Leucine
LPS	Lipopolysaccharide
LUBAC	Linear ubiquitin chain assembly complex

M	Molar (mol/l)
M	(Molecular weight) marker
m	Meter
m	Milli
µ	Micro
min	Minute
MALS	Multi-angle light scattering
MATH	Meprin and TRAF-homology (domain)
MAX	MYC-associated factor X
MBP	Maltose binding protein
MCL1	Induced myeloid leukemia cell differentiation protein 1
MDMX; MDM2	Murine double minute X or 2; E3 ubiquitin ligase
MEF	Mouse embryonic fibroblast cell line
MFN2	Mitofusin 2
Mfr1	Meiotic fizzy-related protein 1; APC/C coactivator
$MgCl_2$	Magnesium chloride
MINDY	Motif interacting with Ub-containing novel DUB famiily
MIZ1	Myc-interacting zinc finger 1
MJD	Machado-Joseph domain-containing protease
mL	Milliliter
MPI	Max-Planck institute
MW	Molecular weight
MWCO	Molecular weight cut-off
MYC	Proto-oncogene; bHLH transcription factor
MYCBP2	MYC binding protein 2
MyoD	Myoblast determination protein
N	Amino (terminus)
n	Nano
n	Number (of performed experiments)
n	Stoichiometry
NAC	Nucleus accumbens associated protein
NaCl	Sodium chloride
Na_2HPO_4	Disodium hydrogen phosphate
NCOR	Nuclear receptor corepressor
NEAA	Non-essential amino acids
NEB	New England Biolabs
NEDD	Neural precursor cell expressed developmentally down-regulated protein
NF-κB	Nuclear factor kappa-light-chain-enhancer of activated B cells
Ni	Nickel
NMR	Nuclear magnetic resonance
NP-40	Nonidet P-40
NPM	Nucleophosmin 1
NTA	Nnitrilotriacetic acid
OD_{600}	Optical density (= absorbance) measured at a wavelength of 600 nm
OUT	Ovarian tumor domain-containing protease
P	Phosphorylation
P	Polarization
P	Proline
%	Percent
PAGE	Polyacrylamide gel electrophoresis
PARKIN	PARKINson´s disease associated protein; E3-ubiquitin-protein ligase
PBS	Phosphate-buffered saline
PBS-T	Phosphate-buffered saline with Tween-20
PCNA	Proliferating cell nuclear antigen
PCR	Polymerase chain reaction
p120ctn	p120 catenin; a component of the cadherin-catenin complex

PDB	Protein data bank
PEG	Polyethylene glycol
PEI	Polyethylenimine
PETRA	Positron-electron tandem ring accelerator
pH	Potentia Hydrogenii (latin)
Phe	Phenylalanine
PINK1	PTEN-induced kinase 1
PIP	PCNA-interacting protein(-box)
PLZF	Promyelocytic leukemia zinc finger protein
PMA	12-O-tetra-decanoylphor-bol-13-acetate
PML	Promyelocytic leukemia
Pol	DNA-polymerase
POZ	Pox virus and zinc finger
PP_i	Pyrophospate
PPARα	Peroxisome proliferator-activated receptor alpha
Prep	Preparation
PROTAC	Proteolysis targeting chimera
PSMD	26S proteasome non-ATPase regulatory subunit
PTEN	Phosphatase and tensin homolog
PTM	Post-translational modification
PVDF	Polyvinylidene difluoride
Q	Glutamine
QM	Quadruple mutant
R	Arginine
R	Reverse
RAC	Ras-related C3 botulinum toxin substrate
Ras	Rat sarcoma
RBR	RING-between-RING E3 ligase
Rbx1	RING-box protein 1
RCC1	Regulator of chromosome condensation 1
RCR	RING-Cys-relay
RE	Response element
Rev	Reverse
RF	Restriction free
RI-BPI	Retroinverso BCL6 peptide inhibitor
RING	Really interesting new gene
RITA	Reactivation of p53 and induction of tumor cell apoptosis
RLD	Regulator of chromosome condensation 1-like domain
rmsd	Root-mean-square deviation
rpm	Revolutions per minute
RNA	Ribonucleic acid
RNF	RING finger protein
R_{pim}	Precision indicating merging R-factor
RPS27A	Ubiquitin-40S ribosomal protein S27A
RSP5	Reverses SPT-phenotype protein 5
RT	Room temperature
RVZ	Rudolf virchow center
RZ	RNF213-ZNFX1
S	Entropy
S	Serine
s	Second
SCF	Skp1-cullin-F-box (multiprotein complex)
SD	Standard deviation
SD	Superdex
SDM	Site directed mutagenesis
SDS	Sodium dodecyl sulfate
SEC	Size-exclusion chromatography

sec	Second
SHARPIN	SHANK-associated RH domain-interacting protein
shRNA	Small hairpin ribonucleic acid
SIAH1	Seven In absentia homolog 1; E3-ligase
Skp	S-phase kinase-associated protein
SMRT	Silencing mediator of retinoic acid and thyroid hormone receptor
SMURF	SMAD ubiquitination regulatory factor
SPOP	Speckle-type POZ protein
Strep	Streptavidin
SUMO	Small ubiquitin-related modifier
T	Thymine
T1	Tetramerization (domain)
TAE	Tris-acetate-EDTA
TBP	TATA box-binding protein
TBS	Tris-buffered saline
TBS-T	Tris-buffered saline with Tween-20
TC	Tandem cysteine
TEMED	N,N,N',N'-tetramethylethylendiamine
TEV	Tobacco etch virus
TGF-β	Transforming growth factor β
TIAM1	T-lymphoma invasion and metastasis-inducing protein 1
TNF	Tumor necrosis factor
TOPBP1	DNA topoisomerase II binding protein 1
TRAF	TNF receptor associated factor
TRIP12	Thyroid hormone receptor interactor 12
Tris	Tris-(hydroxymethyl)-aminomethane
Tsp	Transcription start point
Ub	Ubiquitin
UB (B; C)	Ubiquitin (B; C)
Ub_n	polyubiquitination
UBA	Ubiquitin-associated domain
UBA1	Ubiquitin-activating protein 1
UBA52	Ubiquitin-60S ribosomal protein L40
UBAN	UBD in ABIN proteins and NEMO
UBC	Ubiquitin binding domain
UBCH	Ubiquitin-conjugating enzyme H
UBD	Ubiquitin binding domain
UBE(3B; 3C)	Ubiquitin-protein ligase E3B; 3C
UBE2S	Ubiquitin-conjugating-enzyme E2S
UBM	ubiquitin-binding motif
UBR5	Ubiquitin Protein Ligase E3 Component N-Recognin 5
UCH	Ubiquitin carboxyl-terminal hydrolase
UIM	Ubiquitin-interacting motif
ULP1	Ubiquitin-like-specific protease 1
UPS	Ubiquitin-proteasome system
USP	Ubiquitin-specific protease
UV	Ultraviolet
V	Valine
Val	Valine
VCP	Valosin-containing protein
VHL	Von-Hippel-Lindau
WT	Wild type
WWP1	WW domain containing E3 ubiquitin protein ligase 1
x	Fold
XLID	X-linked intellectual disability
ZBTB	Zinc finger and BTB domain-containing protein
ZF	Zinc finger
ZNFX1	Zinc finger NFX1-type containing protein 1

ZID	Zinc finger protein with interaction domain
Zn	Zinc
ZUP1	Zinc finger containing ubiquitin peptidase 1

7.3 List of figures

7.4 List of tables

7.5 Publication

The main findings of this thesis were published in the following article:

B. Orth, B. Sander, A. Möglich, K. Diederichs, M. Eilers, S. Lorenz, Identification of an atypical interaction site in the BTB domain of the MYC-interacting zinc-finger protein 1, *Structure* **2021**, *29*, 1-11.

7.7 Acknowledgements

I would like to thank Dr. Sonja Lorenz for giving me the opportunity to work on this interesting and exciting project which turned out to be more or differently diverse than expected at the start. Thank you for the support, guidance and encouragement at any time and the certainty of making the best of it together, even in difficult situations.

Thank you also to Prof. Dr. Martin Eilers for his support, the helpful discussions, ideas and advices throughout the project and the always open doors to the cell culture laboratories at the Biocenter.

I also would like to thank Prof. Dr. Volker Dötsch for being part of my committee, his interest and ideas for my PhD project.

Having a good working environment and nice people around makes everything much easier and I am glad that I only made good experiences in this point through the whole time as a PhD student. Therefore, I would like to thank first of all Anna, Bodo, Julia and Lena, who gave me a warm welcome in the Lorenz group and made my start in Würzburg very easy. I am really grateful that Bodo shared all his experience with me and introduced me to all the different methods which was essential and the basis for all the results presented here. Thank you also to Julia for her constant support by taking care of the general stocks, but also for her support in project specific protein preparations. Thanks to Rahul with whom I shared all the time in Würzburg, the lab bench and all the up´s and down´s during the time as a PhD student and a friendship in which one could be sure of mutual support. Thank you to all the other people at the RVZ in Würzburg for the nice working environment, where I always enjoyed working. Thanks also to Theresa, Daniel and Jessy at the Biocenter in Würzburg for their support with the cell culture work and that there was always a bench that I could occupy for some time ;-) Finally, I am happy that with Ayshwarya, Jonas and Thornton great people were part of the move of the Lorenz group to the Max Planck Institute for Biophysical Chemistry in Göttingen where we were given a warm welcome and could be sure of any kind of support, so that we could quickly get used to the new working environment, even during a pandemic.

Any project needs a financial source. Therefore, I am thankful that I could be part of the GRK2243: Understanding Ubiquitylation: From molecular mechanisms to

disease" and that I could benefit from workshops, in addition to those offered by the Graduate School of Life Science in Würzburg which also makes an important contribution to the completion of a doctoral thesis and offers a lot of opportunities to get insights and teaching for a wide range of topics. Thank you for that!

But apart from all the good relationships that I experienced in the scientific environment, I have to say an even bigger THANK YOU to my family. Thank you for encouraging me, thank you for your understanding, thank you for giving me a home where I always could relax from science and simply could enjoy the time with you!

7.8 Affidavit

Affidavit

I hereby confirm that my thesis entitled 'Identification of an atypical binding mode of the BTB domain of the transcription factor MIZ1 with a HUWE1-derived peptide' is the result of my own work. I did not receive any help or support from commercial consultants. All sources and/or materials applied are listed and specified in the thesis.

Furthermore, I confirm that this thesis has not yet been submitted as part of another examination process neither in identical nor in similar form.

Place, Date   Signature

Eidesstattliche Erklärung

Hiermit erkläre ich an Eides statt, die Dissertation „Identifikation eines neuen Bindungsmodus zwischen der BTB-Domäne des Transkriptionsfaktors MIZ1 und eines Peptids aus der HECT-E3-Ligase HUWE1" eigenständig, d.h. insbesondere selbständig und ohne Hilfe eines kommerziellen Promotionsberaters, angefertigt und keine anderen als die von mir angegebenen Quellen und Hilfsmittel verwendet zu haben.

Ich erkläre außerdem, dass die Dissertation weder in gleicher noch in ähnlicher Form bereits in einem anderen Prüfungsverfahren vorgelegen hat.

Ort, Datum   Unterschrift